Endoscopic Optical Coherence Tomography for Clinical Studies in the Gastrointestinal Tract

by

Tsung-Han Tsai

B. S. Electrical Engineering
National Taiwan University, Taiwan, 2003

S.M. Electro-Optical Engineering
National Taiwan University, Taiwan, 2005

SUBMITTED TO THE DEPARTMENT OF ELECTRICAL ENGINEERING AND COMPUTER SCIENCE IN PARTIAL FULFILLMENT OF THE REQUIREMENTS FOR THE DEGREE OF

DOCTOR OF PHILOSOPHY IN ELECTRICAL ENGINEERING AND COMPUTER SCIENCE

AT THE
MASSACHUSETTS INSTITUTE OF TECHNOLOGY

SEPTEMBER 2013

Signature of Author: _____
Department of Electrical Engineering and Computer Science
July 30, 2013

Certified by: _____
James G. Fujimoto
Professor of Electrical Engineering and Computer Science
Thesis Supervisor

Accepted by: _____
Leslie A. Kolodziejski
Professor of Electrical Engineering and Computer Science
Chairman, Committee for Graduate Students

Endoscopic Optical Coherence Tomography for Clinical Studies in the Gastrointestinal Tract

by

Tsung-Han Tsai

Submitted to the Department of Electrical Engineering and Computer Science on July 30, 2013 in Partial Fulfillment of the Requirements for the Degree of Doctor of Philosophy in Electrical Engineering and Computer Science at the Massachusetts Institute of Technology

ABSTRACT

Optical coherence tomography (OCT) performs micrometer-scale, cross-sectional and three dimensional imaging by measuring the echo time delay of backscattered light. OCT imaging is performed using low-coherence interferometry. With the development of Fourier domain detection techniques and fiber-optic based OCT endoscopes, high speed internal body imaging was enabled, which makes OCT suitable for clinical research in the human gastrointestinal (GI) tract. Endoscopic OCT imaging is challenging because fast and stable optical scanning must be implemented inside a small imaging probe to acquire useable volumetric information from internal human bodies. Although several studies have shown the use of endoscopic OCT in human gastrointestinal tracts as a real-time surveillance tool, the capability of OCT has not yet been fully explored in endoscopic applications and OCT is not well accepted as a standard imaging modality for GI clinics due to hardware limitations and lack of comprehensive clinical evidences.

This thesis presents a number of clinical studies using endoscopic OCT that provide solutions to clinical problems in the GI tract supported by statistically significant results and the development of ultrahigh speed endoscopic OCT system that enables advanced OCT imaging applications. In collaboration with medical partners, the structural features in the diseased esophagus identified from OCT images are compared before and immediately after different ablative therapies, and features that predict the treatment response are investigated. Working in collaboration with industrial partners, an ultrahigh speed endoscopic OCT imaging system is constructed for clinical research in gastroenterology. Distally actuated imaging catheters are developed, enabling the visualization of the detailed three-dimensional (3D) structure in the gastrointestinal tract. Finally, clinical pilot studies are conducted and demonstrate the utility of the ultrahigh speed endoscopic OCT imaging for broader surveillance coverage, pathology detection, and dye-less contrast enhancement.

The convergence of 3D spatial resolution, imaging speed, field of view, and minimally invasive access enabled by endoscopic OCT are unmatched by most other biomedical imaging techniques. Though still in its early stage of clinical validation, endoscopic OCT may have a profound impact on human healthcare and industrial inspection by enabling visualization and quantification of 3D microstructure *in situ* and in real time.

Thesis Supervisor: James G. Fujimoto
Title: Professor of Electrical Engineering and Computer Science

Acknowledgements

It has been a true privilege to have the opportunity to be a graduate student at MIT in the Department of Electrical Engineering and Computer Science. During the past years, I have worked with so many wonderful scientists, clinicians, and collaborators who have contributed significantly to the thesis work and have taken interest in my professional development. The intellectual stimulation, abundant research opportunities, and fertile environment found in Professor James Fujimoto's Optics and Quantum Electronics group is extremely unique and I am honored to be a part of this group. I owe a debt of gratitude to those who mentored me, to those who worked with me in the lab and the hospital, and to those who are going to continue the work after I depart. To begin with, I would like to thank Prof. Fujimoto for his guidance and support over these years, as well as sharing his insight of the academic and industrial environment in the real world. To my thesis committee members, Dr. Hiroshi Mashimo and Prof. Elfar Adalsteinsson, I really appreciate all your thoughtful input and advice to polish my thesis work. I also thank Dr. Desmond Adler for his mentorship and friendship, and leading me into the hardcore imaging probe development and passing on the secrets of the Fourier Domain Mode Locked lasers. I would not have accomplished much without his help and will never forget his contributions to my career.

It was a pleasure to work with the GI team in the past few years. I had a good time doing all the hard work with Dr. Yu Chen, Dr. Chao Zhou, Dr. Shu-Wei Huang, Hsiang-Chieh Lee, Osman Ahsen, Kaicheng Liang, and Ning Zhang, as well as the support from Dr. Yuankai Tao and Dr. Michael Giacomelli. The "VA Clinics Monday" is an unforgettable memory in my whole Ph.D. career. Additional praise goes to Dr. Mashimo, Dr. Qin Huang, Dr. Laren Becker, Dr. Tejas Kertane, Dr. Walter Chan, Marisa Figueiredo, Frances Achee, and the VA nursing staff for putting up with temperamental computers, fragile imaging probes, and endoscopy suite full of MIT engineers all for the benefit of science.

I would like to thank our group members, Dr. Aaron Aguirre, Dr. Vivek Srinivasan, Dr. Bernhard Baumann, Dr. Ireneusz Grulkowski, Dr. Iwona Gorczynska, Dr. Yueli Chen, Dr. Umit Demirbas, Dr. Yu Gu, Dr. Hafeez Dhalla, Jonathan Liu, Woo Jhon Choi, Martin Kraus, Chen Lu, Ben Lee, Katharin Mohler, and Duo Li. Although we did not directly work together on the same projects, the intellectual exchanges of experience and comments and the assistance of the lab works and experiments were very helpful all the time, and it was always exciting for me to know people from different cultures and to appreciate the opinions from all different prospective. And of course I thank Dorothy Fleischer for all the administrative assistance and ever-present candy dish over the years.

My thesis work cannot be done without the support from the industrial collaborators. Thank you very much to Dr. Joseph Schmitt at Lightlab Imaging – St. Jude Medical, Inc. for supplying the early imaging engines/catheters, and advice that made much of the clinical studies possible. I thank Dr. Vijarsekhar Jayaraman from Praevium Research, Inc., Dr. Benjamin Potsaid, Dr. James Jiang, and Mr. Alex Cable from Thorlabs, Inc. for their scientific and technical contributions, and the generous support of the VCSEL and equipment that made the development of ultrahigh speed clinical imaging system successful.

I must thank National Institute of Health, the Air Force Office of Scientific Research, and the Center of Integration of Medicine and Innovative Technology, and the Government of Taiwan for the funding assistance during my studies. Finally, I save my last and most appreciative thanks for my family and friends, especially my lovely wife, Chun-Ting Su, who sacrificed a lot with her career in order to take good care of me. Now it is my turn to pay her back with the rest of my life. My parents, Chang-Ju Tsai and Li-Yueh Wang have provided so much so that I can have such great life opportunities, and I will always be grateful for their unwavering love and support. I am blessed with a younger sister, Yu-Han Tsai, who has always been my best friend. She works hard in Taiwan and takes care of my family members so I can focus more on my Ph.D. studies, and for this I am so thankful for all her support.

上堂開示頌

塵勞迥脫事非常，緊把繩頭做一場；
不是一番寒徹骨，爭得梅花撲鼻香。

唐　黃檗禪師

This thesis is dedicated to my wife, Chun-Ting, and to our home Taiwan, the Formosa.

TABLE OF CONTENTS

CHAPTER 1

1.0 Introduction to Swept Source Optical Coherence Tomography

1.1 Introduction to OCT Imaging

OCT is an imaging technology that enables micro scale, cross-sectional and three dimensional (3D) imaging of sample microstructure in real time [1-3] and can work as an "optical biopsy" tool for biomedical applications. The microstructure information of the tissue can be obtained with resolutions approaching that of excisional biopsy and histopathology without the need to remove tissue specimens or apply additional contrast agents on the tissue [4-6]. For material inspection applications, OCT can provide nondestructive profilometry as well as the 3D analysis of depth-resolved sample features. OCT is an optical analogy of ultrasound B mode imaging, which is performed by measuring the echo time delay and intensity of back-reflected or backscattered light. As shown in **Figure 1.1**, an optical beam is scanned across the sample and echoes of backscattered light are measured as a function of axial range (depth) and transverse position. Three-dimensional imaging can be conducted by performing a two-dimensional scan pattern at different transverse positions. Three-dimensional OCT (3D-OCT) enables powerful methods for visualizing tissue architecture. 3D-OCT generates comprehensive, volumetric data sets, which can be used to construct arbitrary cross-sectional images, projections along arbitrary axes, or 3D renderings similar to those used in magnetic resonance imaging (MRI) or computed tomography (CT).

OCT is based on a technique known as low coherence interferometry, which has been previously applied to perform optical ranging measurement [7-9]. OCT imaging is performed using a Michelson interferometer with a low coherence length light source as shown in **Figure 1.2**. One arm of the interferometer contains a scanner that scans the light beam over the sample and collects the backscattered light. In most biomedical applications, this arm usually is a microscope for imaging excised tissue specimens or live small animals, or an endoscopic imaging catheter based on fiber optics for imaging inside the body [6]. A second arm of the interferometer has a scanning reference path delay that is mechanically translated over the desired imaging depth in the traditional time domain OCT (TD-OCT) configuration. Optical interference between the light from the sample and reference occurs only when the optical delays match to within the coherence length of the light [10, 11]. "Coherence" refers to a temporal property of the light, which is inversely related to its wavelength or frequency bandwidth. Low coherence interferometry enables the echo delay time and magnitude of backscattered light from internal tissue microstructures to be measured with high time resolution and sensitivity.

1.2 OCT with Fourier Domain Detection

In early 2000s, dramatic advances in OCT technology have resulted in imaging speeds 10 to 200 times faster than standard TD-OCT techniques [12-14]. These new OCT detection techniques, known as Fourier domain detection, can achieve very high speed and sensitivities by measuring backscattered light in the Fourier domain [12-15], enabling 3D-OCT for real-time *in vivo* biomedical applications.

Conventional OCT directly measures the interference signal, while Fourier domain OCT measures the spectrum of the interference signal. The OCT axial scan is then obtained by applying Fourier transformation on the detected spectrum. Several groups working independently demonstrated that Fourier domain detection enables 10 to 100 fold improvements in detection sensitivity, which gives corresponding improvements in the imaging speed [12-14].

Fourier domain OCT includes two different types of techniques known as spectral/Fourier domain OCT (SD-OCT) and swept source OCT (SS-OCT, also known as optical frequency domain imaging or OFDI). Spectral/Fourier domain detection uses a spectrometer and high speed, line scan camera to measure the spectrum of the OCT interference signal and SD-OCT typically operates at 800 nm or 1 μm wavelengths with imaging speed of 29,000-500,000 lines per second [16-20]. This technology especially has had a great impact on ophthalmic OCT imaging because it enables ultrahigh image resolutions as well as 3D-OCT imaging of retinal pathologies *in vivo* for the first time [21, 22].

On the other hand, SS-OCT uses a wavelength-swept laser light source and a photodetector to measure the interference spectrum [23-26], as shown in **Figure 1.3**. SS-OCT enables operation at longer wavelength of 1 μm and 1.3 μm without the need for expensive InGaAs cameras. Imaging at the wavelength range is important because it reduces optical scattering and improves imaging penetration depths in the tissues [5]. Advances in wavelength-swept lasers have enabled high speed OCT imaging up to multi-megahertz [27-31]. This technology is well suited for imaging scattering tissues in organs such as colon, esophagus, and breast ducts, since scattering is significantly increases at shorter wavelength.

Compared to SD-OCT, SS-OCT can have improved overall sensitivity if operated in shot-noise-limit because there is no spectrometer loss and the photodiodes used for the detection are more sensitive than cameras [32-34]. Improved system dynamic range can also be achieved in SS-OCT because it can easily apply dual-balanced detection and use higher bit depth data acquisition (DAQ) systems. In addition, swept source/Fourier domain detection can provide very large number of axial samples, as determined by the speed of DAQ systems. Currently, SS-OCT has proven its value for applications requiring the fastest possible imaging speeds at wavelength of 1.3 μm and 1 μm. For applications where slower speeds are acceptable but axial resolution is of critical importance, such as retinal imaging, SD-OCT remains the dominant technology.

1.3 Swept Source OCT Theory

In the most basic swept source OCT implementation using a single photodetector as shown in **Figure 1.3**, the power received by the photodetector in the case of a single sample reflector is

$$P_{\text{det}}(t) = P_r(t) + P_s(t) + 2\sqrt{P_r(t)P_s(t)}\cos(2k(t)\Delta z + \varphi) \tag{1.1}$$

where P_r is the reference arm power returned to the detector, P_s is the sample arm power returned to the detector, $k(t) = 2\pi / \lambda(t)$ is the time-varying optical wavevector, φ is the interferometric phase shift associated with the detector signal, and Δz is the path length difference between the reference and sample arms [12, 25]. The photocurrent generated from the photodetector can be written as

$$I_{\det}(t) = \rho P_{\det}(t) = \rho[P_r(t) + P_s(t) + 2\sqrt{P_r(t)P_s(t)}\cos(2k(t)\Delta z + \varphi)] \tag{1.2}$$

The first term in Equation (1.1) results in a constant DC photocurrent due to the reference arm power on the photodetector. The second term results in a DC photocurrent that varies with the intensity of the backscattered sample light and is commonly referred to as the "autocorrelation term". The third term is the desired interferometric photocurrent that encodes the axial reflectance profile of the sample. The complex sample reflectance profile can be recovered by Fourier transformation of the photocurrent, which is typically carried out following digitization with a discrete Fourier transform (DFT) algorithm such as the Fast Fourier Transform (FFT).

1.3.1 Signal to Noise Ratio and Sensitivity

Theoretical signal to noise ratio (SNR) requires an understanding of the signal power F_s^2 and the time-averaged noise power $< F_n^2 >$ where F_s and F_n are the DFT values of the signal and noise photocurrent I_s and I_n. From Equation (1.2), the signal interferometric photocurrent from a single sample reflector located at $\Delta z = z_0$ can be written as

$$I_s(t) = 2\rho\sqrt{P_r(t)P_s(t)}\cos(2k(t)z_0 + \varphi) \tag{1.3}$$

The time averaged noise power $< I_n^2(t) >$ is given by

$$< I_n^2(t) >= \left\{ I_{th}^2 + 2\rho q[P_r(t) + P_s(t)] + \rho^2 RIN[P_r(t) + P_s(t)]^2 \right\} * B_{SS} \tag{1.4}$$

where I_{th} is the thermal noise current in the photodetector, q is the electrical charge constant, and B_{SS} is the detector bandwidth in Hz. The three terms in Equation (1.4) represent thermal, shot, and relative intensity noise (RIN) of the laser source in Hz^{-1}.

The SNR of a swept source OCT system is given by $\text{SNR} = |F_s(z_0)|^2 / < F_n^2 >$. The DFT value of either photocurrent is given by

$$F(z_l) = \sum_{m=0}^{N_s - 1} I(k_m) e^{-j2\pi lm / N_s} \tag{1.5}$$

Here $I(k)$ is the sampled photocurrent and N_s is the number of samples acquired per source wavelength sweep. For the signal component, the DFT is zero-values at all axial positions except for $z_l = z_0$. Using

Parseval's theorem, $\sum F^2 = N_s \sum I^2$, the magnitude-squared of the signal DFT is given by $|F(z_0)|^2 = (N_s^2/2) < I_s^2 >$. The factor of ½ arises from the positive and negative frequency peaks associated with the DFT if the real-valued signal photocurrent. The power of the noice DFT is given by $< F_n^2 >= N_s < I_n^2 >$. The SNR for swept source detection therefore becomes

$$SNR = \frac{N_s}{2} \frac{< I_s^2 >}{< I_n^2 >} \tag{1.6}$$

Equation (1.6) illustrates one fundamental advantage of swept source detection over standard TD-OCT methods, which has the SNR simply the ratio $< I_s^2 > / < I_n^2 >$, so swept source detection gives an $N_s/2$ benefit in terms of SNR. In most swept source OCT setups a dual-balanced detector is used to remove the excess noise from the laser source and effectively doubles the signal level, giving and additional 3 dB improvement to SNR. If the detection system is shot noise limited, with negligible thermal noise and laser RIN, and when $P_s << P_r$, the SNR for a swept source system can be approximated as

$$SNR \approx \frac{N_s}{4} \frac{\rho P_s}{q B_{SS}} \tag{1.7}$$

The sensitivity of an OCT system is defined as the minimum detectable sample reflectivity. The minimum detectable reflectivity results in a signal power that is equal to the noise power (SNR = 1). Using $P_s = r^2 P_o$, where r^2 is the reflectivity and P_o is the output power on the sample arm, and the condition SNR = 1 in Equation (1.7), the minimum detectable reflectivity is given by

$$r_{\min}^2 = \frac{4 q B_{SS}}{N_s \rho P_o} \tag{1.8}$$

Sensitivity is typically expressed in dB as

$$Sensitivity = -10 \log\left(\frac{4 q B_{SS}}{N_s \rho P_o} \right) \tag{1.9}$$

Compared to TD-OCT, swept source detection also has an $N_s/2$ sensitivity benefit directly related to the SNR benefit [12, 25]. This advantage can be used to detect very weak sample reflections if the system is operated at low sweep frequencies. However, the OCT imaging system usually has a finite dynamic range so the ability to simultaneously detect strong and extremely weak reflection is limited.

1.3.2 Axial Resolution

The axial resolution is one of the important parameters that determine the utility of a swept source OCT system. The theoretical value of the axial resolution of SS-OCT is the same as the axial resolution of

traditional TD-OCT [1], and is related to the spectral bandwidth span of the laser source used in the imaging system. Theoretical axial resolution for a laser with a Gaussian power spectrum is given by

$$R_{axial} = \frac{2\ln 2}{\pi}\frac{\lambda_c}{n_s \Delta\lambda} \tag{1.10}$$

where λ_c is the center wavelength of the laser source, n_s is the group refractive index of the sample medium, and $\Delta\lambda$ is the full-width-at-half-maximum (FWHM) spectral bandwidth of the laser source or tuning range of the swept source. Typical axial resolutions for swept source OCT systems operating at 1.3 μm are 7-20 μm [25, 29, 35, 36], while systems operating at 1 μm have achieved axial resolution of 10-20 μm in air [30, 37-39].

1.3.3 Imaging Depth and Sampling Rate

Imaging depth limitations in SS-OCT are fundamentally different than in TD-OCT. In scattering medium such as tissue, optical attenuation in the sample reduced the backscattered light returning from deeper surfaces, which decreases the signal level and limits the useable imaging range or "penetration depth". These multiple scattering effects compound this problem for both SS-OCT and TD-OCT. The maximum sample depth that the system can interrogate, independently of optical effects in the sample, is referred to as the "imaging depth". For TD-OCT systems, the imaging depth is determined by the maximum path difference between reference and sample arms that can be obtained. Hence there is no fundamental limit on imaging depth for TD-OCT systems if there is no physical constraint of the reference and sample scanner construction.

In SS-OCT systems, interference fringes are acquired in the Fourier domain, typically by oscilloscopes or data acquisition systems that provide high speed analogue-to-digital (A/D) conversion. Images are generated by applying DFT on the acquired data. The reflection from regions that have longer path length difference between the reference and sample arms are encoded in the interference fringes with progressively higher frequency so imaging depth is therefore limited by the detection and the data acquisition electronics. The photodetector must have sufficient bandwidth to detect the interference fringe frequency $2k(t)z_{\max}$ associated with the maximum imaging depth $z_{\max}$ [25]. The digitizer used to sample the signal must also have sufficient bandwidth and sample rate to avoid attenuation or aliasing of the highest frequency fringe. Maximum imaging depth can be written as

$$z_{\max} = \frac{F_s \cdot c \cdot D}{4n_s \cdot \Delta f \cdot f_{SS}} \tag{1.11}$$

where F_s is the sampling rate of the digitizer, D is the duty cycle of the usable sweep of the swept source, n_s is the group refractive index of the sample medium, $\Delta f \approx c\Delta\lambda/\lambda_c^2$ is the tuning range of the laser in

frequency domain, and f_{SS} is the sweep rate of the swept source. The interference fringes from regions further than the maximum imaging range have fringe frequency higher than $F_s/2$. Based on Nyquist criteria, the sampled data thus become aliased signal in the images. Therefore, an anti-aliasing low pass filter with cut-off frequency of $F_s/2$ is usually applied on the detected interference fringe signal before A/D conversion to avoid aliasing signal from deeper regions.

1.4 Existing Swept Source Technology for OCT Imaging

Swept source OCT was first demonstrated at MIT in 1997, but performance was limited by available laser technologies [23, 24]. Typical swept laser consist of a broadband gain medium with tunable optical bandpass filter in the cavity. The tunable filter is swept so that the transmission frequency varies in time and sufficient time is needed to allow lasing in the transmission bandwidth to build up from spontaneous emission inside the cavity. This limits the maximum tuning rate of the laser and also results in lower power, broader instantaneous linewidth or shorter instantaneous coherence length. SS-OCT with axial imaging rates of 19 kHz was demonstrated in 2003 [40], and 115 kHz axial imaging rates were achieved in 2005 [41].

Fourier domain mode-locking (FDML), developed by our group in 2006, was a new technology for swept source that overcomes the fundamental tuning speed limits set by cavity roundtrip time and enabling high speed OCT imaging [35]. An FDML laser uses a cavity with a long fiber delay line and a fiber Fabry-Perot tunable filter (FFP-TF) whose sweep rate is synchronized with the roundtrip time of light in the cavity. The long fiber delay line stores the entire frequency sweep in the laser cavity and different sweep frequencies return to the FFP-TF at the time when the filter is tuned to transmit them [35]. Multi-megahertz imaging speed was attained with FDML-based OCT by using multiple buffering stages to increase the sweep rate [27-31]. Dispersion in the long fiber-based cavity is a limiting factor for the instantaneous linewidth or coherent length of FDML lasers and can be improved by using intracavity dispersion compensation [42, 43].

The sensitivity roll off or ranging depth in SS-OCT system can also be improved by applying the frequency-comb filter with extremely narrow instantaneous linewidth [44-47]. Compared to the dispersion compensation method, this method has the advantage that the frequency comb filter can be directly integrated into existing swept lasers without the need of characterizing the dispersion in the individual laser cavities. The frequency-comb filter also helps generating discrete frequency steps that are evenly spaced in optical frequency domain, which can be used as a self-calibration source for the OCT imaging system. **Figure 1.4** shows an example frequency-comb based FDML laser with 120 kHz axial line rate. During the operation, the fiber Fabry-Perot tunable filter (FFP-TF) is continuously tuned across

the sweep range and only frequency components that pass through both the FFP-TF and fiber Fabry-Perot frequency comb (FFP-FC) can be amplified by the gain medium, while all other frequency components are suppressed. The resulting output from the laser is modulated intensity in time and each peak corresponds to a frequency component equally spaced next to each other (**Fig. 1.4B**). As shown in **Figs. 1.4C and D**, the narrow instantaneous linewidth provided by the FFP-FC dramatically improves the sensitivity roll off of the FC-FDML laser compared to that of the conventional FDML laser under the same operation conditions, enabling imaging over a longer imaging range. However, aliasing can occur when the reflection occurs outside the principal measurement range set by the FFP-FC, which requires techniques to remove aliasing when imaging the structures that extend over a very broad range of depth [46, 47].

Short cavity swept lasers, with few centimeter cavity lengths, also enable high sweep rate operation [48, 49]. Although the sweep rate of short cavity lasers is limited compared to FDML lasers, short cavity laser are less sensitive to intracavity dispersion and can usually achieve narrower instantaneous linewidth, which significantly improve the sensitivity roll-off of OCT imaging system and are especially suitable for long range imaging [48].

Recently, a new swept laser source technology was developed based on MEMS-tunable vertical cavity surface emitting laser (VCSEL) [50]. The VCSEL operates with a single longitudinal mode instead of multiple modes and therefore has an extremely narrow instantaneous linewidth that supports a long imaging range. The micron-scale cavity length of VCSELs and the rapid MEMS response also allows wide-range real time adjustability of both the sweep frequency and wavelength tuning range compared with other lasers. Therefore, the VCSEL is a promising technology for high-speed, long range OCT imaging [51].

1.5 Figures

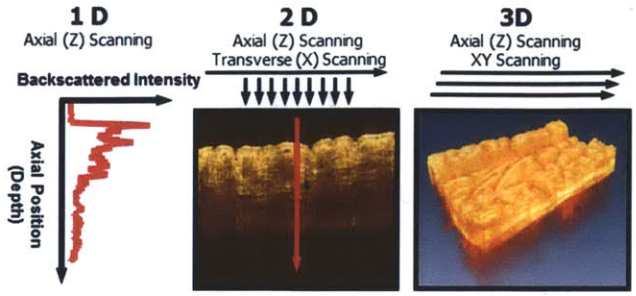

Figure 1.1. OCT generates cross-sectional and 3D images of tissue microstructure by measuring the echo time delay and magnitude of backscattered light. Architectural morphology can be imaged *in vivo* and in real time.

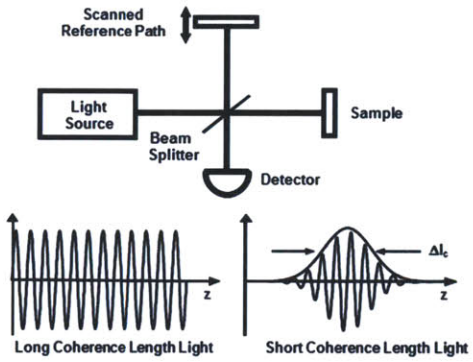

Figure 1.2. OCT uses low coherence interferometry to detect the time delay and magnitude of backscattered light.

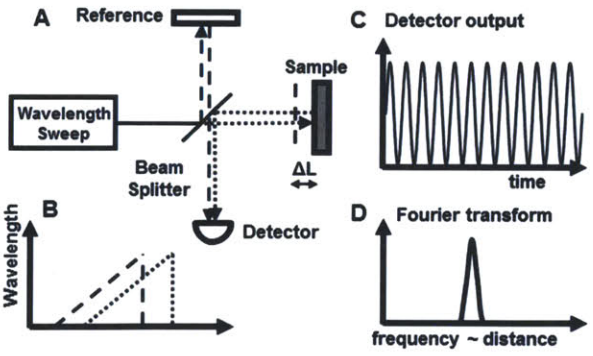

Figure 1.3. Swept source OCT enables a 10-200x increase in imaging speed compared to time domain OCT. A: Interferometer with path difference ΔL and swept laser light source. B: Light from the sample (dotted) and reference path (dashed) are time delayed. C: Interference beat signal frequency is proportional to delay. D: Fourier transform of beat signal measures the delay ΔL.

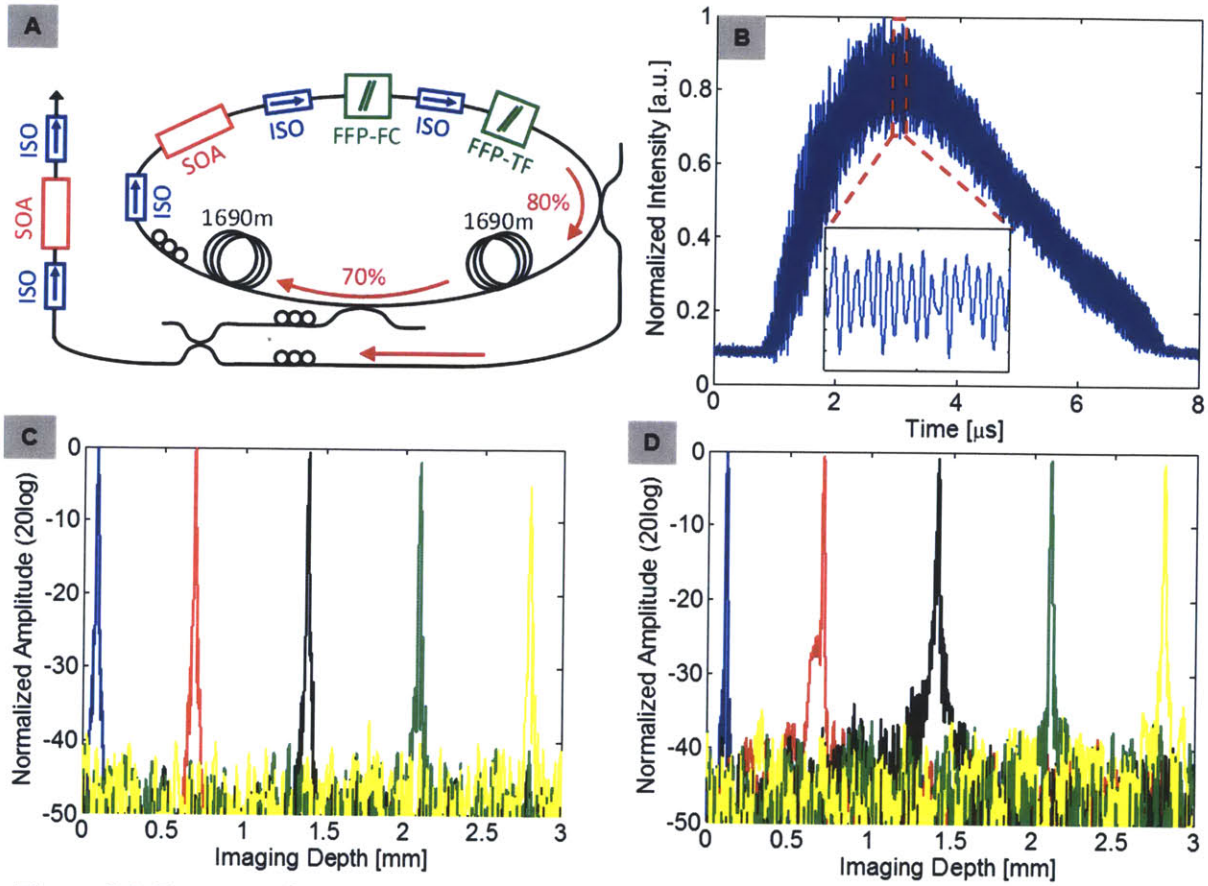

Figure 1.4. Frequency Comb based FDML laser. (A) Schematic diagram of the FC-FDML laser operated at 120 kHz axial line rate. (B) Transient intensity output traces of the FC-FDML laser. Inlet shows the enlarged view from 3.25 us to 3.35 us. (C) Sensitivity roll off from 0.1 mm to 0.28 mm imaging depth using conventional FDML laser (without frequency comb filter). The sensitivity rolls off -5 dB at imaging depth of 0.28 mm. (D) Sensitivity roll off from 0.1 mm to 0.28 mm imaging depth using FC-FDML laser with self-clocking calibration. The sensitivity rolls off -1.3 dB at imaging depth of 0.28 mm. FFP-FC: fiber Fabry-Perot frequency comb filter; FFP-TF: fiber Fabry-Perot tunable filter; ISO: optical isolator; SOA: semiconductor optical amplifier. Originally published in [47].

1.6 References

[1] D. Huang, E. A. Swanson, C. P. Lin, J. S. Schuman, W. G. Stinson, W. Chang, M. R. Hee, T. Flotte, K. Gregory, C. A. Puliafito, and J. G. Fujimoto, "Optical Coherence Tomography," *Science,* vol. 254, pp. 1178-1181, Nov 1991.

[2] J. G. Fujimoto, C. Pitris, S. A. Boppart, and M. E. Brezinski, "Optical coherence tomography: an emerging technology for biomedical imaging and optical biopsy," *Neoplasia,* vol. 2, pp. 9-25, Jan-Apr 2000.

[3] J. G. Fujimoto, "Optical coherence tomography for ultrahigh resolution in vivo imaging," *Nature Biotechnology,* vol. 21, pp. 1361-1367, Nov 2003.

[4] J. G. Fujimoto, M. E. Brezinski, G. J. Tearney, S. A. Boppart, B. Bouma, M. R. Hee, J. F. Southern, and E. A. Swanson, "Optical biopsy and imaging using optical coherence tomography," *Nature Medicine,* vol. 1, pp. 970-972, Sep 1995.

[5] M. E. Brezinski, G. J. Tearney, B. E. Bouma, J. A. Izatt, M. R. Hee, E. A. Swanson, J. F. Southern, and J. G. Fujimoto, "Optical coherence tomography for optical biopsy. Properties and demonstration of vascular pathology," *Circulation,* vol. 93, pp. 1206-1213, Mar 1996.

[6] G. J. Tearney, M. E. Brezinski, B. E. Bouma, S. A. Boppart, C. Pitvis, J. F. Southern, and J. G. Fujimoto, "In vivo endoscopic optical biopsy with optical coherence tomography," *Science,* vol. 276, pp. 2037-2039, Jun 1997.

[7] K. Takada, I. Yokohama, K. Chida, and J. Noda, "New measurement system for fault location in optical waveguide devices based on an interferometric technique," *Applied Optics,* vol. 26, pp. 1603-1608, May 1987.

[8] H. H. Gilgen, R. P. Novak, R. P. Salathe, W. Hodel, and P. Beaud, "Submillimeter optical reflectometry," *IEEE Journal of Lightwave Technology,* vol. 7, pp. 1225-1233, Aug 1989.

[9] R. Youngquist, S. Carr, and D. Davies, "Optical coherence-domain reflectometry: a new optical evaluation technique," *Optics Letters,* vol. 12, pp. 158-160, Mar 1987.

[10] E. A. Swanson, D. Huang, M. R. Hee, J. G. Fujimoto, C. P. Lin, and C. A. Puliafito, "High-speed optical coherence domain reflectometry," *Optics Letters,* vol. 17, pp. 151-153, Jan1992.

[11] E. A. Swanson, J. A. Izatt, M. R. Hee, D. Huang, C. P. Lin, J. S. Schuman, C. A. Puliafito, and J. G. Fujimoto, "In vivo retinal imaging by optical coherence tomography," *Optics Letters,* vol. 18, pp. 1864-1866, Nov 1993.

[12] M. A. Choma, M. V. Sarunic, C. H. Yang, and J. A. Izatt, "Sensitivity advantage of swept source and Fourier domain optical coherence tomography," *Optics Express,* vol. 11, pp. 2183-2189, Sep 2003.

[13] J. F. de Boer, B. Cense, B. H. Park, M. C. Pierce, G. J. Tearney, and B. E. Bouma, "Improved signal-to-noise ratio in spectral-domain compared with time-domain optical coherence tomography," *Optics Letters,* vol. 28, pp. 2067-2069, Nov 2003.

[14] R. Leitgeb, C. K. Hitzenberger, and A. F. Fercher, "Performance of Fourier domain vs. time domain optical coherence tomography," *Optics Express,* vol. 11, pp. 889-894, 2003/04/21 2003.

[15] A. F. Fercher, C. K. Hitzenberger, G. Kamp, and S. Y. Elzaiat, "Measurement of Intraocular Distances by Backscattering Spectral Interferometry," *Optics Communications,* vol. 117, pp. 43-48, May 1995.

[16] B. Cense, N. Nassif, T. C. Chen, M. C. Pierce, S. Yun, B. H. Park, B. Bouma, G. Tearney, and J. F. de Boer, "Ultrahigh-resolution high-speed retinal imaging using spectral-domain optical coherence tomography," *Optics Express,* vol. 12, pp. 2435-2447, May 2004.

[17] N. Nassif, B. Cense, B. H. Park, S. H. Yun, T. C. Chen, B. E. Bouma, G. J. Tearney, and J. F. de Boer, "In vivo human retinal imaging by ultrahigh-speed spectral domain optical coherence tomography," *Opt Lett,* vol. 29, pp. 480-482, Mar 2004.

[18] Y. Zhang, B. Cense, J. Rha, R. S. Jonnal, W. Gao, R. J. Zawadzki, J. S. Werner, S. Jones, S. Olivier, and D. T. Miller, "High-speed volumetric imaging of cone photoreceptors with adaptive optics spectral-domain optical coherence tomography," *Optics Express,* vol. 14, pp. 4380-4394, May 2006.

[19] B. Potsaid, I. Gorczynska, V. J. Srinivasan, Y. L. Chen, J. Jiang, A. Cable, and J. G. Fujimoto, "Ultrahigh speed Spectral/Fourier domain OCT ophthalmic imaging at 70,000 to 312,500 axial scans per second," *Optics Express,* vol. 16, pp. 15149-15169, Sep 2008.

[20] F. LaRocca, S. J. Chiu, R. P. McNabb, A. N. Kuo, J. A. Izatt, and S. Farsiu, "Robust automatic segmentation of corneal layer boundaries in SDOCT images using graph theory and dynamic programming," *Biomed. Opt. Express,* vol. 2, pp. 1524-1538, Jun 2011.

[21] M. Wojtkowski, V. Srinivasan, J. G. Fujimoto, T. Ko, J. S. Schuman, A. Kowalczyk, and J. S. Duker, "Three-dimensional retinal imaging with high-speed ultrahigh-resolution optical coherence tomography," *Ophthalmology,* vol. 112, pp. 1734-46, Oct 2005.

[22] V. J. Srinivasan, M. Wojtkowski, A. J. Witkin, J. S. Duker, T. H. Ko, M. Carvalho, J. S. Schuman, A. Kowalczyk, and J. G. Fujimoto, "High-definition and 3-dimensional imaging of macular pathologies with high-speed ultrahigh-resolution optical coherence tomography," *Ophthalmology,* vol. 113, pp. 2054-2065, Nov 2006.

[23] S. R. Chinn, E. A. Swanson, and J. G. Fujimoto, "Optical coherence tomography using a frequency-tunable optical source," *Optics Letters,* vol. 22, pp. 340-342, Mar 1997.

[24] B. Golubovic, B. E. Bouma, G. J. Tearney, and J. G. Fujimoto, "Optical frequency-domain reflectometry using rapid wavelength tuning of a Cr4+:forsterite laser," *Optics Letters,* vol. 22, pp. 1704-1706, Nov 1997.

[25] S. H. Yun, G. J. Tearney, J. F. de Boer, N. Iftimia, and B. E. Bouma, "High-speed optical frequency-domain imaging," *Optics Express,* vol. 11, pp. 2953-2963, Nov 3 2003.

[26] W. Y. Oh, S. H. Yun, B. J. Vakoc, G. J. Tearney, and B. E. Bouma, "Ultrahigh-speed optical frequency domain imaging and application to laser ablation monitoring," *Applied Physics Letters,* vol. 88, Article 103902, pp. 1-3, Mar 2006.

[27] R. Huber, D. C. Adler, and J. G. Fujimoto, "Buffered Fourier domain mode locking: unidirectional swept laser sources for optical coherence tomography imaging at 370,000 lines/s," *Optics Letters,* vol. 31, pp. 2975-2977, Oct 2006.

[28] D. C. Adler, R. Huber, and J. G. Fujimoto, "Phase-sensitive optical coherence tomography at up to 370,000 lines per second using buffered Fourier domain mode-locked lasers," *Optics Letters,* vol. 32, pp. 626-628, Mar 2007.

[29] T.-H. Tsai, B. Potsaid, M. F. Kraus, C. Zhou, Y. K. Tao, J. Hornegger, and J. G. Fujimoto, "Piezoelectric-transducer-based miniature catheter for ultrahigh-speed endoscopic optical coherence tomography," *Biomed. Opt. Express,* vol. 2, pp. 2438-2448, Aug 2011.

[30] T. Klein, W. Wieser, C. M. Eigenwillig, B. R. Biedermann, and R. Huber, "Megahertz OCT for ultrawide-field retinal imaging with a 1050nm Fourier domain mode-locked laser," *Opt. Express,* vol. 19, pp. 3044-3062, Feb 2011.

[31] W. Wieser, B. R. Biedermann, T. Klein, C. M. Eigenwillig, and R. Huber, "Multi-Megahertz OCT: High quality 3D imaging at 20 million A-scans and 4.5 GVoxels per second," *Opt. Express,* vol. 18, pp. 14685-14704, Jul 2011.

[32] R. Passy, N. Gisin, J. P. Vonderweid, and H. H. Gilgen, "Experimental and Theoretical Investigations of Coherent Ofdr with Semiconductor-Laser Sources," *Journal of Lightwave Technology,* vol. 12, pp. 1622-1630, Sep 1994.

[33] M. A. Choma, A. K. Ellerbee, C. H. Yang, T. L. Creazzo, and J. A. Izatt, "Spectral-domain phase microscopy," *Optics Letters,* vol. 30, pp. 1162-1164, May 2005.

[34] S. J. Moon, A. S. Berger, M. J. Tolentino, and D. M. Misch, "Intravitreal bevacizumab for macular edema from idiopathic juxtafoveal retinal telanglectasis," *Ophthalmic Surgery Lasers & Imaging,* vol. 38, pp. 164-166, Mar-Apr 2007.

[35] R. Huber, M. Wojtkowski, and J. G. Fujimoto, "Fourier Domain Mode Locking (FDML): A new laser operating regime and applications for optical coherence tomography," *Optics Express,* vol. 14, pp. 3225-3237, Apr 2006.

[36] D. C. Adler, Y. Chen, R. Huber, J. Schmitt, J. Connolly, and J. G. Fujimoto, "Three-dimensional endomicroscopy using optical coherence tomography," *Nature Photonics,* vol. 1, pp. 709-716, Dec 2007.

[37] E. C. W. Lee, J. F. de Boer, M. Mujat, H. Lim, and S. H. Yun, "In vivo optical frequency domain imaging of human retina and choroid," *Optics Express,* vol. 14, pp. 4403-4411, May 2006.

[38] R. Huber, D. C. Adler, V. J. Srinivasan, and J. G. Fujimoto, "Fourier domain mode locking at 1050 nm for ultra-high-speed optical coherence tomography of the human retina at 236,000 axial scans per second," *Optics Letters,* vol. 32, pp. 2049-2051, Jul 2007.

[39] V. J. Srinivasan, D. C. Adler, Y. Chen, I. Gorczynska, R. Huber, J. Duker, J. S. Schuman, and J. G. Fujimoto, "Ultrahigh-speed Optical Coherence Tomography for Three-Dimensional and En Face Imaging of the Retina and Optic Nerve Head," *Invest. Ophthalmol. Vis. Sci.,* vol. 49, pp. 5103-5110, Nov 2008.

[40] S. H. Yun, G. J. Tearney, B. E. Bouma, B. H. Park, and J. F. de Boer, "High-speed spectral-domain optical coherence tomography at 1.3 mu m wavelength," *Optics Express,* vol. 11, pp. 3598-3604, Dec 2003.

[41] W. Y. Oh, S. H. Yun, G. J. Tearney, and B. E. Bouma, "115 kHz tuning repetition rate ultrahigh-speed wavelength-swept semiconductor laser," *Optics Letters,* vol. 30, pp. 3159-3161, Dec 2005.

[42] D. C. Adler, W. Wieser, F. Trepanier, J. M. Schmitt, and R. A. Huber, "Extended coherence length Fourier domain mode locked lasers at 1310 nm," *Opt. Express,* vol. 19, pp. 20930-20939, Oct 2011.

[43] W. Wieser, T. Klein, D. C. Adler, F. Trépanier, C. M. Eigenwillig, S. Karpf, J. M. Schmitt, and R. Huber, "Extended coherence length megahertz FDML and its application for anterior segment imaging," *Biomed. Opt. Express,* vol. 3, pp. 2647-2657, Oct 2012.

[44] T. Amano, H. Hiro-Oka, D. Choi, H. Furukawa, F. Kano, M. Takeda, M. Nakanishi, K. Shimizu, and K. Ohbayashi, "Optical frequency-domain reflectometry with a rapid wavelength-scanning superstructure-grating distributed Bragg reflector laser," *Appl. Opt.,* vol. 44, pp. 808-816, Feb 2005.

[45] T. Bajraszewski, M. Wojtkowski, M. Szkulmowski, A. Szkulmowska, R. Huber, and A. Kowalczyk, "Improved spectral optical coherence tomography using optical frequency comb," *Opt. Express,* vol. 16, pp. 4163-4176, Mar 2008.

[46] E. J. Jung, J.-S. Park, M. Y. Jeong, C.-S. Kim, T. J. Eom, B.-A. Yu, S. Gee, J. Lee, and M. K. Kim, "Spectrally-sampled OCT for sensitivity improvement from limited optical power," *Opt. Express,* vol. 16, pp. 17457-17467, Oct 2008.

[47] T. H. Tsai, C. Zhou, D. C. Adler, and J. G. Fujimoto, "Frequency comb swept lasers," *Optics Express,* vol. 17, pp. 21257-21270, Nov 2009.

[48] B. Potsaid, B. Baumann, D. Huang, S. Barry, A. E. Cable, J. S. Schuman, J. S. Duker, and J. G. Fujimoto, "Ultrahigh speed 1050nm swept source / Fourier domain OCT retinal and anterior segment imaging at 100,000 to 400,000 axial scans per second," *Opt. Express,* vol. 18, pp. 20029-20048, Sep 2010.

[49] B. Baumann, W. Choi, B. Potsaid, D. Huang, J. S. Duker, and J. G. Fujimoto, "Swept source / Fourier domain polarization sensitive optical coherence tomography with a passive polarization delay unit," *Opt. Express,* vol. 20, pp. 10229-10241, Apr 2012.

[50] V. Jayaraman, G. D. Cole, M. Robertson, A. Uddin, and A. Cable, "High-sweep-rate 1310 nm MEMS-VCSEL with 150 nm continuous tuning range," *Electronics Letters,* vol. 48, pp. 867-868, Jul 2012.

[51] I. Grulkowski, J. J. Liu, B. Potsaid, V. Jayaraman, J. Jiang, J. G. Fujimoto, and A. E. Cable, "High-precision, high-accuracy ultralong-range swept-source optical coherence tomography using vertical cavity surface emitting laser light source," *Optics Letters,* vol. 38, pp. 673-675, Mar 2013.

CHAPTER 2

2.0 Diseases in the Gastrointestinal Tract and Endoscopic OCT

2.1 Diseases in the Gastrointestinal Tract

Gastrointestinal (GI) cancers will be found in more than 290,000 new people and will cause more than 140,000 deaths in the United States every year [1], and are extremely difficult to detect in the presence of a chronic inflammatory background. Esophageal cancer has a five-year survival rate of only 16% [2], but early detection and treatment achieves a high percentage of regression in patients with dysplasia [3]. Barrett's esophagus (BE) is a precursor to esophageal adenocarcinoma resulting from chronic mucosal injury [4]. BE is characterized by the replacement of squamous epithelium with columnar epithelium in the esophagus caused by long term exposure to the acid environment [5]. Neoplastic changes in BE develop in stages from non-dysplastic metaplasia to increasing grades of dysplasia and eventually to adenocarcinoma [6].

Colorectal cancer is another common GI disease with high morbidity and mortality rates. Colorectal cancer is the third leading cause of cancer death, accounting for about 10% of cancer death overall [2]. Despite its high incidence, colorectal cancer is one of the most detectable, and, if found early, most treatable forms of cancer. Although most colorectal cancers arise from adenomatous polyps that are detectable using conventional endoscopy, many flat (non-ploypoid) lesions are missed during routine examinations [7]. Up to 50% of these more subtle lesions are missed by conventional endoscopy [8]. This is particularly relevant in inflammatory bowel diseases (IBDs) such as ulcerative colitis (UC) and Crohn's disease (CD), where neoplastic tissue is often flat rather than polypoid in form and multifocal in distribution [9]. As many as 1.4 million individuals in the United States have IBDs [10] and are at increased risk for the development of colorectal cancer [11].

This problem is exacerbated in the presence of choronic inflammatory conditions such as Barrett's esophagus and IBD, since early-stage lesion are difficult to distinguish from inflamed GI mucosa. Thus, an imaging modality such as OCT, which can provide sub-surface imaging capabilities is required to allow differentiation of neoplastic tissue from inflamed tissue based on sub-surface architectural morphology.

2.2 Therapies for the GI Diseases

GI diseases can be treated using endoscopic mucosal resection (EMR) [12, 13] or endoscopic ablative therapies, such as argon plasma coagulation (APC) [14], photodynamic therapy (PDT) [3], radiofrequency ablation (RFA) [15], and cryospray ablation (CSA) [16]. RFA and CSA are recently developed methods that utilize thermal gradients to treat dysplastic or cancerous GI diseases.

RFA uses heat generated from the high frequency alternating current to treat the diseased area and has been shown as an effective treatment for dysplastic BE. Ganz, *et al.* reported 90.2% and 80.4% complete response in high grade dysplasia (HGD) and any dysplasia, respectively, from 142 patients with BE who

underwent circumference ablation for HGD [17]. Sharma, *et al.* reported 70% and 98% complete response in BE patientswith 12 months and 30 months follow-up after RFA treatment [18, 19]. Pouw, *et al.* reported 98% complete histological eradication of all dysplasia and intestinal metaplasia in 44 BE patients treated with RFA [20]. One randomized trial using RFA in BE patients with dysplasia has also been published by Shaheen, *et al.*, and 77.4% complete eradication of intestinal metaplasia over 12 months was reported [15].

CSA, on the other hand, uses liquid nitrogen to rapidly freeze and destroy the diseased tissue. CSA has also been shown very effective in eradicating HGD in the esophagus. Johnston, *et al.* reported 78% complete histological eradication of BE in 11 patients using CSA [16]. Greenwald, *et al.*, reported 94%, 88%, and 53% complete response of the HGD, all dysplasia, and intestinal metaplasia in 77 patients with BE and treated CSA [21]. Shaheen, *et al.*, reported 97%, 87%, and 57% complete eradication of HGD, all dysplasia, and intestinal metaplasia in 98 BE patients treated with CSA [22].

Several studies indicate that both RFA and CSA allow broad and superficial treatment fields for GI diseases [15, 16, 23, 24], but some other studies show that the recurrences of the diseases were observed months or years after successful eradication. Vaccaro, *et al.* reported a 25.9% cumulative incident of newly detected intestinal metaplasia in one year [25]. Fleischer, *et al.* reported 8% BE recurrence in 50 patients who had complete eradiation of BE during the 5-year follow-up in a prospective multicenter trial [26]. There are several possible causes that the recurrence of the GI diseases can occur after the complete eradication. One postulate is that, after the ablation therapies, the ablated sites recover with neosquamous epithelium covering on the top. A significant portion (20~30%) of patients show subsquamous intestinal metaplasia (SSIM) under the neosquamous epithelium after the therapeutic treatment [27, 28], which could be associated with a future risk of recurrence of BE or adenocarcinoma under the neosquamous epithelium [14, 29]. Currently, random four-quadrant biopsy is the clinical standard for evaluating dysplasia and adenocarcinoma in BE and colorectal cancer patients [30, 31]. Due to the limitation sampling area (about 1 to 2 mm^2) and sampling depth of biopsy forceps, SSIM was only found in 25% of patients before and in 5% of patients after successful RFA treatment [15, 22, 24, 26]. Neosquamous epithelium recovered from the ablation usually is thicker than normal squamous epithelium, making it more difficult to catch SSIM underneath. A technology such as 3D-OCT that can be used for guiding excisional biopsy and providing subsurface tissue imaging would significantly reduce sampling errors, improving diagnostic sensitivity, treatment follow-up, and outcome.

2.3 Endoscopic OCT in the GI Tract

OCT technology has been successfully applied to numerous biomedical fields including ophthalmology [32], cardiology [33], gastroenterology [34], urology [35], and gynecology [36]. One

particularly promising application for ultrahigh speed 3D-OCT imaging is gastroenterology. OCT can be readily integrated with a wide range of imaging devices such as fiber optic catheters and endoscopes to enable imaging inside the body [37]. The first demonstration of *in vivo* endoscopic OCT was performed by Tearney, *et al.* [38]. This study demonstrated high speed OCT imaging of the gastrointestinal and pulmonary tracts in the rabbit using a 1mm diameter fiber optic catheter. Endoscopic OCT imaging of the human gastrointestinal (GI) tract has been investigated by several groups and studies have been performed in the esophagus and stomach [34, 39-46], small and large intestine [40, 42, 47-51], and bile duct [52, 53]. Barrett's esophagus was clearly differentiated from non-neoplastic tissues. OCT has been demonstrated to detect specialized intestinal metaplasia in BE patients [54, 55] and transmural inflammation in IBD patients [48]. OCT has also been investigated for differentiating hyperplastic from adenomatous polyps in the colon [49]. Recent endoscopic OCT studies have shown promise for detection of HGD in BE. Evan, *et al.* reported a sensitivity of 83% and a specificity of 75% for detecting HGD and intramucosal carcinoma with blinded scoring of OCT images from 55 patients [56]. Isenberg, *et al.* reported a sensitivity of 68% and a specificity of 82%, with an accuracy of 78% for the detection of dysplasia from 33 patients with BE [57]. Using computer-aided tissue classification techniques applied to OCT images, Qi, *et al.* reported a sensitivity of 82% and a specificity of 74% for identifying dysplasia in 13 patients [58].

With the development of Fourier domain OCT technologies, endoscopic OCT imaging has recently been demonstrated with much higher imaging speed and better resolution. Ultrahigh resolution spectral/Fourier domain endoscopic OCT with 2.4 μm axial resolution using a Ti:Sapphire laser with 20 kHz axial scan rates was demonstrated in the mouse colon [59]. Using swept source/Fourier domain technologies, *in vivo* 3D-OCT volumetric imaging of the porcine esophagus and artery has been demonstrated at 10 kHz and 54 kHz axial scan rates, respectively [60, 61]. Using FDML technologies, Prof. Fujimoto' s group at MIT achieved record axial scan rates of 100-500 kHz and demonstrated *in vivo* endoscopic 3D-OCT imaging in the rabbit and human GI tracts with axial resolution of 7-20 μm [62, 63]. Suter, *et al.* combined the laser marking technique with endoscopic OCT to perform the guided biopsies and reported a success rate of 97% to mark the target locations identified by OCT imaging [46]. Hatta, *et al.* reported accuracy rate of 92.7% for the staging of tumor infiltration in superficial esophageal squamous carcinoma [64]. These endoscopic studies demonstrate that OCT imaging can be readily integrated with endoscopic procedures and potentially provides valuable diagnostic information. There are very few clinical studies using endoscopic OCT in the GI tract that provide significant solutions to certain clinical problems, so currently OCT is still not well accepted as a standard imaging modality for GI clinics.

2.4 Recent Achievements of Endoscopic 3D-OCT in Clinical Gastroenterology

In collaboration with Dr. Hiroshi Mashimo at the Veterans Affairs Boston Healthcare System (VABHS) and Lightlab Imaging Inc. / St. Jude Medical, Prof. Fujimoto's group at MIT has been working on the swept source based endoscopic OCT imaging in the human GI tract since 2007. With the 3D-OCT imaging engine developed by Lightlab Imaging Inc. / St. Jude Medical and modifications made by the MIT group [62], endoscopic 3D-OCT imaging has been performed extensively on patients with BE or IBD and several case reports and clinical studies have been published recently. This section briefly goes through the studies recently conducted by the group and more detailed clinical studies will be described in Chapter 3 and 4.

2.4.1 Barrett's Esophagus Study

Figure 2.1 shows an example OCT images from a volumetric data set in a patient with BE [45]. Volumetric data sets enable the generation of *en face* images, thereby enabling precise registration of cross-sectional data with *en face* features. Projection techniques can be used to display specific depths within the tissue selectively, thus enhancing image contrast for specific architectural features. Cross-sectional images with arbitrary orientation can also be generated from the 3D data. The *en face* view (**Fig. 2.1A**) and cross-sectional views (**Figs. 2.1B and C**) illustrate the characteristic glandular structures associated with BE, which can be easily distinguished from the normal esophagus that has fine layered structure. The zoomed-in view of glandular structures (**Fig. 2.1D**) correlates well with the histology of BE shown in **Fig. 2.1E**. Endoscopic 3D-OCT is capable of differentiating glandular and squamous epithelium *in vivo*. This is important such as the assessment of endoscopic therapies at multiple time points, since it provides an inherent positional registration that is difficult to obtain with cross-sectional OCT images alone.

The 3D-OCT imaging is able to further distinguish BE glands from any normal glands found near the gastroesophageal junction (GEJ) or in the esophagus. **Figure 2.2** provides cross-sectional OCT images and corresponding histology from and *ex vivo* endoscopic mucosal resection (EMR) nodule and an *in vivo* region near the GEJ. Normal esophageal glands in a well circumscribed lobular form are large (1 mm) with a heterogeneous moderately-scattering center, as shown in **Figs. 2.2A and B**. BE glands are irregular, smaller (100-300 μm), have sharp borders in the OCT image, and are devoid of signal in the centers, as shown in **Figs. 2.2C and D**. Gastric glands are found underneath gastric pits and may have slightly more diffuse border in the OCT image, which is shown in **Figs. 2.2E and F**.

2.4.2 Cervical Inlet Patch

Cervical inlet patch (CIP) is characterized by the presence of heterotopic columnar gastric mucosa in the upper esophagus, most commonly located just below the upper esophageal sphincter (UES). The incident of CIP has been reported from as low as 1% to as much as 10% of endoscopic cases in different adult studies [65, 66]. It is unclear whether CIP is congenital or acquired. One postulate is that CIP originates from incomplete embryonic replacement of the stratified epithelium, which normally starts at the 4th month of gestation. Immunohistochemical studies suggest an embryologic origin for CIP on account of differences in endocrine markers such as serotonin, glucagon, pancreatic polypeptide, somatostatin and neurotensin in histologic specimens of CIP and BE [67]. A second postulate is that CIP, especially as noted in adults, is an acquired metaplastic change occurring in the squamous mucosa of the esophagus and is associated with predisposing factors for gastroesophageal reflux disease (GERD), such as sliding hiatal hernia [68]. Its incidence is up to four-fold higher in patients having BE [69] and CIP was found in almost one third of patients having dysplastic BE or adenocarcinoma [70]. Thus, long-standing acid reflux is thought to lead to columnar metaplasia in the upper esophagus, similar to BE. Several reports suggest that CIP may progress to adenocarcinoma [71-74].

Figure 2.3 shows an endoscopic view of and volumetric 3D-OCT data set of CIP obtained from a 30-year-old patient. During retraction of the endoscope, a pink circular lesion was observed under white light endoscopy in the upper esophagus (**Fig. 2.3A**). The *en face* projection image (**Fig. 2.3B**) at 400 μm depth underneath the tissue surface showed columnar epithelium consistent with the CIP and surrounding squamous epithelium. Cross-sectional OCT images (**Figs. 2.3C, D, and F**) clearly demonstrated columnar and squamous epithelium in the CIP region and the surrounding esophagus, respectively. Biopsy specimens taken from the imaged lesion confirmed the finding of CIP. The OCT features matched representative hematocylin and eosin (H&E) histology (**Figs. 2.3E and G**). These results demonstrated the feasibility of using OCT to evaluate GI tissue morphology *in situ* and in real-time [75, 76]. Since OCT imaging can be performed with small diameter catheters introduced orally or nasally, this emerging technology might be used to screen patients with troublesome upper esophagus symptom for CIP, BE and other changes in the epithelium , even without endoscopy or the need for conscious sedation.

2.4.3 Characterization of Subsquamous Intestinal Metaplasia

As mentioned in Section 2.2, subsquamous intestinal metaplasia (SSIM), also known as buried glands, is usually underappreciated with current surveillance protocol with standard white light endoscopy. Endoscopic 3D-OCT imaging uniquely enables depth-resolved imaging of a broad area with near-microscope resolution and can be used for identifying and characterizing SSIM before and after ablative therapies [45]. **Figure 2.4** shows examples of cross-sectional OCT images and corresponding histology. **Figs. 2.4A and B** was acquired *in vivo* at the position of the GEJ. SSIM were identified with 3D-OCTat

the GEJ of a patient during the imaging procedure. The corresponding histological micrograph shown in **Fig. 2.4C** confirmed the presence of SSIM with intestinal metaplasia underneath the neosquamous epithelium. **Figs. 2.4D and E** was obtained from an *ex vivo* EMR specimen to enable more accurate correspondence of OCT images with histology. From cross-sectional OCT images, squamous epithelium is characterized by a low scattering, homogeneous layer at the mucosal surface. SSIM was identified as sparsely distributed hyposcattering structures underneath the squamous epithelium with various sizes and shapes. The histological micrograph of the EMR specimen (**Fig. 2.4F**) also confirmed the presence of buried glands with intestinal metaplasia.

In the study of 27 patients with short-segment BE, 3D-OCT was demonstrated to provide a 30 to 60 times larger field of view compared with jumbo and standard forceps biopsy and sufficient imaging depth to the lamina propria/muscularis mucosa to facilitate the detection of SSIM before and after the treatment. A high prevalence of SSIM was found in 72% of patients who had residual BE and in 63% of patients who achieved complete response to the ablation treatment. The high prevalence is consistent with biopsy results from previous studies when accounting for difference in sampling area between OCT imaging and excisional biopsy [77]. The number of SSIM per patient decreased significantly after the patients achieved complete response ($P = 0.02$). However, the size and distribution of the SSIM did not change significantly in patients with short-segment BE whether the patients achieved complete response or not. This study suggested that OCT may be used to stratify the patient risk and could help direct areas for re-ablation. Furthermore, OCT can also be used to evaluate other subsurface features and may be used to evaluate the efficacy of other endoscopic therapies, such as CSA and PDT [78].

2.5 Figures

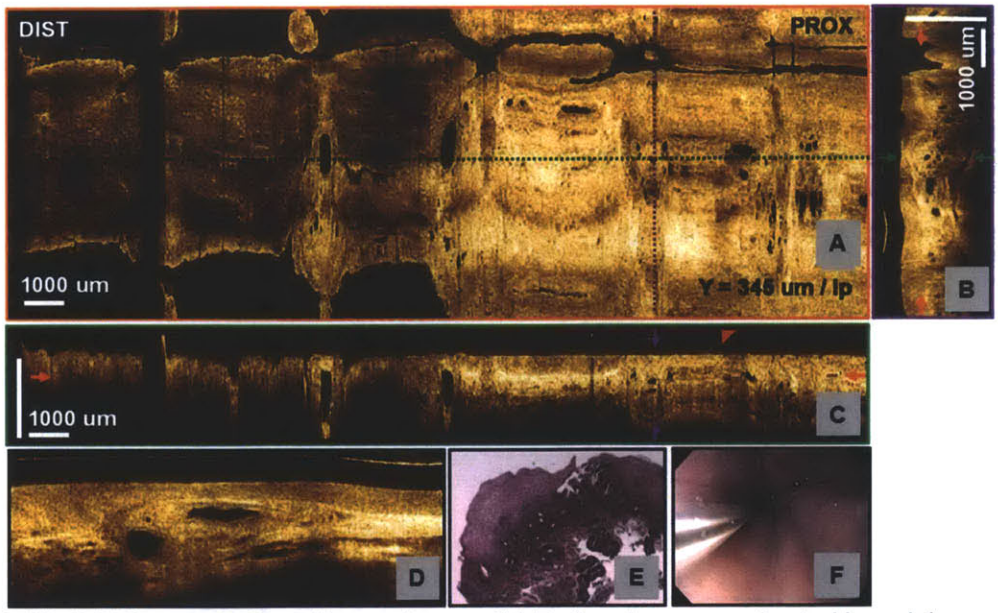

Figure 2.1. 3D-OCT images in Barrett's esophagus. (A) *En face* image constructed by axial summation of a thin slice (~20 um) in the data. (B) XZ cross section shows the characteristic glandular structures associated with Barrett's esophagus. (C) YZ cross section shows the glandular structures. (D) Close-up view of YZ cross-section. (E) Representative histology of Barrett's esophagus. (F) White-light video endoscopy image of region analyzed with 3D-OCT. Originally published in [45].

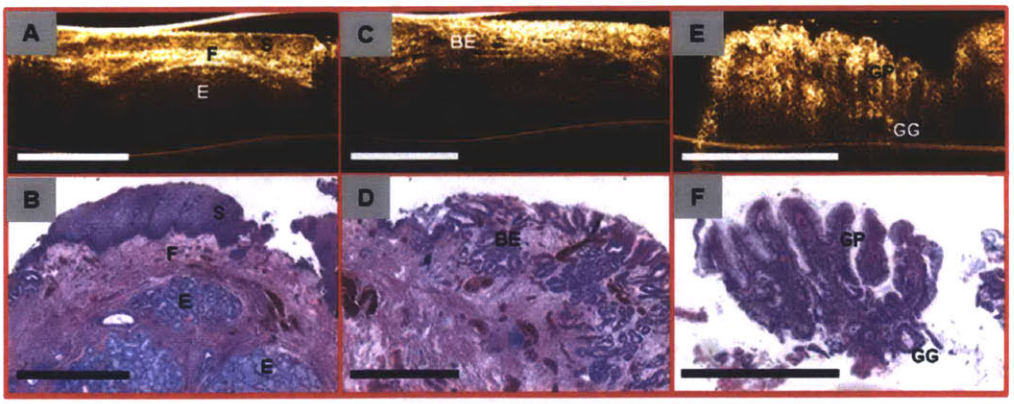

Figure 2.2. OCT images and corresponding histology of esophageal, BE, and gastric glands obtained from an *ex vivo* esophageal EMR nodule (A-D) and an *in vivo* image near the GEJ (E-F). (A, B) OCT and corresponding histology demonstrate representative esophageal glands (E) with a diameter of about 1 mm underneath squamous epithelium (S) and fibrous tissue (F). (C, D) BE glands (BE) were also observed from the same nodule. (E, F) A gastric gland (GG) was observed underneath hyperplastic gastric pits (GP). Scale bars: 1 mm.

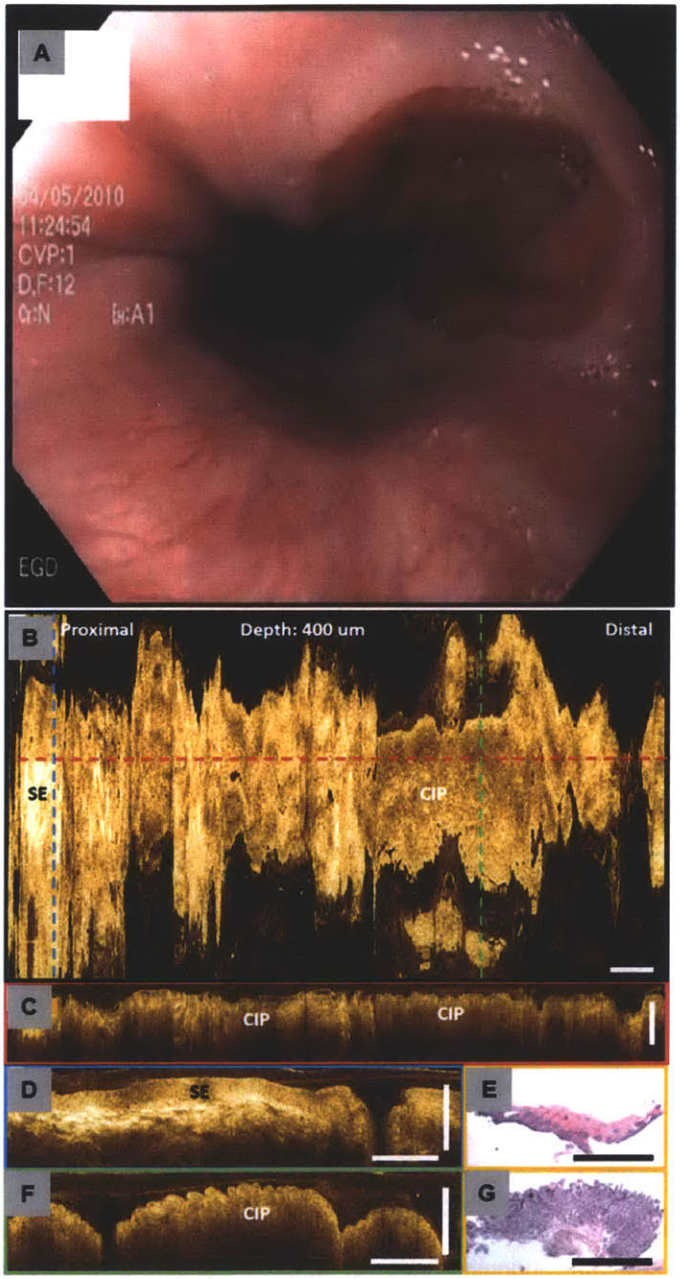

Figure 2.3. Endoscopic view and 3D-OCT images of cervical inlet patch (CIP). (A) Endoscopic view. (B) En face projection OCT image at 400 um underneath the tissue surface. Regions with CIP and surrounding squamous epithelium (SE) can be identified. (C) Cross-sectional OCT image along the probe pullback direction, corresponding to the red dashed line marked in (B). (D, F) Cross-sectional OCT images of squamous epithelium and CIP, respectively. The OCT images correspond to the blue and green dashed lines marked in (B), respectively. (E, G) Representative histology of normal squamous epithelium and CIP. Scale bars: 1mm. Originally published in [76].

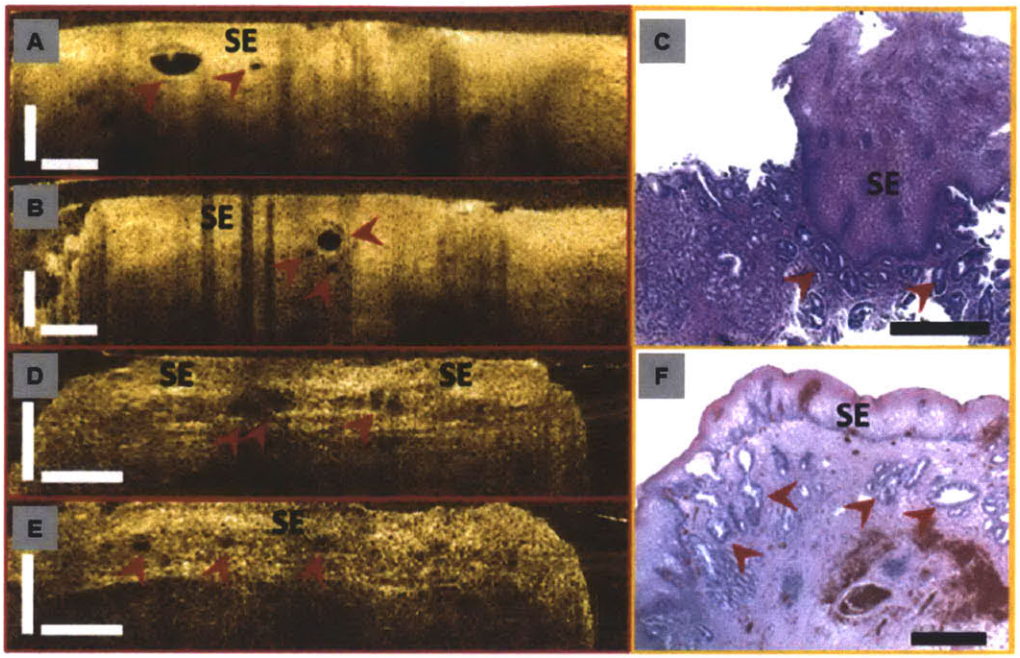

Figure 2.4. Cross-sectional optical coherence tomography images and corresponding histology showing buried glands (red arrowheads) from one patient *in vivo* (A-C) and one *ex vivo* EMR specimen (D-F). C, F, Histological micrographs confirmed the presence of buried glands with intestinal metaplasia. SE, squamous epithelium. Scale bars, 500 um. Originally published in [78].

2.6 References

[1] "Cancer Facts and Figures," American Cancer Society 2013.

[2] A. Jemal, R. Siegel, E. Ward, T. Murray, J. Xu, and M. J. Thun, "Cancer statistics, 2007," *CA Cancer J Clin,* vol. 57, pp. 43-66, Jan-Feb 2007.

[3] B. F. Overholt, M. Panjehpour, and J. M. Haydek, "Photodynamic therapy for Barrett's esophagus: follow-up in 100 patients," *Gastrointestinal Endoscopy,* vol. 49, pp. 1-7, Jan 1999.

[4] N. J. Shaheen, "Advances in Barrett's esophagus and esophageal adenocarcinoma," *Gastroenterology,* vol. 128, pp. 1554-1566, May 2005.

[5] X. Chen and C. S. Yang, "Esophageal adenocarcinoma: a review and perspectives on the mechanism of carcinogenesis and chemoprevention," *Carcinogenesis,* vol. 22, pp. 1119-1129, Aug 2001.

[6] A. J. Cameron and H. A. Carpenter, "Barrett's esophagus, high-grade dysplasia, and early adenocarcinoma: a pathological study," *Am J Gastroenterol,* vol. 92, pp. 586-591, Apr 1997.

[7] D. K. Rex, "Maximizing detection of adenomas and cancers during colonoscopy," *American Journal of Gastroenterology,* vol. 101, pp. 2866-2877, Dec 2006.

[8] R. Kiesslich, M. von Bergh, M. Hahn, G. Hermann, and M. Jung, "Chromoendoscopy with indigocarmine improves the detection of adenomatous and nonadenomatous lesions in the colon," *Endoscopy,* vol. 33, pp. 1001-1006, Dec 2001.

[9] S. H. Itzkowitz and N. Harpaz, "Diagnosis and management of dysplasia in patients with inflammatory bowel diseases," *Gastroenterology,* vol. 126, pp. 1634-1648, May 2004.

[10] E. V. Loftus, "Clinical epidemiology of inflammatory bowel disease: Incidence, prevalence, and environmental influences," *Gastroenterology,* vol. 126, pp. 1504-1517, May 2004.

[11] J. A. Eaden, K. R. Abrams, and J. F. Mayberry, "The risk of colorectal cancer in ulcerative colitis: a meta-analysis," *Gut,* vol. 48, pp. 526-535, Apr 2001.

[12] H. Inoue and M. Endo, "Endoscopic esophageal mucosal resection using a transparent tube," *Surgical Endoscopy,* vol. 4, pp. 198-201, Dec 1990.

[13] T. Oyama, A. Tomori, K. Hotta, S. Morita, K. Kominato, M. Tanaka, and Y. Miyata, "Endoscopic Submucosal Dissection of Early Esophageal Cancer," *Clinical Gastroenterology and Hepatology,* vol. 3, pp. S67-S70, Jul 2005.

[14] J. L. Van Laethem, M. O. Peny, I. Salmon, M. Cremer, and J. Deviere, "Intramucosal adenocarcinoma arising under squamous re-epithelialisation of Barrett's oesophagus," *Gut,* vol. 46, pp. 574-577, Apr 2000.

[15] N. J. Shaheen, P. Sharma, B. F. Overholt, H. C. Wolfsen, R. E. Sampliner, K. K. Wang, J. A. Galanko, M. P. Bronner, J. R. Goldblum, A. E. Bennett, B. A. Jobe, G. M. Eisen, M. B. Fennerty, J. G. Hunter, D. E. Fleischer, V. K. Sharma, R. H. Hawes, B. J. Hoffman, R. I. Rothstein, S. R. Gordon, H. Mashimo, K. J. Chang, V. R. Muthusamy, S. A. Edmundowicz, S. J. Spechler, A. A. Siddiqui, R. F. Souza, A. Infantolino, G. W. Falk, M. B. Kimmey, R. D. Madanick, A. Chak, and C. J. Lightdale, "Radiofrequency Ablation in Barrett's Esophagus with Dysplasia," *New England Journal of Medicine,* vol. 360, pp. 2277-2288, May 2009.

[16] M. H. Johnston, J. A. Eastone, J. D. Horwhat, J. Cartledge, J. S. Mathews, and J. R. Foggy, "Cryoablation of Barrett's esophagus: a pilot study," *Gastrointestinal Endoscopy,* vol. 62, pp. 842-848, Dec 2005.

[17] R. A. Ganz, B. F. Overholt, V. K. Sharma, D. E. Fleischer, N. J. Shaheen, C. J. Lightdale, S. R. Freeman, R. E. Pruitt, S. M. Urayama, F. Gress, D. A. Pavey, M. S. Branch, T. J. Savides, K. J. Chang, V. R. Muthusamy, A. G. Bohorfoush, S. C. Pace, S. R. DeMeester, V. E. Eysselein, M. Panjehpour, and G. Triadafilopoulos, "Circumferential ablation of Barrett's esophagus that contains high-grade dysplasia: a U.S. multicenter registry," *Gastrointestinal Endoscopy,* vol. 68, pp. 35-40, Jul 2008.

[18] V. K. Sharma, K. K. Wang, B. F. Overholt, C. J. Lightdale, M. B. Fennerty, P. J. Dean, D. K. Pleskow, R. Chuttani, A. Reymunde, N. Santiago, K. J. Chang, M. B. Kimmey, and D. E. Fleischer, "Balloon-based, circumferential, endoscopic radiofrequency ablation of Barrett's

esophagus: 1-year follow-up of 100 patients (with video)," *Gastrointestinal Endoscopy,* vol. 65, pp. 185-195, Feb 2007.

[19] D. E. Fleischer, B. F. Overholt, V. K. Sharma, A. Reymunde, M. B. Kimmey, R. Chuttani, K. J. Chang, C. J. Lightdale, N. Santiago, D. K. Pleskow, P. J. Dean, and K. K. Wang, "Endoscopic ablation of Barrett's esophagus: a multicenter study with 2.5-year follow-up," *Gastrointestinal Endoscopy,* vol. 68, pp. 867-876, Oct 2008.

[20] R. Pouw, J. Gondrie, C. Sondermeijer, F. ten Kate, T. van Gulik, K. Krishnadath, P. Fockens, B. Weusten, and J. Bergman, "Eradication of Barrett Esophagus with Early Neoplasia by Radiofrequency Ablation, with or without Endoscopic Resection," *Journal of Gastrointestinal Surgery,* vol. 12, pp. 1627-1637, 2008.

[21] B. D. Greenwald, J. A. Dumot, J. D. Horwhat, C. J. Lightdale, and J. A. Abrams, "Safety, tolerability, and efficacy of endoscopic low-pressure liquid nitrogen spray cryotherapy in the esophagus," *Diseases of the Esophagus,* vol. 23, pp. 13-19, Jan 2010.

[22] N. J. Shaheen, B. D. Greenwald, A. F. Peery, J. A. Dumot, N. S. Nishioka, H. C. Wolfsen, J. S. Burdick, J. A. Abrams, K. K. Wang, D. Mallat, M. H. Johnston, A. M. Zfass, J. O. Smith, J. S. Barthel, and C. J. Lightdale, "Safety and efficacy of endoscopic spray cryotherapy for Barrett's esophagus with high-grade dysplasia," *Gastrointestinal Endoscopy,* vol. 71, pp. 680-685, Apr 2010.

[23] R. D. Odze and G. Y. Lauwers, "Histopathology of Barrett's esophagus after ablation and endoscopic mucosal resection therapy," *Endoscopy,* vol. 40, pp. 1008-1015, Dec 2008.

[24] J. J. G. H. M. Bergman, "Radiofrequency Ablation - Great for Some or Justified for Many?," *New England Journal of Medicine,* vol. 360, pp. 2353-2355, May 2009.

[25] B. Vaccaro, S. Gonzalez, J. Poneros, P. Stevens, K. Capiak, C. Lightdale, and J. Abrams, "Detection of Intestinal Metaplasia After Successful Eradication of Barrett's Esophagus with Radiofrequency Ablation," *Digestive Diseases and Sciences,* vol. 56, pp. 1996-2000, Jul 2011.

[26] D. E. Fleischer, B. F. Overholt, V. K. Sharma, A. Reymunde, M. B. Kimmey, R. Chuttani, K. J. Chang, R. Muthasamy, C. J. Lightdale, N. Santiago, D. K. Pleskow, P. J. Dean, and K. K. Wang, "Endoscopic radiofrequency ablation for Barrett's esophagus: 5-year outcomes from a prospective multicenter trial," *Endoscopy,* vol. 42, pp. 781-789, Oct 2010.

[27] J. P. Byrne, G. R. Armstrong, and S. E. Attwood, "Restoration of the normal squamous lining in Barrett's esophagus by argon beam plasma coagulation," *Am J Gastroenterol,* vol. 93, pp. 1810-5, Oct 1998.

[28] C. J. Kelty, R. Ackroyd, N. J. Brown, T. J. Stephenson, C. J. Stoddard, and M. W. Reed, "Endoscopic ablation of Barrett's oesophagus: a randomized-controlled trial of photodynamic therapy vs. argon plasma coagulation," *Aliment Pharmacol Ther,* vol. 20, pp. 1289-96, Dec 2004.

[29] K. Ragunath, N. Krasner, V. S. Raman, M. T. Haqqani, C. J. Phillips, and I. Cheung, "Endoscopic ablation of dysplastic Barrett's oesophagus comparing argon plasma coagulation and photodynamic therapy: a randomized prospective trial assessing efficacy and cost-effectiveness," *Scand J Gastroenterol,* vol. 40, pp. 750-8, Jul 2005.

[30] S. J. Spechler, "Screening and surveillance for complications related to gastroesophageal reflux disease," *The American journal of medicine,* vol. 111 Suppl 8A, pp. 130S-136S, Dec 2001.

[31] H. Mashimo, M. S. Wagh, and R. K. Goyal, "Surveillance and screening for Barrett esophagus and adenocarcinoma," *J Clin Gastroenterol,* vol. 39, pp. S33-41, Apr 2005.

[32] W. Drexler, U. Morgner, R. K. Ghanta, F. X. Kärtner, J. S. Schuman, and J. G. Fujimoto, "Ultrahigh-resolution ophthalmic optical coherence tomography," *Nature Medicine,* vol. 7, pp. 502-507, Apr 2001.

[33] G. J. Tearney, M. E. Brezinski, S. A. Boppart, B. E. Bouma, N. Weissman, J. F. Southern, E. A. Swanson, and J. G. Fujimoto, "Catheter-based optical imaging of a human coronary artery," *Circulation,* vol. 94, p. 3013, Dec 1996.

[34] B. E. Bouma, G. J. Tearney, C. C. Compton, and N. S. Nishioka, "High-resolution imaging of the human esophagus and stomach in vivo using optical coherence tomography," *Gastrointestinal endoscopy,* vol. 51(4) Pt 1, pp. 467-74, Apr 2000.

[35] G. J. Tearney, M. E. Brezinski, J. F. Southern, B. E. Bouma, S. A. Boppart, and J. G. Fujimoto, "Optical biopsy in human urologic tissue using optical coherence tomography," *The Journal of urology,* vol. 157, pp. 1915-9, May 1997.

[36] P. F. Escobar, J. L. Belinson, A. White, N. M. Shakhova, F. I. Feldchtein, M. V. Kareta, and N. D. Gladkova, "Diagnostic efficacy of optical coherence tomography in the management of preinvasive and invasive cancer of uterine cervix and vulva," *International Journal of Gynecological Cancer,* vol. 14, pp. 470-474, May-Jun 2004.

[37] G. J. Tearney, M. E. Brezinski, B. E. Bouma, S. A. Boppart, C. Pitris, J. F. Southern, and J. G. Fujimoto, "In vivo endoscopic optical biopsy with optical coherence tomography," *Science,* vol. 276, pp. 2037-2039, Jun 1997.

[38] G. J. Tearney, M. E. Brezinski, B. E. Bouma, S. A. Boppart, C. Pitvis, J. F. Southern, and J. G. Fujimoto, "In vivo endoscopic optical biopsy with optical coherence tomography," *Science,* vol. 276, pp. 2037-2039, Jun 1997.

[39] A. M. Sergeev, V. M. Gelikonov, G. V. Gelikonov, F. I. Feldchtein, R. V. Kuranov, N. D. Gladkova, N. M. Shakhova, L. B. Suopova, A. V. Shakhov, I. A. Kuznetzova, A. N. Denisenko, V. V. Pochinko, Y. P. Chumakov, and O. S. Streltzova, "In vivo endoscopic OCT imaging of precancer and cancer states of human mucosa," *Optics Express,* vol. 1, pp. 432-440, Dec 1997.

[40] M. V. Sivak, Jr., K. Kobayashi, J. A. Izatt, A. M. Rollins, R. Ung-Runyawee, A. Chak, R. C. Wong, G. A. Isenberg, and J. Willis, "High-resolution endoscopic imaging of the GI tract using optical coherence tomography," *Gastrointestinal endoscopy,* vol. 51(4) Pt 1, pp. 474-9, Apr 2000.

[41] S. Jäckle, N. Gladkova, F. Feldchtein, A. Terentieva, B. Brand, G. Gelikonov, V. Gelikonov, A. Sergeev, A. Fritscher-Ravens, J. Freund, U. Seitz, S. Schröder, and N. Soehendra, "In vivo endoscopic optical coherence tomography of esophagitis, Barrett's esophagus, and adenocarcinoma of the esophagus," *Endoscopy,* vol. 32, pp. 750-5, Oct 2000.

[42] S. Jäckle, N. Gladkova, F. Feldchtein, A. Terentieva, B. Brand, G. Gelikonov, V. Gelikonov, A. Sergeev, A. Fritscher-Ravens, J. Freund, U. Seitz, S. Soehendra, and N. Schrödern, "In vivo endoscopic optical coherence tomography of the human gastrointestinal tract--toward optical biopsy," *Endoscopy,* vol. 32, pp. 743-9, Oct 2000.

[43] X. D. Li, S. A. Boppart, J. Van Dam, H. Mashimo, M. Mutinga, W. Drexler, M. Klein, C. Pitris, M. L. Krinsky, M. E. Brezinski, and J. G. Fujimoto, "Optical coherence tomography: advanced technology for the endoscopic imaging of Barrett's esophagus," *Endoscopy,* vol. 32, pp. 921-30, Dec 2000.

[44] G. Zuccaro, N. Gladkova, J. Vargo, F. Feldchtein, E. Zagaynova, D. Conwell, G. Falk, J. Goldblum, J. Dumot, J. Ponsky, G. Gelikonov, B. Davros, E. Donchenko, and J. Richter, "Optical coherence tomography of the esophagus and proximal stomach in health and disease," *The American journal of gastroenterology,* vol. 96, pp. 2633-9, Sep 2001.

[45] D. C. Adler, C. Zhou, T. H. Tsai, H. C. Lee, L. Becker, J. M. Schmitt, Q. Huang, J. G. Fujimoto, and H. Mashimo, "Three-dimensional optical coherence tomography of Barrett's esophagus and buried glands beneath neosquamous epithelium following radiofrequency ablation," *Endoscopy,* vol. 41, pp. 773-776, Sep 2009.

[46] M. J. Suter, P. A. Jillella, B. J. Vakoc, E. F. Halpern, M. Mino-Kenudson, G. Y. Lauwers, B. E. Bouma, N. S. Nishioka, and G. J. Tearney, "Image-guided biopsy in the esophagus through comprehensive optical frequency domain imaging and laser marking: a study in living swine," *Gastrointestinal Endoscopy,* vol. 71, pp. 346-353, Feb 2010.

[47] A. Das, M. V. Sivak, Jr., A. Chak, R. C. Wong, V. Westphal, A. M. Rollins, J. Willis, G. Isenberg, and J. A. Izatt, "High-resolution endoscopic imaging of the GI tract: a comparative study of optical coherence tomography versus high-frequency catheter probe EUS," *Gastrointestinal endoscopy,* vol. 54, pp. 219-24, Aug 2001.

[48] B. Shen, G. Zuccaro, Jr., T. L. Gramlich, N. Gladkova, P. Trolli, M. Kareta, C. P. Delaney, J. T. Connor, B. A. Lashner, C. L. Bevins, F. Feldchtein, F. H. Remzi, M. L. Bambrick, and V. W. Fazio, "In vivo colonoscopic optical coherence tomography for transmural inflammation in inflammatory bowel disease," *Clin Gastroenterol Hepatol,* vol. 2, pp. 1080-7, Dec 2004.

[49] P. R. Pfau, M. V. Sivak, Jr., A. Chak, M. Kinnard, R. C. Wong, G. A. Isenberg, J. A. Izatt, A. Rollins, and V. Westphal, "Criteria for the diagnosis of dysplasia by endoscopic optical coherence tomography," *Gastrointest Endosc,* vol. 58, pp. 196-202, Aug 2003.

[50] C. Zhou, D. C. Adler, L. Becker, Y. Chen, T.-H. Tsai, M. Figueiredo, J. M. Schmitt, J. G. Fujimoto, and H. Mashimo, "Effective treatment of chronic radiation proctitis using radiofrequency ablation " *Therapeutic Advances in Gastroenterology,* vol. 2, pp. 149-156, May 2009.

[51] D. C. Adler, C. Zhou, T. H. Tsai, J. Schmitt, Q. Huang, H. Mashimo, and J. G. Fujimoto, "Three-dimensional endomicroscopy of the human colon using optical coherence tomography," *Optics Express,* vol. 17, pp. 784-796, Jan 2009.

[52] U. Seitz, J. Freund, S. Jaeckle, F. Feldchtein, S. Bohnacker, F. Thonke, N. Gladkova, B. Brand, S. Schröder, and N. Soehendra, "First in vivo optical coherence tomography in the human bile duct," *Endoscopy,* vol. 33, pp. 1018-1021, Dec 2001.

[53] J. M. Poneros, G. J. Tearney, M. Shiskov, P. B. Kelsey, G. Y. Lauwers, N. S. Nishioka, and B. E. Bouma, "Optical coherence tomography of the biliary tree during ERCP," *Gastrointestinal endoscopy,* vol. 55, pp. 84-88, Jan 2002.

[54] J. M. Poneros, S. Brand, B. E. Bouma, G. J. Tearney, C. C. Compton, and N. S. Nishioka, "Diagnosis of specialized intestinal metaplasia by optical coherence tomography," *Gastroenterology,* vol. 120, pp. 7-12, Jan 2001.

[55] J. A. Evans, B. E. Bouma, J. Bressner, M. Shishkov, G. Y. Lauwers, M. Mino-Kenudson, N. S. Nishioka, and G. J. Tearney, "Identifying intestinal metaplasia at the squamocolumnar junction by using optical coherence tomography," *Gastrointestinal Endoscopy,* vol. 65, pp. 50-56, Jan 2007.

[56] J. A. Evans, J. M. Poneros, B. E. Bouma, J. Bressner, E. F. Halpern, M. Shishkov, G. Y. Lauwers, M. Mino-Kenudson, N. S. Nishioka, and G. J. Tearney, "Optical coherence tomography to identify intramucosal carcinoma and high-grade dysplasia in Barrett's esophagus," *Clinical Gastroenterology and Hepatology,* vol. 4, pp. 38-43, Jan 2006.

[57] G. Isenberg, M. V. Sivak, A. Chak, R. C. K. Wong, J. E. Willis, B. Wolf, D. Y. Rowland, A. Das, and A. Rollins, "Accuracy of endoscopic optical coherence tomography in the detection of dysplasia in Barrett's esophagus: a prospective, double-blinded study," *Gastrointestinal Endoscopy,* vol. 62, pp. 825-831, Dec 2005.

[58] X. Qi, M. V. Sivak, G. Isenberg, J. E. Willis, and A. M. Rollins, "Computer-aided diagnosis of dysplasia in Barrett's esophagus using endoscopic optical coherence tomography," *Journal of Biomedical Optics,* vol. 11, p. 10, Jul-Aug 2006.

[59] A. R. Tumlinson, J. K. Barton, B. Povazay, H. Sattman, A. Unterhuber, R. A. Leitgeb, and W. Drexler, "Endoscope-tip interferometer for ultrahigh resolution frequency domain optical coherence tomography in mouse colon," *Optics Express,* vol. 14, pp. 1878-1887, Mar 2006.

[60] S. H. Yun, G. J. Tearney, B. J. Vakoc, M. Shishkov, W. Y. Oh, A. E. Desjardins, M. J. Suter, R. C. Chan, J. A. Evans, I. K. Jang, N. S. Nishioka, J. F. de Boer, and B. E. Bouma, "Comprehensive volumetric optical microscopy in vivo," *Nature Medicine,* vol. 12, pp. 1429-1433, Dec 2006.

[61] B. J. Vakoc, M. Shishko, S. H. Yun, W. Y. Oh, M. J. Suter, A. E. Desjardins, J. A. Evans, N. S. Nishioka, G. J. Tearney, and B. E. Bouma, "Comprehensive esophageal microscopy by using optical frequency-domain imaging (with video)," *Gastrointestinal Endoscopy,* vol. 65, pp. 898-905, May 2007.

[62] D. C. Adler, Y. Chen, R. Huber, J. Schmitt, J. Connolly, and J. G. Fujimoto, "Three-dimensional endomicroscopy using optical coherence tomography," *Nature Photonics,* vol. 1, pp. 709-716, Dec 2007.

[63] T.-H. Tsai, B. Potsaid, M. F. Kraus, C. Zhou, Y. K. Tao, J. Hornegger, and J. G. Fujimoto, "Piezoelectric-transducer-based miniature catheter for ultrahigh-speed endoscopic optical coherence tomography," *Biomed. Opt. Express,* vol. 2, pp. 2438-2448, Aug 2011.

[64] W. Hatta, K. Uno, T. Koike, S. Yokosawa, K. Iijima, A. Imatani, and T. Shimosegawa, "Optical coherence tomography for the staging of tumor infiltration in superficial esophageal squamous cell carcinoma," *Gastrointestinal Endoscopy,* vol. 71, pp. 899-906, May 2009.

[65] P. Tang, M. J. McKinley, M. Sporrer, and E. Kahn, "Inlet Patch: Prevalence, Histologic Type, and Association With Esophagitis, Barrett Esophagus, and Antritis," *Archives of Pathology & Laboratory Medicine,* vol. 128, pp. 444-447, Apr 2004.

[66] F. Borhan-Manesh and J. B. Farnum, "Incidence of heterotopic gastric mucosa in the upper oesophagus," *Gut,* vol. 32, pp. 968-972, Sep 1991.

[67] G. E. Feurle, V. Helmstaedter, A. Buehring, U. Bettendorf, and V. F. Eckardt, "Distinct immunohistochemical findings in columnar epithelium of esophageal inlet patch and of Barrett's esophagus," *Digestive Diseases and Sciences,* vol. 35, pp. 86-92, Jan 1990.

[68] İ. Yüksel, O. Üsküdar, S. Köklü, Ö. Başar, S. Gültuna, S. Ünverdi, Z. A. Öztürk, D. Şengül, A. T. Arikök, O. Yüksel, and Ş. Çoban, "Inlet patch: Associations with endoscopic findings in the upper gastrointestinal system," *Scandinavian Journal of Gastroenterology,* vol. 43, pp. 910-914, Aug 2008.

[69] B. Avidan, A. Sonnenberg, G. Chejfec, T. G. Schnell, and S. J. Sontag, "Is there a link between cervical inlet patch and Barrett's esophagus?," *Gastrointestinal Endoscopy,* vol. 53, pp. 717-721, Jun 2001.

[70] N. Malhi-Chowla, R. K. Ringley, and H. C. Wolfsen, "Gastric metaplasia of the proximal esophagus associated with esophageal adenocarcinoma and Barrett's esophagus: What is the connection? Inlet patch revisited," *Digestive Diseases,* vol. 18, pp. 183-185, 2000.

[71] F. Mion, R. Lambert, C. Partensky, M. Cherkaoui, and F. Berger, "High-grade dysplasia in an adenoma of the upper esophagus developing on heterotopic gastric mucosa," *Endoscopy,* vol. 28, pp. 633-635, Sep 1996.

[72] R. M. Sperling and J. H. Grendell, "Adenocarcinoma arising in an inlet patch of the esophagus," *American Journal of Gastroenterology,* vol. 90, pp. 150-152, Jan 1995.

[73] B. H. A. von Rahden, H. J. Stein, K. Becker, D. Liebermann-Meffert, and J. R. Siewert, "Heterotopic gastric mucosa of the esophagus: Literature-review and proposal of a clinicopathologic classification," *American Journal of Gastroenterology,* vol. 99, pp. 543-551, Mar 2004.

[74] C. Berkelhammer, M. Bhagavan, A. Templeton, R. Raines, and J. Walloch, "Gastric inlet patch containing submucosally infiltrating adenocarcinoma," *Journal of Clinical Gastroenterology,* vol. 25, pp. 678-681, Dec 1997.

[75] C. Zhou, T. Kirtane, T. H. Tsai, H. C. Lee, D. C. Adler, J. M. Schmitt, Q. Huang, J. G. Fujimoto, and H. Mashimo, "Cervical inlet patch-optical coherence tomography imaging and clinical significance," *World Journal of Gastroenterology,* vol. 18, pp. 2502-2510, May 2012.

[76] C. Zhou, T. Kirtane, T.-H. Tsai, H.-C. Lee, D. C. Adler, J. Schmitt, Q. Huang, J. G. Fujimoto, and H. Mashimo, "Three-dimensional endoscopic optical coherence tomography imaging of cervical inlet patch," *Gastrointestinal Endoscopy,* vol. 75, pp. 675-677, Mar 2012.

[77] M. J. Cobb, J. H. Hwang, M. P. Upton, Y. C. Chen, B. K. Oelschlager, D. E. Wood, M. B. Kimmey, and X. D. Li, "Imaging of subsquamous Barrett's epithelium with ultrahigh-resolution optical coherence tomography: a histologic correlation study," *Gastrointestinal Endoscopy,* vol. 71, pp. 223-230, Feb 2010.

[78] C. Zhou, T.-H. Tsai, H.-C. Lee, T. Kirtane, M. Figueiredo, Y. K. Tao, O. O. Ahsen, D. C. Adler, J. M. Schmitt, Q. Huang, J. G. Fujimoto, and H. Mashimo, "Characterization of buried glands before and after radiofrequency ablation by using 3-dimensional optical coherence tomography (with videos)," *Gastrointestinal Endoscopy,* vol. 76, pp. 32-40, Jul 2012.

CHAPTER 3

3.0 Assessment of Tissue Architectural Changes after Ablation Therapies in Barrett's Esophagus

3.1 Motivation

Ablative therapies including argon plasma coagulation (APC), photodynamic therapy (PDT), radiofrequency ablation (RFA), and cryospray ablation (CSA) are increasingly performed for diseases in the gastrointestinal (GI) tract such as Barrett's esophagus (BE). Among them, RFA and CSA are two main nonsurgical endoscopic approaches recently developed for ablating dysplastic and early cancer lesions in the esophagus. As described in Chapter 2, both therapeutic technologies allow broad and superficial treatment for BE. Recent clinical trials using RFA treatment have shown that complete eradication of dysplasia (CE-D) was achieved in 98% and 93% of patients with low-grade dysplasia (LGD) and high-grade dysplasia (HGD) at two-year follow-up [1]. Complete eradication of intestinal metaplasia (CE-IM) was achieved in 92% of patients with nondysplastic BE (NDBE) at up to 5 years follow-up [2]. CSA is a newer therapeutic technology, so fewer large-scale trials have been conducted. However, several pilot studies have shown that CSA is highly effective in eradicating HGD. Complete eradication of the HGD, CE-D, and CE-IM in 94%, 88%, and 53% of BE patients was reported in a multicenter study [3]. Another multicenter study also reported 97%, 87% and 57% complete eradication of HGD, CE-D, and CE-IM at 10.5 months of follow-up [4].

Although these studies indicate that both therapeutic technologies allow broad and superficial treatment field for BE, repeated RFA/CSA treatments were generally required to achieve after over 3.4 sessions using RFA [1, 2, 5] and 4.2 sessions using CSA [3, 6] for patients with BE. Considering the recovery time between consecutive therapeutic procedures (6-8 weeks for RFA treatment and 4-6 weeks for CSA treatment), the overall treatment process to achieve CE-IM can be over a year long. Multiple repeated esophagogastroduodenoscopy (EGD) and therapeutic procedures also increase costs to the healthcare system [4, 7, 8]. Thus, methods to improve the efficacy of each therapeutic procedure would reduce the total number of treatment sessions, reduce patient anxiety, and improve the benefit from these endoscopic therapeutic techniques.

In this section of the thesis work, an endoscopic 3D-OCT system and spiral scanning imaging catheter were used to assess the differences in architectural changes in the esophageal tissue immediately following RFA and CSA. Due to the increased hazard of immediately taking biopsies from the treated sites, the treatment efficacy typically can only be confirmed in the follow-up sessions. 3D-OCT has the depth-resolved capability and is uniquely suited for the acute assessment of the ablation therapies. This investigation can help clinicians understand more about the tissue destruction and may improve the efficacy of these treatment methods in the future. The prototype high speed data acquisition and data processing system used in this study was built by Dr. Joseph Schmitt at LightLab and an FDML laser was built and interfaced to the system by former PhD candidate, Dr. Desmond Adler. The FDML laser was later reconstructed during this thesis work to provide better sensitivity roll off over the imaging range.

The endoscopic OCT data that is presented in this chapter was taken in collaboration with Dr. Hiroshi Mashimo, MD, PhD who performed all of the endoscopy sessions. Multiple group members including Dr. Chao Zhou, PhD, Dr. Yuankai Tao, PhD, Hsiang-Chieh Lee, and Osman Ahsen shared the experimental responsibilities in the endoscopy clinics on alternating weekly basis. All the data processing and analysis were done by the author of the thesis work.

3.2 Endoscopic 3D-OCT Imaging System Description

The system used in this study was developed with the joint work of MIT and LightLab Imaging Inc. – St. Jude Medical Inc. The system schematic is shown in **Figure 3.1**. The OCT imaging engine operates at sustained speeds compatible with FDML lasers by using an optical frequency clock (OFC) integrated with a 200 Msample/s 12 bit analog-to-digital converter (ADC).

The FDML laser shown in **Figure 3.2** provides a fundamental sweep rate of 59 kHz and effective sweep rate of 118 kHz if using both forward and backward sweeps. Only the backward sweep was used to acquire data in the system with sweep linearization to temporally shape the output sweep, increase the duty cycle of the backward sweep, and effectively increase the maximum imaging depth with a given ADC sampling rate [9]. The fiber Fabry-Perot tunable filter (FFP-TF) used in the FDML laser was acquired from LambdaQuest. The FFP-TF had a finesse of 1,000 and a free spectral range (FSR) of 180 nm, giving a linewidth of 0.18 nm. The output coupling ratio was chosen to provide maximum tuning range while maintaining a post-booster output power that was sufficiently high to reach the tissue exposure limit of 20 mW after transmission through the OCT interferometers and imaging catheters. With a 50% output coupler, the total tuning range was 175 nm, corresponding to an axial resolution of 5 μm in tissue, and the average output power after booster amplification was 50 mW. Power output directly from the cavity is ~5 mW.

The OCT imaging engine developed here used an optical triggering technique to automatically correct for nonlinear ν spacing during data acquisition without acquiring and storing a separate reference signal. 5% of the laser output was routed to an asymmetric Mach-Zehnder interferometer (MZI) that produces interference fringes with zero crossing evenly spaced in ν. This concept is shown in the left insect of **Fig. 3.1**. The MZI fringes are detected by a dual-balanced photoreceiver and the zero-crossings are identified by an analog voltage comparator in the clock generator, creating a digital pulse train that functions as an OFC. The OFC is synchronized to the start of each laser sweep by a trigger signal from the FDML laser.

A dual-balanced Michelson interferometer consisting of a pair of optical circulators and a 50/50 fiberoptic splitter is used to generate the OCT interference fringes. Dual-balanced detection cancels excess noise, reducing the dynamic range requirements of the DAQ system and improving sensitivity. The same frequency sweep from the laser generated both MZI and OCT fringes, so the spacing of the

OFC pulses corresponded to evenly spaced ν intervals in the OCT signal. The OFC triggers the circularly buffered ADC that samples the OCT fringes. Since the resulting signal is evenly spaced in ν, only the digitized OCT signal needed to be stored and no post-processing was required for sweep recalibration. The sample arm of the Michelson interferometer included a Patient Interface Unit (PIU), supplied by Lightlab, which produced high-speed rotational motion at up to 80 Hz (4,800 rpm) and linear pullback motion at 0.5-2.0 mm/s. The PIU attached to the proximal end of the imaging catheter and produces a spiral scanning pattern at the distal end of the catheter.

After digitization the OCT signal was continuously streamed to the computer RAM over a PCI-X link at an average of 46 MB/s and a peak of 150 MB/s. Hamming windowing and a fast Fourier transform (FFT) were then performed in software to synthesize the image. Each frame was interpolated into polar coordinates and displayed as a radial image in real-time at >20 frame per second (fps). During 3D acquisition, sustained acquisition rates of 100 kHz were achieved while maintaining real-time display. The system had a lateral resolution of 15 μm, an axial resolution of 5 μm, imaging depth of 2 mm in tissue, and the sensitivity of 103 dB.

3.3 Patient Enrollment and Study Protocol

This study was conducted in collaboration with Dr. Hiroshi Mashimo and Dr. Qin Huang at the Veterans Affairs Boston Healthcare System (VABHS), Jamaica Plain Campus, and the study protocol was approved by institutional review boards (IRB) of the VABHS, Harvard Medical School, and the Massachusetts Institute of Technology. Patients in this study were recruited from volunteers aged from 30 to 80 undergoing diagnostic endoscopy and biopsy for Barrett's esophagus at VABHS based on a history of a biopsy positive for moderate-grade dysplasia within the previous 18-month period. Patients were diagnosed with standard white light endoscopy, and the length of visible BE was recorded based on the Prague C&M criteria [10]. Informed consent was obtained from each patient. Patients were assigned to receive RFA or CSA treatments based on physician judgment.

For each RFA treatment, the patient received two sets of ablations using BARRX Halo90 catheter (Covidien, Inc.). A treatment set consisted of 300 Watts at 12 J/cm^2 applied twice for any treatment surface and repeated consecutively to adjacent areas until the entire BE region was ablated. Desquamated epithelium was removed by rigorous scraping between the two sets of ablations, per standard protocol set by the manufacture. For each CSA treatment, the CSA Medical system was used. The tissue area was sprayed with liquid nitrogen to freeze for 20 seconds, allowed to thaw completely, and then followed by another 20 seconds freezing. 3D-OCT imaging was performed before and immediately after the completion of RFA and CSA.

3.4 3D-OCT Imaging and Post Analysis

3D-OCT was performed with the imaging catheter introduced through the accessory channel of the endoscope (GIF Q180, Olympus America, Inc.), enabling simultaneous video endoscopy. Volumetric OCT data was acquired at 60,000 axial lines per second and 60 frames per second. The imaging catheter scanned a helical pull-back patter with an 8 mm circumference and 20 mm pull-back length within 20 seconds. The imaging catheter was placed at 6 o'clock in the endoscopic field, and the pull-back imaging overlapped the gastroesophageal junction (GEJ). For RFA patients, multiple 3D-OCT data sets were acquired at the GEJ before the ablation treatments, immediately after the first set of RFA ablations (but prior to vigorous scraping of the desquamated epithelium), and after the second set of RFA ablations. For CSA patients, multiple 3D-OCT data sets were similarly obtained before the ablation treatment and immediately after the entire CSA treatment for each endoscopic session.

Each 3D-OCT data set was reviewed and analyzed after the endoscopy session using a 3D rendering software (Amira,Visage Imaging, Inc.). The volumetric data was cylindrically shaped but was converted to rectangular form by unfolding to better visualization *en face* features. For each patient, tissue morphological changes at 3~5 locations from the 3D-OCT data sets were identified as regions of interest (ROIs). The maximum depth of architectural changes was measured for each ROI, and comparison was made between the two treatment groups.

3.5 Comparison of Tissue Architectural Changes between RFA and CSA

3D-OCT imaging was performed on patients following RFA (n = 10) and CSA (n = 3) treatments for BE with the BARRX Halo90 system and the CSA Medical system, respectively. There were no adverse events after the RFA or CSA treatments.

3.5.1 Tissue Architectural Changes after RFA

Representative 3D-OCT volumetric datasets obtained from the treated site of a 70-year-old patient before and right after RFA treatment are shown in **Figure 3.3** and **Figure 3.4**. The patient was diagnosed with 3 cm BE with HGD around the GEJ based on the biopsy taken 4 months before the treatment. These three orthoplanes show 3D-OCT data spanning the RFA treatment site immediately after the second set of ablation, with colored dotted lines indicating the locations of the complementary planes. At a tissue depth of 150 μm, the *en face* orthoplane shows clear delineation between regions with and without hyperscattering features, which are consistent with burned esophageal tissues. The burned tissues were recognized by conventional endoscopic examination as areas of removed squamous epithelium and "shammy" appearance of the mucosa, occasionally with overlying white debris.

Cross-sectional orthoplanes revealed clear differences in layered architecture in the esophagus. In this study, the cross-sectional imaging capability can be used to characterize the tissue morphologic changes after the ablation therapies. **Figure 3.5** shows the magnified orthoplanes of ROIs marked in **Figure 3.4**. Superficial burned tissues showed hyperscattering features. The endoscopic imaging field was covered with blood and tissue debris immediately after the RFA treatment, so it is difficult to evaluate the presence of residual glands or unburned BE using conventional white light endoscopy of narrow band imaging (NBI) due to the limited visibility. Areas with incomplete ablation can be distinguished in the OCT images taken immediately after the RFA. **Figs. 3.5D-F** show the magnified orthoplanes of the ROI (gray box) marked in **Figure 3.4**. Hyposcattering features of typical BE glands can be observed at the edge of the ablated area, indicating this location might require further treatment. At the follow-up two month later, the BE length was reduced to 1 cm around the GEJ, and most of the prior treated site was covered with neosquamous tissue.

3.5.2 Tissue Architectural Changes after CSA

Representative of 3D-OCT volumetric datasets of the treated site from a 72-year-old patient before and immediately after CSA treatment are shown in **Figure 3.6** and **Figure 3.7**. The patient was diagnosed with 4 cm BE with HGD in the distal esophagus based on the biopsy taken 9 months before the treatment. These three orthoplanes show 3D-OCT data spanning the CSA treated site immediately after the procedure. In some ablated regions, thin hyperscattering structure can be observed on top of the tissue. At a depth of 170 μm, regions with edema-like changes can be clearly observed from the *en face* OCT images in some areas of the ablation field. Conventional white light endoscopy shows the distal esophagus after the tissue was thawed completely. **Figure 3.8** shows the magnified orthoplanes of the ROI marked with a ref box in **Figure 3.7**. In the OCT images taken immediately after the CSA treatment, there was no structural features observed that indicates areas that require re-ablation. However, at the follow-up 3 months later, there was still BE distributed at the distal 1/3 esophagus with neosquamous tissue covering ~60% of the previously treated sites.

Compared to RFA, there was less desquamation, but edema-like changes creating a "spongy" appearance observed as hyposcattering structures reaching a depth of 650 μm in certain areas of the ablation field. These results suggest that 3D-OCT imaging can be a useful tool for providing immediate feedback about therapy-induced architectural changes on esophageal tissues.

3.5.3 Analysis of the Tissue Destruction Caused by RFA and CSA

The comparison between RFA and CSA is summarized in **Table 3.1**. Among all the patients receiving RFA therapy, burned and desquamated tissue appeared hyperscattering, measuring 263.3 μm

(SD = 31.4 μm) after the first set of the ablations. However, the depth of structural changes measured after the second RFA set may not reflect the actual depth of the second ablation if tissue was incompletely removed after the first RFA sets. The second RFA sets at the same site caused structural changes with depth of 237 μm (SD = 34.9 μm). In patient of the CSA group, tissue architectural changes with edema-like "spongy" appearance caused by freezing were observed measuring 643 μm (SD = 30 μm) in depth. Compared to CSA, RFA caused more visible architectural changes observed on 3D-OCT imaging (including sloughing mucosa and more visible debris). However, the spongiform architectural changes caused by CSA appear deeper.

Table 3.1 Summary of the comparison between RFA and CSA

Treatment method	**RFA**	**CSA**
Enrollment, no.	10	3
Characteristics	Burned tissues with hyperscattering desquamation and debris	Edema-like spongiform appearance and minimal hyperscattering desquamation caused by freezing
Maximum depth of architectural changes (Mean ± SD)	(i) 263.33 ± 31.4 μm for the first set of ablation (ii) 237 ± 34.9 μm for the second set of ablation	(i) 643 ± 30 μm for the whole treatment

SD: standard deviation; *RFA*: radiofrequency ablation; *CSA*: cryospray ablation.

3.6 Clinical Implications and Limitations

With the advent of endoscopic ablative therapies for dysplastic and early cancer lesions in the gastrointestinal tract, methods to visualize the treatment field and optimize therapy will be in demand. While endoscopic 3D-OCT does not possess the same magnification or contrast as conventional histopathologic analysis, it is capable of visualizing tissue microstructures *in vivo* over a large field of view and provides real-time tissue depth information at micron-scale resolution. RFA was observed to induce about 230-260 μm depth of architectural changes for each application, while CSA was observed to induce adema-like spongiform changes to 660 μm deep. The depth of tissue structural changes for both therapies meets the required depth of tissue destruction for BE [11], which was confirmed by histology from 100 cases of BE patients.

The ability to detect micron-scale tissue structural changes during the ablation therapy sessions makes 3D-OCT an ideal tool to assess treatment efficacy and may provide real-time feedback for treatment dosing and for identifying regions that need additional treatments. The correlation of the depth of such

physical structural changes on OCT to actual depth of biological cell death and the extent of persistent tissue destruction compared to transient thermal effect remain unclear and will require histological correlates from samples taken during the ablation session. However, the growth of neosquamous epithelium over the treated sites was consistently observed upon endoscopic follow-up visits after both RFA and CSA treatments, suggestive of a persistent and eventually similar tissue architectural change after both treatment modalities. In order to further study the acute treatment response at the cellular level, future studies will require correlation of architectural changes identified by OCT immediately after the ablation with histological analysis of deep jumbo forceps biopsies from the same locations and perhaps use of biomarkers of necrosis and apoptosis.

Traditional assessment of the efficacy of the ablation therapies requires from weeks to months for patients revisit the clinics. Patients would require retreatment if residual BE is observed endoscopically, including the regions that were missed in the previous treatment session. Endoscopic 3D-OCT may enhance the real-time assessment of BE patients prior to and following ablative therapies such as RFA and CSA by enabling comprehensive imaging of tissue microstructure over a large surface area. The increased analysis volume and high imaging acquisition speed of 3D-OCT may be used to guide ablation, with improved imaging of subsurface tissue structure in real time. To date, there is no other real-time imaging technology that can achieve the high imaging speed, broad imaging coverage, and subsurface visibility while having the spatial resolution that can show detail structural information from the tissue. Moreover, OCT is not dependent on contrast agents, as in confocal endomicroscopy, which would seep and obliterate the view during the ablative therapies. Using endoscopic 3D-OCT, the data sets can be acquired in 20 seconds and reviewed immediately, suggesting the possibility of performing volumetric assessment of treated sites immediately after the treatment, improvement of the treatment efficacy with the guided ablation, and better quality of life with the reduction of the number of treatment sessions.

3.7 Figures

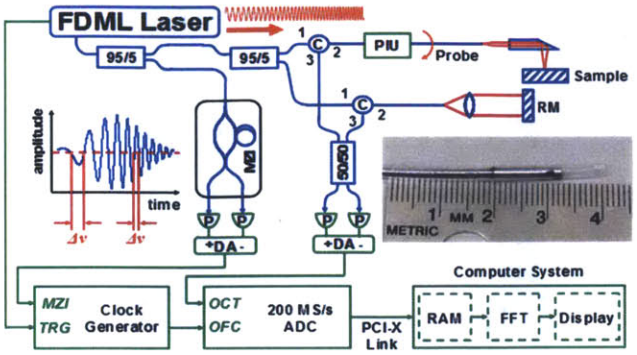

Figure 3.1. Endoscopic OCT system schematic. An OCT imaging engine from LightLab Imaging - St. Jude will be used to enable *in vivo* 3D-OCT imaging at axial line rates of 50 – 100 kHz. Left inset: MZI produces fringes that are evenly spaced in *v*, which are used for optical clocking of the ADC. Right inset: photograph of distal tip of the side imaging probe developed at MIT.

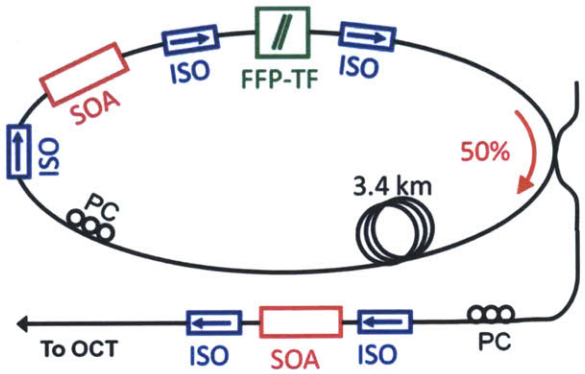

Figure 3.2. FDML laser used in the endoscopic 3D-OCT system. FFP-TF: fiber Fabry-Perot tunable filter. ISO: isolator. SOA: semiconductor optical amplifier. PC: Polarization controller.

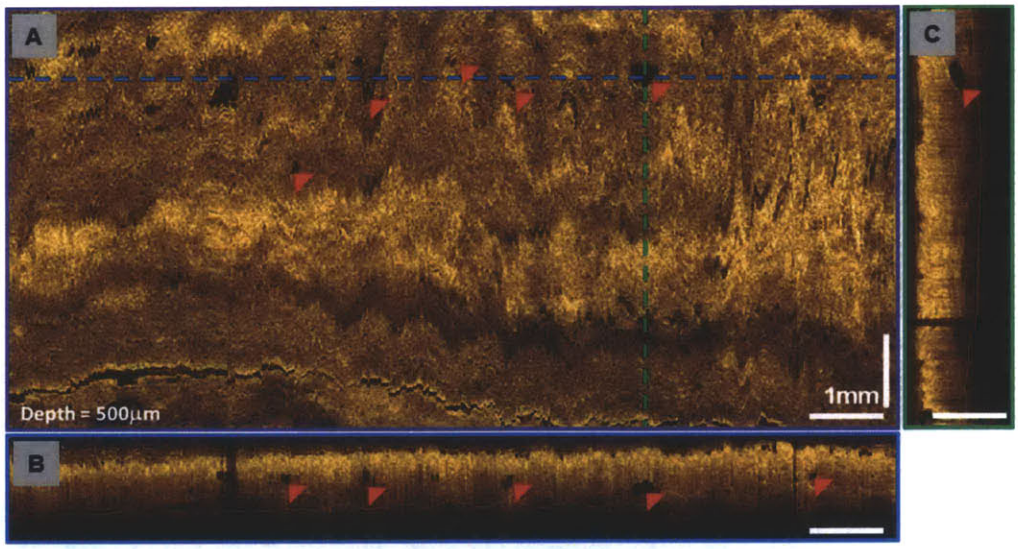

Figure 3.3. 3D-OCT orthoplanes from the BE region before RFA treatment. (A) The *en face* orthoplane is located at a depth of 500 um. The colored dotted lines indicate location of complementary orthoplanes (B) and (C). Red arrows indicate the locations of the BE glands. (B) The cross-sectional YZ orthoplane shows the epithelium (ep), lamina propria (lp), and muscularis mucosa (mm). (C) The cross-sectional XZ orthoplane shows the hyposcattering feature of the BE glands on top of the lp/mm layer. Originally published in [12].

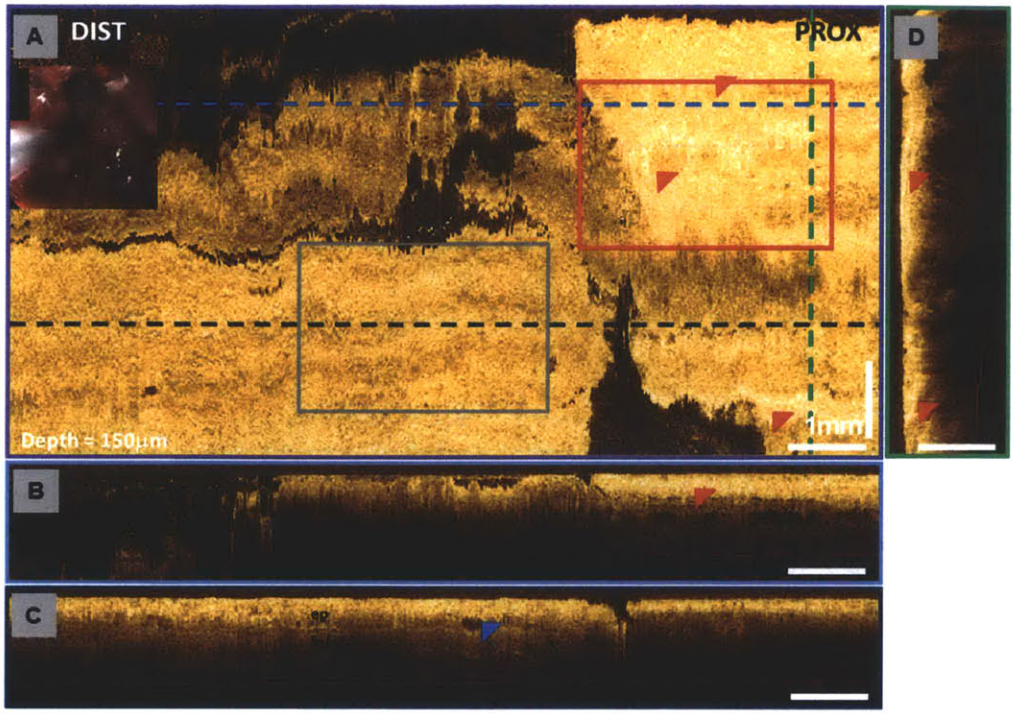

Figure 3.4. 3D-OCT orthoplanes from the BE region immediately after RFA treatment. (A) The *en face* orthoplane is located at a depth of 150 um. The colored dotted lines indicate location of complementary orthoplanes (B), (C) and (D). Red arrows indicate the locations of the burned tissue on top of the treated regions and the blue arrow indicates the location of the residual gland. (B-C) The cross-sectional YZ orthoplanes show the epithelium (ep), lamina propria (lp), and muscularis mucosa (mm). (D) The cross-sectional XZ orthoplane shows the burned tissue right on top of the muscularis mucosal layer. Inset shows a video endoscopy image with the 3D-OCT probe in position prior to image acquisition. Red box and gray box indicate regions of interest in **Figs. 3.5** (A-C) and **Figs.3.5** (D-F) respectively. Originally published in [12].

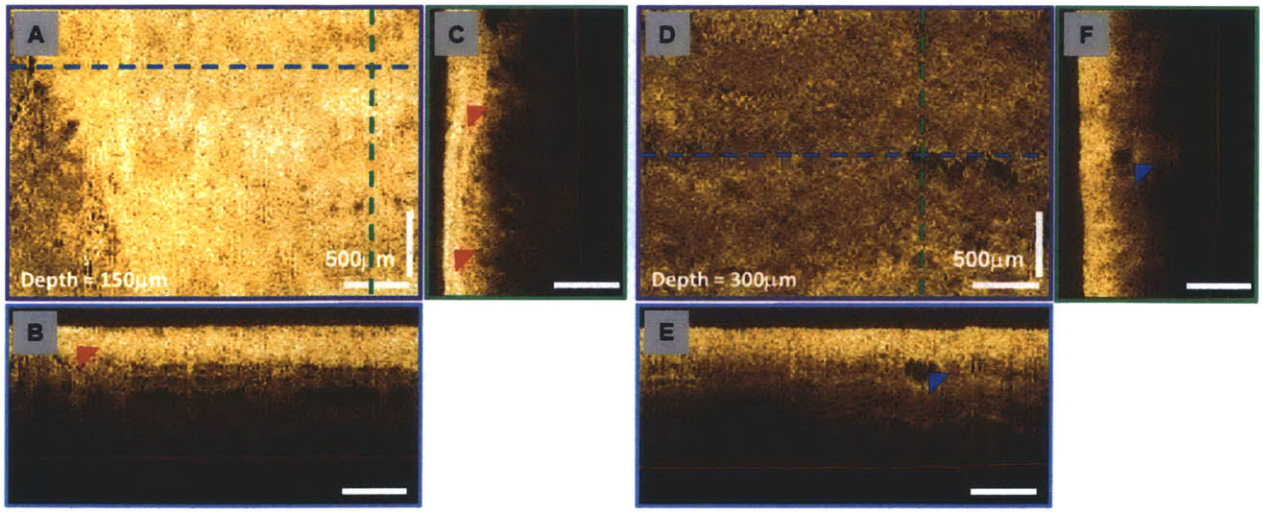

Figure 3.5. Magnified orthoplanes of the treated area showing the hyperscattering feature of the burned tissue as the red arrows indicated and the hyposcattering feature of the residual BE glands as the blue arrows indicated. Originally published in [12].

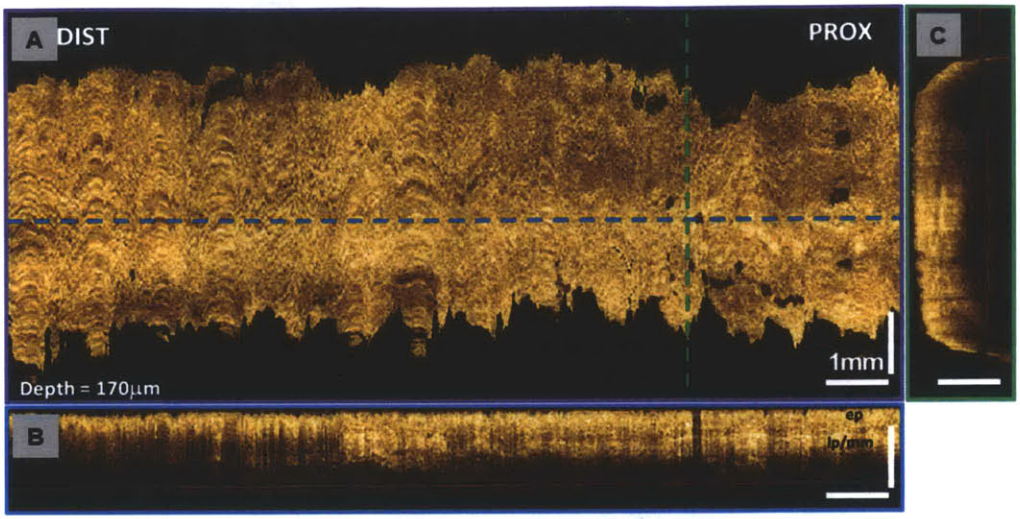

Figure 3.6. 3D-OCT orthoplanes from the BE region before CSA treatment. (A) The *en face* orthoplane is located at a depth of 170 um. The colored dotted lines indicate location of complementary orthoplanes (B) and (C). (B) The cross-sectional YZ orthoplane shows the epithelium (ep), lamina propria (lp), and muscularis mucosa (mm). (C) The cross-sectional XZ orthoplane shows the typical BE structure. Originally published in [12].

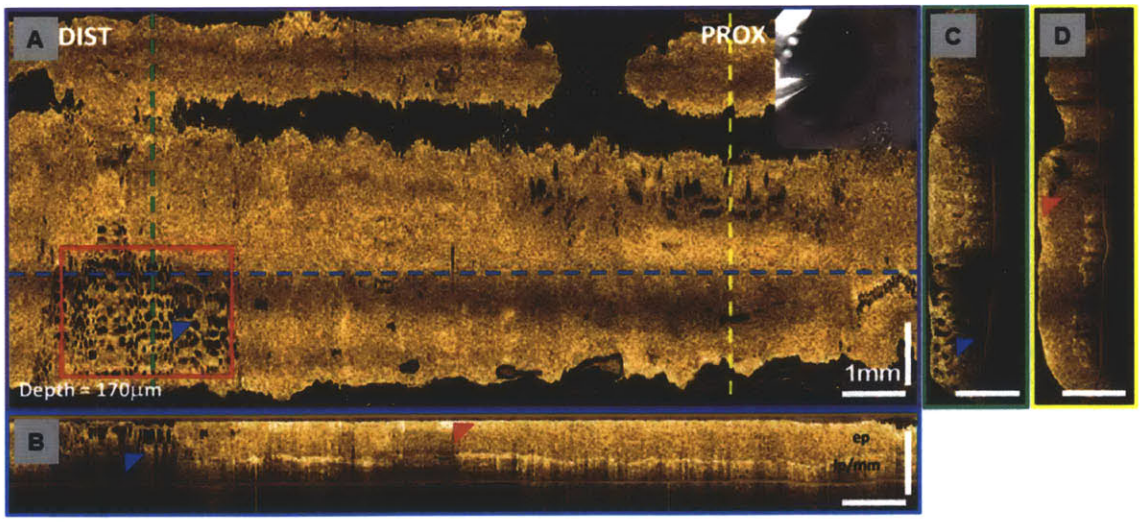

Figure 3.7. 3D-OCT orthoplanes from the BE region immediately after CSA treatment. (A) The *en face* orthoplane is located at a depth of 170 mm. The colored dotted lines indicate location of complementary orthoplanes (B), (C) and (D). Blue arrows indicate the locations of the edema-like tissues and red arrows indicate the hyperscattering necrotic tissues on top of the treated regions. (B) The cross-sectional YZ orthoplane shows the epithelium (ep), lamina propria (lp), and muscularis mucosa (mm). (C) The cross-sectional XZ orthoplane shows the edema-like tissue extending into the muscularis mucosal layer. (D) The cross-sectional XZ orthoplane shows the hyperscattering, detached tissue on top of the treated area. Inset shows a video endoscopy image with the 3D-OCT probe in position prior to image acquisition. Red box indicates region of interest in **Figure. 3.8**. Originally published in [12].

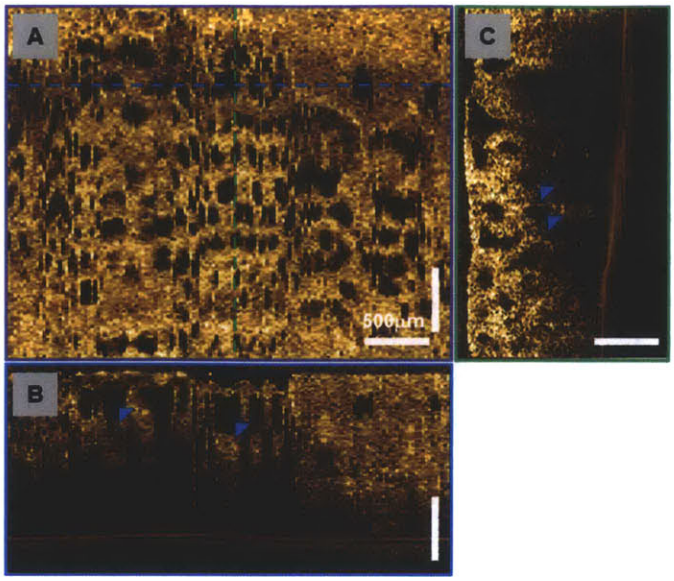

Figure 3.8. Magnified orthoplanes of the treated area showing the spongiform appearance due to the edematous tissue caused by freezing, as indicated by blue arrows. Originally published in [12].

3.8 References

[1] N. J. Shaheen, B. F. Overholt, R. E. Sampliner, H. C. Wolfsen, K. K. Wang, D. E. Fleischer, V. K. Sharma, G. M. Eisen, M. B. Fennerty, J. G. Hunter, M. P. Bronner, J. R. Goldblum, A. E. Bennett, H. Mashimo, R. I. Rothstein, S. R. Gordon, S. A. Edmundowicz, R. D. Madanick, A. F. Peery, V. R. Muthusamy, K. J. Chang, M. B. Kimmey, S. J. Spechler, A. A. Siddiqui, R. F. Souza, A. Infantolino, J. A. Dumot, G. W. Falk, J. A. Galanko, B. A. Jobe, R. H. Hawes, B. J. Hoffman, P. Sharma, A. Chak, and C. J. Lightdale, "Durability of Radiofrequency Ablation in Barrett's Esophagus With Dysplasia," *Gastroenterology,* vol. 141, pp. 460-468, Aug 2011.

[2] D. E. Fleischer, B. F. Overholt, V. K. Sharma, A. Reymunde, M. B. Kimmey, R. Chuttani, K. J. Chang, R. Muthasamy, C. J. Lightdale, N. Santiago, D. K. Pleskow, P. J. Dean, and K. K. Wang, "Endoscopic radiofrequency ablation for Barrett's esophagus: 5-year outcomes from a prospective multicenter trial," *Endoscopy,* vol. 42, pp. 781-789, Oct 2010.

[3] B. D. Greenwald, J. A. Dumot, J. D. Horwhat, C. J. Lightdale, and J. A. Abrams, "Safety, tolerability, and efficacy of endoscopic low-pressure liquid nitrogen spray cryotherapy in the esophagus," *Diseases of the Esophagus,* vol. 23, pp. 13-19, Jan 2010.

[4] N. J. Shaheen, B. D. Greenwald, A. F. Peery, J. A. Dumot, N. S. Nishioka, H. C. Wolfsen, J. S. Burdick, J. A. Abrams, K. K. Wang, D. Mallat, M. H. Johnston, A. M. Zfass, J. O. Smith, J. S. Barthel, and C. J. Lightdale, "Safety and efficacy of endoscopic spray cryotherapy for Barrett's esophagus with high-grade dysplasia," *Gastrointestinal Endoscopy,* vol. 71, pp. 680-685, Apr 2010.

[5] N. J. Shaheen, P. Sharma, B. F. Overholt, H. C. Wolfsen, R. E. Sampliner, K. K. Wang, J. A. Galanko, M. P. Bronner, J. R. Goldblum, A. E. Bennett, B. A. Jobe, G. M. Eisen, M. B. Fennerty, J. G. Hunter, D. E. Fleischer, V. K. Sharma, R. H. Hawes, B. J. Hoffman, R. I. Rothstein, S. R. Gordon, H. Mashimo, K. J. Chang, V. R. Muthusamy, S. A. Edmundowicz, S. J. Spechler, A. A. Siddiqui, R. F. Souza, A. Infantolino, G. W. Falk, M. B. Kimmey, R. D. Madanick, A. Chak, and C. J. Lightdale, "Radiofrequency Ablation in Barrett's Esophagus with Dysplasia," *New England Journal of Medicine,* vol. 360, pp. 2277-2288, May 2009.

[6] J. A. Dumot, J. J. Vargo, G. W. Falk, L. Frey, R. Lopez, and T. W. Rice, "An open-label, prospective trial of cryospray ablation for Barrett's esophagus high-grade dysplasia and early esophageal cancer in high-risk patients," *Gastrointestinal endoscopy,* vol. 70, pp. 635-644, Oct 2009.

[7] A. Das, C. Wells, H. J. Kim, D. E. Fleischer, M. D. Crowell, and V. K. Sharma, "An economic analysis of endoscopic ablative therapy for management of nondysplastic Barrett's esophagus," *Endoscopy,* vol. 41, pp. 400-408, May 2009.

[8] J. M. Inadomi, M. Somsouk, R. D. Madanick, J. P. Thomas, and N. J. Shaheen, "A Cost-Utility Analysis of Ablative Therapy for Barrett's Esophagus," *Gastroenterology,* vol. 136, pp. 2101-2114, Jun 2009.

[9] C. M. Eigenwillig, B. R. Biedermann, G. Palte, and R. Huber, "K-space linear Fourier domain mode locked laser and applications for optical coherence tomography," *Optics Express,* vol. 16, pp. 8916-8937, Jun 2008.

[10] P. Sharma, J. Dent, D. Armstrong, J. J. G. H. M. Bergman, L. Gossner, Y. Hoshihara, J. A. Jankowski, O. Junghard, L. Lundell, G. N. J. Tytgat, and M. Vieth, "The Development and Validation of an Endoscopic Grading System for Barrett's Esophagus: The Prague C & M Criteria," *Gastroenterology,* vol. 131, pp. 1392-1399, Nov 2006.

[11] R. Ackroyd, N. J. Brown, T. J. Stephenson, C. J. Stoddard, and M. W. R. Reed, "Ablation treatment for Barrett oesophagus: what depth of tissue destruction is needed?," *Journal of Clinical Pathology,* vol. 52, pp. 509-512, Jul 1999.

[12] T. H. Tsai, C. Zhou, H. C. Lee, Y. K. Tao, O. O. Ahsen, M. Figueiredo, D. C. Adler, J. M. Schmitt, Q. Huang, J. G. Fujimoto, and H. Mashimo, "Comparison of Tissue Architectural Changes between Radiofrequency Ablation and Cryospray Ablation in Barrett's Esophagus Using

Endoscopic Three-Dimensional Optical Coherence Tomography," *Gastroenterology Research and Practice,* Article 684832, pp. 1-8, May 2012.

CHAPTER 4

4.0 Investigation of Structural Markers Correlating with Barrett's Esophagus Radiofrequency Ablation Treatment Response

4.1 Motivation

Recent studies have shown that radiofrequency ablation (RFA) is an effective therapy for ablating Barrett's esophagus (BE) and it can completely eradicate dysplastic BE in up to 93% of BE patients with high grade dysplasia (HGD). Although there is no indication to treat low grade dysplasia (LGD) or non-dysplastic BE (NDBE), several studies have shown high eradication rate in these patients. However, as mentioned in Chapter 3, repeated RFA treatments are generally required to achieve complete eradication of the diseased tissue. Considering the follow-up time between RFA procedures, usually 6-8 weeks, the entire treatment process can easily span half a year or even longer. In addition, the cost to achieve complete eradication mounts with each endoscopy and RFA procedure and has tempered the enthusiasm for treating all non-dysplastic BE by using RFA. Therefore, improving the effectiveness of each RFA procedure would reduce the number of treatment sessions, improve the cost effectiveness, reduce patient anxiety, and make this therapy available to a wider patient population.

According to the previous experience of the buried glands and RFA/CSA comparison studies using endoscopic OCT, it is known that the cross-sectional imaging capability of OCT can identify the subsurface structural features in normal esophagus as well as BE [1]. In this section of the thesis work, the endoscopic 3D-OCT imaging was used to identify possible structural markers that can predict RFA treatment response. With the information regarding the factors associated with RFA treatment response, it is possible to improve the effectiveness of therapy to reduce the number of treatments required to achieve complete response in the future.

4.2 Patient Enrollment and Study Protocol

This study was conducted in collaboration with Drs. Hiroshi Mashimo and Qin Huang at the Veterans Affairs Boston Healthcare System (VABHS), Jamaica Plain Campus, over the past 2 years. The study protocol was approved by the VABHS, Harvard Medical School, and Massachusetts Institute of Technology. Patients were diagnosed with standard white light endoscopy, and the length of visible BE was recorded based on the Prague C&M criteria. Thirty-three patients with short-segment (<3 cm) BE, including one woman, were recruited for this study. The study also included patients who initially presented with long-segment BE that was reduced to <3 cm segment by prior circumferential RFA treatment using the BARRX Halo360 catheter (Covidien, Inc.).

Informed consent was obtained from each patient. Only patients with short-segment BE were imaged in order to ensure consistent OCT imaging catheter placement at the gastroesophageal junction (GEJ) and ascertaining the presence of BE, its thickness, and the presence of residual glands relative to the GEJ within the OCT pullback image. This study focused on patients receiving ablation with the BARRX Halo90 catheter (Covidien, Inc.). For each RFA treatment, the patient received two sets of ablations that

were done with the Halo90 catheter (300 W at 12 J/cm^2 for each set of ablations), with rigorous scraping to remove desquamated epithelium between the two ablations, per standard protocol set by the manufacture. Patients with circumferential short-segment BE also were treated with the Halo90 catheter in order to maintain a consistent procedure and ablation energy level. After the RFA, patients were treated with a proton pump inhibitor (PPI), that is, 40 mg of esomeprazole or omeprazole twice daily. At 6 to 8 weeks follow-up, the presence of residual BE was evaluated by using white light endoscopy and narrowband imaging as well as random 4-quadrant pinch biopsies. If no visible BE was observed endoscopically, and no intestinal metaplasia was found from biopsies at the GEJ, the patient was classified as complete eradication of intestinal metaplasia (CE-IM). There were 13 patients in the CE-IM group and 20 patients in the non-CE-IM group in this study.

Table 4.1 listed demographic information of the patients enrolled in this study. The average age for the CE-IM and non-CE-IM groups was comparable ($P = 0.86$). The CE-IM group consisted of 4 patients with NDBE, 2 patients with LGD, and 7 patients with HGD at presentation. The non-CE-IM group consisted of 10 patients with NDBE, 4 patients with LGD, and 6 patients with HGD at presentation. Patients in the non-CE-IM group are presumed to eventually have a treatment response with additional RFA treatments and convert to the CE-IM group, and investigation of this group is ongoing. The number of prior RFA treatments and the length of BE was not statistically different between the two groups. There were no adverse events after all RFA treatment sessions.

Table 4.1 Patient demographic information.

	CE-IM group	Non-CE-IM group	*P* value
Enrollment, no.	13	20	
Sex, male/female, no.	12/1	20/0	
Age, mean (SD), range, y	64.9 (7.7) 51-77	65.6 (15.8) 33-92	0.86
Initial diagnosis, no.			
BE w/o dysplasia	4	10	
Low-grade dysplasia	2	4	
High-grade dysplasia	7	6	
Prior RFA treatment, mean (SD), range	2.4 (1.9) 0-7	1.7 (1.6) 0-6	0.34
Length of BE, mean (SD), range, cm	1.3 (0.8) 0.5-3	1.0 (0.7) 0.5-3	0.29

CE-IM: complete eradication of intestinal metaplasia; *SD*: standard deviation; *BE*: Barrett's esophagus; *RFA*: radiofrequency ablation.

4.3 Endoscopic 3D-OCT Imaging

The specification of the endoscopic 3D-OCT imaging system used in this study was the same as the system used in the RFA/CSA comparison studies and was described in Chapter 3. Three-dimensional OCT imaging was performed with the OCT catheter introduced through the accessory channel of the endoscope (GIF Q180; Olympus America, Inc.), enabling simultaneous video endoscopy. Volumetric OCT data were acquired at 60,000 axial lines per second and 60 frames per second. The imaging catheter scanned a helical pullback pattern with an 8-mm circumference and 20-mm pullback length within 20 seconds. The endoscope was at the neutral position, with the imaging catheter placed at 6 o'clock in the endoscopic field. The imaging catheter was in contact with the esophagus wall, and the pullback imaging spanned the GEJ. The esophagus was deflated and naturally wrapped around the OCT catheter during imaging acquisition to maintain a consistent catheter contact for all patients. Multiple 3D-OCT data sets were acquired at the GEJ before and immediately after the RFA treatment.

4.4 Imaging Analysis

Each 3D-OCT data set was reviewed and analyzed by using 3D rendering software (Amira, Visage Imaging, Inc.). The BE epithelium thickness was measured from cross-sectional OCT images obtained before the RFA treatment. As indicated in **Figure 4.1**, the BE thickness was measured as the vertical distance from the top of the lamina propria/muscularis mucosa layer to the surface of the BE epithelium at the center position where the OCT catheter had the best contact with the esophagus. Multiple BE thickness measurements were obtained from each 3D data set every 1 mm along the entire BE length. The average and maximum BE thickness were recorded for each patient for statistical comparison between the CE-IM and non-CE-IM groups.

In addition, two types of residual glandular structures were observed by reviewing 3D OCT images obtained immediately after the second RFA. The first type of glandular structure was unburned BE epithelium that was likely missed by RFA and showed an epithelial structure similar to that of regular BE. The second type of glandular structure consisted of hyposcattering glandular structures above the lamina propria/muscularis mucosa layer at the RFA treatment sites, representing residual glands. The presence or absence of these residual glands was recorded for each patient.

4.5 Statistical Analysis

The primary study outcome was to determine the accuracy of using BE thickness measured with OCT before RFA to predict the treatment response (presence or absence of endoscopically visible residual BE at follow-up). A *t*-test was used to compare the average and maximum BE thickness from the CE-IM and non-CE-IM groups. To evaluate BE thickness can be used to predict the RFA treatment response, receiver

operating characteristic curves were plotted by using a discrimination threshold ranging from 100 μm to 800 μm for average and maximum BE thickness, respectively. A decision threshold was determined from the receiver operating characteristic curves to achieve maximum overall accuracy. Sensitivity, specificity, positive predictive value, negative predictive value, and accuracy of the prediction were then calculated.

The secondary study outcome was to evaluate the correlation between the presence/absence of residual glands on OCT imaging immediately after RFA versus RFA treatment response assessed endoscopically on follow-up. The correlation between the BE thickness before RFA versus the presence or absence of residual glands immediately after RFA was also evaluated. The sensitivity, specificity, positive predictive value, negative predictive value, and accuracy of the prediction were calculated.

All statistical analyses were performed by using MATLAB software (Mathworks, Inc.). All tests were 2-sided, and a P value of <0.05 was considered statistically significant.

4.6 Structural Features of BE Before and After the RFA Treatment

Figure 4.1A shows an endoscopic image of the GEJ before focal RFA treatment was applied. Three-dimensional OCT imaging was performed at the GEJ over the area of BE, which appeared to be pink-reddish area in the endoscopic field of view. **Figure 4.1B** shows a representative cross-sectional OCT image obtained at the GEJ before the RFA treatment, together with the corresponding histology obtained from the same site (**Fig. 4.1C**). The thickness of the BE epithelium was measured from the OCT image as distance between the BE surface to the top of the lamina propria/muscularis mucosa layer.

Figure 4.2A shows an endoscopic image of the GEJ immediately after focal RFA treatment with scraping to remove desquamated epithelium between first and second RFA applications. The RFA-treated area was covered with blood and burned tissue, making difficult to identify residual BE patches on white light endoscopy or narrowband imaging (NBI). **Figure 4.2B** shows a representative cross-sectional OCT image obtained immediately after RFA. A similar epithelium structure was observed compared with **Fig. 4.1B**, indicating the presence of residual BE that was missed by the RFA treatment. Another type of residual glandular structure usually can be observed after insufficient power delivery on the tissue, leading to hyposcattering features above the lamina propria/muscularis mucosa layer at the RFA-treated site in OCT images. **Figure 4.2C** shows residual glands (red arrows) above the muscularis mucosal layer, suggesting that these glands were not effectively removed by the RFA treatment. A biopsy was taken from the same site immediately after the OCT imaging and confirmed the presence of residual BE glands immediately after the RFA treatment (**Fig. 4.2D**). **Figure 4.2E** shows a representative cross-sectional OCT image demonstrating effective RFA treatment, where the muscularis mucosa layer was on top of the tissue surface with no epithelial structures above it.

4.7 Correlation Between the Structural Features and the Treatment Response

The BE thickness measured with OCT before RFA was found to be a predictor of the RFA treatment response. Both the average and maximum BE thickness before RFA were significantly thinner for the CE-IM group compared with the non-CE-IM group (average BE thickness, 257 ± 60 μm versus 403 ± 86 μm; $P < 0.0001$; maximum BE thickness, 293 ± 64 μm versus 471 ± 107 μm; $P < 0.0001$). The scatter plot in **Fig. 4.3A** shows the difference between the average BE thickness for the two groups. **Figure 4.3B** shows receiver operating characteristic curves in which average and maximum BE thickness were used to predict RFA treatment response. The area under the curve (AUC) was 0.942 ($P < 0.001$) and 0.934 ($P < 0.001$) using the average and maximum BE thickness, respectively. An average BE thickness of 333 μm was determined from the receiver operating characteristic curve to achieve the best prediction accuracy. By using this decision threshold, a sensitivity of 92.3% (12/13), specificity of 85% (17/20), positive predictive value of 80%, negative predictive value of 94.4%, and an accuracy of 87.9% (29/33) were obtained for predicting treatment response evaluated by the presence or absence of endoscopically visible residual BE at follow-up visit by using the average BE thickness measured with OCT before the RFA treatment (**Table 4.2**). Considering only the patients with dysplastic BE (19/33), a sensitivity of 100% (9/9), specificity of 90% (9/10), positive predictive value of 90%, negative predictive value of 100%, and an accuracy of 94.7% (18/19) were obtained for predicting treatment response evaluated by the presence or absence of endoscopically visible residual BE at follow-up visit by using the average BE thickness measured with OCT before the RFA treatment. The BE thickness measured with OCT was not correlated with the length of the BE ($P = 0.88$) or the number of prior RFA treatment ($P = 0.24$).

Table 4.2 Average BE thickness measured by OCT before RFA predicts the presence or absence of endoscopically visible residual BE at follow-up visit.

	Absence of residual BE at follow-up	**Presence of residual BE at follow-up**	**Total**	
Average BE thickness <333 μm	12	3	15	PPV 80%
Average BE thickness ≥333 μm	1	17	18	NPV 94.4%
Total	13	20	33	
	Sensitivity 92.3%	Specificity 85%	Accuracy 87.9%	

BE: Barrett's esophagus; *PPV*: positive predictive value; *NPV* negative predictive value.

A BE thickness of over 333 μm also was found to correlate with the presence of residual glands immediately after RFA (**Table 4.3**; sensitivity 91.7% [11/12], specificity 85% [17/20], positive predictive value 78.6%, negative predictive value 94.4%, and accuracy 87.5% [28/32]). Note that one patient was excluded from this analysis due to the lack of OCT images immediately after RFA. Finally, the presence of residual glands observed with OCT immediately after RFA was found to be another predictor of the RFA treatment response (**Table 4.4**). Sensitivity of 83.3% (10/12), specificity of 95% (19/20), positive predictive value of 90.9%, negative predictive value of 90.5%, and accuracy of 90.6% (29/32) were achieved by using the presence of residual glands visible on OCT immediately after RFA to predict the presence of endoscopically visible residual BE at follow-up.

Table 4.3 Average BE thickness measured by OCT before RFA predicts the presence or absence of residual glands measured by OCT immediately after RFA.

	Absence of residual glands immediately after RFA	**Presence of residual glands immediately after RFA**	**Total**	
Average BE thickness <333 μm	11	3	14	PPV 78.6%
Average BE thickness ≥333 μm	1	17	18	NPV 94.4%
Total	12	20	32	
	Sensitivity 91.7%	Specificity 85%	Accuracy 87.5%	

BE: Barrett's esophagus; *PPV*: positive predictive value; *NPV* negative predictive value.

Table 4.4 Presence or absence of residual glands measured by OCT immediately after RFA predicts the presence or absence of endoscopically visible residual BE at follow-up visit.

	Absence of residual BE at follow-up	**Presence of residual BE at follow-up**	**Total**	
Absence of residual glands after RFA	10	1	11	PPV 90.9%
Presence of residual glands after RFA	2	19	21	NPV 90.5%
Total	12	20	32	
	Sensitivity 83.3%	Specificity 95%	Accuracy 90.6%	

BE: Barrett's esophagus; *PPV*: positive predictive value; *NPV* negative predictive value.

4.8 Clinical Implications

While endoscopic 3D-OCT does not possess the same magnification or contrast as conventional histopathology, it can visualize tissue microstructure *in vivo* over a large field of view and provides real-time, depth-resolved information with micron scale resolution. Each 3D-OCT dataset in our study covers ~160 mm^2 in the distal esophagus. Although this is only a fraction of the field observed with white light endoscope it is many times larger than the field covered by pinch biopsy and 3D-OCT provides complementary information about BE thickness as well as tissue morphology. This is especially important immediately after the RFA treatment, when the endoscopic imaging field is covered with blood and tissue debris. Due to the limited visibility immediately after the RFA treatment, it is difficult to evaluate the presence of residual glands or unburned BE using white light endoscopy or NBI. Similarly, imaging modalities that require contrast agents such as confocal endomicroscopy have limited use since extravasation of the contrast obliterates the viewing area after RFA. However, as demonstrated, residual glandular structures can be observed using 3D-OCT.

In this study, 3D-OCT identified structural markers, including the thickness of the BE epithelium prior to RFA and the presence of residual glands immediately after RFA, which might be used to predict RFA treatment response at follow-up with high accuracy. It was found that patients with an average BE thickness of over 333μm were likely to have endoscopically visible residual BE at the follow-up visit 6-8 weeks after the RFA treatment. This result was not surprising, however, since the dosage of the RFA treatment has been set to achieve best efficacy with minimum injury depth [2, 3]. The energy delivery of a standard RFA application might not reach deep enough when the BE epithelium is thick. There are other possible confounding variables that may contribute to depth variation or incompleteness of the ablation, including variation of the RFA electrode contact with the esophagus and coagulated/sloughing debris building up on the electrode surface with repeated ablations in a patient [3]. Indeed, a correlation was found between the BE epithelium thickness and the presence of residual glands immediately after RFA, suggesting not all RFA applications were effective. Insufficient energy delivery at the treatment sites or leaving BE unburned may be factors that lead to endoscopically visible residual BE at follow-up.

The efficacy of ablation therapies is generally assessed by follow-up endoscopy 6-8 weeks after RFA, and patients undergo repeated ablation if residual BE is observed. These results suggest that patient response rate may be stratified based on the BE thickness measured before RFA. Using this structural marker, it may be possible to adjust RFA treatment for each patient to optimize response. For patients with thicker BE epithelium, a more rigorous ablation may be required. This may involve a thorough cleaning of the ablation catheter and treatment areas to remove debris between the two sets of ablations, and if indicated, increased dosage for the RFA treatment. The ability of OCT to differentiate residual

glands from normal tissue structures and debris caused by the ablation may also provide immediate information about the RFA treatment for the endoscopist. This may enable real-time evaluation of ablation depth and identification of regions requiring further treatment. The RFA treatment might be guided to further improve the efficacy of each ablation procedure. As a result, the number of treatment sessions might be reduced to reduce overall treatment time, patient anxiety and health care cost.

Fourteen patients with NDBE were also enrolled in this study. However, two recent large cohort studies from Northern Ireland and Denmark showed that the annual risk for adenocarcinoma in non-dysplastic BE was less than 0.2%, suggesting RFA treatment for patients with non-dysplastic BE holds no benefit [4, 5]. On the other hand, an earlier study performed in the U.S. Veteran population, and perhaps better reflective of this study's population, showed a relatively higher annual risk (0.4%) for adenocarcinoma in non-dysplastic BE patients [6]. The National Cancer Institute estimates that the incidence of esophageal cancer in the general population of the United States (all races, both sexes, all ages) is approximately 4.5 per 100,000 (0.0045%) [7]. Given that about 5.6% of population in the US is found to have BE, the incidence of esophageal cancer for patients with non-dysplastic BE still appears to be much higher than the general population [8]. Notwithstanding, by current clinical guidelines there is no indication for RFA treatment of patients with non-dysplastic BE, and endoscopic ablation therapies are recommended mainly for patients with high-grade dysplasia [9, 10].

Surveillance endoscopy with biopsy is recommended for patients with LGD or NDBE. However, due to the recognized limitations of the surveillance strategy, such as biopsy sampling errors, lack of compliance with surveillance protocols, cost-utility considerations, and failure to avert cancer in many cases, endoscopic therapies intended to completely remove LGD and NDBE can be considered as alternative strategies. Indeed, recent studies have shown that complete eradication of intestinal metaplasia (CE-IM) can be achieved in 92% of patients with non-dysplastic BE at 5-year follow-up after RFA treatment. Although currently there is no indication to treat NDBE with RFA, in this study the BE epithelial thickness was found to be a strong predictor for RFA treatment response in all patients, both with and without dysplastic BE, indicating that this structural marker can be useful regardless of the dysplasia status of the patients.

4.9 Limitations of the Study

There are several limitations in the current study. First, the study was limited to a cohort of patients with short-segment BE. This was done because the OCT system had a limited pull back imaging length and it was desirable to image the GEJ in each data set in order to enable consistent placement of the OCT imaging catheter. Future OCT systems will be able to acquire larger data sizes and we plan to extend the study to patients with long segment BE and evaluate the efficacy of circumferential RFA treatment. The

study was also focused on patients receiving Halo90 ablation rather than Halo360, to be consistent with the actual ablation method. In addition, the dysplasia status of the patients was evaluated before the patients went through the initial RFA treatment. As presented in **Table 4.1**, on average 2.4 and 1.7 RFA procedures were performed before the time of OCT imaging for patients in the CE-IM and non-CE-IM groups, respectively. Biopsies were generally not performed at time of RFA and OCT imaging to confirm the dysplasia status. Variations in disease severity of the patients at the time of treatment may be a cofounding variable for treatment response. Future studies will be conducted to investigate the relation between the BE mucosal thickness and treatment response in patients with different dysplasia status.

Secondly, the thickness of BE epithelium may vary if the contact pressure of the OCT catheter on the tissue changes. An *ex vivo* study using human colon tissues reported that the epithelium thickness was reduced when the contact pressure is increased [11]. This effect may induce variability in the BE thickness measurement. In the current study, the OCT catheter was in contact with the esophagus with the endoscope at the neutral position and the esophagus was deflated during imaging acquisition. The esophagus naturally wrapped around the OCT catheter to maintain a consistent catheter contact for all patients. More detailed quantitative investigations are needed to understand the influence of catheter contact pressure on the BE thickness measurement.

Thirdly, while OCT structural markers may predict RFA treatment response, the current study does not address whether the RFA treatment efficacy can be improved and the number of treatments reduced using structural information provided by 3D-OCT. A rigorous longitudinal study is needed to further establish the utility of endoscopic 3D-OCT for guiding RFA treatment of BE in clinical practice.

Finally, although the imaging coverage of the current 3D-OCT catheter is significantly larger than standard biopsy, a single 3D-OCT scan only covered about one sixth of the circumference of the distal esophagus. If unburned BE or residual glands were missed by 3D-OCT immediately after RFA, the patient might fail to achieve CE-IM at follow-up even though OCT imaging may still predict complete response. To overcome these potential sampling errors, multiple 3D-OCT sets will need to be acquired to achieve comprehensive coverage over different quadrants of the distal esophagus. Other OCT probe designs, such as balloon probes, may also be employed to improve coverage and reduce potential sampling errors in the future.

4.10 Figures

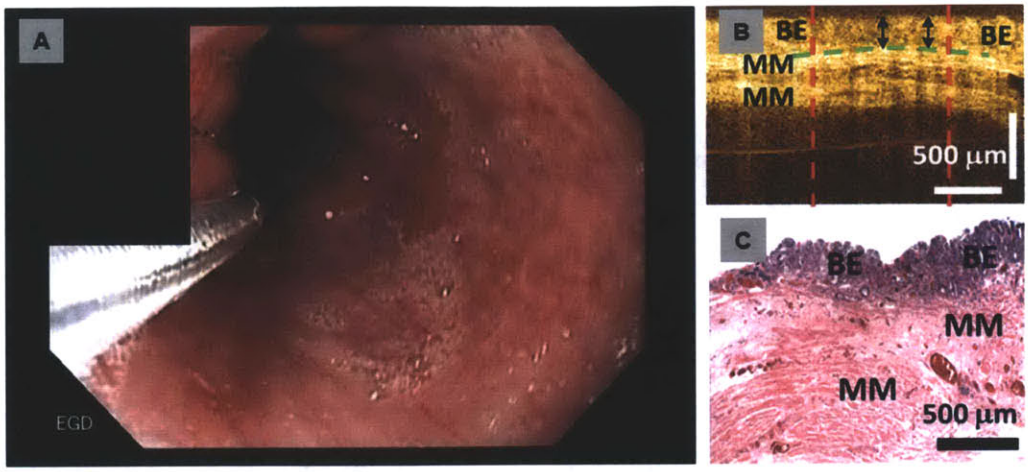

Figure 4.1. (A) Representative endoscopic image of the GEJ before RFA treatment. (B) Representative cross-sectional OCT image and (C) corresponding histology illustrating the BE epithelium thickness measurement. Originally published in [1].

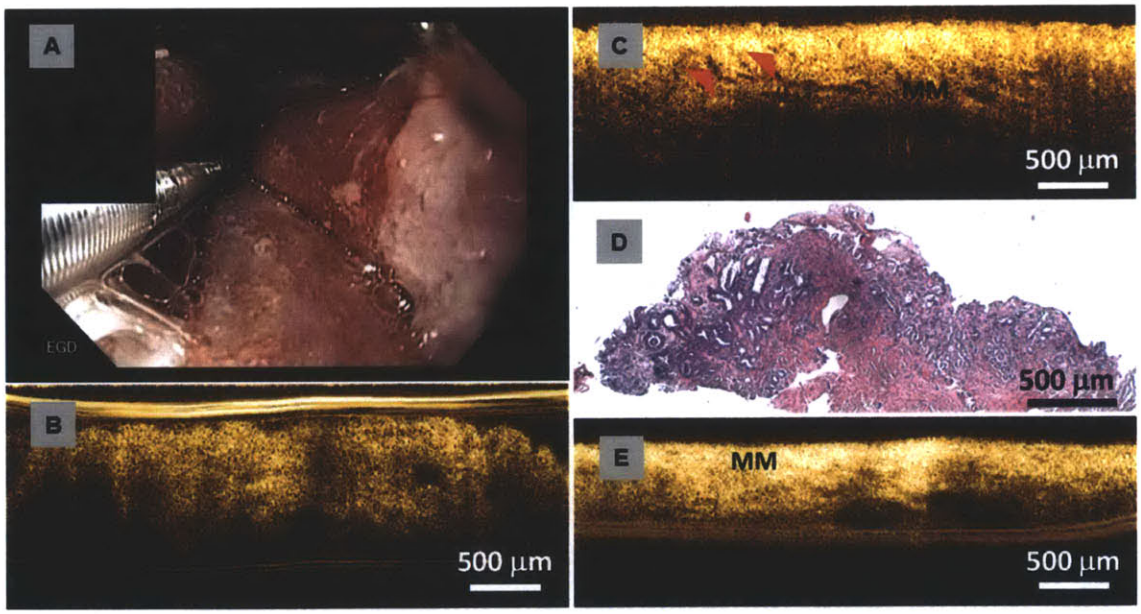

Figure 4.2. (A) Representative endoscopic image of the GEJ immediately after RFA treatment. (B) Representative cross-sectional OCT image showing unburned BE epithelium missed by RFA. (C) Representative cross-sectional OCT image showing residual glands after RFA. (D) Corresponding histology of (C) confirming residual BE glands after RFA. (E) Representative cross-sectional OCT image showing effective RFA treatment. The entire BE epithelium was ablated, resulting in exposed muscularis mucosa (MM) on the surface. Originally published in [1].

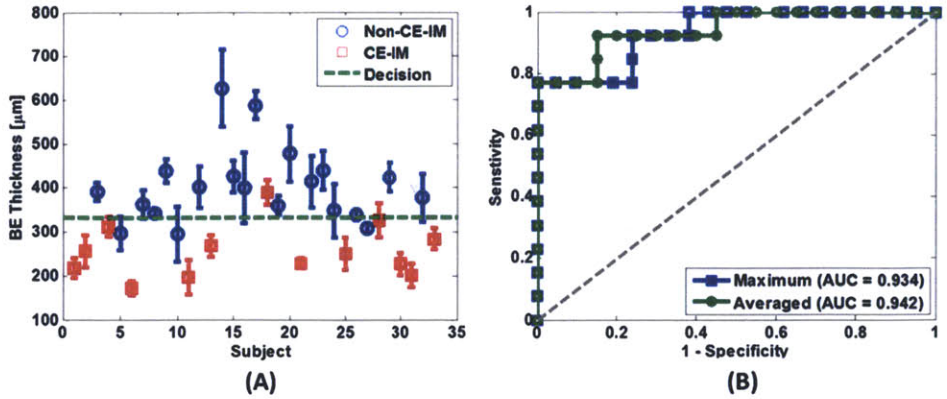

Figure 4.3. (A) Scatter plot of the average BE epithelium thickness measured by OCT. Blue circles: Non-CE-IM group; Red crosses: CE-IM group; Green dotted line: discrimination threshold at 333 um as determined from the average BE thickness ROC curve in (B). (B) ROC curves of treatment response prediction using average (green) and maximum (blue) BE thickness. The area-under-the-curve (AUC) values were 0.942 ($p<0.001$) and 0.934 ($p<0.001$) using the average and maximum BE thickness, respectively. Originally published in [1].

4.11 References

[1] T.-H. Tsai, C. Zhou, H.-C. Lee, Y. K. Tao, O. O. Ahsen, M. Figueiredo, D. C. Adler, J. M. Schmitt, Q. Huang, J. G. Fujimoto, and H. Mashimo, "Comparison of Tissue Architectural Changes between Radiofrequency Ablation and Cryospray Ablation in Barrett's Esophagus Using Endoscopic Three-Dimensional Optical Coherence Tomography," *Gastroenterology Research and Practice,* Article 684832, pp. 1-8, May 2012.

[2] B. Dunkin, J. Martinez, P. Bejarano, C. Smith, K. Chang, A. Livingstone, and W. Melvin, "Thin-layer ablation of human esophageal epithelium using a bipolar radiofrequency balloon device," *Surgical Endoscopy,* vol. 20, pp. 125-130, Jan 2006.

[3] J. Trunzo, M. McGee, B. Poulose, J. Willis, B. Ermlich, M. Laughinghouse, B. Champagne, C. Delaney, and J. Marks, "A feasibility and dosimetric evaluation of endoscopic radiofrequency ablation for human colonic and rectal epithelium in a treat and resect trial," *Surgical Endoscopy,* vol. 25, pp. 491-496, Feb 2011.

[4] S. Bhat, H. G. Coleman, F. Yousef, B. T. Johnston, D. T. McManus, A. T. Gavin, and L. J. Murray, "Risk of Malignant Progression in Barrett's Esophagus Patients: Results from a Large Population-Based Study," *Journal of the National Cancer Institute,* vol. 103, pp. 1-9, Jun 2011.

[5] F. Hvid-Jensen, L. Pedersen, A. r. M. Drewes, H. T. SÃ¸rensen, and P. Funch-Jensen, "Incidence of Adenocarcinoma among Patients with Barrett's Esophagus," *New England Journal of Medicine,* vol. 365, pp. 1375-1383, Oct 2011.

[6] S. J. Spechler, E. Lee, D. Ahnen, R. K. Goyal, I. Hirano, F. Ramirez, J. P. Raufman, R. Sampliner, T. Schnell, S. Sontag, Z. R. Vlahcevic, R. Young, and W. Williford, "Long-term outcome of medical and surgical therapies for gastroesophageal reflux disease - Follow-up of a randomized controlled trial," *Jama-Journal of the American Medical Association,* vol. 285, pp. 2331-2338, May 2001.

[7] N. A. Howlader N, Krapcho M, Neyman N, Aminou R, Altekruse SF, Kosary CL, Ruhl J, Tatalovich Z, Cho H, Mariotto A, Eisner MP, Lewis DR, Chen HS, Feuer EJ, Cronin KA (eds). "SEER Cancer Statistics Review, 1975-2009 (Vintage 2009 Populations)," *National Cancer Institute. Bethesda, MD, http://seer.cancer.gov/csr/1975_2009_pops09/, based on November 2011 SEER data submission, posted to the SEER web site,* 2012.

[8] T. J. Hayeck, C. Y. Kong, S. J. Spechler, G. S. Gazelle, and C. Hur, "The prevalence of Barrett's esophagus in the US: estimates from a simulation model confirmed by SEER data," *Diseases of the Esophagus,* vol. 23, pp. 451-457, Aug 2010.

[9] K. K. Wang and R. E. Sampliner, "Updated Guidelines 2008 for the Diagnosis, Surveillance and Therapy of Barrett's Esophagus," *Am J Gastroenterol,* vol. 103, pp. 788-797, Mar 2008.

[10] S. J. Spechler, P. Sharma, R. F. Souza, J. M. Inadomi, and N. J. Shaheen, "American Gastroenterological Association Technical Review on the Management of Barrett's Esophagus," *Gastroenterology,* vol. 140, pp. e18-e52, Mar 2011.

[11] V. Westphal, A. M. Rollins, J. Willis, M. V. Sivak, and J. A. Izatt, "Correlation of endoscopic optical coherence tomography with histology in the lower-GI tract," *Gastrointest Endosc,* vol. 61, pp. 537-46, Apr 2005.

CHAPTER 5

5.0 Imaging Catheter Development for Endoscopic 3D-OCT

5.1 Motivation

Clinical studies shown in Chapter 3 and Chapter 4 have demonstrated the superb depth-resolving capability and broad coverage of endoscopic 3D-OCT, and it can potentially be a powerful imaging modality for surveillance, diagnosis, post-treatment assessment, and real-time guided treatment in the human GI tract. With the further improvement of image quality obtained from the OCT systems, more detail features in the tissue can be identified in real time and therefore more accurate feedback to the clinicians can be provided. To improve the image quality, one logical solution is to improve the design of the imaging catheter so the catheter can provide smaller spot size, that is, better transverse resolution to reveal more detailed tissue structure, larger imaging coverage to enable the registration of the imaged location, more stable scanning to sustain various operation conditions, and more flexible to be able to acquire images in different organs. The other solution is to modify the OCT imaging engine, so it can support higher axial line rate to increase the sampling density of images, broader swept source tuning range to improve the axial resolution, higher data acquisition speed to increase the imaging depth, or higher output power, if necessary, to increase the sensitivity of the system. This chapter will focus on the imaging catheter development and the improvement of the OCT imaging engine will be discussed in Chapter 9.

There are two main applications for endoscopic scanning. The first type is imaging a large area of the lumen. The objective is to map pathology and measure areas. An example of this application is follow-up for ablative therapy in the esophagus. Since the area to be imaged is large, it will not be possible to image in all dimensions with high pixel resolution. The second type is imaging focal areas with high magnification. The objective is to view detailed morphology before biopsy. If a very high magnification image is desired, there must be an approach for stabilizing the imaging catheter or tissue to avoid motion. If a very high magnification is used, there must be an approach to focus the imaging catheter.

In this section of the thesis work, a full analysis of a variety of scanning mechanisms was done and discussed. Important parameters needed to be considered while designing an imaging catheter will be described and the examples of the calculation and selection of these parameters for certain application purposes will be presented. General catheter design problems with different imaging configuration will also be discussed. This chapter can provide a design guideline for future imaging catheter development.

5.2 Overview of Scanning Mechanisms for Endoscopic Imaging Catheter

Generally speaking, there are two main categories of scanning methods. The first category is proximal actuation and the second one is distal actuation. The imaging catheter with proximal actuation usually contains actuators or the patient interface unit (PIU) outside of human body or far away from the specimens. The actuation is usually transferred to the distal end of the imaging catheter via a torque coil

or a guide wire. Fast axis scan can be done in high speed rotary or push-pull methods. To acquire volumetric OCT data set, slow axis scan is also required. High speed rotary plus slower pulling back of the probe is the most common method to achieve the 3D OCT dataset acquisition [1-7].

On the other hand, the actuator of the scanning probe with distal actuation is placed at the distal end of the imaging catheter that goes into the human body or close to the specimens. Hence the actuator must be made as small as possible to go through the working channel of endoscope or go alongside with the endoscope without increasing the overall size too much. There are several miniaturized actuators used in the distal actuation probe such as piezoelectric transducer (PZT) based devices [8, 9] and microelectromechanical system (MEMS) based device [10]. Miniaturized actuators can achieve either 1 dimensional (1D) or 2 dimensional (2D) scanning. The actuators are usually controlled electronically and very close to human bodies or samples, so electrical isolation must be paid extra attention for this kind of imaging catheters.

In this section, we will compare several representative imaging catheters including (1) proximally rotary side imaging, (2) proximally rotary balloon imaging, (3) raster scan side imaging, (4) raster forward imaging, and (5) spiral forward imaging. **Figure 5.1** shows the schematics of these different scanning methods.

5.2.1 Proximally Rotary Side Imaging

This is the scanning method used in most of the studies conducted with endoscopic OCT imaging, which was firstly developed by Prof. Fujimoto's group at MIT in 1996 [1], as shown in **Fig. 5.1A**. Rotation is produced by a high speed motor and transferred to the distal end of the imaging probe via a torque coil. Slow scan is done by slowly pulling back the whole probe to achieve 3D data acquisition. This design requires a fiber optic rotary joint so the imaging catheter can keep rotating in one direction. The rotary joint typically has maximum rotary speed of 2000 to 10,000 revolutions per minutes (rpm), corresponding to 33 to 166 revolutions per second, so the frame rate limit of this method is around 150 frames per second (fps). Since the light is always on axis, the effect of spherical aberration caused by the optics is small. Therefore, this method is easier for optics design and the beam profile is not distorted due to the rotary scanning. Moreover, the distal end can be made very small and the rigid length can be short with the simple optic design. Typically the outer diameter (OD) of whole probe including sheath can be thinner than 2 mm and the rigid length can be less than 2 cm.

One intrinsic disadvantage of this method is that the rotation and pull back uniformity is hard to control due to the rotation and pulling-back transfer through a long distance (>2 meters typically). During the imaging procedures, it's very easy to generate torque or resistance due to the bend of the torque coil, which makes the scanning non-uniformity more severe. Another disadvantage of this method is the lack

of stability on the sample during the imaging procedures. It's very hard to control the position of the probe with the endoscope even by pressing hard on the tissue. Therefore, due to the intrinsic non-uniformity and environmental instability, the post processing for the volumetric dataset is more complex and good quality *en face* view for the dataset is hard to achieve.

5.2.2 Proximally Rotary Balloon Imaging

In order to reduce the environmental instability of the high speed rotary probe, balloon technique was adopted to stabilize the probe in the human body, especially for studies in the GI tract, as shown in **Fig. 5.1B**. With the balloon design, it is easier to image the whole lumen around the imaging catheter and co-register the imaging locations at different time points. Using balloon increases the working distance (~1cm level) of the imaging catheter so this will increase the size of the probe while keeping the spot size on the imaging plane is small enough to maintain reasonable transverse resolution. With the long working distance, the aberration of the focal spot caused by the curvature of the transparent sheath is more severe compared to the non-balloon design, so additional optical design for the curvature correction is required.

For single balloon design, the balloon gives pressure to the surrounding tissue and may deform the tissue structure [4]. Double balloon design, which put the imaging probe between two balloons, can solve the deformation issue, but the imaging location in the human body will be limited [7]. For example, double balloon cannot be used to image the gastroesophageal junction (GEJ) because the distal balloon will be in the stomach and cannot stable the imaging catheter anymore. One general disadvantage of the balloon design is that the probe might not always be at the central position of the balloon, so some part of the tissue can be out of the imaging range even if the probe is well stabilized in the human body.

5.2.3 Raster Scan Side Imaging

Proximally actuated imaging catheters generally have the problem that the intrinsic scanning uniformity cannot be controlled quite well, which limits the OCT images to reveal structural information and difficult to provide information of the smaller features due to the lack of image registration mechanism. Hence, distally actuated scanning probes are preferable in terms of revealing small features of the tissue, although they cover less scanning range than the rotary ones. Raster scanning method is one of the distal actuation that can be used for the endoscopic OCT imaging. The fiber tip at the distal end of the imaging catheter can be swept either by a PZT bender or some electromagnet actuators to achieve raster scanning. The beam from the fiber tip is then focused by a lens and deflected by a prism or mirror. PZT based benders can easily achieve over 1 kHz scanning speed but their scanning range is limited by their own length, so most of the PZT based probe designs are using the resonance of the fiber tip to get a

larger scanning range while keep everything short and small. By changing the length of the fiber tip or the loading mass on the fiber tip, the resonant frequency of the fiber can be adjusted.

The deflected scan can be done either perpendicular or parallel to the optical axis by the orientation of the prism/mirror. For the perpendicular case, the slow scan can be done by pulling back the whole imaging catheter, as shown in **Fig. 5.1C**. By pulling back the probe, the scan can eventually cover a very long area but it also has the drawback of imaging registration issue. For the parallel case, the slow scan can be done by slowly rotating the whole imaging catheter, as shown in **Fig. 5.1D**. Slow speed rotation is more challenging than high speed one, because the effects of the torque and friction to the torque coil are much more apparent under the slow motion. Hence the uniformity of the slow scan will be a big issue for this design since it still needs proximal actuation.

The other important issue for the raster scan is the imaging plane distortion caused by the aberration of the lens and sheath. For the raster scanning design, compound lens is preferable because it can correct the aberration caused by a single lens or GRIN lens [11]. Also the distortion by the curvature of sheath can affect the beam quality while scanning to off axis position. Raster scanning perpendicular to the imaging catheter (**Fig. 5.1C**) has high aberration because the beam is incident with a large angle on the curved surface of the probe sheath. Raster scanning parallel to the imaging catheter with rotation and pull back (**Fig. 5.1D**) has less aberration because the beam is scanning along the probe axis.

5.2.4 Raster Scan Forward Imaging

The other method using raster scan is forward imaging geometry. In contrast to the side imaging geometry, the light from the fiber tip is focused by the lens and then go through a transparent window that is used in contact with the tissue or specimens. The imaging area is limited by the allowable scanning range of the fiber (the diameter of the probe) and the magnification of the optics design. Hence this type of design usually requires larger probe diameter, which make it more difficult to go through the working channel of the conventional endoscope.

There are several ways to obtain the slow scan. One way is to slowly rotate the whole imaging catheter to get a circular imaging field, as shown in **Fig. 5.1E**. Again this suffers from the slow scan non-uniformity that is actuated proximally. With this raster plus slow rotation design, there exist other issues such as non-uniform exposure, non-uniform scanning density, and imaging registration for off-center rotation. The inner part of the circular field always gets denser scan compared to the outer part of the field, so the effective exposure time and the pixel density for the inner part is higher. These issues need to be considered to meet the ANSI standard and to re-map/reconstruct the 3D data set.

5.2.5 Spiral Scan Forward Imaging

Forward imaging using quadruple PZT tubes is also a feasible way to get endoscopic OCT images [8]. As **Fig. 5.1F** shows, the fiber goes through the PZT tube and can be actuated two-dimensionally. By applying amplitude-varying sinusoidal waves with 90^{o} phase difference to the two pairs of the electrodes, the fiber tip can be actuated in a spiral pattern and obtain 3D OCT data. Since both axes are actuated distally, the scan can be controlled precisely so this scanning mechanism is particularly suitable for the high magnification, small field imaging, such as optical coherence microscopy (OCM) and multi-photon microscopy (MPM). Recently there is a new method that drives two scanning directions with slightly different frequency [12]. The resulting scanning pattern is a Lissajou pattern with the frame rate of the difference of the two driving frequency. These methods eliminates the need of additional slow scan so the probe design can be less complex and size can be smaller than the raster scanning one.

However, these methods highly requires precise mapping of the pixels during the scanning. The scanning density of the spiral and Lissajou pattern are also non-uniform. Another issue for the scanning method is that the fiber tip is driven with frequencies close to the resonance. If there is any environmental perturbation or something hit the probe while imaging, the scanning pattern might be easily messed up and the mapping of the pixels thus can be wrong. This actually is the common problem for raster, spiral, and Lissajou methods because they both vibrate the fiber with frequency close to resonance.

Table 5.1 shows the summarized comparison of the methods mentioned above. Depending on the application, different scanning mechanism can be used. After determining which scanning method is preferred, the next step will be to determine the scanning parameters for the probe such as scanning range, scanning speed, number of pixels in a frame, and so on.

Table 5.1 Comparison between difference scanning methods.

	Advantage	Disadvantage
Proximally rotary	• Simple optical design • Small • No aberration • Large scanning range • Water can be used to reduce reflections / aberration	• Rotary non-uniformity • Pull back non-uniformity • Unstable slow scan
Rotary with single balloon	• Simple optical design • Small • More stable for slow scan • Large scanning range • Water can be used to reduce reflections / aberration	• Rotary non-uniformity • Deformation of tissue • Probe off-centered • Aberration from sheath
Rotary with double balloon	• Simple optical design • Small • More stable for slow scan • No tissue deformation • Large scanning range • Water can be used to reduce reflections / aberration	• Requires balloon and inflation • Rotary non-uniformity • Probe off-centered • Aberration from sheath • Imaging location limited
Raster scan side (perpendicular)	• Higher scanning speed • Large scanning range • No fast scan non-uniformity	• Image area is long strip • Larger probe • Sine wave correction • Sensitive to perturbation • Aberration from scanning at high angle to sheath • Water cannot be used
Raster scan side (parallel)	• Higher scanning speed • Large scanning range • No fast scan non-uniformity • Could be combined with balloon design	• Image area is spiral strip, covering large area • Larger probe • Sine wave correction • Sensitive to perturbation • Requires rotary and electrical connector • Water cannot be used
Raster forward	• Higher scanning speed • No fast scan non-uniformity • More stable for slow scan	• Large • Limited imaging range • Sine wave correction • Sensitive to perturbation
Spiral/Lissajou scan	• Small • Simple design • No fast scan non-uniformity • Simultaneous 2D scan	• Limited imaging range • Lissajou pattern correction • Sensitive to perturbation • Slower scanning speed

5.3 Important Parameters for Imaging Catheter Design

In OCT imaging, the line rate of the imaging system determines the basic scanning speed. For time domain OCT (TD-OCT), the line rate is determined by the scanning speed of the mirror in the reference arm; for spectral domain OCT (SD-OCT), the line rate is determined by the speed of the spectrometer (or the line scan camera); for swept source OCT (SS-OCT), the line rate is determined by the sweep rate of the swept source. For different applications, the image requirements are also different in terms of transverse resolution, the size of the imaging field, and data acquisition time.

For a certain application, the required transverse resolution and scanning range should be determined first. Typically transverse resolution of 10 μm to 20 μm is good enough for applications that require imaging over a larger area, and 3 μm to 5 μm for applications that require high magnification imaging. After determine the transverse resolution, the line pitch of the scanning can also be determined. Typically the line pitch can be the same as the transverse resolution but it can be smaller to achieve denser scan. With the line pitch and the required scanning range, the number of lines per frame can be determined. For rotary scanning methods, the scanning range (circumference) is determined by the working distance (radius) of the probe; for raster scan, it is usually in the millimeter level.

For example, typical scanning ranges of 8 mm, 56 mm, and 2 mm are chosen for rotary, rotary with balloon, and raster scan, respectively. For a transverse resolution of 15 μm and line pitch of 15 μm for the proximal rotary and rotary with balloon cases, the corresponding number of lines per frame are ~550, ~3,800, respectively; for a transverse resolution of 5 μm for the raster case, the corresponding number of lines per frame is 400. With the number of lines per frame and the OCT system line rate, the frame rate for the scanning probes can be calculated. For a SS-OCT with 250 kHz swept source, the maximum frame rate of the proximally rotary probe is 460 fps to keep the line pitch matching the transverse resolution. With the line pitch and the frame rate, the fastest speed of the slow scan can also be determined. Usually the memory limitation of the computer limits the maximum time that can be used to acquire a 3D data set, typically 20 to 30 seconds, which then determines the maximum slow scan range with the known slow scan speed. From the slow scan range and slow scan speed, the number of frames per dataset can be determined. **Table 5.2** shows the example the scanning parameters of different scanning methods under the line rate of 250 kHz.

Recently high speed OCT imaging systems were demonstrated, higher OCT line rate can also be achieved. With higher line rate, it is possible to reduce the line pitch to get denser scanning or increase the scanning range with the same line pitch. **Table 5.3** shows the example of the scanning parameters of different scanning methods under the line rate of 1 MHz.

Table 5.2 Scanning parameters of different scanning methods at 250 kHz axial line rate.

General Parameters			
Line rate of the system [Lines/sec.]	250,000		
Maximum acquisition time [sec.]	20		
Scanning Parameters			
	Proximally rotary	**Rotary with balloon**	**Raster**
Required transverse resolution [μm]	15	15	5
Working distance [mm]	1.3	9	0.5
Required scanning range (fast) [mm]	8.17	56.55	2
Line pitch (fast) [μm]	15	15	5
Number of lines per frame	544.54	3,769.91	400
Frame rate [fps]	459.10	66.31	625
Line pitch (slow) [μm]	15	15	5
Maximum Slow scanning speed [mm/sec.]	6.89	1	3.12
Maximum slow scan range [mm]	137.8	20	62.4

Table 5.3 Scanning parameters of different scanning methods at 1 MHz axial line rate.

General Parameters			
Line rate of the system [Lines/sec.]	1,000,000		
Maximum acquisition time [sec.]	20		
Scanning Parameters			
	Proximally rotary	**Rotary with balloon**	**Raster**
Required transverse resolution [μm]	15	15	5
Working distance [mm]	1.3	9	0.5
Required scanning range (fast) [mm]	8.17	56.55	2
Line pitch (fast) [μm]	15	15	5
Number of lines per frame	544.54	3,769.91	400
Frame rate [fps]	1,836	265	2500
Line pitch (slow) [μm]	15	15	5
Maximum slow scanning speed [mm/sec.]	27.5	4	12.5
Maximum slow scan range [mm]	550	80	250

5.4 General Imaging Catheter Design Problem

Once the scanning parameters are determined and evaluated, then we need to consider some practical problems that may occur while we are designing the probe. Without taking care of these issues, the performance of the probe will not be optimized and may fail in the real-world applications.

5.4.1 Choice of Imaging Lens

As mentioned in the Section 5.3, the choice of the imaging lens plays an important role for fiber-sweeping based scanning method, because the off-axis aberration is quite severe in GRIN lens or single

lens. In this section, ZEMAX simulation of a simple fiber scanning optical system was done and different types of lens were used for comparison. The optical path begins from a single mode fiber (SMF) with core diameter of 9.2 μm, corresponding to the numerical aperture of 0.128. The light then goes through a lens and is focused on the imaging plane 3.5 mm from the back surface of the lens. Different lenses including a GRIN lens, a singlet, and a doublet were simulated. The focal length and the diameter of these lenses are similar so the magnifications of all configurations are very close, which is around 2. The beam profiles and sizes on the imaging plane were recorded when light is on axis and when the light is scanned 400 μm off axis.

Figure 5.2 shows the optical scanning system using a GRIN lens. When the light is on axis, the beam is focused quite well. However, when the light is off axis, the beam size increases quite a lot, indicating the focal point is not on the imaging plane anymore. **Figure 5.3** shows the optical scanning system using a singlet. When the light is off axis, it is very apparent that the light is focused very far away from the imaging plane, which is even worse than the GRIN lens. Although using a singlet can save a lot of space, it is not a good choice for a fiber sweeping probe. **Figure 5.4** shows the optical scanning system using a doublet, which is actually a combination of two lenses with lower power. After optimize the relative distance of the two lenses, the beam profile is not distorted a lot when the light is off axis. This indicates that a doublet or compound lens designs are preferable for the fiber sweeping probe.

5.4.2 Aberration Effect from the Sheath

For the side imaging probes, the curvature of the sheath can also provide an aberration source to the optical system. With the same doublet configuration in the previous section, a FEP plastic sheath with 1mm radius of curvature and thickness of 200 μm is inserted at different location between the lens and the imaging plane. **Figure 5.5** shows the situation with the sheath very close to the imaging plane (500 μm working distance). In this case, the sheath does not provide too much aberration to the beam profile and focal plane, and the sheath improves the off-axis beam profile compared to the configuration without the sheath. On the other hand, when the sheath is far away from the imaging plane (2.5 mm working distance), as **Figure 5.6** shows, the aberration effect caused by the sheath become very severe. This is the reason why the balloon based imaging probe requires astigmatism correction.

For the raster scan perpendicular to the axis of the imaging catheter, there is an additional issue needs to be considered. Since the beam is usually scanned by 0.5 to 1 mm and the sheath has a 1 mm radius of curvature, the beam is at high incident angle to the sheath near the edge of the scan. This can be a limiting factor for the usable imaging range when designing this type of the imaging catheter.

5.4.3 Dimension of Imaging Catheters

The other practical issue that needs to be considered is the final catheter size, including the outer diameter and the rigid length. These two dimensions determine whether a probe can go through the working channel of the endoscope. Typical diameter of the endoscope working channel is between 2.8 mm to 3.7 mm. Although there are some endoscopes with larger working channel (>5 mm diameter), the ~30 degree turn in the proximal part of the working channel still limits the diameter of the imaging catheter that can go through the channel. Hence, if the imaging catheter needs to go through the working channel of conventional endoscope, the preferable catheter diameter should be less than 2.5 mm and rigid length less than 25 mm. For most of the proximal actuated imaging catheter, these dimension requirements are easy to meet because there is no scanning part in the distal end.

The other insertion method is the "overtube" configuration. Rather than going through the working channel of the endoscope, the imaging catheter is attached outside of the endoscope tip. This allows the imaging catheter being made with larger size. However, the overall diameter of the imaging catheter should not be larger than 5 mm. Otherwise the endoscope is very difficult to be inserted into the human body with the catheter attached.

5.5 Figures

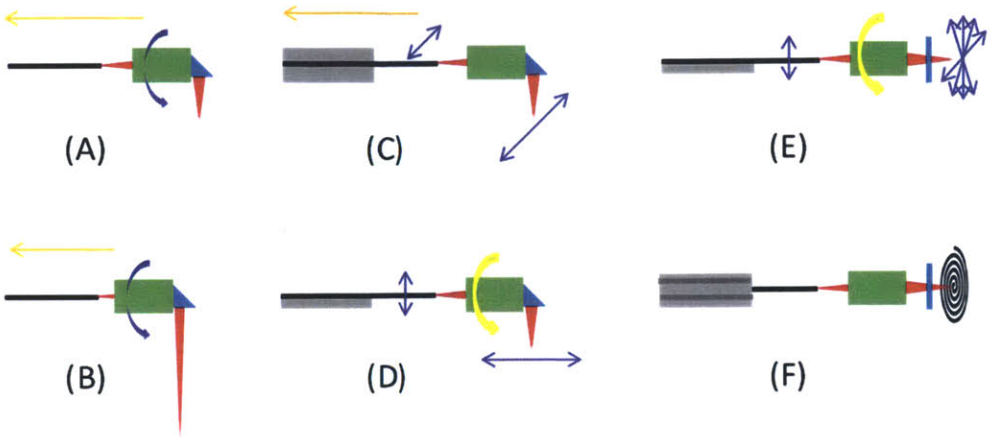

Figure 5.1. Schematics of the different scanning method. (A) Standard rotary scan with pull back. (B) Rotary scan with balloon and pull back. (C) Raster scan perpendicular to axis with rotation and pull back. (D) Raster scan parallel to axis with pull back. (E) Raster forward imaging with rotation. (F) Spiral scan. Purple arrow: fast scan. Yellow arrow: slow scan.

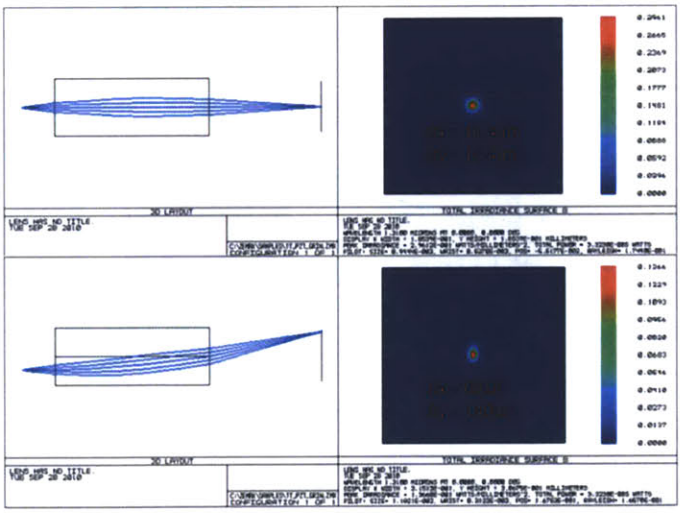

Figure 5.2. Optical scanning simulation using single GRIN lens.

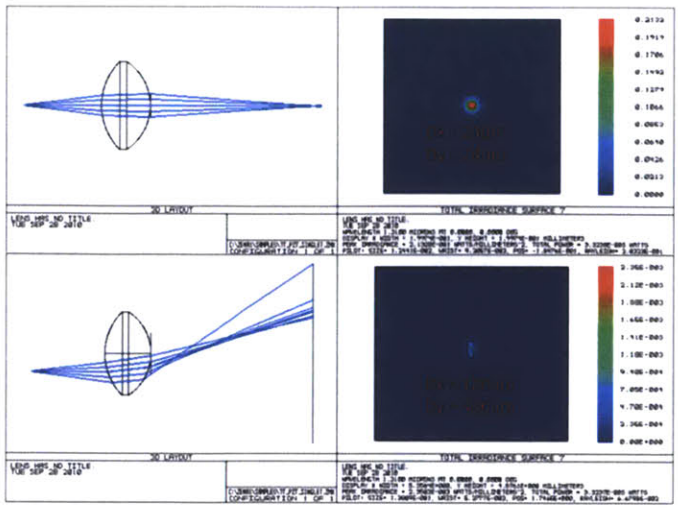

Figure 5.3. Optical scanning simulation using singlet.

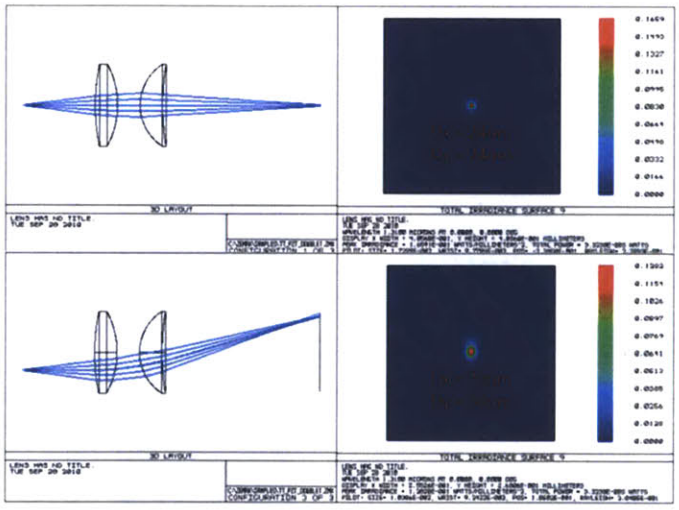

Figure 5.4. Optical scanning simulation using doublet.

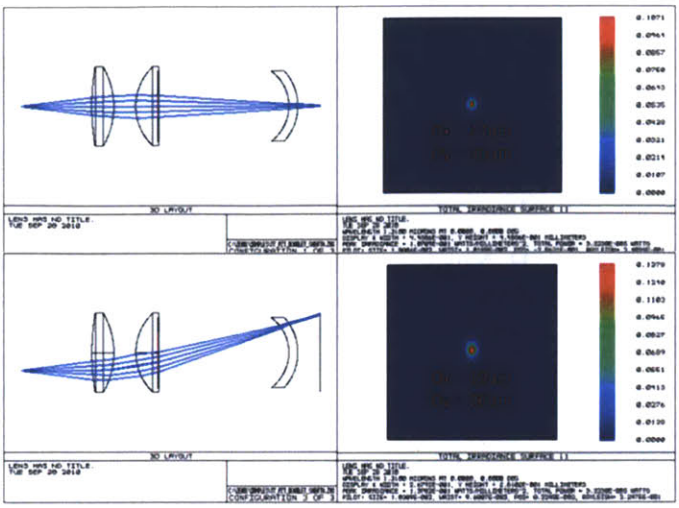

Figure 5.5. The aberration effect from the sheath with short working distance.

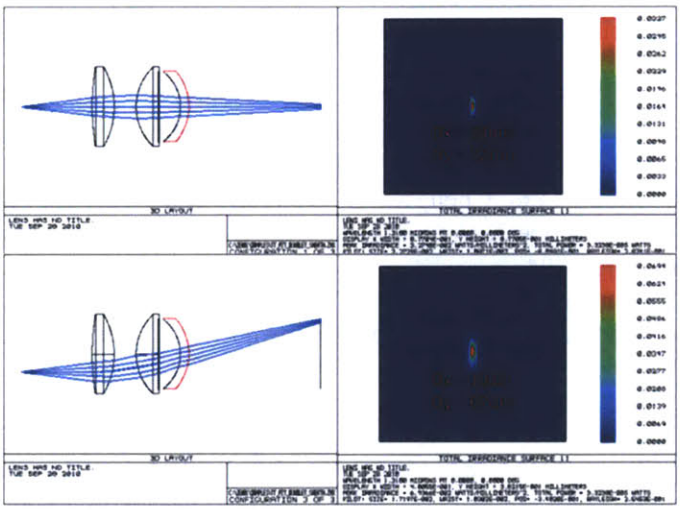

Figure 5.6. The aberration effect from the sheath with long working distance.

5.6 References

[1] G. J. Tearney, S. A. Boppart, B. E. Bouma, M. E. Brezinski, N. J. Weissman, J. F. Southern, and J. G. Fujimoto, "Scanning single-mode fiber optic catheter-endoscope for optical coherence tomography," *Optics Letters,* vol. 21, pp. 543-5, Apr 1996.

[2] S. H. Yun, G. J. Tearney, B. J. Vakoc, M. Shishkov, W. Y. Oh, A. E. Desjardins, M. J. Suter, R. C. Chan, J. A. Evans, I. K. Jang, N. S. Nishioka, J. F. de Boer, and B. E. Bouma, "Comprehensive volumetric optical microscopy in vivo," *Nature Medicine,* vol. 12, pp. 1429-1433, Dec 2006.

[3] B. J. Vakoc, M. Shishko, S. H. Yun, W. Y. Oh, M. J. Suter, A. E. Desjardins, J. A. Evans, N. S. Nishioka, G. J. Tearney, and B. E. Bouma, "Comprehensive esophageal microscopy by using optical frequency-domain imaging (with video)," *Gastrointestinal Endoscopy,* vol. 65, pp. 898-905, May 2007.

[4] M. J. Suter, B. J. Vakoc, P. S. Yachimski, M. Shishkov, G. Y. Lauwers, M. Mino-Kenudson, B. E. Bouma, N. S. Nishioka, and G. J. Tearney, "Comprehensive microscopy of the esophagus in human patients with optical frequency domain imaging," *Gastrointestinal Endoscopy,* vol. 68, pp. 745-753, Oct 2008.

[5] H. L. Fu, Y. X. Leng, M. J. Cobb, K. Hsu, J. H. Hwang, and X. D. Li, "Flexible miniature compound lens design for high-resolution optical coherence tomography balloon imaging catheter," *Journal of Biomedical Optics,* vol. 13,Nov-Dec 2008.

[6] J. F. Xi, L. Huo, Y. C. Wu, M. J. Cobb, J. H. Hwang, and X. D. Li, "High-resolution OCT balloon imaging catheter with astigmatism correction," *Optics Letters,* vol. 34, pp. 1943-1945, Jul 2009.

[7] W. Kang, H. Wang, Y. S. Pan, M. W. Jenkins, G. A. Isenberg, A. Chak, M. Atkinson, D. Agrawal, Z. L. Hu, and A. M. Rollins, "Endoscopically guided spectral-domain OCT with double-balloon catheters," *Optics Express,* vol. 18, pp. 17364-17372, Aug 2010.

[8] X. M. Liu, M. J. Cobb, Y. C. Chen, M. B. Kimmey, and X. D. Li, "Rapid-scanning forward-imaging miniature endoscope for real-time optical coherence tomography," *Optics Letters,* vol. 29, pp. 1763-1765, Aug 2004.

[9] A. D. Aguirre, J. Sawinski, S. W. Huang, C. Zhou, W. Denk, and J. G. Fujimoto, "High speed optical coherence microscopy with autofocus adjustment and a miniaturized endoscopic imaging probe," *Optics Express,* vol. 18, pp. 4222-4239, Mar 2010.

[10] Y. T. Pan, H. K. Xie, and G. K. Fedder, "Endoscopic optical coherence tomography based on a microelectromechanical mirror," *Optics Letters,* vol. 26, pp. 1966-1968, Dec 2001.

[11] J. Xi, Y. Chen, Y. Zhang, K. Murari, M.-J. Li, and X. Li, "Integrated multimodal endomicroscopy platform for simultaneous en face optical coherence and two-photon fluorescence imaging," *Optics Letters,* vol. 37, pp. 362-364, Feb 2012.

[12] S. Moon, S.-W. Lee, M. Rubinstein, B. J. F. Wong, and Z. Chen, "Semi-resonant operation of a fiber-cantilever piezotube scanner for stable optical coherence tomography endoscope imaging," *Optics Express,* vol. 18, pp. 21183-21197, Sep 2010.

CHAPTER 6

6.0 Endoscopic 3D-OCT Balloon Imaging

6.1 Motivation

Although the imaging coverage of the standard proximally rotary imaging catheter used in the clinical system is significantly larger than standard biopsy, a single volumetric 3D-OCT data set only cover about one sixth of the entire circumference of the distal esophagus. If the features of interest in the esophagus are missed, such as buried glands or unburned BE immediately after the ablation therapies, these sampling errors can create uncertainty in the results and affect the accuracy of the experiment. To overcome these potential sampling error issues, multiple 3D-OCT data sets will need to be acquired to achieve more comprehensive coverage over different quadrant of the esophagus. However, some other features such as BE epithelium thickness may vary if the contact of the imaging catheter on the tissue changes as the catheter is placed at different quadrant of the esophagus. In the RFA prediction study shown in Chapter 4, the imaging catheter was in contact with the esophagus at the certain position to maintain a consistent catheter contact for every patient, and only a small range in the cross-sectional images was used for the measurement of BE epithelium thickness. Therefore, a different probe design that can provide a full circumferential coverage and consistent contact pressure around the whole catheter is important to reduce those potential sampling errors and pressure-induced variation for the future studies.

In this section of the thesis work, a new design of balloon based imaging catheter for endoscopic 3D-OCT is developed, which can provide larger imaging field compared to the standard rotary imaging catheter. The balloon imaging catheter is specially designed so it is compatible with the new 3D-OCT engine, which is modified from the cardiovascular imaging system developed by Lightlab Imaging, Inc. / St. Jude Medical, Inc. The detailed design of the balloon imaging catheter including the optics simulation, correction of aberration, disinfection requirement, and final specifications will be presented. Finally, examples of the 3D-OCT data sets taken in human esophagus using the balloon imaging catheter will also be shown to demonstrate the performance of this catheter design. The high speed OCT engine used in this study was built by Dr. Joseph Schmitt and Dr. Desmond Adler at LightLab. The endoscopic OCT data that is presented in this chapter was taken in collaboration with Dr. Hiroshi Mashimo, MD, PhD who performed all of the endoscopy sessions. Dr. Yuankai Tao, PhD, participated in the discussion of balloon catheter design and helped the documentation of disinfection procedures. Multiple group members including Dr. Tao, Hsiang-Chieh Lee, Osman Ahsen, and Kaicheng Liang shared the experimental responsibilities in the endoscopy clinics on alternating weekly basis. All the data processing and analysis were done by the author of the thesis work.

6.2 Optical Design of Balloon Imaging Catheters

Figure 6.1 shows a schematic diagram of the balloon based imaging catheter and the complete distal tip of the catheter. The imaging catheter employs a medical balloon that is inflated and in contact with the

esophagus during the image acquisition. A length of SMF-28 fiber ringing to the proximal end of the imaging catheter is terminated in a glass ferrule. The beam exiting the fiber expands in an epoxy spacer. The epoxy spacer allows the input aperture of a bulk GRIN lens to be filled more effectively. The GRIN lens with a pitch of 0.12 at 1,310 nm was modified from a commercially available element with a numerical aperture (NA) of 0.46 and a pitch of 0.25 at 1,310 nm. A cylindrical mirror with angle of 40^{o} was used to direct focused beam out the side of the imaging catheter and compensate the aberration caused by the cylindrical surfaces from the plastic sheath. All of the micro-optic components were glues to a stainless steel hypo tube. The lens system was glued inside of the flexible torque coil. A transparent plastic sheath encapsulated the entire imaging catheter, providing electrical and biological isolation. The distal end of the plastic sheath is sealed to avoid any biological fluid contaminating the optics of the imaging catheter.

6.2.1 Medical Balloon Selection

Medical balloon catheters are mainly used for medical procedures including percutaneous transluminal coronary angioplasty (PTCA), stent delivery, and lumen dilation [1, 2]. Recently the balloon catheter is integrated with imaging technologies such as OCT to maintain the imaging position in the human body and increase the imaging area compared to standard imaging catheter [3, 4]. There are two types of medical balloons, compliant and non-compliant. Compliant balloons are used for occlusion and anchoring in a variety of medical procedures. The complaint balloons are typically fabricated from polyurethane and nylon elastomers, and the burst pressure ranges from 0-30 pounds per inch (psi). The compliance range of this type of balloons can be 20-100% more than their original size depending on the volume of the gas inflated into the balloon. Since the variation of the size of the compliant balloons is large, this type of balloon is not suitable for the imaging technologies, which require fixed working distance. Non-compliant balloons, on the other hand, are typically fabricated from polyethylene (PET) and nylon and can sustain very high pressure up to 400 psi, so the compliance range is 0-10%, which is more suitable for OCT imaging.

In the imaging catheter design, a transparent PET balloon with the outer diameter of 16 mm and overall length of 6 cm is chosen for OCT imaging in the esophagus. The average human esophagus can be distended to approximately 2 cm in the anterior-posterior dimension and up to 3 cm laterally to accommodate a swallow bolus [5]. In order to cover the full circumference of the esophagus without provide too much pressure and suppress the tissue features, the diameter of the balloon is chosen to be slightly smaller than the average size of the esophagus. The balloon has a wall thickness of 50 μm and a burst pressure of 180 psi. The diameter of the balloon remains the same when the balloon is inflated up to 90 psi and the typical pressure of inflation during the imaging is about 3.5 psi.

6.2.2 ZEMAX Modeling

A complete ZEMAX model of the balloon imaging catheter, including the sheath, balloon, and tissue, was constructed to optimize the length of GRIN lens and the curvature of the cylindrical mirror. The ZEMAX model is shown in **Fig. 6.2**. The sheath and balloon are modeled as two surfaces with one-dimensional curves corresponding to the inner and outer radius of the sheath and the balloon. An 8° angle is introduced at the second surface to account for the angle polish on the glass ferrule. Note that the ray trace used to generate **Fig. 6.2** begins inside the ferrule, whereas the Gaussian beams used for optimization and spot size estimation were launched from the output surface of the ferrule.

After selection of an appropriate epoxy spacer (2 mm in this design) and an appropriate GRIN lens from the catalogue of a commercial supplier, there are two free parameters in this model, which are the length of the GRIN lens and the radius of curvature of the cylindrical mirror. These parameters were optimized by constructing a merit function that placed a beam waist at the desired focal plane in the tissue, which is determined by the size of the balloon. The merit function equally weighted the spot in both dimensions at the focal plane to ensure the spot size is as circular as possible. After optimization the spot size (diameter) in tissue was estimated to be 30 μm in X and 28 μm in Y. The spot diagram at the focal plane in tissue is shown in the inset of **Fig. 6.2**. Minimal astigmatism is observed when the radius of curvature of the cylindrical mirror (32 mm in this design) completely compensates the radius of curvature of the plastic sheath (1.05 mm in this design).

6.2.3 Minimization of Backreflection

For 3D-OCT imaging applications it is critical to minimize backreflected light from each surface in the catheter. Backreflected light creates significant amounts of image noise by flooding the photodetector with incoherent photons. Backreflected intensities should generally be several orders of magnitude less than the expected reference arm power to minimize this effect. With typical power levels of 20 mW transmitted into the imaging catheter, backreflection levels of lower than -50 dB are required. Standard antireflection coatings provide -10 to -20 dB of reflection suppression and are not suitable for this application. Backreflection levels were reduced to -50 to -65 dB in the imaging catheter by angle polishing the end surface of the glass ferrule and the first surface of the GRIN lens, and by using an epoxy spacer instead of an air spacer. An angle of +8° was introduced to the glass ferrule to reduce backreflection between the interface fiber and epoxy. The epoxy used in the spacer was chosen to have a refractive index of 1.4, which is very close to the refractive index of the fiber core (1.467). The first surface of the GRIN lens was polished at an angle of -8° in order to direct reflected light away from the fiber in the center of the ferrule. The dominant source of remaining backreflection was the second surface

of the GRIN lens, which is a glass/air interface. The backreflection can be reduced by polishing the surface at an angle of 5° to 6°. The angle of the surface cannot be larger than 6°, otherwise the output angle of the beam will be far away from the optical axis of the imaging catheter and aberration cannot be corrected properly by the cylindrical mirror. In the future a custom cylindrical mirror made from an angled prism with slightly tilted output surface could be used to further minimize backreflection, if necessary.

6.2.4 Performance Measurement

The balloon imaging catheter design provided good performance and high assembly yields of better than 90%. Measurement of transmission, back coupling, working distance, and backreflection levels are shown in **Table 6.1**. Working distance was measured in air from the plastic sheath, and thus is very close to the actual working distance when considering the balloon and in tissue. A working distance of 8.5 mm in air is desired for an optimal final working distance.

Transmission levels were high (75%) and showed a very low standard deviation across the three balloon probes measured (±2.5%). Back coupling was 54% in average and the standard deviation was ±8.5%, which is slightly high but understandable given the sensitivity of back coupling to wavefront aberration. The working distance was 8.63 mm ± 0.15 mm compared to an ideal value of 8.5 mm. The working distance was precisely set for each individual catheter by placing a mirror 8.5 mm from the sheath outer surface and adjusting the axial position of the glass ferrule relative to the GRIN lens to maximize the back-coupled power. Backreflection levels were very low (-52.3 dB ± 2 dB).

Table 6.1 Measured performance of three balloon imaging catheter.

Probe Number	Transmission	Back Coupling	Working Distance [mm]	Backreflection [dB]
1	75%	63%	8.6	-54
2	78%	53%	8.5	-53
3	73%	46%	8.8	-50
Mean	*75.33%*	*54%*	*8.63*	*-52.3*
SD	*2.5%*	*8.5%*	*0.15*	*2*

The beam profile at the focal plane and the spot size were measured by using a laser beam imager (WinCamD, DataRay, Inc.) that is sensitive to wavelength of 1.3 μm. The CCD chip of the camera is 10 mm away from the imaging window (the minimum distance between the light source to the CCD ship is 10 mm) but the working distance of the balloon probe is ~8.5mm, so the beam imager cannot directly

measure the spot size of the imaging catheter at the focal plane. Therefore, according to the Gaussian beam propagation theorem, it is possible to calculate the spot size at the focal plane by measuring the spot sizes from difference imaging planes. **Figure 6.3** and **Figure 6.4** show the measurement of the spots taken at the plane 2 mm and 4.2 mm away from the focal plane using probe #2. The beam profile appears to be slightly elliptical, which corresponds well with the ZEMAX simulation result shown in **Fig. 6.2**, indicating the cylindrical mirror can compensate the aberration caused by the plastic sheath. The measured FWHM spot sizes are ~55 μm at the 2 mm plane and ~90 μm at the 4.2 mm plane. Using the formula of the Gaussian beam propagation [6, 7],

$$w(z) = w_0 \sqrt{1 + \left(\frac{z}{z_R}\right)^2} \tag{6.1}$$

where w_0 is the spot size at the focal plane, $w(z)$ is the spot size measured at the imaging plane away from the focal plane with distance of z, and $z_R = \pi w_0^2 / \lambda$ is the Rayleigh range, the spot size at the focal plane can be calculated based on the measured spot sizes at the two difference imaging planes. The calculated spot size at the focal plane was ~30 μm, which also corresponds well with the ZEMAX simulation. **Figure 6.5** shows the plot of the spot size comparison between the theoretical value based on Equation (6.1) and the measured values at different imaging plane, indicating this method is valid for the back calculation of the focal spot size.

6.3 Mechanical Design of Balloon Imaging Catheters

The mechanical design of the imaging catheter is equally important to the optical design, since stable transmission of the rotational and pullback motion from the proximal PIU to the distal tip is required to generate a high quality spiral scan pattern of the imaging beam. Due to the multiple lumens nature of the balloon based catheter, the disinfection procedures of the imaging catheter need to satisfy the regulations at the Veterans Affairs Boston Healthcare System (VABHS). Hence the balloon imaging catheter is specially designed to allow thorough disinfection of all parts and can be assembled prior to the use in the human body. In addition, the imaging catheter must be designed to be flexible and robust enough to survive multiple usages. The following sections describe the mechanical design of the torque coil, proximal joint between the torque coil and the rigid hypodermic metal tube, balloon catheter assembly that allows thorough disinfection, and the patient interface unit (PIU) adapter for the balloon imaging catheter.

6.3.1 Torque Coil Selection

A flexible torque coil usually comprises of multiple layers of densely wound wires so it can be used to transmit rotational and pullback motion from the PIU to the distal tip of the imaging catheter. Torque coil designs inherently trade of stiffness against torque transmission; a very stiff coil accurately transmits rotation and translation, whereas a flexible coil is more compressible or stretchable and therefore transmits motion less accurately. Two torque coil designs with different stiffness characteristics were tested for GI endoscopy applications. The more flexible design can produce stable rotational motion at up to 120 Hz, but its push/pull translation was degraded compared to the rigid torque coil. The more rigid design was found to translate the stable rotational motion at no more than 80 Hz, but can translate both push/pull and rotary motion very effectively, so the overall performance was significantly better. The final torque coil used in the balloon imaging probe was a single layer design with an outer diameter of 1.8 mm and an inner diameter of 1.26 mm. The outer diameter of the lens holder is 1.23 mm so the lens holder can perfectly fit inside the torque coil, which do not increase the diameter of the imaging catheter at the distal end and thus no additional friction is generated. The overall length of the torque coil was 2 meters, making the imaging catheter compatible with conventional GI endoscopes.

6.3.2 Proximal Joint

A potential failure point is present at every location where two probe components are jointed together. Therefore, it is important to design each joint for high strength while still allowing for high speed translational and rotational motion. As described in Section 6.3, the joint between the lens holder and the torque coil is putting lens holder in the torque coil and filling the joint with epoxy to prevent separation of the lens from the coil. A similar method is employed at the proximal end of the imaging catheter. Here the torque coil joins a long, rigid hypo tube that is glued to a standard SC/APC fiber connector on the other end using epoxy. The connector and hypo tube allow the imaging catheter to be attached to the PIU. The joint between the hypo tube and the torque coil is shown in **Figure 6.6**. The distal end of the hypo tube that goes into the torque coil is drilled several small holes, so the epoxy can fill into these gaps and enhance the strength of the joint. A free floating inner hypo tube is positioned over the top of the SMF-28 fiber to prevent epoxy from adhering to the fiber and causing stress when the probe is flexed. This joint structure provides strain relief and high strength while still permitting the fiber to flex within the torque coil.

6.3.3 Balloon Catheter Assembly

According to the VABHS guidelines of sterilization/disinfection for instruments from other institutes, any instrument that was brought to VABHS from other institutes or facilities requires to be sterilized or disinfected before it can be used in the human body, especially the instruments with lumens. The

commercialized instruments such as biopsy forceps, guide wires, and dilation balloons typically are sterilized using either ethylene oxide (EO)/gas or gamma/radiation and packaged and then transported to the hospitals, so these instruments can be directly used during the medical procedures. However, custom-built devices such as the standard rotary imaging catheter can balloon imaging catheter do not go through the sterilization process, so their external surfaces and lumens need to be at least disinfected prior to use. The standard disinfection method is to wipe the external surface of the instrument and flush the lumens with disinfection solution such as enzymatic detergent, clean the external surface and lumens with clean water, and dry the external surface and lumens. The balloon imaging catheter design has multiple closed lumens (the plastic sheath plus the balloon), which makes it very difficult to perform the standard disinfection procedures.

In order to satisfy the disinfection guideline and follow the standard disinfection procedures at VABHS, the balloon imaging catheter was designed into two parts: (1) reusable imaging catheter with sealed inner sheath and (2) disposable balloon sheath with an open lumen. **Figure 6.7** shows the schematic diagram of this balloon imaging catheter assembly concept. The imaging catheter part is very similar to the standard rotary imaging catheter, but with the distal end of the sheath completely sealed to prevent any biological fluid getting into the imaging catheter. Since the imaging catheter is completely sealed, it can be considered as an instrument with no lumen and thus only its external surface needs to be disinfected. This also makes the disinfection procedures for the reusable imaging catheter less time-consuming. The balloon sheath part can be disinfected based on the standard disinfection procedures because it has an open lumen. The lumen of the balloon sheath can be flushed with disinfection solution and water, and then dried by flushing air through the sheath. Before performing OCT balloon imaging, these two parts will be assembled together by inserting the imaging catheter into the balloon sheath. The outer diameter of the imaging catheter was designed to be a tight fit to the distal neck of the balloon, which completely seals the distal end of the balloon catheter, so the assembled balloon imaging catheter can be inflated/deflated via the air flushing port during the imaging.

6.3.4 PIU Adapter

An SC/FPC connector and air flush port are attached to the proximal end of the imaging catheter as shown in **Figure. 6.8**. The outer diameter of the hypo tube is matched with the fiber insertion channel of the SC/FPC connector to ensure the fiber centered inside the connector. To keep the fiber in the center is critical to prevent off-axis motion of the imaging catheter when the PIU motor is rotating. A plastic adapter to secure the imaging catheter in the PIU is fastened over a metal sleeve and a standard Tuohy-Borst flush port is used to allow air inflation of the balloon catheter during the imaging. The plastic sheath containing the torque coil ad fiber is glued to the flush port to form a tight seal.

6.4 System Description

For the balloon imaging in the GI tract, a new endoscopic 3D-OCT engine modified from the cardiovascular OCT system (M4 Optical Coherence Tomography Imaging System) developed by Lightlab Imaging, Inc. / St. Jude Medical, Inc. was used. This system can support ~2x longer imaging range compared to the previous imaging system so it is suitable for the balloon imaging, which is potentially sensitive to the off-center of the catheter during the image acquisition. As a part of the longitudinal study and to maintain the consistency of the data format, the imaging system operates using the same optical frequency clock (OFC) mechanism, which was discussed in Chapter 3, and the acquired OCT signal is digitized by a 200 Msample/sec 14 bit analog-to-digital converter (ADC). The imaging system was original designed for clinical cardiovascular imaging so whole system is fit within one compact cart and easy to transport between rooms. The light source is a compact 1.3 μm FDML laser with axial line rate of 45 kHz, tuning range of 140 nm, axial resolution of 8 μm in tissue, and system sensitivity of 90 dB. Since the FDML laser has long fiber in the cavity, the axial line rate is sensitive to the temperature change in the environment. The FDML laser can be automatically tuned by the Lightlab developed software to maintain the correct axial line rate.

Table 6.2 Summary and comparison of specifications between systems.

	Prototype System	**M4 System**
Light source	FDML laser	FDML laser
Axial line rate [Hz]	60,000	45,000
Central wavelength [nm]	1,310	1,310
Tuning range [nm]	175	140
Axial resolution (tissue) [μm]	5	8
Sampling rate [MSPS]	200	200
ADC bit depth [bits]	12	14
Imaging range (tissue) [mm]	2	4
Sensitivity [dB]	103	90
Pullback speed [mm/s]	0.5-2	0-10
Maximum pullback range [mm]	20	50

The patient interface unit (PIU) of the system can automatically load and unload the imaging catheter, which requires a special adapter at the proximal end of the imaging catheter. The PIU provides high speed rotation of 30 Hz to 100 Hz, maximum pull back range of 50 mm, and pullback speed from 0 mm/s to 10

mm/s. The system can support imaging depth of 5 mm in air and total acquisition time up to 30 seconds per data set. **Table 6.2** lists a summary and comparison of specifications between the precious prototype Lightlab system and the M4 system.

6.5 *In Vivo* 3D-OCT Balloon Imaging

To evaluate the performance of the balloon imaging catheter, *in vivo* OCT imaging was performed using the Lightlab M4 Imaging System described in Section 6.2 on human hand as well as human esophagus. The frame rate of OCT imaging was 30 fps and the imaging catheter was pulled with pullback speed of 1.5 mm/s, corresponding to a 30 mm for a 20-seconds acquisition. The pixel spacing with these imaging parameters is 33 μm x 50 μm x 8 μm (rotary direction x pullback direction x axial direction). The pixel spacing in the pullback direction is larger than the resolution due to the need of pullback range, and can be reduced by decreasing the pullback speed if necessary.

6.5.1 Preliminary Imaging Test on the Human Hand

Figure 6.9 shows an example 3D-OCT data set taken from a human hand grabbing the inflated balloon catheter. Since the scanning was a spiral pattern, the acquired volumetric data set was a series of radial, cross-sectional images, which forms a cylindrical volume as shown in **Fig. 6.9A**. Although the actual tissue structure is cylindrical shape, it is not easy to visualize the features in perspectives other than cross-sectional images such as **Fig. 6.9C**. To better visualize the volumetric data sets, the acquired cross-sectional images can be transformed into unwrapped rectangular images shown as **Fig. 6.9B** so the tissue volume can be viewed in different orientations such as orthogonal views. The *en face* image (**Fig. 6.9D**) shows the large coverage of the balloon imaging and can be used as a map of certain features such as finger/palm prints and it is also possible to distinguish different tissue types by the projection along the full depth of the tissue. Cross-sectional images along the pullback direction can show the variation of the tissue features over the pullback range and are very sensitive to the stability of the scanning. If the rotary scan or pullback is not stable, the images will show discontinuity or jumps/stretching, respectively, and will miss the detail features that are important for diagnosis. The torque coil chosen for the balloon imaging catheter is especially suitable for pullback and for relatively slow rotation, which is a good fit for this type of applications. **Fig. 6.9E** shows the cross-sectional image along the pullback direction on the hand and the spiral shape of the sweat duct can be clearly distinguished, indicating both the rotary and pullback scan were stable.

6.5.2 In Vivo Imaging in the Human Esophagus

The clinical imaging was performed at the Veterans Affairs Boston Healthcare System (VHABS) Jamaica Plain campus in collaboration with Drs. Hiroshi Mashimo and Qin Huang. Subjects were recruited from the pool of patients undergoing endoscopy for screening, surveillance, or treatment of BE. Subjects followed a standard preparation procedure for upper endoscopy, including cessation of blood thinners and fasting prior to the appointment. Before performing OCT balloon imaging, the disinfected balloon sheath and imaging catheter were assembled together by inserting the imaging catheter into the balloon sheath. The outer diameter of the imaging catheter was designed to be a tight fit to the distal neck of the balloon, which completely seals the distal end of the balloon catheter, so the assembled balloon imaging catheter can be inflated/deflated via the air flushing port during the imaging. 3D-OCT balloon imaging was performed in tandem with standard video endoscopy. Due to the relatively large diameter of the balloon imaging catheter, the balloon imaging catheter had to be completely deflated, wrapped as compact as possible, and inserted through an overtube in the beginning of the imaging session. The reason to pre-load the catheter into the overtube was to avoid the extra friction during the insertion generated by the bent overtube in the esophagus. The pre-loaded overtube was attached to the side of the endoscope with two silicon attachment bands. The current version of the attachment band was a single band, which can simply attach the overtube with the distal end of the endoscope but was not able to maintain adequate or commensurate flexion with the endoscope during the procedure. This made the introduction of the endoscope/overtube into patients' esophagus particularly challenging, since the overtube could not be adequately flexed to avoid the vallecula or to pass the narrow upper esophageal sphincter without difficulty. To overcome this difficulty, a redesign of the attachment band is required, such as customized band that can hold both the endoscope and the overtube individually. During the OCT imaging, the balloon maintained inflated and in contact with the full circumference of the esophagus. Balloon OCT imaging was performed from the gastroesophageal junction (GEJ) and multiple 3D-OCT data sets were acquired every 2 cm higher in the esophagus if the initial BE length of the subject is longer than 3 cm. After the OCT imaging, the imaging catheter along with the endoscope was retracted from the patient and the balloon sheath was disposed.

Table 6.3 Summary of 3D-OCT balloon data collected during upper endoscopy.

Type of BE	Number of Patients	Number of Imaging Sites
BE with LGD	1	4
BE with HGD	5	17

BE: Barrett's esophagus; *LGD*: Low grade dysplasia; *HGD*: High grade dysplasia.

In total, 6 BE patients undergone RFA treatment were imaged with the balloon imaging catheter from the end of January to March 2013. **Table 6.3** shows a summary of the collected 3D-OCT balloon imaging data. Note that the types of BE were the initial diagnosis so some of the patients have already achieved complete eradication of intestinal metaplasia (CE-IM) or complete eradication of dysplasia (CE-D) when the 3D-OCT imaging were performed. The following sections show representative 3D-OCT balloon data sets and discussions regarding the clinical implications. No adverse event was reported in all cases.

Figure 6.10 shows a 3D-OCT balloon imaging data set taken from a patient who initially had BE with low grade dysplasia (LGD) and achieved CE-IM after two focal RFA treatment sessions. Hence the esophagus of the patient was normal looking after the neosquamous layer recovered from the ablation. **Fig. 6.10A** shows a volumetric rendering of the entire 1,500 x 600 x 500 (lines x frames x axial pixels) data set, which was acquired in 20 seconds. The rotation circumference was 50 mm, the pullback length was 30 mm, and the imaging range was 4 mm in tissue. The orthogonal planes shown in **Fig. 6.10A** illustrate the locations used to extract en face and cross-sectional image slices for closer examination.

Fig. 6.10B shows an *en face* image extract in the middle of the imaging range of the data set, so the imaging depth is about 600 μm underneath the tissue surface in the middle of the *en face* view and is about 2 mm underneath the tissue surface on the edge of the *en face* view. The image is similar in concept to a conventional microscopy image obtained by setting the focus to the middle of the imaging range. The image was constructed by axial summation of a thin slice (~50 μm). Consistent with previous 2D-OCT and 3D-OCT studies [8, 9], the normal squamous epithelium is featureless and unremarkable. The small, hyperscattered regions in the image are artifacts caused by debris on the balloon surface. Slight transverse jitter oriented primary along the rotary direction is due to patient heartbeat and respiration artifacts. The green and blue dashed lines in **Fig. 6.10B** indicate the positions of the cross-sectional images shown in **Figs. 6.10C and D**.

One of the main benefits of balloon OCT imaging compared to 3D-OCT imaging performed using standard rotary probe is the imaging coverage is much larger, so it is capable to visualize the tissue features in a larger scale. In the en face image, the network of the vessels can be clearly identified over the large field of view. Vessels have structures similar to dilated subsquamous glands in the cross-sectional images, but can be distinguished when examining the en face images due to its connective nature. This is especially helpful for the clinical studies of the subsquamous intestinal metaplasia (SSIM) since it is important to precisely record the distribution and size of the buried glands without mixing up with the similar structures from the vessels. Another benefit is the larger circumference of the balloon imaging catheter allows the esophagus naturally wrapped around the inflated balloon, so the whole circumference of the esophagus can be covered in one single cross-sectional image and can avoid the sampling error issue with the use of standard rotary probe.

Fig. 6.10C shows a cross-sectional image along the pullback direction at the position indicated by the green dashed line in **Fig. 6.10B**. A regular, well-defined layered architecture of the normal esophagus can be appreciated throughout the length of the pullback. **Fig. 6.10D** shows a cross-sectional image along the rotary direction at the position indicated by the blue dashed line in **Fig. 6.10B**. The regular layered architecture is visible in this orthogonal view as well. In both cross-sections, the epithelium layer is devoid of glands or vessels. The lamina propria and submucosa tissue layers (first and second hyperscattering layers) contain small vessel (~100 μm level), identifiable by their interconnectivity across numerous cross-sectional images as well as in the *en face* image. The lamina propria also contains scattered, non-shadowing glandular structures that may represent SSIM. The ability to definitively distinguish vascular from glandular features without the use of Doppler processing is unique to 3D-OCT imaging.

The dense spatial sampling density and high optical resolution of balloon OCT imaging enables high-magnification analysis of each tissue later over regions of interest (ROIs). This principle is demonstrated in **Figs. 6.10F and G**. **Fig. 6.10F** shows the cross-sectional image at the ROI shown as a purple dashed box in **Fig. 6.10E** while **Fig. 6.10G** shows the cross-sectional image at the ROI shown as a brown dashed box in **Fig. 6.10C**. The vessel architectures (blue arrows) are visible underneath the lamina propria and SSIM (red arrows) usually mix within lamina propria or between epithelium and lamina propria layers. The enlarged views allow the detailed analysis such as quantification of the size of the vascular or glandular structure and are valuable in the assessment of pathologic tissue.

The large coverage advantage of the balloon imaging catheter can also be used for mapping certain structural features in the esophagus. **Figure 6.11** shows an example of mapping the BE mucosa thickness over the entire balloon OCT data set. The balloon OCT data set was acquired from a BE patient with high grade dysplasia (HGD) and undergone cryospray ablation (CSA) treatment once. The patient had ~2.5 cm endoscopically visible BE from extending from the GEJ and had several BE islands distributed 2~3 cm higher in the esophagus. The patient received focal RFA treatment after the OCT imaging to treat the residual BE found endoscopically. This balloon OCT data was taken around the GEJ, covering most of the BE region. **Fig. 6.11A** shows an *en face* image extract in the middle of the imaging range of the data set, so the imaging depth is about 400 μm underneath the tissue surface in the middle of the *en face* view and is about 800 μm underneath the tissue surface on the edge of the *en face* view. The image was constructed by axial summation of a thin slice (~100 μm), corresponding to averaging the signal within roughly one third of the epithelium layer. Based on the intensity distribution in the en face image, it is possible to distinguish different tissue type as the irregular structures in BE mucosa typically attenuate the OCT signal more than the signal in normal esophagus. However, the intensity of the OCT signal can also be affected by the balloon contact and the depth of the focal plane in the tissue caused by the off-centered

imaging catheter in the balloon, so it is helpful to determine the tissue types with the use of the cross-sectional images.

Figs. 6.11B and C show cross-sectional images along the rotary direction at the positions indicated by the red and green dashed lines in **Fig. 6.11A**. In cross-section, the BE mucosa exhibits distortion of the normal layered architecture and the presence of discrete hyposcattering glands, consistent with previous 2D-OCT and 3D-OCT studies [8, 9]. With the knowledge from previous studies and Chapter 4, the thickness of the BE epithelium can be determined by the vertical distance from the top of the lamina propria/muscularis mucosa layer to the surface of the BE epithelium across the full circumference of the esophagus, since the contact between the balloon and the surrounding esophagus was consistent.

By marking and recording the thickness of the BE epithelium in each cross-sectional frame over the pullback range, the thickness map of the BE epithelium can be developed (**Fig. 6.11D**), which not only can show the distribution of the BE in the esophagus, but also can present the thickness variation of the BE. In this data set, the average BE thickness is 295 μm with a standard deviation of 103 μm and more detailed analysis can be performed such as dividing the data set into sub-sections, as shown in **Fig. 6.11D**. To understand the BE thickness variation is important because this can avoid overtreatment to reduce the complication rate during the ablation treatments or help identifying regions that may require additional ablation to eliminate diseased tissue completely. This information can potentially very useful for the guided ablation as well as the determination of dosage in the future.

The BE thickness map was developed by manually marking the BE layer frame by frame, which is time-consuming and not practical for clinical applications. One method is to go through the cross-sectional images immediately after the volumetric data set is acquired and record the approximated thickness of BE epithelium for real-time feedback, but this method is labor intensive and the results may vary depending on the experience of the readers/operators. With the advance of high speed imaging processing and segmentation algorithm [10-12], it is possible to develop the automatic thickness mapping function and the BE thickness can be recorded right after the cross-sectional images are acquired. Computer aided mapping of other structural features such as the vascular network or SSIM distribution can also be implemented, so accurate information can be provided in real time and help the clinician determine suitable following procedures.

6.6 Figures

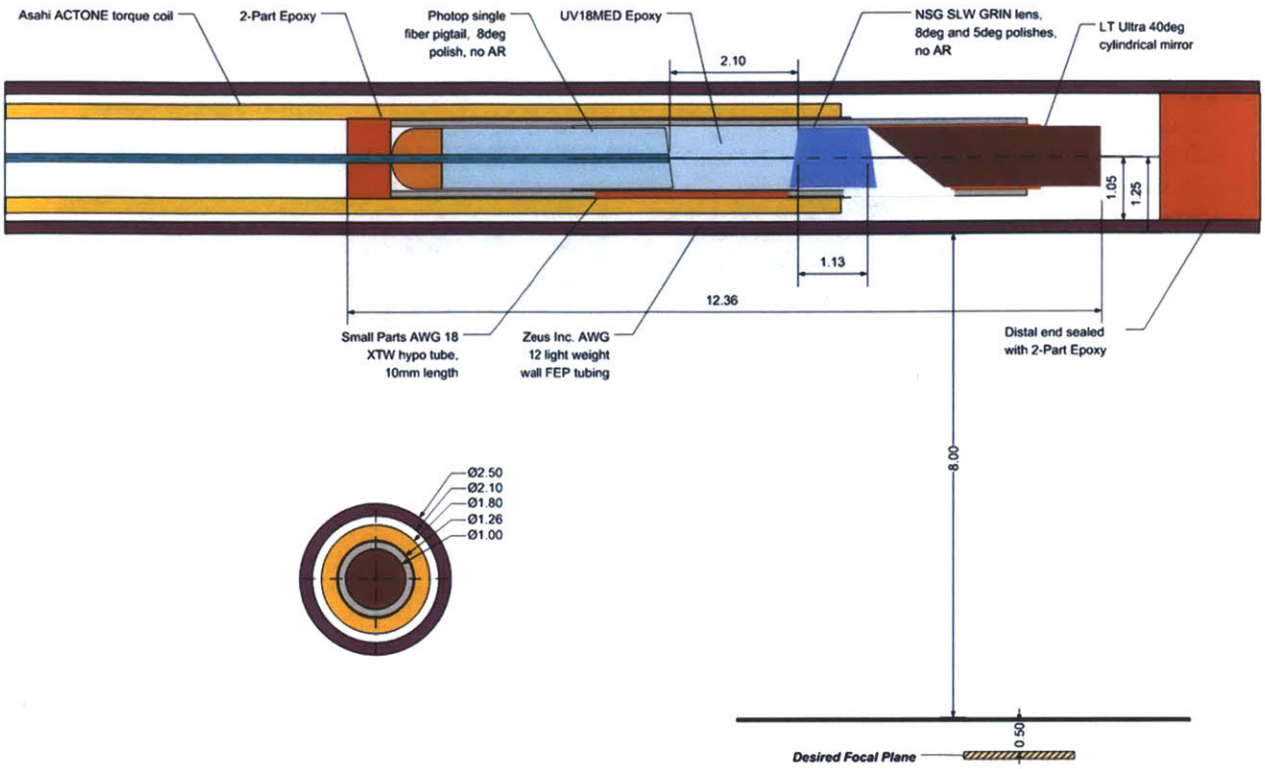

Figure 6.1. Schematic diagram of optical design of the balloon imaging catheter and the distal tip of the imaging catheter. All dimensions are in mm. Focal plane is set at 500 um from the balloon surface. Inset shows an end view of the imaging catheter.

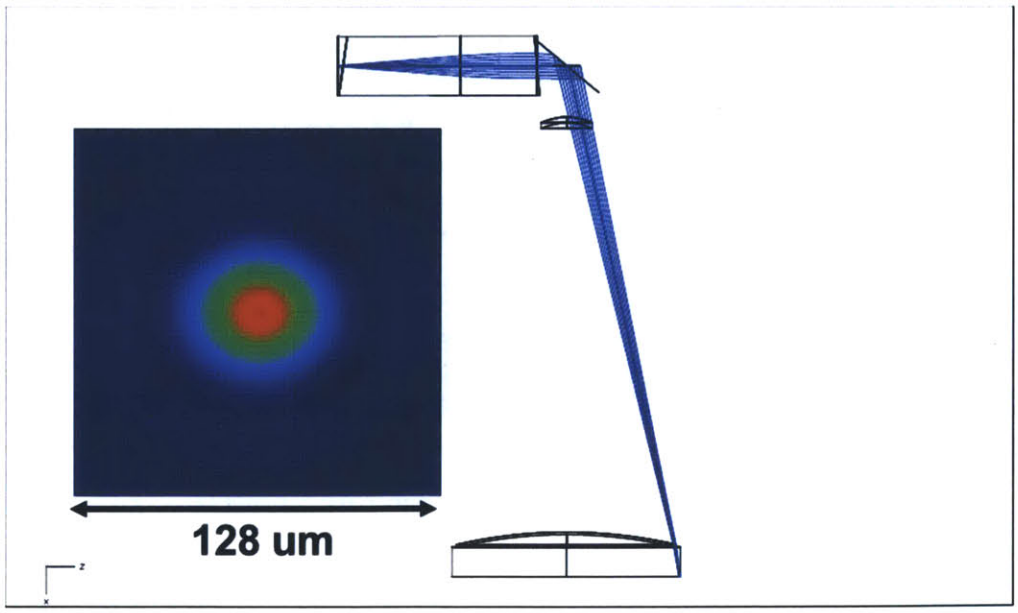

Figure 6.2. ZEMAX model of the optical design of the balloon imaging catheter. The 3D layout shows optimized design. The model is constructed to achieve minimized aberration of the spot on the focal plane. The inset shows the spot diagram on the focal plane. Estimated FWHM spot size is 30 um x 28 um (XY) at a working distance of 500 um in tissue.

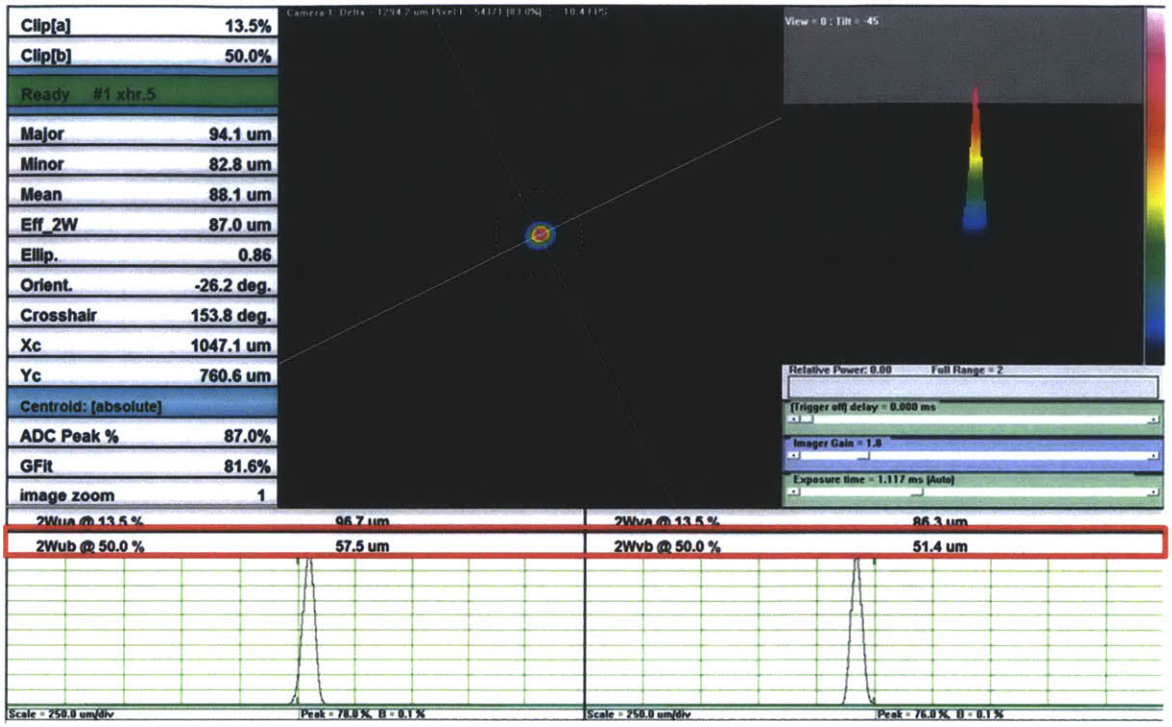

Figure 6.3. Beam profile measured at the imaging plane 2 mm away from the focal plane.

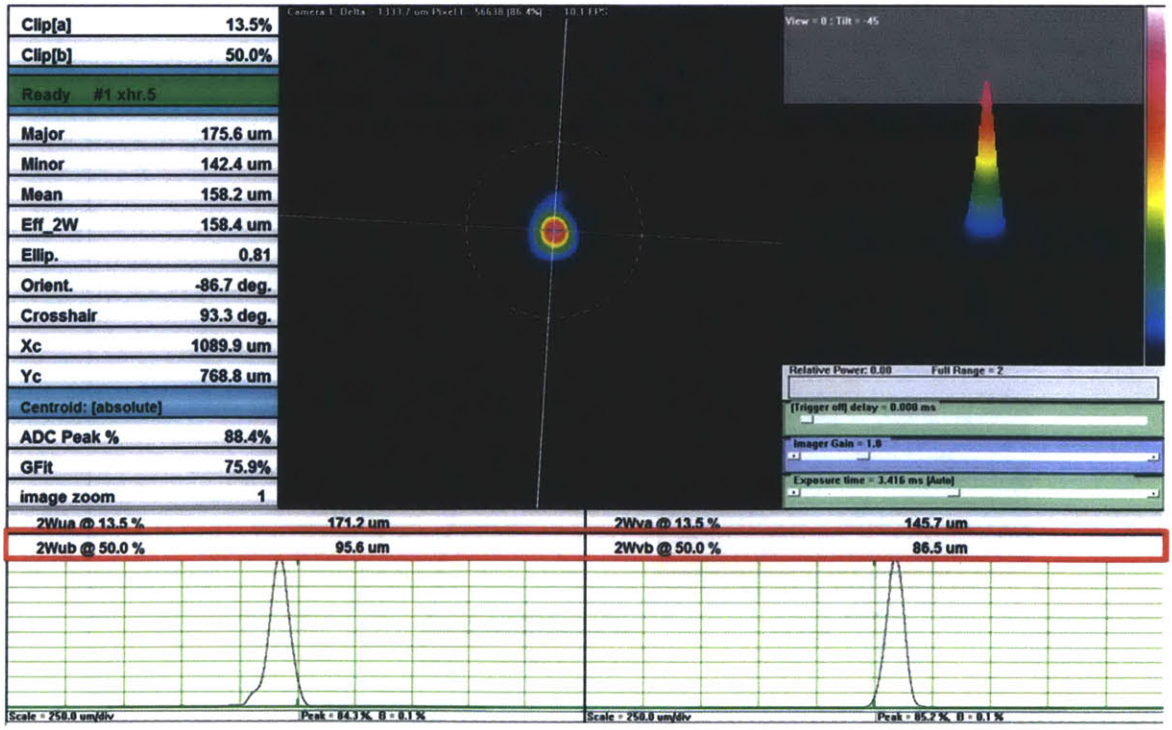

Figure 6.4. Beam profile measured at the imaging plane 4.2 mm away from the focal plane.

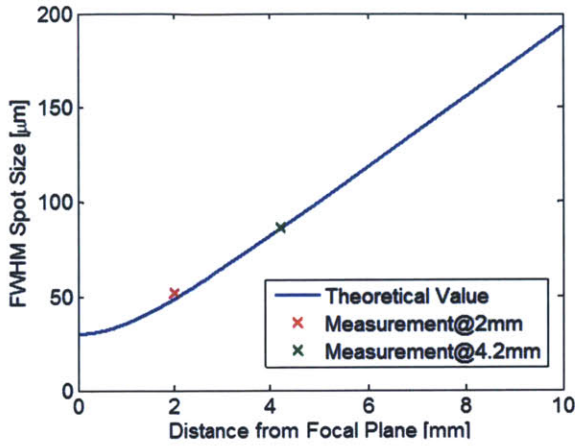

Figure 6.5. Spot size comparison between the theoretical value and the measured values at different imaging plane.

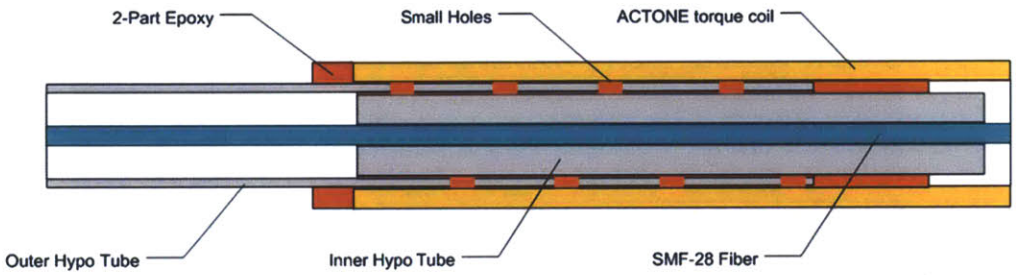

Figure 6.6. Schematic diagram of the proximal joint between the torque coil and rigid hypo tube for the balloon imaging catheter. A freely floating hypo tube is used to prevent epoxy from stressing the fiber.

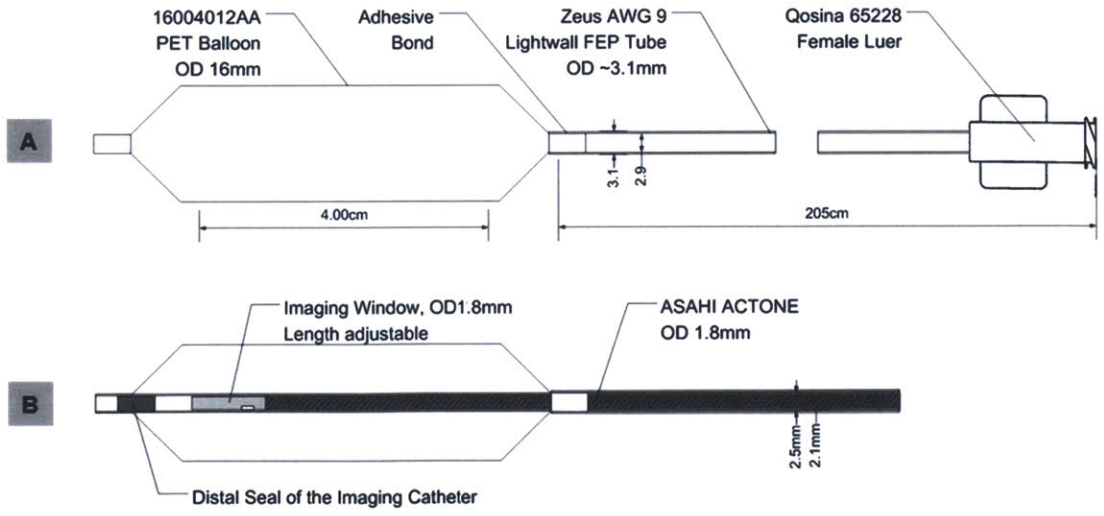

Figure 6.7. (A) Schematic diagram of the balloon sheath design which has open distal end and allows disinfection of the lumen. (B) Schematic diagram of the assembled balloon imaging catheter with the distal end of the balloon sealed by the imaging catheter.

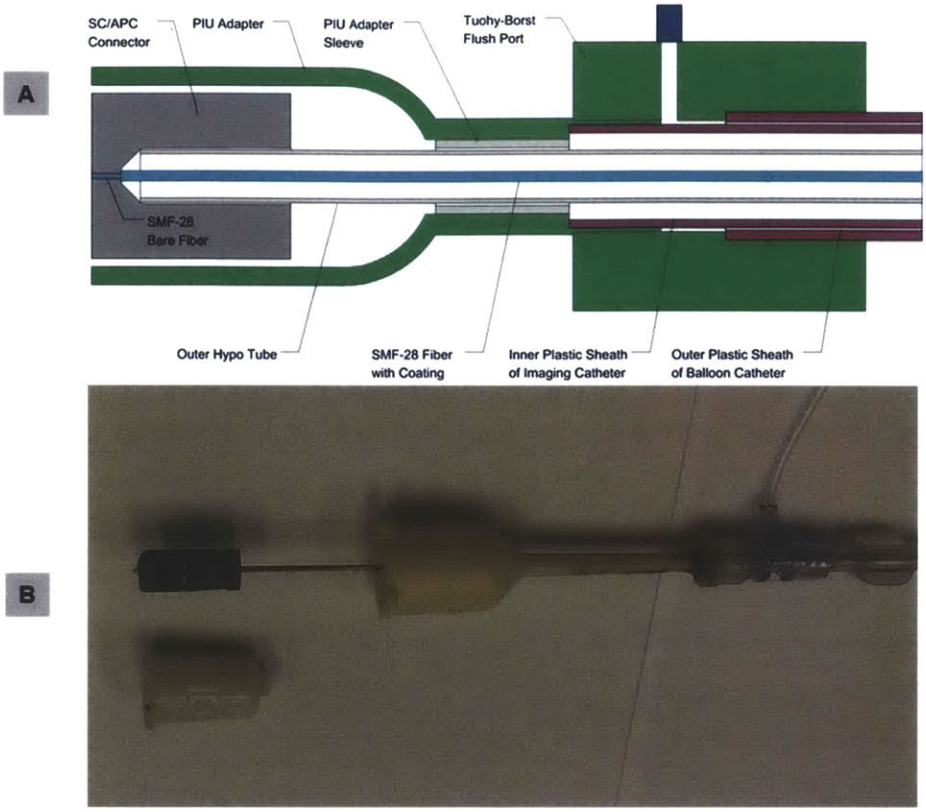

Figure 6.8. (A) Schematic diagram of the SC/FPC connector and the PIU adapter for the balloon imaging catheter. (B) The photo of the actual proximal end of the imaging catheter.

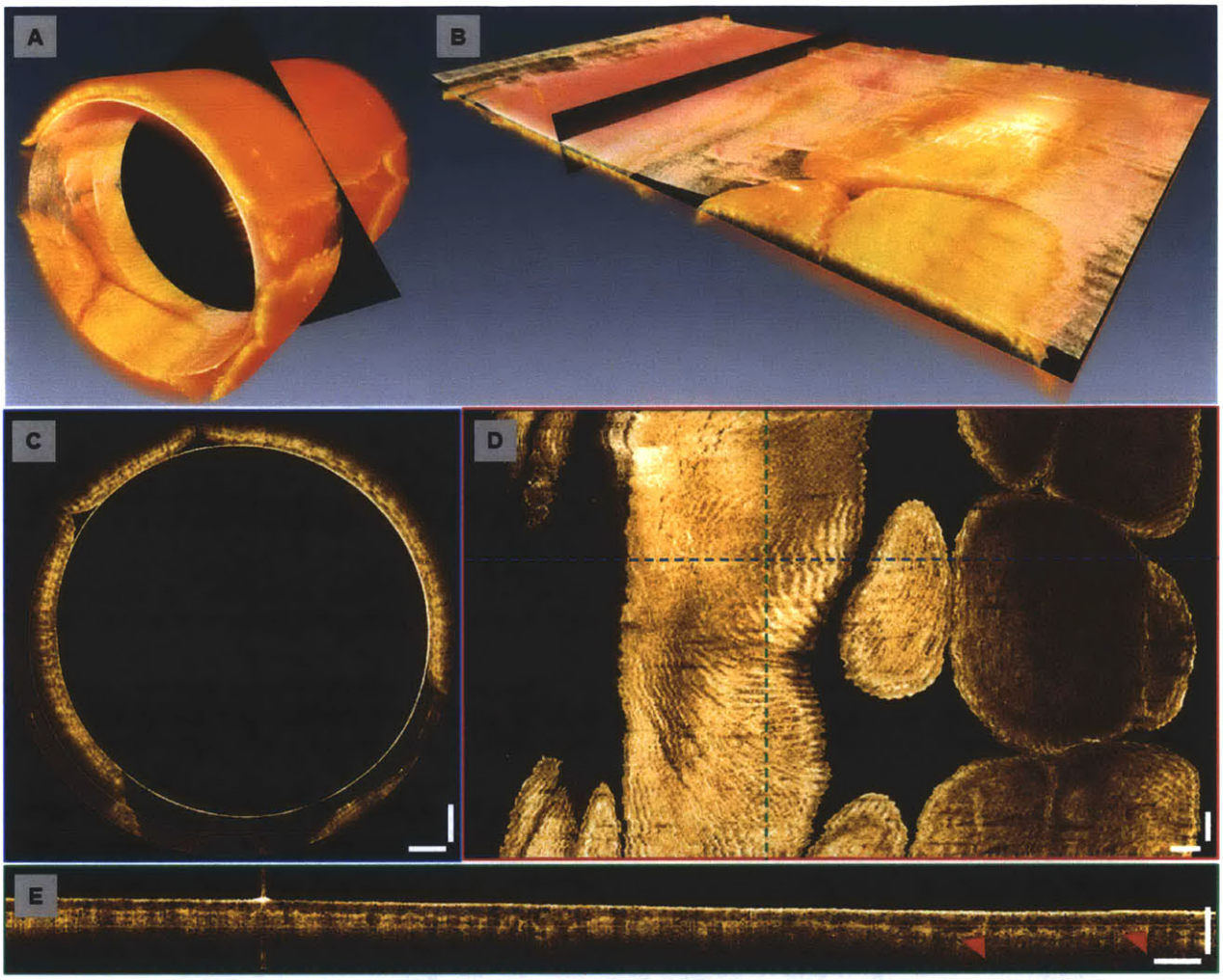

Figure 6.9. 3D-OCT data set of human palm using the balloon imaging catheter. (A) 3D rendering of the balloon imaging data set, showing the original geometry of imaging dimensions using the spiral scanning pattern. (B) 3D rendering of data set by unfolding the radial cross-sectional images into rectangular images, allowing better visualization of the volumetric data set. (C) Cross-sectional image of the palm along the fast rotary direction. (D) *En face* image constructed by axial summation of a thin slice (~20 um) in the data set. The palm print can be clearly identified. (E) Cross-sectional image along the pullback direction shows the sweat ducts indicated by red arrows. Scale bar: 2 mm.

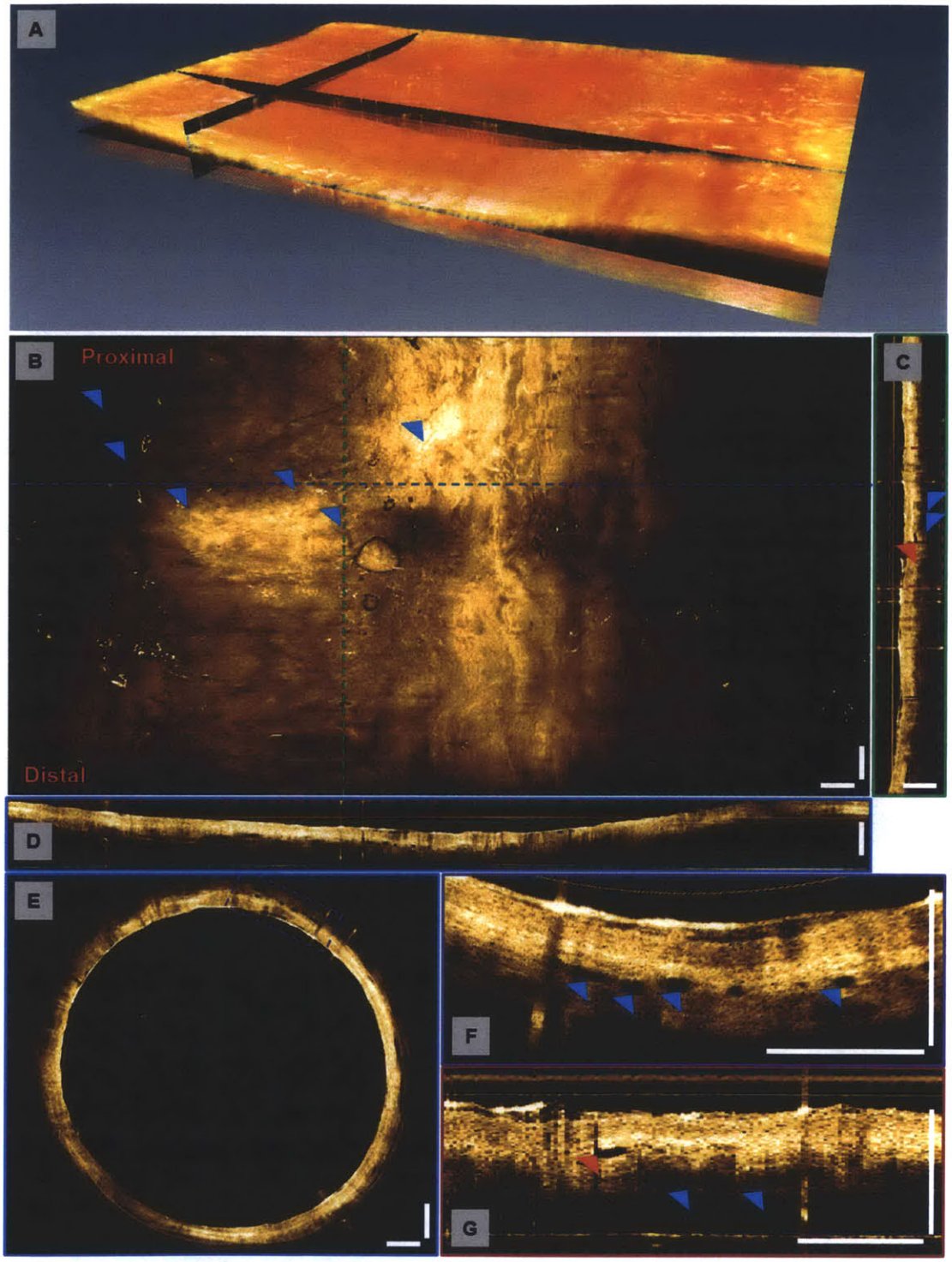

Figure 6.10. *In vivo* 3D-OCT data set of human esophagus using the balloon imaging catheter. (A) 3D rendering of data set by unfolding the radial cross-sectional images into rectangular images. (B) *En face* image constructed by axial summation of a thin slice (~50 um) in the data set. Large area coverage allows the visualization of the vessel network underneath the lamina propria layer, indicated by blue arrows. (C) Cross-sectional image along the pullback direction shows the possible buried glands (red arrow) structure. (D) Cross-sectional image along the rotary direction shows the layered structures in the esophagus. (E) Radial image taken from the same frame as (D) shows the actual dimensions of the esophagus. (F) Enlarged view of (C) shows the buried gland within the lamina propria layer. (G) Enlarged view of (E) shows the vessels underneath the lamina propria layer. Scale bar: 2 mm.

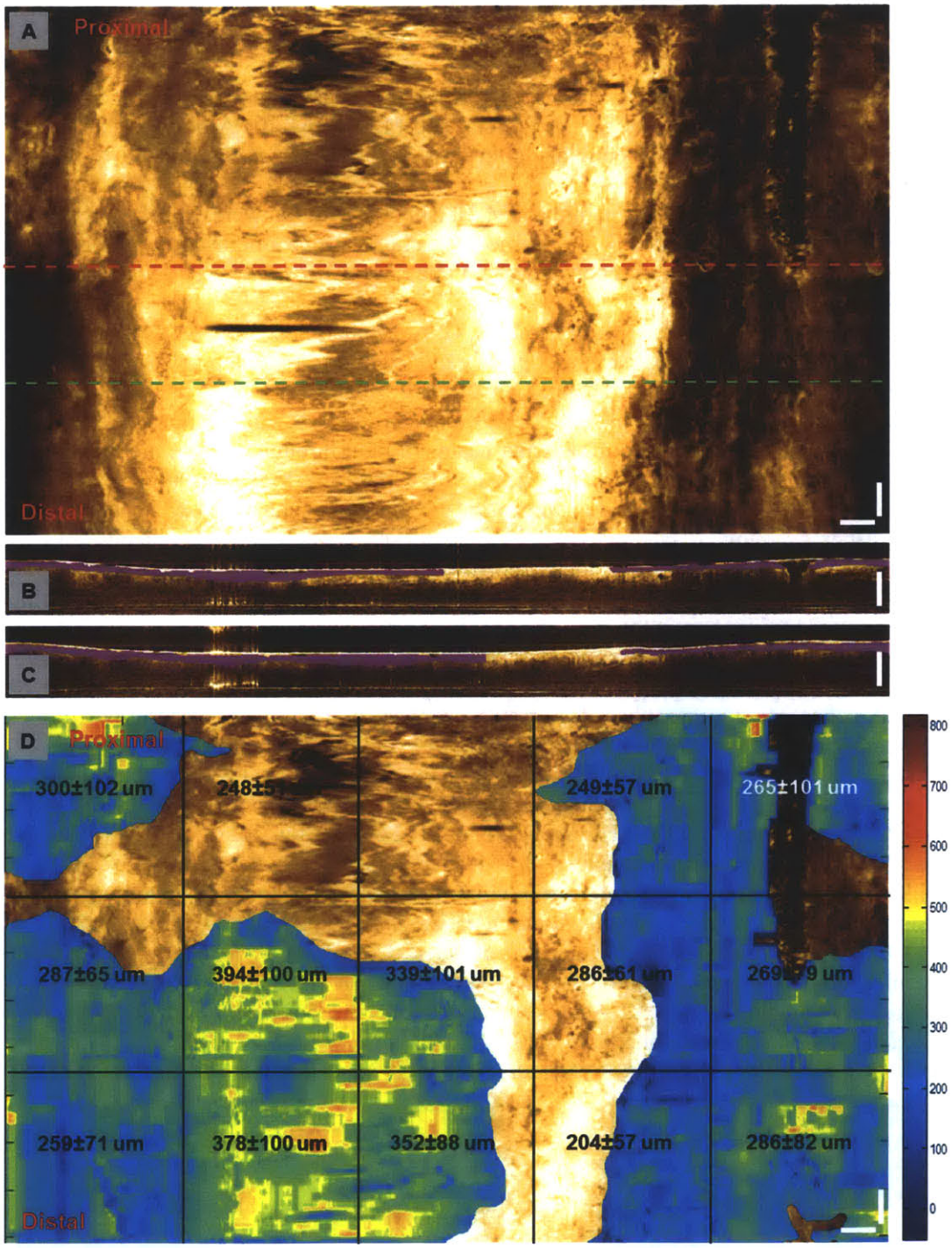

Figure 6.11. BE thickness mapping using *In vivo* 3D-OCT data set of human esophagus using the balloon imaging catheter. (A) *En face* projection constructed by axial summation of a thin slice (~250 um) in the data set. BE mucosa thickness can be measured using the cross-sectional images along the rotary direction. (B) BE layer marked by purple area in the cross-sectional image corresponding to the red dotted line in (A). (C) BE layer marked by purple area in the cross-sectional image corresponding to the green dotted line in (A). (D) BE thickness map obtained from all cross-sectional images overlaying on the *en face* image, showing the BE thickness variation over the imaged area. Scale bar: 2 mm.

6.7 References

[1] A. R. Gruntzig, A. Senning, and W. E. Siegenthaler, "Nonoperative dilatation of coronary-artery stenosis - percutaneous trans-luminal coronary angioplasty," *New England Journal of Medicine,* vol. 301, pp. 61-68, Jul 1979.

[2] G. W. Stone, S. G. Ellis, D. A. Cox, J. Hermiller, C. O'Shaughnessy, J. T. Mann, M. Turco, R. Caputo, P. Bergin, J. Greenberg, J. J. Popma, and M. E. Russell, "A polymer-based, paclitaxel-eluting stent in patients with coronary artery disease," *New England Journal of Medicine,* vol. 350, pp. 221-231, Jan 2004.

[3] M. J. Suter, B. J. Vakoc, P. S. Yachimski, M. Shishkov, G. Y. Lauwers, M. Mino-Kenudson, B. E. Bouma, N. S. Nishioka, and G. J. Tearney, "Comprehensive microscopy of the esophagus in human patients with optical frequency domain imaging," *Gastrointestinal Endoscopy,* vol. 68, pp. 745-753, Oct 2008.

[4] W. Kang, H. Wang, Y. S. Pan, M. W. Jenkins, G. A. Isenberg, A. Chak, M. Atkinson, D. Agrawal, Z. L. Hu, and A. M. Rollins, "Endoscopically guided spectral-domain OCT with double-balloon catheters," *Optics Express,* vol. 18, pp. 17364-17372, Aug 2010.

[5] F. J. Ingelfinger, "Esophageal motility," *Physiological Reviews,* vol. 38, pp. 533-584, 1958 1958.

[6] H. Kogelnik, "On propagation of gaussian beams of light through lenslike media including those with a loss or gain variation," *Applied Optics,* vol. 4, pp. 1562-1569, Dec 1965.

[7] B. E. A. Saleh and M. C. Teich, *Fundamentals of Photonics*: John Wiley & Sons, 2007.

[8] D. C. Adler, C. Zhou, T. H. Tsai, H. C. Lee, L. Becker, J. M. Schmitt, Q. Huang, J. G. Fujimoto, and H. Mashimo, "Three-dimensional optical coherence tomography of Barrett's esophagus and buried glands beneath neosquamous epithelium following radiofrequency ablation," *Endoscopy,* vol. 41, pp. 773-776, Sep 2009.

[9] Y. Chen, A. D. Aguirre, P. L. Hsiung, S. Desai, P. R. Herz, M. Pedrosa, Q. Huang, M. Figueiredo, S. W. Huang, A. Koski, J. M. Schmitt, J. G. Fujimoto, and H. Mashimo, "Ultrahigh resolution optical coherence tomography of Barrett's esophagus: preliminary descriptive clinical study correlating images with histology," *Endoscopy,* vol. 39, pp. 599-605, Jul 2007.

[10] F. LaRocca, S. J. Chiu, R. P. McNabb, A. N. Kuo, J. A. Izatt, and S. Farsiu, "Robust automatic segmentation of corneal layer boundaries in SDOCT images using graph theory and dynamic programming," *Biomed. Opt. Express,* vol. 2, pp. 1524-1538, Jun 2011.

[11] A. Wang, J. Eggermont, N. Dekker, H. M. Garcia-Garcia, R. Pawar, J. H. C. Reiber, and J. Dijkstra, "Automatic stent strut detection in intravascular optical coherence tomographic pullback runs," *International Journal of Cardiovascular Imaging,* vol. 29, pp. 29-38, Jan 2013.

[12] G. J. Ughi, T. Adriaenssens, K. Onsea, P. Kayaert, C. Dubois, P. Sinnaeve, M. Coosemans, W. Desmet, and J. D'Hooge, "Automatic segmentation of in-vivo intra-coronary optical coherence tomography images to assess stent strut apposition and coverage," *International Journal of Cardiovascular Imaging,* vol. 28, pp. 229-241, Feb 2012.

CHAPTER 7

7.0 Piezoelectric Transducer Based Miniature Catheter

7.1 Motivation

The state-of-the-art endoscopic 3D-OCT systems described in Chapter 3, 4, and 6 were all based on the proximally rotary side imaging mechanism described in Chapter 5, which has relatively simple optical and mechanical design and thus has been used in majority of clinical applications. Ease to assemble and produce also makes this type of imaging catheter a good candidate for commercialized imaging systems. However, with the dramatic increase of OCT imaging speed in recent years, the proximally rotary scan start facing a main drawback that its stability and scanning speed are limited due to the long translation distance from the proximal scanner to the distal imaging head. Under high speed rotation, the scanning uniformity of the distal end is very sensitive to the bending of the whole imaging catheter because of the friction generated between the sheath and the torque coil. The unstable scanning can degrade the image quality especially when the transverse resolution is high, and can also cause the loss of the detailed volumetric information from the 3D-OCT data set. The rotation is translated through a long torque cable to the distal optics assembly can limit the rotary speed, because any asymmetric structure in the imaging catheter can induce strong vibration when the rotary speed goes higher than 9,000 rpm, which is not ideal for clinical uses. Therefore, to truly gain the advantages from high speed 3D-OCT imaging, a more reliable scanning method is necessary to provide volumetric OCT data that can reveal detailed 3D features.

Scanners using piezoelectric transducer (PZT) can provide micron-level motion control precision and has been used in several applications using OCT as well as other imaging modalities [1-3]. By setting two pairs of PZT benders orthogonally mounted in a "push-pull" configuration with the optical fiber mounted in the center of the PZT array using cross connect, the scanner can perform two-dimensional (2D) scanning patterns in non-resonant mode [1, 2]. With the use of the PZT tube with quadruple electrodes, 2D scan can also be achieved by applying modulated sinusoidal waveforms with 90° phase difference on the orthogonal pairs of the electrodes [3]. Using probes developed with these scanners, optical coherence microscopy (OCM) images with cellular-level resolution were demonstrated, indicating extremely high scanning stability of the PZT based actuators.

In this section of thesis work, a PZT based miniature imaging catheter was developed with an outer diameter of 3.5 mm for ultrahigh-speed endoscopic OCT imaging. The combination of a miniaturized PZT bender and cantilever fiber has the advantage of large deflection with low driving voltage, ease of adjustment of the scanning speed, and flexibility to implement slow scan methods to achieve three-dimensional (3D) imaging. The side viewing probe can be pulled back over a long distance to acquire 3D data sets covering a large area on the specimens. An ultrahigh speed endoscopic OCT imaging system based on a buffered Fourier domain mode-locked (FDML) laser and high-speed data acquisition was used to provide high frame rate while maintaining sufficient lines per frame, as well as acquire larger

volumetric data set in a few second acquisition times. *In vivo* imaging was performed in the rabbit gastrointestinal (GI) tract to demonstrate the stability of the imaging catheter. Dr. Benjamin Potsaid, PhD, tested and solved the initial A/D acquisition problems and wrote the code to control high speed A/Ds that were used in the study. Martin Kraus visiting from Prof. Joachim Hornegger's group at Friedrich-Alexander-Universität Erlangen-Nürnberg wrote the software that controlled the data acquisition including the graphic user interface and database. Dr. Alison Hayward and CatrinaWong from MIT animal facility helped the rabbit imaging experiment.

7.2 Optical Design of the PZT Based Imaging Catheters

Figure 7.1 shows the schematic diagram of the distal design of the PZT based imaging catheter. A tapered 15 mm PZT bender (Piezo Systems, Inc.) was used to deflect the fiber. UV cured epoxy was used to fix the fiber at the distal end of the PZT bender to support the cantilever vibration. A drop of epoxy (~40 mg) was fixed on the fiber tip to reduce the resonant frequency of the fiber cantilever to ~500 Hz. The fiber tip was angle cleaved at 8^{0} to reduce backreflection. The scanning fiber tip imaged onto the tissue with a GRIN lens with pitch of 0.25 (Newport, Inc.). The working distance and the focal spot size are adjustable by changing the distance between the fiber tip and the GRIN lens. In the prototype imaging catheter, the working distance was set to be 500 μm in tissue. A micro-prism (Tower Optical, Inc.) was glued on the distal end of the GRIN lens to reflect the light to the side. The focused spot size (full width at half-maximum, FWHM) of intensity is 20 μm in air, corresponding to ~23 μm in tissue.

7.2.1 ZEMAX Modeling

The ZEMAX model of the PZT based imaging catheter is shown in **Figure 7.2**. The laser beam coming out from the angle cleaved SMF-28 fiber is focused by a commercially available GRIN lens with length of 4.8 mm and pitch of 0.25, reflected by a aluminum coated micro-prism made of BK7 glass, passing through a FEP sheath with outer diameter of 3.5 mm, and finally focuses 500 μm underneath the tissue with average refractive index of 1.38.

Optimization of the design was performed by setting the distance between the fiber tip and the GRIN lens as the variable. The optimization function was set up to place a beam waist at the output plane, effectively setting the focus at the final surface in the model. Equal weight was placed on the X and Y components of the beam for optimization. A Gaussian skew beam with a diameter of 9.2 μm was launched from the first surface of the model to emulate the mode field of SMF-28 fiber, and Gaussian modeling was used for the optimization loop. Optimization resulted in the air gap distance between the fiber tip and the GRIN lens is shown in **Fig. 7.2A**. **Fig. 7.2B** shows the spot diagram at output surface, giving an estimated beam radius of 10 μm. This spot size is ~2 times larger than ideally desired for

imaging small features such as crypts or Barrett's esophagus glands in the human GI tract, but would provide reasonable performance for many applications. **Figs. 7.2C-F** show the ray tracing results and the spot diagrams when the fiber start deflecting to achieve a scanning range up to ±1 mm, indicating the off-axis aberration from this single GRIN lens design.

7.2.2 Performance Measurement

The transmission, back coupling, backreflection, and working distance were measured during the catheter assembly process. The working distance is measured in air from the sheath surface to the focal plane, and is close to the actual working distance when considering in tissue. A working distance of 300 μm in air is desired for an optimal final working distance. The spot size was measured using the knife edge method, which records the total output power as a knife edge at the focal plane is translated through the output beam using a calibrated translation stage. The measured power indicates integral of the Gaussian beam and can be expressed as a function of the position of the knife, so the spot size can be calculated based on the power variation in relation to the knife position.

The final PZT based imaging catheter produced a transmission of 79%, back-coupling efficiency of 40%, backreflection of -47 dB, and working distance of 310 μm in air. **Figure 7.3** shows the results of the knife edge measurement and the measured spot size at the focal plane was ~20 μm, which corresponds well with the ZEMAX simulation result.

7.3 Mechanical Design of the PZT Based Imaging Catheters

In order to achieve larger scanning range using low operation voltage to drive the PZT bender, the catheter was operated at a frequency close to the resonance of the fiber cantilever, which is proportional to the inverse square of the cantilever length [3, 4]. The resonant frequency of a cantilever with a round cross-section is

$$f = \frac{\beta}{4\pi}\left(\frac{R}{L^2}\right)\sqrt{\frac{E}{\rho}}, \tag{7.1}$$

where L and R are the length and radius of the cantilever, respectively; E and ρ are the Young's modulus and the mass density, respectively; and β is a constant determined by the vibration mode number and boundary condition of the cantilever. For the zeroth-order vibration mode, $\beta = 3.52$ [4]. **Fig. 7.4A** shows the resonant frequency of the fiber cantilever with different cantilever length. For the target operation frequency of ~500 Hz, a cantilever length of 15 mm is required using an uncoated fiber and 33 mm using a coated fiber, which makes the rigid length of the catheter too long and not practical for use in an endoscope. In this prototype imaging catheter, the cantilever length was chosen to be 8 mm using an

uncoated fiber, so the rigid length of the catheter is within 30 mm. By adding weight at the cantilever tip, the resonant frequency can be decreased [5]. **Fig. 7.4B** shows the change of the resonant frequency of the 8 mm fiber cantilever with different epoxy weight on the fiber. With no weight, the resonant frequency is ~1 kHz. The resonant frequency can be reduced to 500 Hz by loading with a mass of 40 mg and to lower than 200 Hz using a mass of 200 mg. Therefore, this method enables a shorter cantilever length with adjustable operation frequency and the catheter can provide sufficient scanning range at low operating voltage satisfying the electrical safety in medical applications [6]. In this imaging catheter, the current is ~3 μA with a drive voltage of 10 V (peak to peak), both of which are lower than the 42 V or 10 μA safety requirement for direct cardiac application devices defined in the International Standard [6].

The lateral scanning range of the imaging beam was about 2 mm (±1 mm) with the PZT bender driven with a voltage of 10 V (peak to peak) at a frequency of 480 Hz. A thin stainless steel hypo tube holder was used to fix the PZT bender to a 2 mm outer diameter torque coil (Asahi Intecc, Inc.), which is the same type of torque that was used in the balloon imaging catheter mentioned in Chapter 6 but with slightly larger diameter to hold the fiber and wires of the imaging catheter. The torque coil can be pulled back uniformly by a translation stage at the proximal end of the catheter. The final imaging catheter had an overall outer diameter of 3.5 mm, a rigid length at the distal end of ~30 mm, and the total length including the torque coil and the protective sheath was 1 meter.

7.4 System Description

Figure 7.5 shows the OCT system used for the PZT based imaging catheter. A portion of the laser output was coupled to a Mach-Zehnder interferometer (MZI) to produce interference fringes with zero-crossings evenly spaced in frequency. The MZI was set to a delay of 1 mm path difference and fringes were detected by a 200 MHz bandwidth dual-balanced photodetector (Thorlabs, Inc.) to generate the phase information to recalibrate the OCT interference fringe signals. The OCT system consisted of a dual-balanced Michelson interferometer with a pair of optical circulators and a 50/50 fiber-optic splitter (AC Photonics, Inc.). The OCT signal was acquired with the same dual-balanced photodetector with MHz bandwidth (Thorlabs, Inc.). To enable the preview of the acquired images in real time, the calibration MZI interference fringes were acquired once prior to the acquisition of the OCT signal and the acquired OCT signal was recalibrated by the set of the calibration signal. The calibration and OCT signals were digitized using a high-speed A/D card (Innovative Integration, Inc.). The catheter was housed in transparent fluorinated ethylene propylene (FEP) sheath (Zeus, Inc.) and pulled back with a motorized translation stage (Klinger Scientific, Inc.) at its proximal end to acquire volumetric data. For the OCT imaging using the PZT based catheter, a pullback speed of 2 mm/s was used while acquiring the 3D-OCT data sets. The power on the sample was about 15 mW.

7.4.1 FDML Laser with 480 kHz Axial Scan Rate

Fig. 7.6A shows a schematic diagram of the triple-buffered FDML laser. The laser has a ring resonator geometry with two optical isolators (AC Photonics, Inc.), a semiconductor optical amplifier (SOA, Covega, Inc.) gain medium and a fiber Fabry-Perot tunable filter (FFP-TF, Lambda Quest, Inc.). The FFP-TF is driven with a sinusoidal waveform at 59.8 kHz, synchronous to the optical round-trip time of the 3,436 m long cavity. Two copies of the backward sweeps, sweeping from long wavelength to short wavelength, are extracted at evenly spaced points within the cavity using 80/20 and 70/30 fiber-optic splitters. These copies are again split, copied, time delayed by 4 μs, and recombined in the external buffering stage. To achieve an effective sweep rate of 480 kHz, an additional external buffering stage was added to again double the effective sweep rate of the FDML laser. The laser output is amplified with a second SOA outside the cavity, which served as a booster amplifier. The FFP-TF has a free spectral range (FSR) of 160 nm centered at 1,310 nm and finesse of 1,000. The average output power of the laser after the booster was 40 mW. **Fig. 7.6B** shows the output spectrum of the FDML laser. The central wavelength was ~1,315 nm. The total tuning range of the spectrum is 150 nm, with an 80 nm FWHM. **Fig. 7.6C** shows the instantaneous fringe trace from a Mach-Zehnder interferometer. The duty cycle is almost 100% with ~2 μs sweep duration, and seven sweep copies are almost identical.

7.4.2 High Speed and Large Volume Data Acquisition

The ultrahigh-speed OCT imaging system can acquire large data sets with only a few-second acquisition times. In order to support data sets larger than 4 Gigabytes, the instrument control computer used a 64-but operation system. The high speed A/D card can sample up to 400 MSPS at 14 bit resolution. Customized user interface and data acquisition software were developed in C++ to coordinate instrument control and enable user interaction. Improved imaging performance was obtained by modifying a commercially available 350 MHz InGaAs dual-balanced photodetector (Thorlabs, Inc.) to increase the transimpedance gain by ~2x to 2.4 kΩ and reduce the bandwidth to 200 MHz [7]. The imaging system thus can acquire OCT data for over 15 seconds at 480 kHz axial scan rate or 960 frames per second (fps) with 500 lines per frame.

7.4.3 Signal Processing of the OCT Images

The MZI calibration traces were acquired in the beginning of each imaging session and used to calibrate all of the OCT data for that session. Calibration traces were not required for each axial scan sweep because the sweep-by-sweep variation of FDML lasers is extremely small. Each MZI sweep contains 832 A/D sample points. The acquired MZI traces were first fast Fourier transformed (FFT), zero-

padded to 2,048 points, and then inverse Fourier transformed (IFFT) to obtain an interpolated frequency sweep. The interpolated MZI traces were then Hilbert transformed to obtain the phase of the frequency sweep. The phase information was then used to resample the OCT interference traces from constant time intervals to linear phase, or equal frequency interval samples. Similar to MZI traces, the OCT traces were interpolated to 2,048 points/sweep using the FFT/zero-padding/IFFT method, and then re-sampled using cubic-spline interpolation to linear phase using the phase calibration information from the MZI traces. The re-sampled OCT traces were then FFT to obtain the axial point spread functions. The axial scans consisted of ~400 samples, spaced by 5.7 μm with a maximum imaging range of 2.3 mm in air.

7.4.4 Imaging System Performance

To characterize the sensitivity of the imaging system, a calibrated -54 dB reflection was used in the sample arm. The reference arm power was set to 150-200 microwatts. The sensitivity was measured as the ratio of the peaks of the PSFs to the standard deviation of the noise floor, which was measured with the sample arm blocked. The estimated system losses were ~3 dB arising from losses in the optics, mirror reflectivity, and back coupling. The measured sensitivity values are not adjusted for these losses. **Figure 7.7** shows the sensitivity roll off and the point spread function from a fixed reflection. The measured sensitivity of the system is 103 dB with 11 μm axial resolution in air (8 μm in tissue) and 2.3 mm imaging depth range in air (1.7 mm in tissue). The sensitivity rolls off ~7.5 dB at imaging depth of 2.25 mm, and the R-number is 2.93 mm/dB, which was calculated from the inverse decay constant of the exponential decay curve fitted to the signal maxima of the linear PSFs [8].

The PZT scanner was driven by a sinusoidally, so the pixels are denser on the edge of the B-scan due to the slower scanning speed. Hence the B-scan images were converted from sinusoidal transverse scan to linear transverse scan by re-mapping the axial scan positions along the PZT scanning direction. The scan length of the sine was 2 mm, so that spacing between axial scans was 6.3 μm in the center of the scan and decreased to zero near the edges of the scan where the sine reverses direction. The axial scans were averaged near the edges and cubic-spline interpolated in the center portion of the image. The number of axial scans per frame was kept the same as the number of axial scans in the original frame. The pullback speed was 2 mm/s so that spacing of axial scans in the pullback direction was 2.1 μm.

To evaluate the scanning stability of the PZT based imaging catheter under different bending curvature, a custom grid sheet printed by a laser printer with 600 dpi resolution was wrapped around the plastic sheath and OCT imaging was performed to acquire the *en face* images with different catheter curvature. The grid pattern had size of ~700 μm and the line width of 100 μm. The imaging catheter was bent with radius of curvature from 20 cm to 3 cm to simulate possible scenarios during the *in vivo* endoscopic OCT imaging. **Figure 7.8** shows a series of *en face* views of 3D-OCT data sets taken from the

custom grid sheet when the imaging catheter was bent with different radius of curvature. Instability of ~50 μm along the fast scan direction can be observed in the enlarged view when the radius of curvature is smaller than 5 cm, which may be caused by the vibration during the pullback. However, during the clinical endoscopic OCT imaging, situations that require this tight bending rarely happen, unless the retroflexion of the imaging catheter is required, so these results indicate that the scanning of the PZT based imaging catheter generally is quite stable even with a small radius of curvature during the image acquisition.

7.5 *In Vivo* 3D-OCT Imaging in the Rabbit GI Tract

To demonstrate the ability to image microscopic structures in the gastrointestinal tract, *in vivo* volumetric 3D-OCT data sets of the rabbit esophagus and colon were acquired. These studies were performed under a protocol approved by the Committee on Animal Care (CAC) at M.I.T. **Figure 7.9** shows a 3D-OCT data set from the esophagus of a female New Zealand White rabbit. The ultrahigh speed imaging system enables the acquisition of very large data sets, which cover long segments of tissue with dense spatial sampling. In this data set, 9,600 frames of 500 axial scans were acquired in 10 seconds, covering a volume size of 2 mm x 20 mm x 1.7 mm (fast-scan direction x pullback direction x axial direction) in the rabbit esophagus. The OCT images (**Figs. 7.9A-C**) allow visualization of the normal esophageal layers including the epithelium (EP), the lamina propria (LP), the muscularis mucosa (MM), the submucosa (SM), the circular muscle (Ci), and the longitudinal muscle (LM). The OCT images correlate well with representative histology of the rabbit esophagus (**Fig. 7.9D**). The volumetric data set can be processed and displayed in three dimensions. **Figs. 7.9E and F** show the *en face* view and cross-sectional view along the pullback direction respectively. The *en face* view (**Fig. 7.9E**) shows features such as vessels over a large field of view. Vessels have similar structures to dilated glands in the cross-sectional views, but can be distinguished when examining the *en face* images. Due to the ultrahigh frame rate, the data set can be sampled with a high spatial density and still cover a large field of view. The cross-sectional images (**Fig. 7.9F**) provide structural information over a very long region of the esophagus, with enhanced imaging contrast due to dense sampling along the pull-back direction. **Figs. 7.9G and H** show the enlarged view of the regions marked with red and orange boxes in **Fig. 7.9E**. With the large field of view, the data set can provide comprehensive structural information from different regions in the esophagus.

Figure 7.10 shows a 3D-OCT data set from the colon of a female New Zealand White rabbit. The OCT images (**Fig. 7.10A**) allow visualization of the colonic layers including the colonic mucosa (CM), the lamina propria (LP), the muscularis mucosa (MM), the submucosa (SM), the circular muscle (Ci), and the longitudinal muscle (LM), which correlate well with representative histology of the rabbit colon in

Fig. 7.10C. The *en face* view at a depth of 250 μm (**Fig. 7.10D**) shows the crypt structures in the rabbit colon. In comparison with human tissue, crypts in the rabbit colon are smaller (~50 μm) and more tightly packed. Crypts in the rabbit colon are often separated by only a few micrometers of lamina propria, usually making it difficult to identify single crypts in the *en face* images. Nevertheless, the crypts are visible in the enlarged *en face* view shown in **Fig. 7.10E**, which correlates well with representative *en face* histology (**Fig. 7.10F**). The ultrahigh speed imaging also makes 3D-OCT acquisition less sensitive to vibration or motion. **Fig. 7.10G** shows the cross-sectional image along the pullback direction. Motion artifacts were relatively small throughout the pullback procedure. Therefore, requirements for image post processing, such as frame alignment can be reduced.

7.6 *Ex Vivo* 3D-OCT Imaging on Human Colon Specimens

To evaluate the imaging probe for future clinical endoscopic OCT studies, *ex vivo* imaging using the ultrahigh speed OCT system was also performed in human colon specimens. Specimens were obtained under a protocol approved by the Committee for the Use of Humans as Experimental Subjects (COUHES) at M.I.T. **Figure 7.11** shows a 3D-OCT data set from a freshly excised human colon tissue. **Fig. 7.11A** shows an *en face* OCT image at a depth of 350 μm averaged over 15 μm depth. The individual crypts in the human colon are larger than those in the rabbit colon and are more easily visualized. **Fig. 7.11B** and **Fig. 7.11E** show the cross-sectional images along the fast-scan and pullback directions, respectively. Both the *en face* and the cross-sectional images show the columnar structure of the epithelium in the colon and correlate well with representative histology of human colon shown in **Figs. 7.11C and D**.

Densely sampled volumetric 3D-OCT data sets contain comprehensive information about tissue microstructure and enable contrast enhancement of the images by averaging with the consecutive slices. **Figure 7.12** shows an example by averaging a 15-μm-thick section, corresponding to 7 consecutive slices. This dimension corresponds to less than two epithelial cells, so tissue structure is largely constant and minimal blurring is observed. **Figs. 7.12A and B** show the images from the same *ex vivo* human colon data set with and without averaging respectively. The speckle pattern is decorrelated over the section and image averaging enhances tissue contrast. The arrow indicates a narrow line in the crypts, which is possibly the boundary of the lumen in the crypt. The averaging reduces speckle noise and thus reveals more detailed information from the tissue.

7.7 Discussion and Performance Improvement

The PZT bender based imaging catheter enables high scanning speed and broad scanning range with low driving voltage. The distally scanning mechanism is less sensitive to bending of the catheter, and is therefore more stable than catheters, which use proximally rotary actuation. The PZT catheter had the

limitation that it provides only a limited transverse field of view compared with a rotary actuated catheter that scans a full 360° angle around the device. However, the PZT catheter is more stable and suitable for clinical endoscopy studies. The FDML laser with triple-buffered configuration has both very high sweep rate and broad wavelength tuning range, providing high axial line rate for *in vivo* imaging and good axial resolution that reveals important structural features in tissues. With the fast data acquisition, the imaging system can support good imaging depth range with ultrafast line rate. In this project, the PZT scanning frequency is 480 Hz and the laser line rate is 480 kHz, so each frame contains 500 lines over the scanning range of 2 mm, corresponding to an axial scan spacing of ~6.3 μm in the center and nearly zero on the edges. The pullback speed is 2 mm/s, corresponding a frame spacing of 2.1 μm. The data acquisition rate is 400 MSPS, which can provide an imaging depth range of 2.3 mm in air.

The performance of the current prototype can be further improved. Although the GRIN lens performs well when the scanning laser beam is on axis, it causes severe aberration of the focused spot while the laser beam is off-axis. This is the main factor that limits the scanning range of the current prototype catheter. The off-axis aberrations can be reduced by using a compound lens design [9] with either a doublet or a triplet lens combination. The transverse resolution (the spot size on the focal plane) can also be improved by using a fiber with higher numerical aperture (NA) or changing the magnification of the optical design. A higher NA requires larger diameter optics because the beam from the fiber diverges more rapidly. Changing magnification makes the spot size smaller at the cost of reduced scanning range. The PZT scanning in the transverse direction is highly repeatable, however there are potential discontinuities of motion when the optics are pulled back along the longitudinal direction. This can be a limiting factor in the image continuity when using a long catheter because of the friction between the catheter cable and the sheath along its length. Typical endoscopic applications in humans would require a 2 meters length. The effects of friction may be reduced by different choices of the catheter cable or sheath materials. Finally, the length of the PZT scanner, fiber and lens are 30 mm. This is too long to be introduced though the working channel of an endoscope. The working channel has a sharp radius bend at the proximal end of the endoscope that requires a very short rigid length of the catheter, even for small outer diameter catheters. Therefore, the rigid length of the catheter needs to be reduced in future designs.

In conclusion, an ultrahigh speed endoscopic OCT imaging system with record frame rate using a PZT bender based imaging catheter, a triple-buffered FDML laser, and a high speed data acquisition system was demonstrated. The system can support 960 frames per second with 480 kHz axial line rate, 11 μm axial resolution, 20 μm transverse resolution and 2.3 mm imaging depth range in air, corresponding to 8 μm axial resolution, 23 μm transverse resolution and 1.7 mm imaging depth range in tissue. High imaging speed was demonstrated *in vivo* in an animal model, enabling the visualization of microscopic features as small as colonic crypts. Three dimensional endoscopic OCT data sets enable powerful

visualization techniques including manipulation of tissue geometry, speckle reduction by averaging, generation of *en face* views similar to endoscopic images, and the generation of cross-sectional images with arbitrary orientations. Future improvements in the catheter design and data acquisition technology will allow volumetric imaging with enhanced microscopic resolution and at even higher frame rates and should enable a wide range of clinical endoscopic 3D-OCT applications.

7.8 Figures

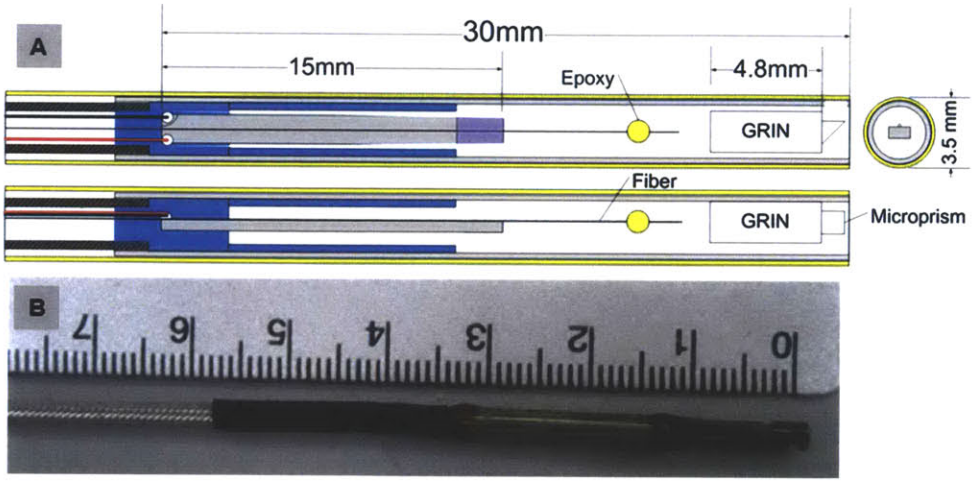

Figure 7.1. (A) Schematic diagrams of the PZT-based imaging catheter and (B) the photo of the prototype probe.

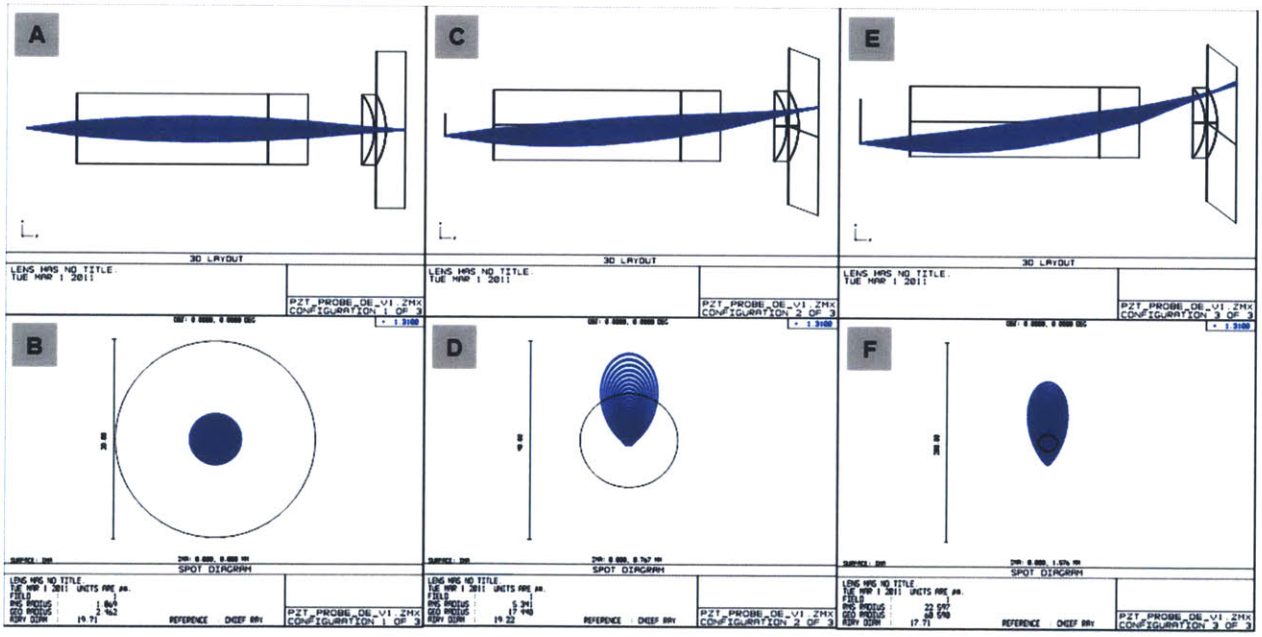

Figure 7.2. ZEMAX model of the optical design of the PZT-based imaging catheter. The 3D layout shows optimized design. The model is constructed to achieve minimized aberration of the spot on the focal plane when the light is on axis. (A) Ray tracing when the fiber is not deflected (on axis). (B) Spot diagram at the focal plane when the fiber is not deflected (on axis). (C) Ray tracing when the fiber is deflected to achieve ±0.5 mm scan. (D) Spot diagram at the focal plane when the fiber is deflected to achieve ±0.5 mm scan. (E) Ray tracing when the fiber is deflected to achieve ±1 mm scan. (F) Spot diagram at the focal plane when the fiber is deflected to achieve ±1 mm scan. Estimated FWHM spot size is 19 um at a working distance of 500 um in tissue.

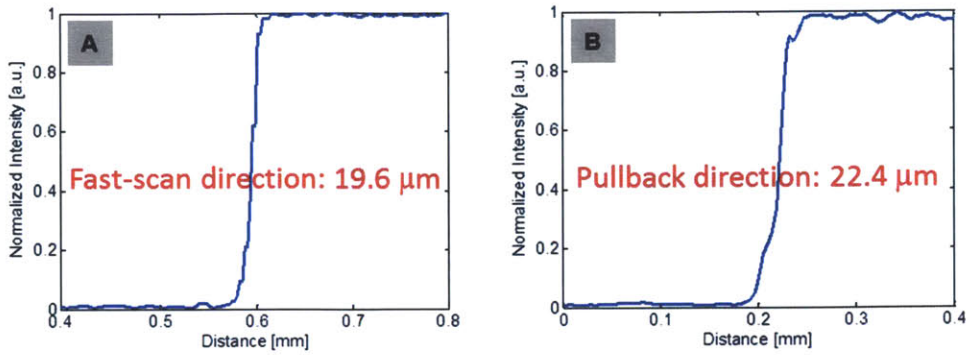

Figure 7.3. Spot size measurement using the knife edge method. (A) The FWHM spot size along the fast-scan direction. (B) The FWHM spot size along the pullback direction..

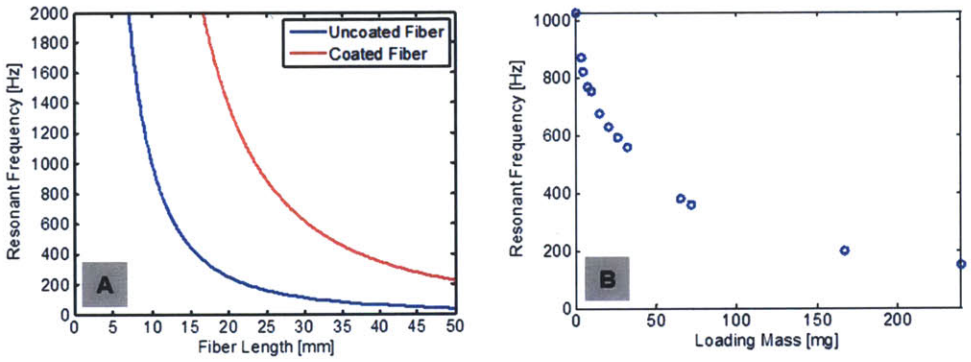

Figure 7.4. (A) Resonant frequency of the fiber cantilever, versus cantilever length. (B) The resonant frequency of an 8 mm fiber cantilever versus the weight of loading mass applied on the fiber.

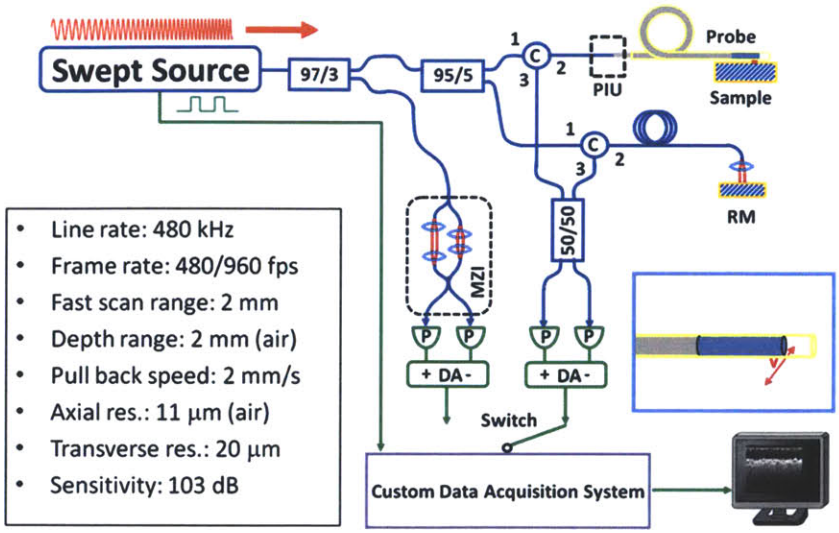

Figure 7.5. Schematic of swept source OCT system (optics: blue; electronics: green) and a summary of the system performance. The inset showing the catheter indicates the lateral scanning direction of the focused spot. C: circulator; MZI: Mach-Zehnder interferometer; RM: reference mirror; DA: differential amplifier; P: photodetector; PIU: patient interface unit. Originally published in [10].

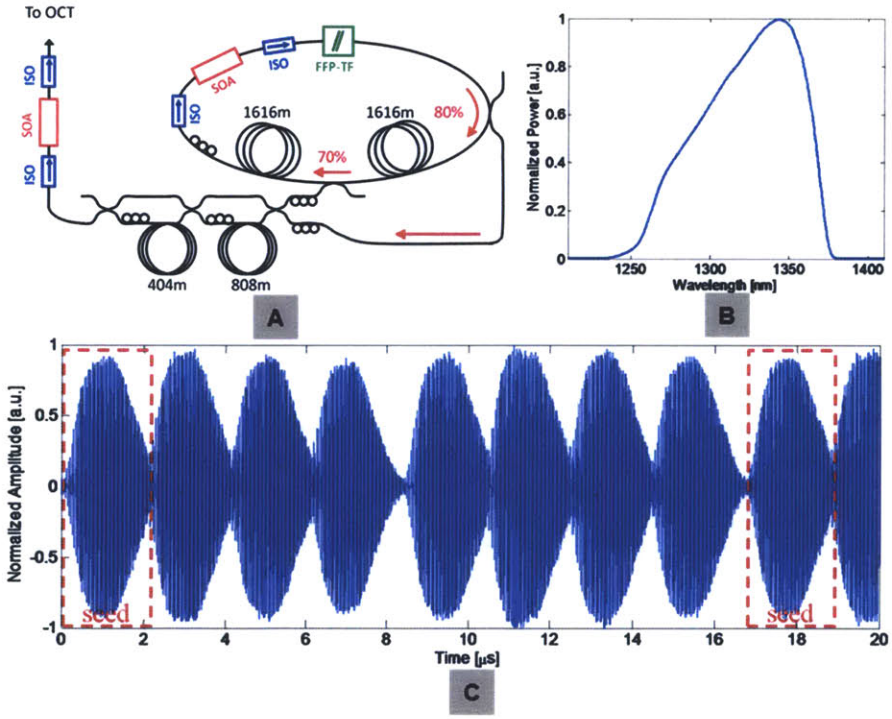

Figure 7.6. (A) Schematic of the 480 kHz triple-buffered FDML laser. (B) Optical spectrum of the laser. (C) Interferometric trace of the 480 kHz laser from the Mach-Zehnder interferometer. The sweeps indicated by "seed" were generated from the laser cavity. ISO: optical isolator; FFP-TF: fiberoptic Fabry-Perot tunable filter; SOA: semiconductor optical amplifier. Originally published in [10].

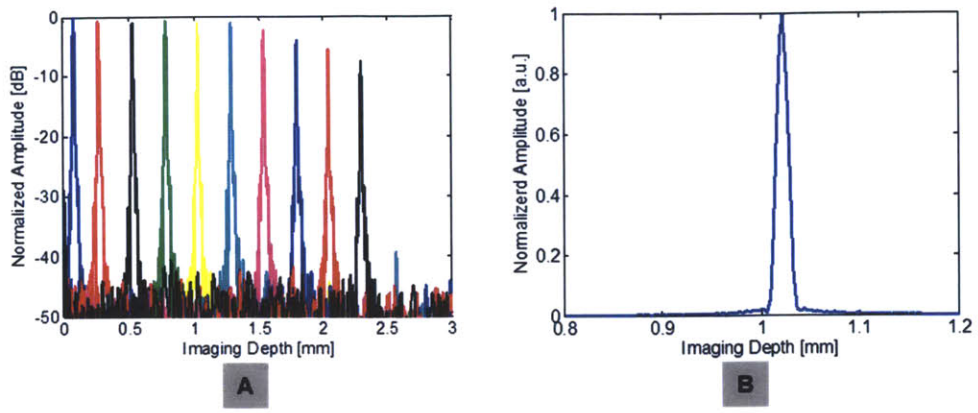

Figure 7.7. (A) Sensitivity roll-off and (B) point spread function at imaging depth around 1 mm from the ultrahigh speed endoscopic OCT system. Originally published in [10].

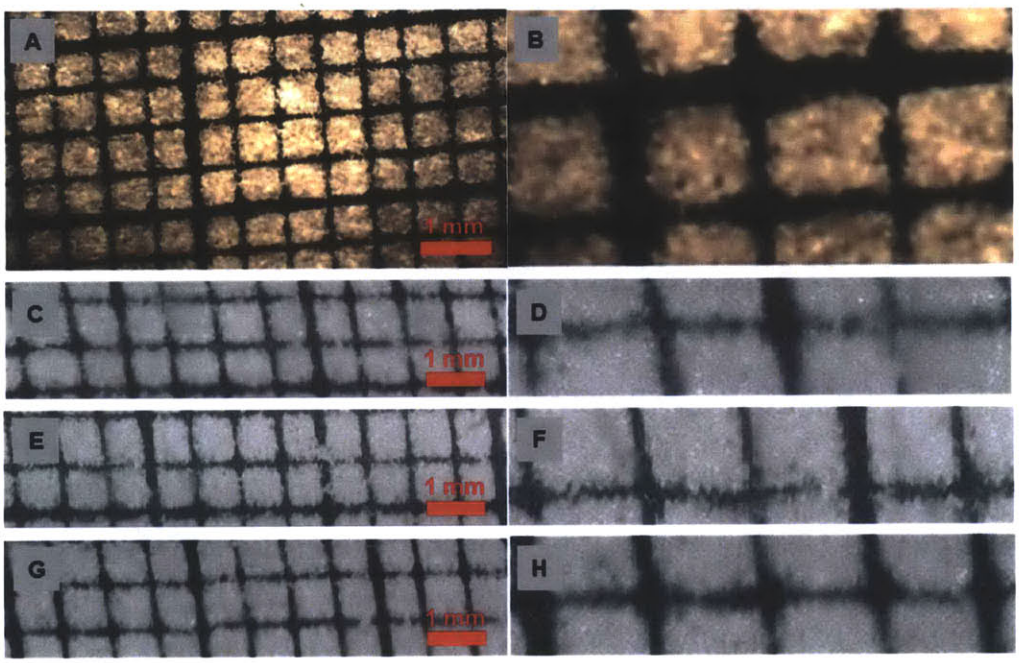

Figure 7.8. (A) Micrograph of the grid pattern and (B) enlarged view of (A). (C) *En face* OCT image of the grid pattern acquired with the imaging catheter under 20 cm radius of curvature bending and (D) enlarged view of (C). (E) *En face* OCT image of the grid pattern acquired with the imaging catheter under 5 cm radius of curvature bending and (F) enlarged view of (E). (G) *En face* OCT image of the grid pattern acquired with the imaging catheter under 3 cm radius of curvature bending and (H) enlarged view of (G).

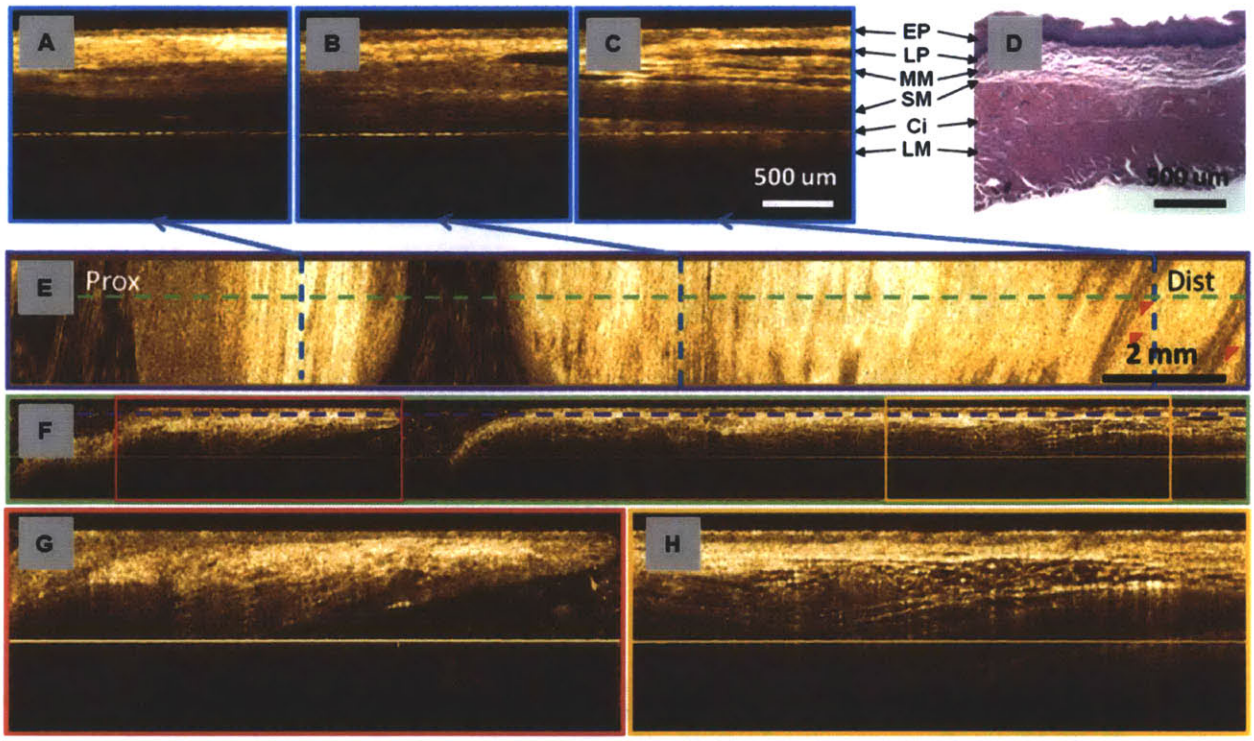

Figure 7.9. *In vivo* volumetric OCT images from rabbit esophagus. (A-C) A series of cross-sectional images along the fast-scan direction at different locations. (D) Representative histology of the rabbit esophagus. (E) *En face* image at imaging depth of 160 um. (F) Cross-sectional image along the pullback direction. (G-H) Enlarged views in (F). Red arrows: vessels. Originally published in [10].

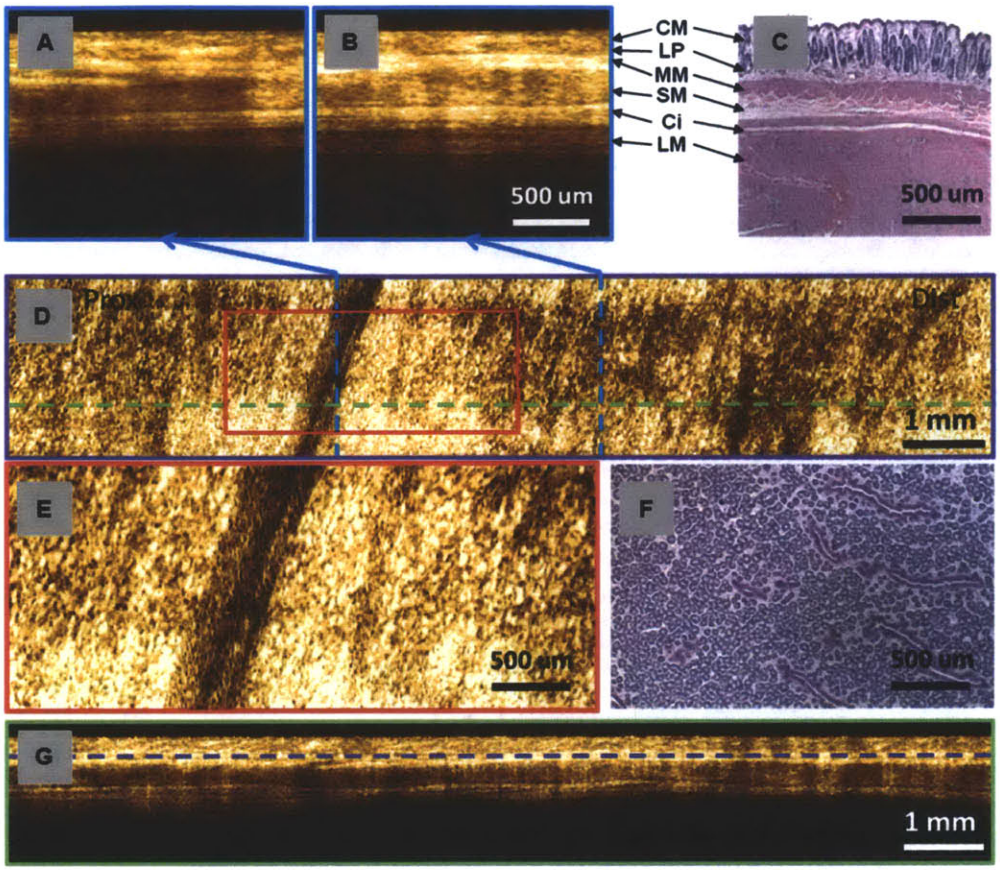

Figure 7.10. *In vivo* volumetric OCT images from rabbit colon. (A-B) A series of cross-sectional images along the fast-scan direction at different locations. (C) Representative cross-sectional histology of the rabbit colon with hematoxylin and eosin stain. (D) En face image at imaging depth of 250 um. (E) Enlarged view of the red box in (D). (F) Representative rabbit colon *en face* histology with hematoxylin and eosin stain. (G) Cross-sectional image along the pullback direction. Originally published in [10].

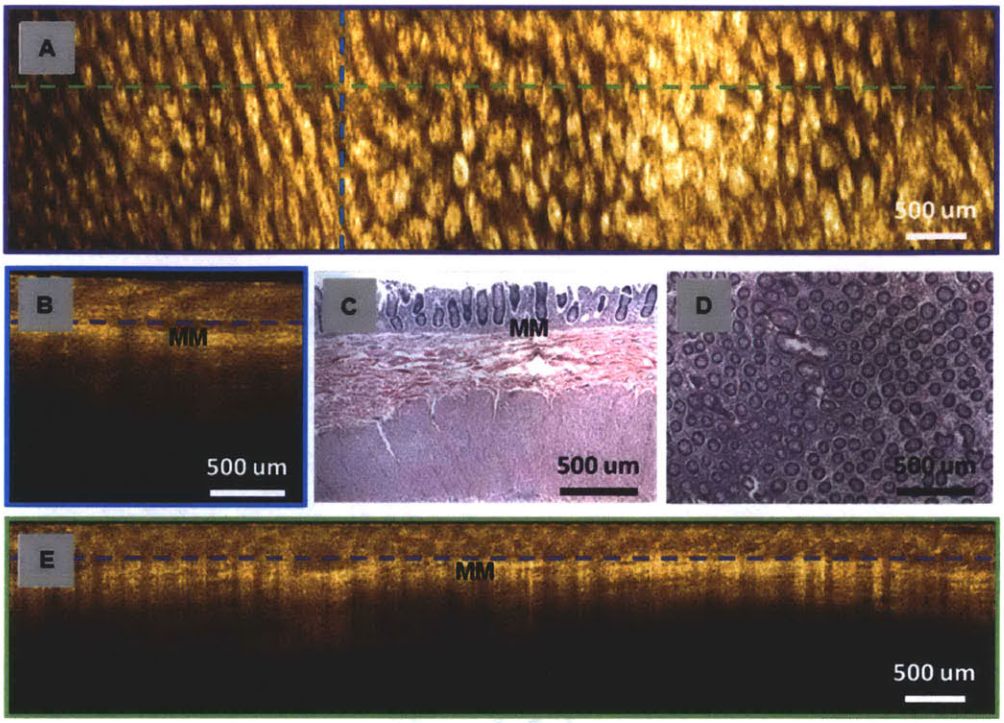

Figure 7.11. *Ex vivo* volumetric OCT images from human colon. (A) En face image at imaging depth of 350 um. (B) Cross-sectional image along the fast-scan direction. (C) Representative cross-sectional histology of the human colon with hematoxylin and eosin stain. (D) Representative *en face* histology of the human colon with hematoxylin and eosin stain. (E) Cross-sectional image along the pullback direction. MM: muscularis mucosa. Originally published in [10].

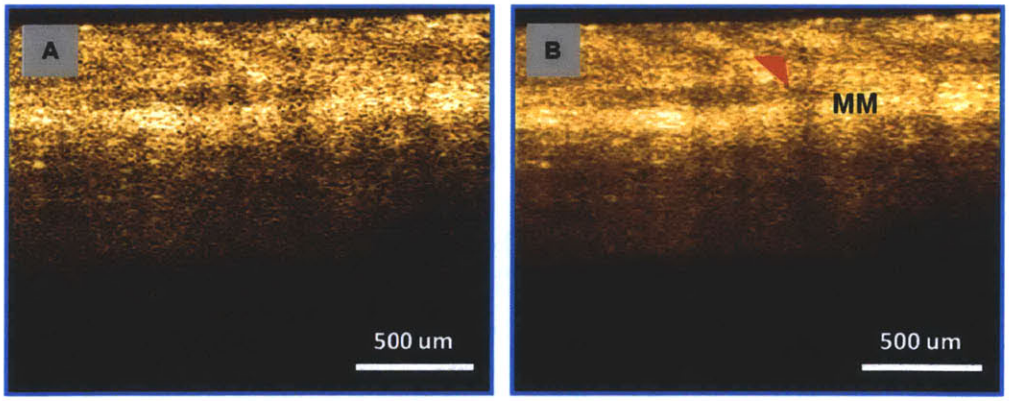

Figure 7.12. Image contrast enhancement by averaging. (A) Single slice. (B) Averaged image of a 15-um-thick section. MM: muscularis mucosa. Originally published in [10].

7.9 References

[1] J. Sawinski and W. Denk, "Miniature random-access fiber scanner for in vivo multiphoton imaging," *Journal of Applied Physics,* vol. 102, Article 034701, pp. 1-8, Aug 1 2007.

[2] A. D. Aguirre, J. Sawinski, S. W. Huang, C. Zhou, W. Denk, and J. G. Fujimoto, "High speed optical coherence microscopy with autofocus adjustment and a miniaturized endoscopic imaging probe," *Optics Express,* vol. 18, pp. 4222-4239, Mar 2010.

[3] X. M. Liu, M. J. Cobb, and X. D. Li, "Rapid scanning all-reflective optical delay line for real-time optical coherence tomography," *Optics Letters,* vol. 29, pp. 80-82, Jan 2004.

[4] L. E. Kinsler, A. R. Frey, A. B. Coppens, and J. V. Sanders, *Fundamentals of Acoustics*, 4 ed. New York: Wiley, 1982.

[5] L. Huo, J. Xi, Y. Wu, and X. Li, "Forward-viewing resonant fiber-optic scanning endoscope of appropriate scanning speed ?for 3D OCT imaging," *Opt. Express,* vol. 18, pp. 14375-14384, Jul 2010.

[6] "Medical electrical equipment - Part 1: General requirements for basic safety and essential performance," 3rd ed: International Electrotechnical Commission, 2005.

[7] B. Potsaid, B. Baumann, D. Huang, S. Barry, A. E. Cable, J. S. Schuman, J. S. Duker, and J. G. Fujimoto, "Ultrahigh speed 1050nm swept source / Fourier domain OCT retinal and anterior segment imaging at 100,000 to 400,000 axial scans per second," *Opt. Express,* vol. 18, pp. 20029-20048, Sep 2010.

[8] B. R. Biedermann, W. Wieser, C. M. Eigenwillig, T. Klein, and R. Huber, "Dispersion, coherence and noise of Fourier domain mode locked lasers," *Optics Express,* vol. 17, pp. 9947-9961, Jun 2009.

[9] Y. Wu, J. Xi, M. J. Cobb, and X. Li, "Scanning fiber-optic nonlinear endomicroscopy with miniature aspherical compound lens and multimode fiber collector," *Opt. Lett.,* vol. 34, pp. 953-955, Apr 2009.

[10] T. H. Tsai, B. Potsaid, M. F. Kraus, C. Zhou, Y. K. Tao, J. Hornegger, and J. G. Fujimoto, "Piezoelectric-transducer-based miniature catheter for ultrahigh-speed endoscopic optical coherence tomography," *Biomedical Optics Express,* vol. 2, pp. 2438-2448, Aug 2011.

CHAPTER 8

8.0 Micromotor Based Imaging Catheter

8.1 Motivation

Chapter 7 shows the advantages of distally scanning mechanism under the high speed operation, which overcomes the stability and speed limitation of traditional proximally rotary scanning mechanism. Distal scanning methods using PZT or MEMS based actuators can provide micron-level precision scanning because the mechanical motion can be directly controlled. However these methods usually have a limited imaging area because the size of the scanner is limited by the catheter size. With advances in micromotor technology, imaging using distal rotary scanning can be achieved, which can provide large scanning area while maintaining high speed, uniform rotation without degrading the image quality. Micromotor catheters for ultrahigh resolution *in vivo* imaging in animals were firstly demonstrated in 2004 [1, 2], which used time domain OCT (TF-OCT) imaging systems so the overall imaging speed was relatively low compared to the state-of-the-art OCT technology. Nevertheless, these studies did demonstrate the in-frame stability using the micromotor technology in the imaging catheter design. Other groups have used micromotor based OCT catheters to study smoke induced airway injury [3] and combined fluorescent contrast for intravascular atherosclerotic imaging [4]. Recently, Li, *et al.* have developed a miniaturized OCT catheter using a two-phase micromotor and demonstrated an imaging speed of 52 fps with 980 axial scans per frame in ex vivo pig bronchus and 208 fps with 208 axial scans per frame in the human finger [5]. This study demonstrated high frame rates, however the sampling density was limited at higher frame rates due to the OCT system imaging speed [5].

There are several existing wavelength swept lasers that can support high imaging speed more than 200 kHz axial line rate, including Fourier domain mode-locked (FDML) lasers [6], short cavity swept lasers [7], and vertical cavity surface emitting lasers (VCSEL) [8]. These different types of swept lasers were introduced in Chapter 1. Among these technologies, the VCSEL has the advantage that it operates with a single longitudinal mode instead of multiple modes and therefore has an extremely narrow instantaneous linewidth that supports a long imaging range. The micron-scale cavity length of VCSELs and the rapid MEMS response also allows wider-range real time adjustability of both the sweep frequency and wavelength tuning range compared with other lasers. Therefore, the VCSEL is a promising technology for high-speed, long range OCT imaging [8, 9].

In this section of the thesis work, a micromotor based miniature catheter with outer diameter of 3.2 mm was built for ultrahigh speed endoscopic OCT imaging. The micromotor has the advantage of high rotary speed with low driving voltage, ease of rotary speed adjustment and small size. The side-viewing probe can be pulled back over a long distance to acquire three-dimensional (3D) datasets covering a large field of view. *In vivo* imaging in the rabbit gastrointestinal (GI) tract and *ex vivo* imaging on the human colon specimen were performed using the imaging catheter and a bench-top OCT imaging system based on a VCSEL as the high speed light source. Using the high speed data acquisition (DAQ) system,

ultrahigh speed endoscopic OCT imaging can be achieved and large volume data sets can be acquired with only a few seconds acquisition time. The choices of optical and mechanical designs such as distal imaging head will be compared and discussed in the following sections. The VCSEL light source was developed in collaboration with Praevium and Thorlabs. Dr. Vijaysekhar Jayaraman, PhD, from Praevium designed and fabricated the VCSEL. Drs. Benjamin Potsaid and James Jiang from Thorlabs performed detailed studies of the VCSEL dynamics and output characteristics. These developments enabled the use of high speed VCSEL light sources for the study. Dr. Robert Marini and Wayne Au from MIT animal facility helped the rabbit imaging experiment.

8.2 Optical Design of the Micromotor Based Imaging Catheters

Figure 8.1 shows a ZEMAX model of the basic design for micromotor based imaging catheter. Similar to the optical design of the PZT-based imaging catheter, a single GRIN lens was used to focus the laser beam coming out from the fiber. Since the fiber was not deflected, the laser beam was always on-axis and thus the parameters such as the distance between the fiber and the GRIN lens are relatively easier to determine. After passing through the GRIN lens, the laser beam then was reflected by a micro-mirror (or a micro-prism) to the side and focused outside of the catheter sheath.

The micro-mirror was glued on the shaft of the micromotor, so the size of the motor also accounts for the total distance from the back surface of the GRIN lens to the focal plane. Considering a micromotor with a diameter of 2 mm, a 100~200 μm wall thickness of the lens/motor assembly, and a clearance of 200~300 μm for smooth pulling back of the catheter, a plastic sheath with an inner diameter of 2.8 mm is required to hold the entire imaging catheter, giving a total distance of ~3.2 mm from the GRIN lens to the focal plane if the wall thickness of the sheath is 300 μm and the working distance is 500 μm. For a commercially available GRIN lens, which usually has pitch of 0.23~0.29, it is not possible to keep the magnification of the lens system low with the focal plane this far away from the GRIN lens. In order to keep the spot size as small as possible, one solution is to reduce the pitch of the GRIN lens, that is, increase the effective focal length of the GRIN lens. Based on the optimization result using the ZEMAX model, a pitch of 0.15 is determined to achieve a spot size 8 μm in tissue, as **Fig. 8.1B** shows.

A commercially available GRIN lens with a pitch of 0.25 originally (NSG, Inc.) was shortened by angle polishing one end of the GRIN lens. The angle of the polishing is 5^{o} to reduce the backreflection from the GRIN lens surface. The transmission, back-coupling, backreflection, and working distance were measured during the catheter assembly process. The working distance is measured in air from the sheath surface to the focal plane, and is close to the actual working distance when considering in tissue. A working distance of 300 μm in air is desired for an optimal final working distance. The spot size was measured using the knife edge method, which records the total output power as a knife edge at the focal

plane is translated through the output beam using a calibrated translation stage. The final micromotor based imaging catheter produced a transmission of 75%, back coupling efficiency of 60%, backreflection of -47 dB, and working distance of 270 μm in air. The beam profile of the focal spot is circular and the measured spot size at the focal plane was 7 μm in air, which corresponds well with the ZEMAX simulation result.

8.3 Mechanical Design of the Micromotor Based Imaging Catheters

A commercially available micromotor (Namiki Precision of California, Inc.) with diameter of 2 mm and length of 6mm was used to build the imaging catheter. The micromotor can be operated with a driving voltage less than 5V at a speed from 1,200 revolutions per minute (rpm) to 72,000 rpm, corresponding to an imaging frame rate of 20 fps to 1,200 fps. The micromotor is controlled via four electrical cables, which are bundled as one single sheathed cable with a total length of 2.5 m. The cable was folded back to the proximal end along the entire length of the imaging catheter, which passed through the scanning field of the laser beam and blocked a portion of the imaging circumference. There are several methods to package the distal end of the micromotor imaging catheter. One typical method is encapsulating and fixed all the components inside a plastic tube or sheath [3, 5], which is the simplest way for assembling and the overall catheter size can be very compact. However, for high speed OCT imaging, pulling or push the imaging catheter to achieve the second dimensional scan is required. The single sheath design can be pulled or pushed directly by a proximal translation stage, but the motion is translated through the whole catheter body that is directly in contact with the environment. Hence it is very difficult to maintain steady control of the distal end, especially for the endoscopic applications, which usually require long imaging catheters and high scan precision to capture small features in the tissue. To overcome this limitation, two packaging methods are proposed here.

The micromotor was a three-phase and brushless motor design with a terminal resistance of ~100 Ω, which allowed high rotation uniformity and much longer lifetime compared to brushed motor. The maximum no-load speed and the stall torque of the micromotor were 82,000 rpm and 0.0033 $mN \cdot m$ respectively, indicating the micromotor could provide a torque of $4x10^{-4}$ $mN \cdot m$ while operating at 72,000 rpm. The speed of the brushless motor is limited by the torque the motor can generate and the torque is inversely proportional to the rotary speed of the motor.

Figure 8.2 shows a schematic diagram of a micromotor imaging catheter with double sheaths design. In this design, the inner short sheath made of rigid and transparent plastic material works as a holder that contained the lens-motor assembly and connects with the torque coil for the pullback translation. The imaging catheter was protected by an outer plastic sheath that serves the same function as those in the standard rotary catheters. This design thus has much better push-pull control precision compared to the

single sheath design, because the outer sheath helps preventing the direct contact of the imaging catheter with the environment. With both sheaths transparent, this design also provides nearly full circumference scanning range except for the field block by the electrical cable. One drawback of the double sheath design is the multiple surfaces from the sheath in the optical path, which potentially increase the backreflection and reduce the signal to noise (S/N) ratio of the OCT imaging. In addition, the distances of these surfaces are very short (around tens micron level) so they can cause the self-interference effect and generate ghost signal in the acquired images.

Figure 8.3 shows a schematic diagram of the other proposed micromotor based imaging catheter design. Similar to the double sheath design, the imaging catheter is also protected by an outer plastic sheath, but the lens-motor assembly is held by a metal hypo tube with an imaging window that allows the laser beam coming out. Since there is no additional surface along the optical path, the imaging quality of this design is the same as that of the single sheath design. Metal hypo tubes are easier to machine and can remain rigid even with a part of the circumference removed. Rigid plastic tubes can also be used as the holder, but they usually are more fragile after removing a portion of the circumference and the chance of breakage is much higher during *in vivo* imaging sessions. The size of the imaging window is a limitation of this design because a certain portion of the circumference of the hypo tube must remain intact so the holder can be rigid enough to sustain any bending while introducing the imaging catheter to its target imaging locations. For a stainless steel hypo tube with wall thickness of ~100 μm, an intact portion that covers 20%~30% of the circumference is robust enough for most of the endoscopic applications.

As shown in **Fig. 8.3A**, the imaging catheter was built using the metal hypo tube design where the optical and motor assembly was mounted inside a stainless steel hypo tube with a 2.1 mm inner diameter and 2.37 mm outer diameter. The hypo tube was used to fix the micromotor to a 1.8 mm outer diameter torque coil (Asahi Intecc, Inc.). The hypo tube enables imaging over approximately 70% of the micro-mirror rotation. The FEP plastic sheath, which covered the motor and the hypo tube was 2.8 mm inner diameter and 3.2 mm outer diameter (Zeus, Inc.). By pulling the optical and motor assembly from the proximal end of the torque coil during the rotary imaging acquisition, a spiral scanning pattern could be performed. The catheter had a 3.2 mm outer diameter and 18.2 mm rigid length and could pass through a 3.7 mm endoscope working channel. The total length of the torque coil and sheath for the imaging catheter was 2 meters. **Fig. 8.3B** shows a photograph of the assembled imaging catheter.

8.4 System Description

Figure 8.4 shows the OCT system used to assess the imaging performance of the micromotor based imaging catheter. A portion of the laser output was coupled to a Mach-Zehnder interferometer (MZI) to generate interference fringes, which are used to calibrate the VCSEL frequency sweep. The MZI was

dispersion balanced and set at 1 mm path difference and fringes were detected by a modified 200 MHz dual-balanced photodetector to generate phase information to recalibrate the OCT interference fringe signals. The detector was modified from a commercially available 350 MHz dual balanced detector (Thorlabs, Inc.) to increase the transimpedance gain by ~2X to 2.4 kOhms and trading off the bandwidth to 200 MHz [7, 10]. The OCT system consisted of a dual-balanced Michelson interferometer with a pair of optical circulators and a 50/50 fiber-optic splitter (AC Photonics, Inc.) [10-12]. The OCT signal was acquired with the same modified photodetector. To enable real time image preview, the MZI calibration interference fringes were acquired once prior to the OCT signal acquisition and the OCT signal was recalibrated by resampling and spline-interpolation using the MZI calibration. The MZI calibration and OCT signals were digitized using a high speed A/D card with 500 MSPS sample rate. The power on the sample was approximately 20 mW.

8.4.1 VCSEL with 1 MHz Axial Scan Rate

Figs 8.5A and B show a schematic of the VCSEL swept laser (Praevium Research, Inc. and Thorlabs, Inc.) system and device structure. The quantum well active region of the VCSEL was optically pumped at 980 nm through a wavelength-division multiplexer and wavelength tuning was performed by electrostatic deflection of a MEMS tunable filter. The resonant frequency of the MEMS tunable filter was approximately 500 kHz and it was driven with a sinusoidal waveform at 500 kHz. The forward and backward sweeps were both used for image acquisition to achieve an effective sweep rate of 1 MHz. The laser output was amplified with two semiconductor optical amplifiers (SOAs, Thorlabs, Inc.) before the OCT system. Two SOAs were used because of wavelength mismatches and limited gain in available single SOAs. The amplified spontaneous emission (ASE) spectrum of the first booster SOA had a peak wavelength at 1,270 nm and a full width at half maximum (FWHM) of 60 nm. The first booster ASE was used as a pre-amplification stage that increased the power in shorter wavelength range and matched the ASE spectrum of the second booster SOA. The ASE spectrum of the second SOA had a peak wavelength at 1,310 nm and a FWHM of 90 nm. The second booster SOA had higher gain and was used to amplify the output from the first booster SOA. With the wavelengths matched, the VCSEL output can be amplified without decreasing the overall FWHM bandwidth. A redesign should allow a single SOA to be used in the future. By tuning the driving current of the first and second SOAs, the full width half maximum of the output spectrum and the output power could be adjusted based on the application requirements. The maximum output power was 110 mW if both SOAs were driven at their maximum driving current. However, in this study, the SOAs were set to optimize sweep range and the average output power after the booster stage was 40 mW. **Fig. 8.5C** shows the time integrated VCEL output spectrum measured by an optical spectrum analyzer. The central wavelength was ~1310 nm and the total

sweep range was 107 nm, with a 70 nm FWHM. **Fig. 8.5D** shows the fringe signal from a Mach-Zehnder interferometer. The duty cycle was >90% with a 1 μs sweep duration and symmetric forward and backward sweeps.

8.4.2 High Speed and Large Volume Data Acquisition

A 64-bit computer with 32 GB memory was used to support continuous acquisition and streaming of the swept source OCT data. The high speed A/D card (AlazarTech, Inc.) was used to sample the OCT signal at up to 500 MSPS with 12 bit resolution. Customized user interface and data acquisition software were developed in C++ to coordinate instrument control and enable user interaction. The imaging system could acquire OCT data for over 10 seconds at 1 MHz axial scan rate acquiring a data set size larger than 10 GB.

8.4.3 Signal Processing of the OCT Images

An MZI calibration trace was acquired in the beginning of each imaging session and used to calibrate all of the OCT fringe data for that session. Calibration traces were not required for each axial scan sweep. Each MZI sweep contains 1000 A/D sample points, covering both forward and backward scans for each laser sweep. The MZI fringe data was first interpolated by fast Fourier transforming (FFT), zero-padding to 2,048 points, and then inverse Fourier transforming (IFFT). The interpolated MZI traces were then Hilbert transformed to extract the phase of the frequency sweep. The phase information was then used to resample the OCT interference signals from equal time intervals to linear phase, or equal frequency interval samples. The OCT interference signals were interpolated to 2,048 points/sweep using FFT/zero-padding/IFFT, then re-sampled using cubic-spline interpolation to be equally sampled in k or frequency using the phase calibration information from the MZI traces. The re-sampled OCT fringe data was then Fourier transformed (FFT) to obtain the axial scans. The axial scans consisted of ~250 samples, spaced by ~4.8 μm with a maximum imaging range of 1.2 mm in tissue. Images were generated by computing the log of the magnitude of the axial scans.

8.4.4 Imaging System Performance

To characterize the system sensitivity, a calibrated -52 dB reflection was used in the sample arm. The reference arm power was set to 150-200 microwatts. The sensitivity was measured as the ratio of the peaks of the PSFs to the standard deviation of the noise floor, which was measured with the sample arm blocked. The estimated system losses were ~4 dB arising from losses in the optics, mirror reflectivity and backcoupling. The measured sensitivity values were not adjusted for these losses. **Figure 8.6** shows the sensitivity roll off and the point spread function from a fixed reflection. The measured sensitivity of the system was 103.1 dB with an incident power of 20 mW and the image depth range was 1.65 mm in air

(1.2 mm in tissue). **Figs. 8.6A and B** show the sensitivity roll off measured by the 500 MSPS A/D card versus a 1 GHz bandwidth oscilloscope (Tektronix, Inc.). The sensitivity rolls off ~7 dB at 1.5 mm in **Fig. 8.6A** and was limited by the bandwidth of the A/D card (250 MHz). In contrast, the sensitivity was relatively constant over the entire imaging range in **Fig. 8.6B** when measured using the 1 GHz bandwidth oscilloscope and the R-number was 4 mm/dB, calculated from the inverse decay constant of the exponential decay curve fitted to the signal maxima of the linear PSFs [13]. The axial resolution was 11 μm in air (8 μm in tissue), as shown in **Fig. 8.6C**.

The micromotor scanning in the rotary direction is highly repeatable, however there are potential discontinuities of motion when the motor and optics are distally pulled back along the longitudinal direction. This can be a limiting factor in the image continuity when using a long catheter because of the friction between the catheter cable and sheath along its length. Typical endoscopic applications in humans would require a 2-meter-long catheter. The effects of friction may be reduced by choosing different torque coils or sheath materials. To evaluate the scanning stability of the micromotor based imaging catheter under a tight bending curvature, a custom grid sheet with two different orientations (90° and 45°) printed by a laser printer with 600 dpi resolution was wrapped around the plastic sheath and OCT imaging was performed to acquire the en face images with different catheter curvature. The 90° grid shows the stability of rotary scan while the 45° grid shows the stability of pullback. The grid pattern had size of ~250 μm and the line width of 50 μm. The imaging catheter was bent with ~5 cm radius of curvature to simulate possible scenarios during the in vivo endoscopic OCT imaging. **Figure 8.7** shows a series of *en face* views of 3D-OCT data sets taken from the custom grid sheet when the imaging catheter was bent with 5 cm radius of curvature. The *en face* images were slightly distorted due to the actual contact of the imaging catheter and the grid paper but there was no apparent skipping or jumping observed along different orientations, indicating the imaging catheter can provide extremely stable scan in both rotary and pullback directions under the tightly bent situation. In the enlarged views shown in **Figs. 8.7C and D**, the OCT *en face* images were able to show the resolution limit of the laser printer, which is ~45 μm, as well as the ink permeating the plain paper that made inconsistent line width in the grid pattern.

8.5 *In Vivo* 3D-OCT Imaging in the Rabbit GI Tract

To demonstrate the ability to image microscopic structures in the gastrointestinal tract, volumetric 3D-OCT data sets of the esophagus and colon of a female New Zealand White rabbit were acquired *in vivo*. The animal was anesthetized prior to imaging. Studies were performed under a protocol approved by the Committee on Animal Care (CAC) at M.I.T.

8.5.1 OCT Imaging in the Rabbit Esophagus

Figure 8.8 shows example of cross-sectional images of rabbit esophagus along the rotary direction transverse to the probe, with and without averaging. The micromotor imaging catheter could provide extremely high rotary stability and thus enabled contrast enhancement by averaging consecutive images. The image data was displayed in Cartesian coordinates, although the images were acquired by angle scanning the beam and therefore should be in polar form, as shown in **Fig. 8.8D**. This display produces a transverse distortion of the image with increasing axial distance or depth but enables more efficient visualization than polar images. The axial dimension was divided by the tissue index of refraction (n = 1.38) so the axial scale corresponded to physical thickness. The imaging catheter sheath was visible at the top of the images. The sheath outer diameter was 3.1 mm, corresponding to a ~ 10 mm circumference, determining the transverse scale at the top of the image. Since only 70% of the rotary scan produced an image, the transverse direction was cropped to 7.5 mm. Increased axial distance from the sheath corresponded to an increased scan circumference. At an axial distance of 1 mm from the sheath, the scan circumference is 16.2 mm. This produces an artifact, where features are compressed in the transverse direction with increasing depth. It is also important to note that if the esophagus was not in contact with the sheath around the entire scan, the OCT beam did not intersect the esophagus perpendicularly. The esophageal layers appeared thicker away from the point of contact because the axial scan was at an angle to the layers.

Figure 8.9 shows a 3D-OCT data set from the rabbit esophagus. The ultrahigh speed imaging system enabled the acquisition of very large data sets, which cover large areas of tissue with dense spatial sampling. In the data set, 3,000 frames of 2,500 axial scans each were acquired in 7.5 seconds, covering a volume size of 7.5 mm x 7.5 mm x 1.2 mm (rotary x pullback x axial directions). The pixel spacing was 4 μm x 2.5 μm x 4.8 μm in the rotary x pullback x axial directions, respectively. The cross-sectional OCT images (**Figs. 8.9B-D**) allowed visualization of the entire normal esophageal layers including the epithelium (EP), lamina propria/muscularis mucosa (LP/MM), submucosa (SM), circular muscle (Ci), and longitudinal muscle (LM). The layered structure in the OCT images correlated well with representative histology of the rabbit esophagus (**Fig. 8.9E**). The volumetric data set could be processed and displayed in three dimensions. All images shown here were displayed by averaging three consecutive images perpendicular to the viewing direction. **Fig. 8.9A** and **Fig. 8.9C** show the *en face* and cross-sectional view along the pullback direction respectively. The *en face* view (**Fig. 8.9A**) averaged over a depth of 15 μm, showed features such as vessels over a large field of view. Vessels had similar structures to dilated glands in the cross-sectional views, but could be distinguished in the *en face* images. Periodic motion due to the cardiac cycle was visible in the *en face* view.

The longitudinal cross-sectional images were averaged over 7.5 μm (**Fig. 8.9C**) and provided structural information over a long region of the esophagus, with enhanced imaging contrast due to dense

sampling along the pullback direction. The longitudinal image (**Fig. 8.9C**) did not have image distortion artifacts, which occurred in transverse images (**Figs. 8.8A-C** and **Fig. 8.9A**) because they were generated by axial scans orientated in a radial plane through the probe. **Fig. 8.9D** shows the enlarged view of the region marked with green box in **Fig. 8.9C**. High speed imaging allowed the visualization of tissue dynamics *in vivo*

8.5.2 OCT Imaging in the Rabbit Colon

Figure 8.10 shows a 3D-OCT data set covering a volume of 7.5 mm x 7.5 mm x 1.2 mm (rotary x pullback x axial directions) in the rabbit colon. All images displayed here were generated by averaging three consecutive images perpendicular to the viewing direction. The rabbit was not under special fasting before the imaging session, so the stool can also be observed from the OCT images. The *en face* view at a depth of 300 μm (**Fig. 8.10A**) shows crypt structures in the colon as well as vessels underneath the colon surface. Compared to human tissue, crypts in the rabbit colon are smaller (~50 μm) and more tightly packed. Crypts in the rabbit colon were often separated by only a few micrometers of lamina propria, making it usually difficult to identify single crypts in the *en face* images. Nevertheless, the crypts were visible in some enlarged *en face* views as shown in the inset of **Fig. 8.10A**. Ultrahigh speed imaging also made 3D-OCT acquisition less sensitive to motion. **Fig. 8.10C** shows a longitudinal cross-sectional image along the pullback direction. Motion artifacts were relatively small throughout the pullback procedure. Therefore, requirements for image post processing, such as frame alignment could be reduced.

8.6 *Ex Vivo* 3D-OCT Imaging on Human Colon Specimens

To evaluate the imaging system for future clinical endoscopic OCT studies, we also imaged human colon specimens *ex vivo* using the ultrahigh speed OCT system. Specimens were obtained under a protocol approved by the Committee for the Use of Humans as Experimental Subjects (COUHES) at M.I.T. Fresh unfixed colon specimens were stored in refrigerated DMEM for less than three hours prior to imaging. **Figure 8.11** shows a 3D-OCT data set from freshly excised human colon tissue covering a volume size of 7 mm x 7.5 mm x 1.2 mm (rotary x pullback x axial directions). **Fig. 8.11B** shows an *en face* OCT image at a depth of 350 μm averaged over 2 pixels, corresponding to a 10 μm depth. The individual crypts in the human colon are larger than those in the rabbit colon and were more easily visualized. **Figs. 8.11A and D** show cross-sectional images transverse to the probe along the rotary direction and longitudinal to the probe in the pullback direction, respectively. Both the *en face* and the cross-sectional images show the columnar epithelial structure of the colon (as shown in the enlarged views in **Fig. 8.11C, F, and G**) and the *en face* view correlates well with representative histology of human colon shown in **Fig. 8.11E**. Densely sampled volumetric 3D-OCT data sets contained

comprehensive information about tissue microstructure. **Fig. 8.11C** shows the detailed structure in the crypts. The arrow indicates a narrow line in the crypts, which is possibly the boundary of the crypt lumen.

8.7 Discussion and Performance Improvement

The micromotor based imaging catheter enables high speed scanning with low driving voltage. The distal scanning mechanism is less sensitive to catheter bending, and is therefore more stable than catheters which use proximal rotary actuation. The current micromotor catheter has the limitation that the wiring and mounting of the micromotor blocks a portion of the imaging field, which requires adjusting the orientation of the imaging probe before image acquisition. The VCSEL light source has both very high sweep rate and broad wavelength tuning range, providing high axial line rate for *in vivo* imaging and good axial resolution. With the high speed data acquisition, the imaging system can support good imaging depth range with ultrafast line rate. In this study, the effective laser scan repetition rate is 1 MHz and the rotary speed of the micromotor is 400 Hz (24,000 rpm), so each frame contains 2,500 lines over the circumferential scanning range of 10 mm, corresponding to an axial scan spacing of ~4 μm at the surface of the imaging catheter. The pullback speed was 1 mm/s, corresponding a frame spacing of 2.5 μm. The data acquisition rate is 500 MS/s, which can provide an imaging depth range of 1.65 mm in air, or 1.2 mm in tissue. Imaging range can be improved using high speed detection and data acquisition.

The VCSEL was operated at its resonant frequency, so the sweep-to-sweep repeatability was high enough so the OCT fringe data can be calibrated using a single MZI calibration trace acquired in the beginning of each imaging session. Our previous OCT studies with VCSELs showed noticeable sweep-to-sweep variations in the frequency/wavelength scanning if the MEMS tunable filters in the VCSELs were operated off resonance, so the OCT signal could not be re-calibrated by single MZI interference fringe in this case [9, 14]. Advanced calibration methods such as optical clocking or simultaneous acquisition of MZI and OCT signals are needed to ensure the PSFs not affected by the sweep-to-sweep variations when the VCSEL is not operated at its resonant frequency [9, 14].

With high frame rate of the imaging system, the acquired data sets are less sensitive to motion, especially when performing *in vivo* endoscopic imaging. In upper endoscopy, cardiac motion and breathing often induce motion artifacts in OCT images. The high frame rate can reduce the total data acquisition time, while maintaining data acquisition volume. High imaging speed enables rapid acquisition of a densely sampled 3D volumetric data set covering a broad area with minimum motion artifacts. The volumetric data set can be viewed in a variety of orientations. Cross-sectional views provide depth and structural information in the tissue, while *en face* views can reveal the tissue structure over the field of view at a given depth. Moreover, with the densely sampled data sets, image contrast can be enhanced by image averaging to reduce speckle noise.

The performance of the current prototype can be further improved. The distance from the lens distal surface to the focal plane is relatively long due to the diameter of the micromotor, so the transverse resolution (the spot size on the focal plane) is limited if standard GRIN lenses are used. In this prototype imaging catheter, a standard GRIN lens with pitch of 0.25 was shortened to 0.15 in order to achieve longer effective focal length, which enables a smaller spot size for the long working distance. The transverse resolution can also be improved by using a fiber with higher numerical aperture (NA). A higher NA requires larger diameter optics because the beam from the fiber diverges more rapidly. The micromotor scanning in the rotary direction is highly repeatable, however there are potential discontinuities of motion when the motor and optics are distally pulled back along the longitudinal direction. This can be a limiting factor in the image continuity when using a long catheter because of the friction between the catheter cable and sheath along its length. Typical endoscopic applications in humans would require a 2-meter-long catheter. The effects of friction may be reduced by choosing different torque coils or sheath materials. The pullback speed used in this study was 1 mm/s, which is 1.6x slower than the minimum scanning speed required to achieve Nyquist sampling given the 8 μm spot size. The slower pullback speed was used to demonstrate image averaging to reduce speckle and faster pullback speeds can be used in the future. Finally, the rigid length of the distal catheter, including the micromotor and optics is ~20 mm and the outer diameter is ~3.2 mm. The imaging catheter can be inserted through an endoscope with a 3.7 mm diameter working channel, but is still too large to be introduced through the 2.8 mm working channel of most commonly used esophagogastroduodenal (EGD) endoscopes. The endoscope working channel has a sharp radius bend at the proximal end, which requires either a short rigid length or a smaller catheter outer diameter. Therefore, the size of the catheter needs to be reduced to enable use with the more common 2.8 mm working channels. Alternately, the catheter could be used with an overtube, and carried on the side of the standard endoscope.

In conclusion, an ultrahigh speed endoscopic OCT imaging was demonstrated using a micromotor based imaging catheter, a MEMS-tunable VCSEL light source and a high speed data acquisition system. The imaging system can support 400 frames per second with 1 MHz axial line rate, 11 μm axial resolution, 7 μm transverse resolution and 1.65 mm imaging depth range in air, corresponding to 8 μm axial resolution, 8 μm transverse resolution and 1.2 mm imaging depth range in tissue. The micromotor can operate 1,200-72,000 rpm (corresponding to 20-1,200 fps) so even faster frame rates can be achieved by trading off pixel density. High imaging speed was demonstrated *in vivo* in the rabbit esophagus and colon as well as *ex vivo* in human colon specimens, enabling the visualization of microscopic features. Three dimensional endoscopic OCT data sets enable powerful visualization techniques including speckle reduction by averaging, generation of *en face* views similar to endoscopic images, and the generation of cross-sectional images with arbitrary orientations. Future improvements in the catheter design and data

acquisition technology will allow volumetric imaging with enhanced microscopic resolution and at even higher frame rates and should enable a wide range of clinical 3D-OCT endomicroscopy applications.

8.8 Figures

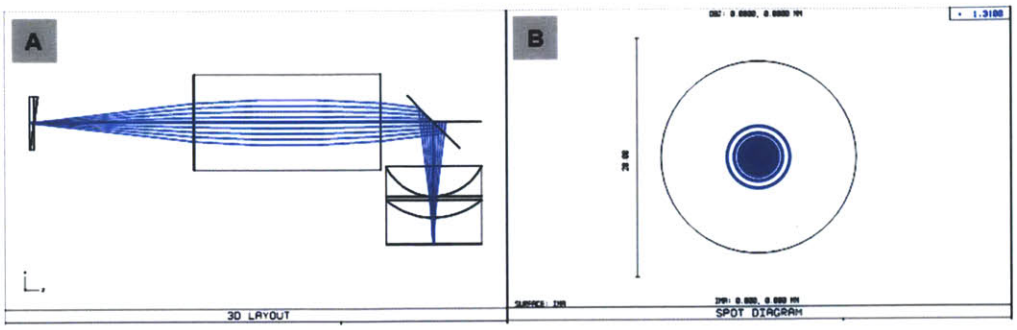

Figure 8.1. ZEMAX model of the optical design of the micromotor-based imaging catheter. (A) 3D layout shows the ray tracing of the optimized design. The model is constructed to achieve minimum spot size on the focal plane by changing the length of the GRIN lens given a pre-determined distances from the fiber to the GRIN lens and from the GRIN lens o the focal plane. (B) Spot diagram at the focal plane, showing the focal spot with 16 um airy disk and 8 um FWHM in tissue.

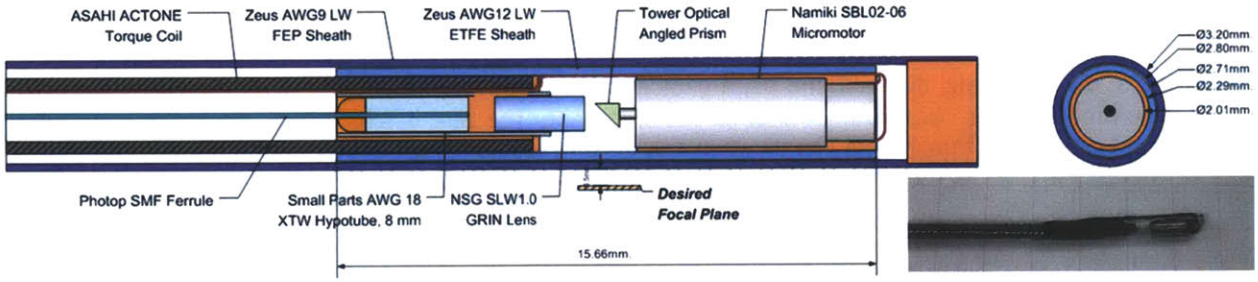

Figure 8.2. Schematic diagrams of the micromotor-based imaging catheter using the dual sheaths design. The inlet shows the photograph of a prototype catheter built based on this design.

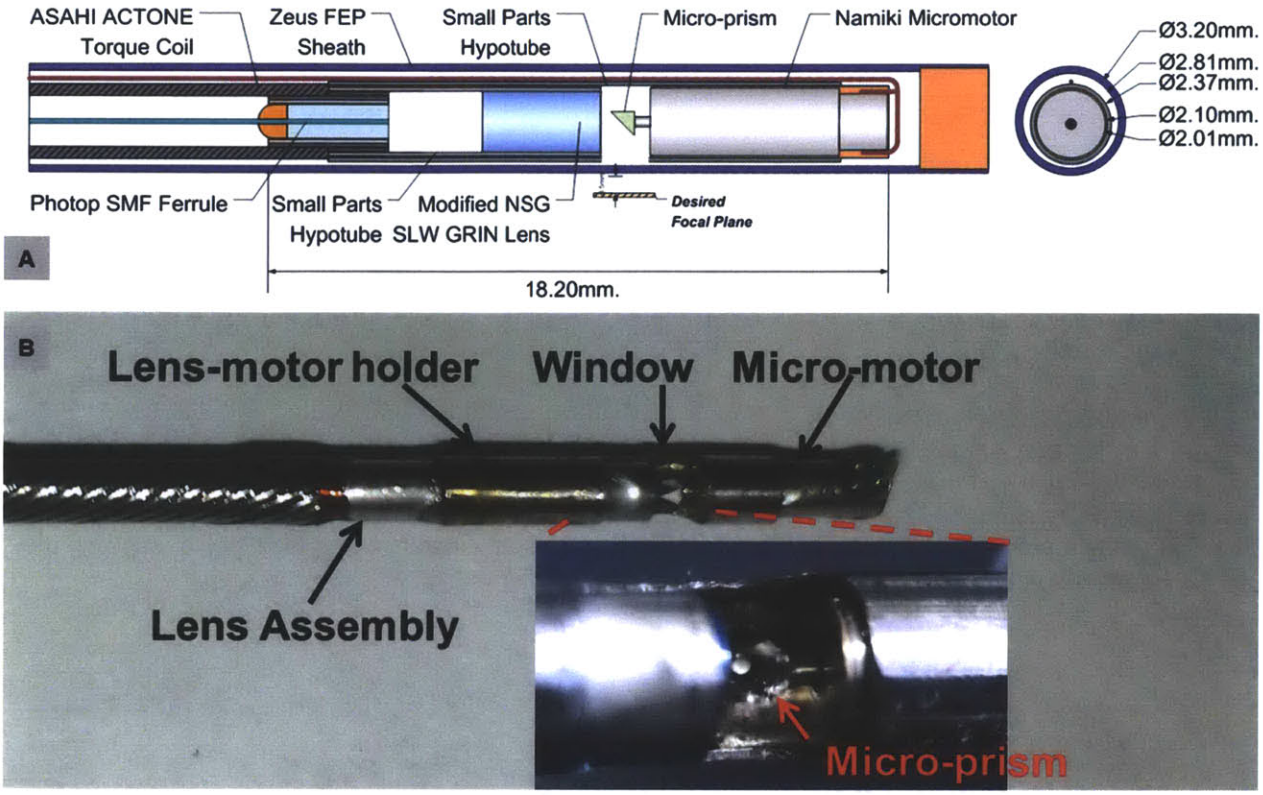

Figure 8.3. (A) Schematic diagram and (B) a photograph of the micromotor probe. The micromotor is held by a hypo tube which is open over 70% of its circumference. The wire is folded back along the hypo tube and it is covered with a transparent sheath when fully assembled. Originally published in [15].

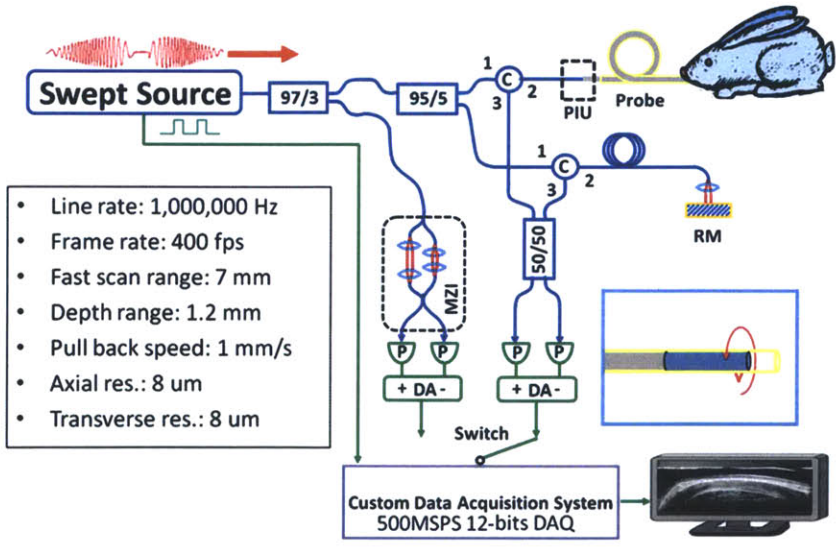

Figure 8.4. Schematic of swept source OCT system (optics: blue; electronics: green) and a summary of the system performance (the depth range, axial resolution, and transverse resolution are the numbers in tissue). The inset showing the catheter indicates the rotary scanning direction of the focused spot. C: circulator; MZI: Mach-Zehnder interferometer; RM: reference mirror; DA: differential amplifier; P: photodetector; PIU: patient interface unit. Originally published in [15].

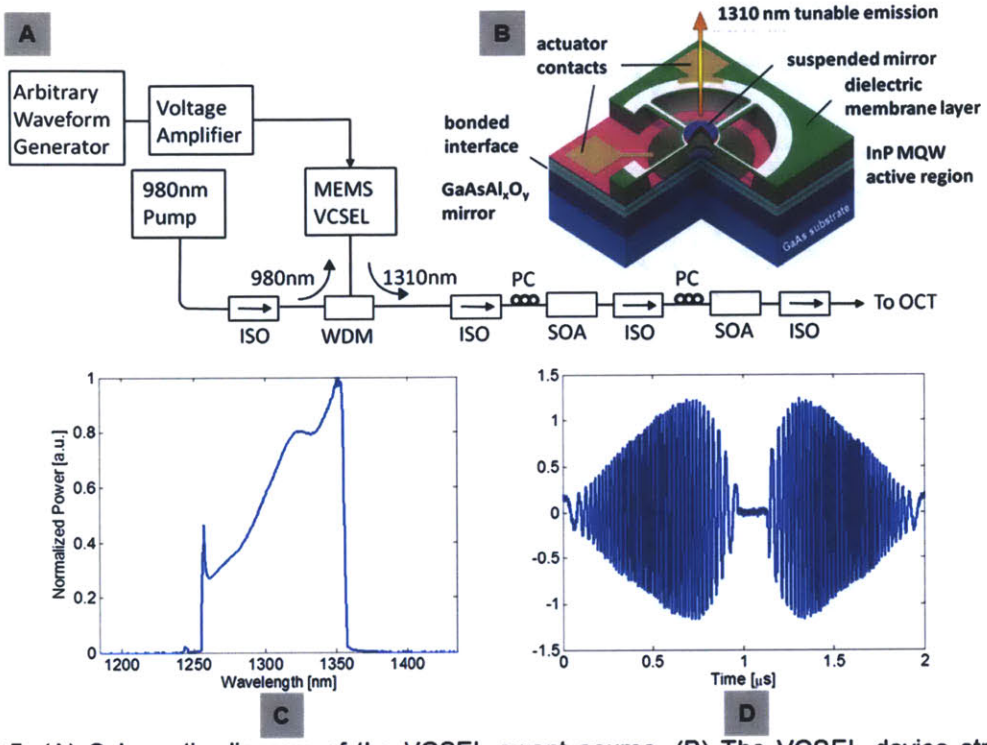

Figure. 8.5. (A) Schematic diagram of the VCSEL swept source. (B) The VCSEL device structure. (C) Optical spectrum of the laser output. (D) Interferometric trace from the Mach-Zehnder interferometer. ISO: optical isolator; WDM: wavelength-division multiplexer; SOA: semiconductor optical amplifier; PC: polarization controller. Originally published in [15].

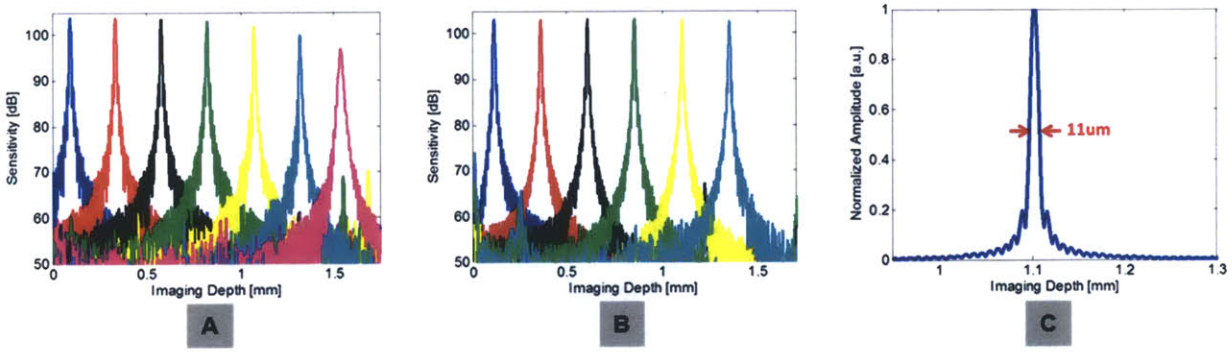

Figure 8.6. (A) Sensitivity roll-off measured using the 500 MSPS A/D card, (B) sensitivity roll-off measured using the 1 GHz oscilloscope, and (C) point spread function of the ultrahigh speed endoscopic OCT system. The point spread function was measured at imaging depth of ~1.1 mm and has 11 um axial resolution, corresponding to 8 um in tissue. Originally published in [15].

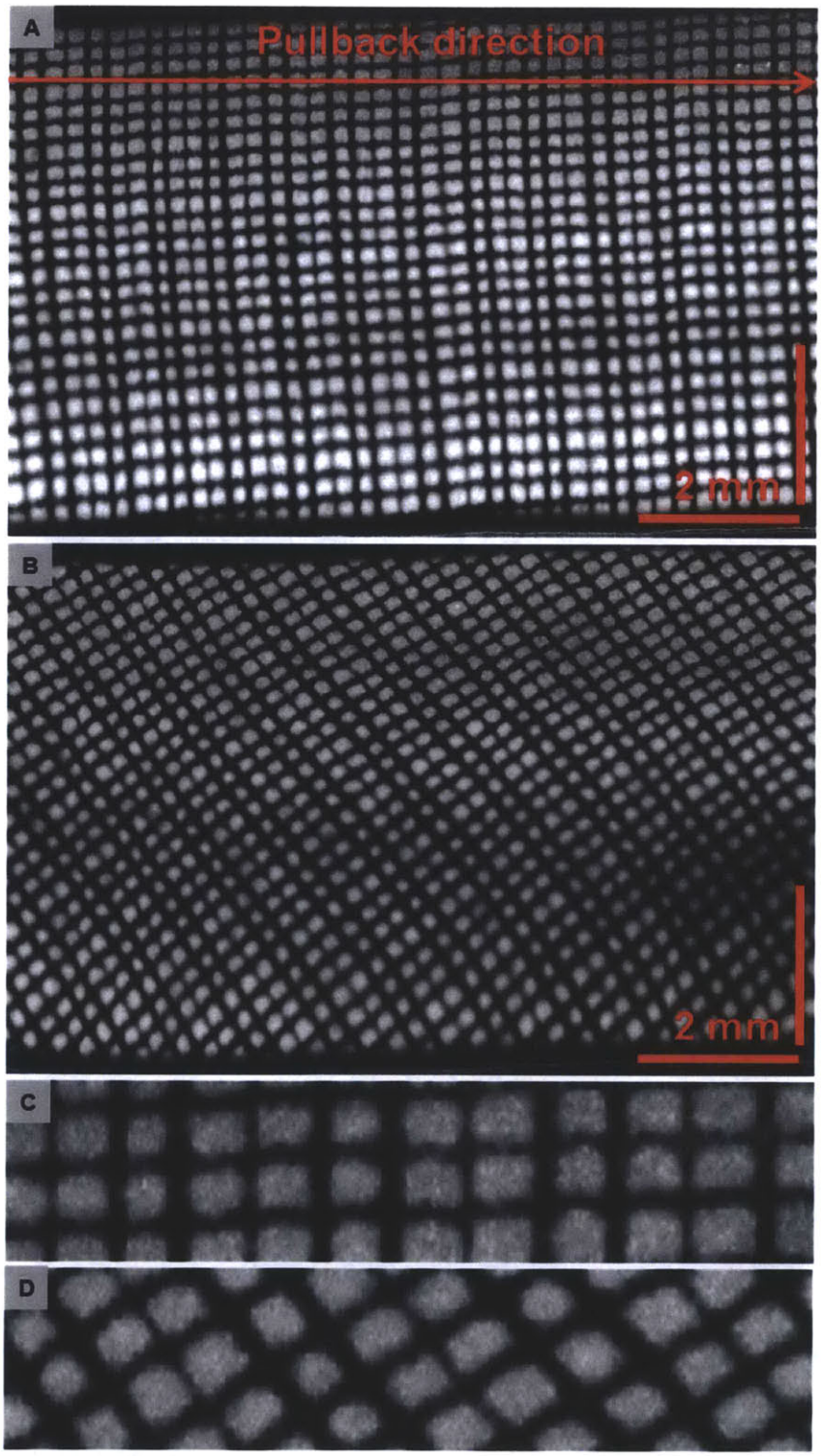

Figure 8.7. (A) *En face* OCT image of the 90° grid pattern acquired with the imaging catheter under 5 cm radius of curvature bending. (B) *En face* OCT image of the 45° grid pattern acquired with the imaging catheter under 5 cm radius of curvature bending. (C) 2x enlarged view of (A). (D) 2x enlarged view of (C).

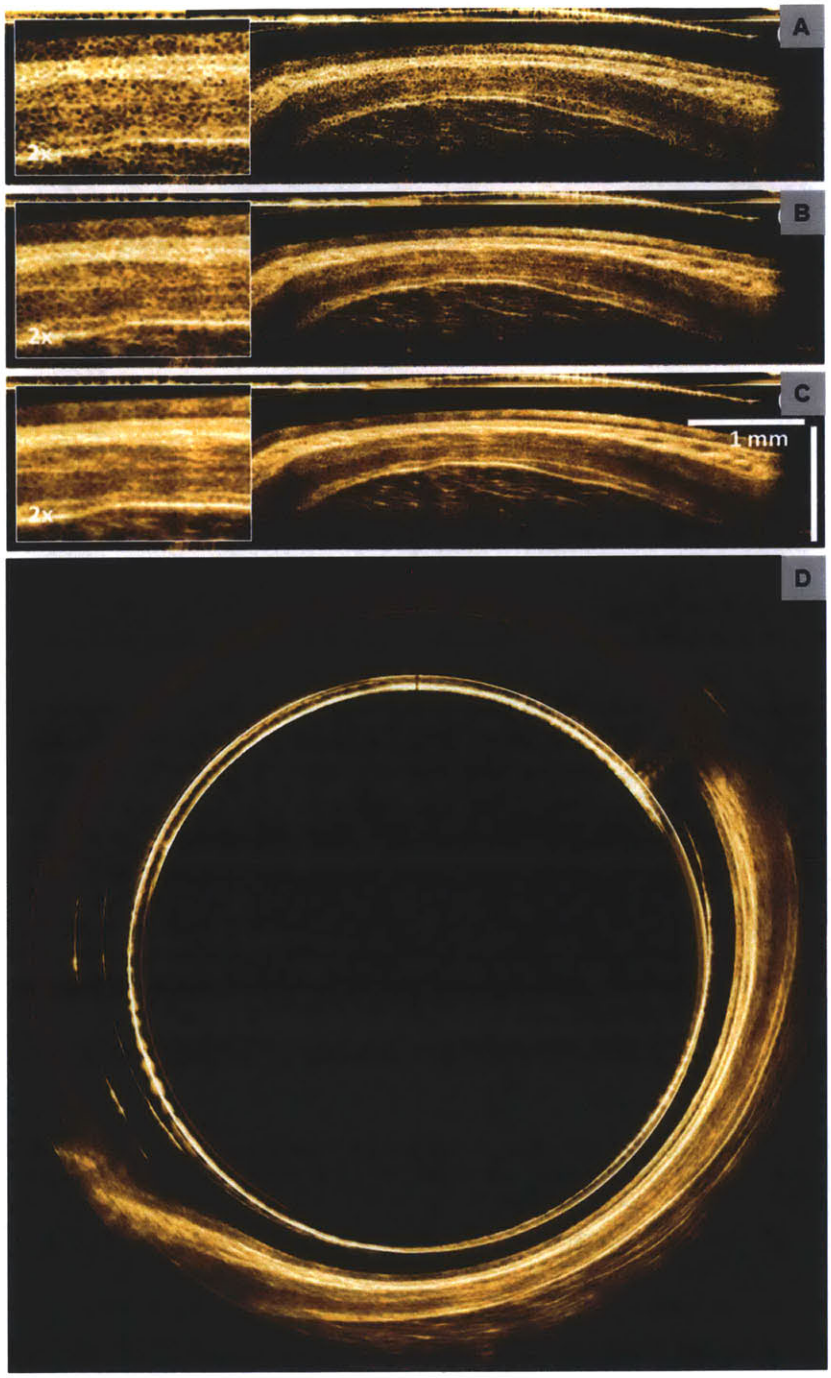

Figure 8.8. Image contrast enhancement by averaging. (A) Single image with 2x enlargement in box on left. (B) Averaged of 2 consecutive images, corresponding to a 5 um pullback distance. (C) Averaged of 4 consecutive images, corresponding to a 10 um pullback distance. (D) The same image as (C) but is displayed in polar form, showing the actual esophagus in contact with the imaging catheter. Originally published in [15].

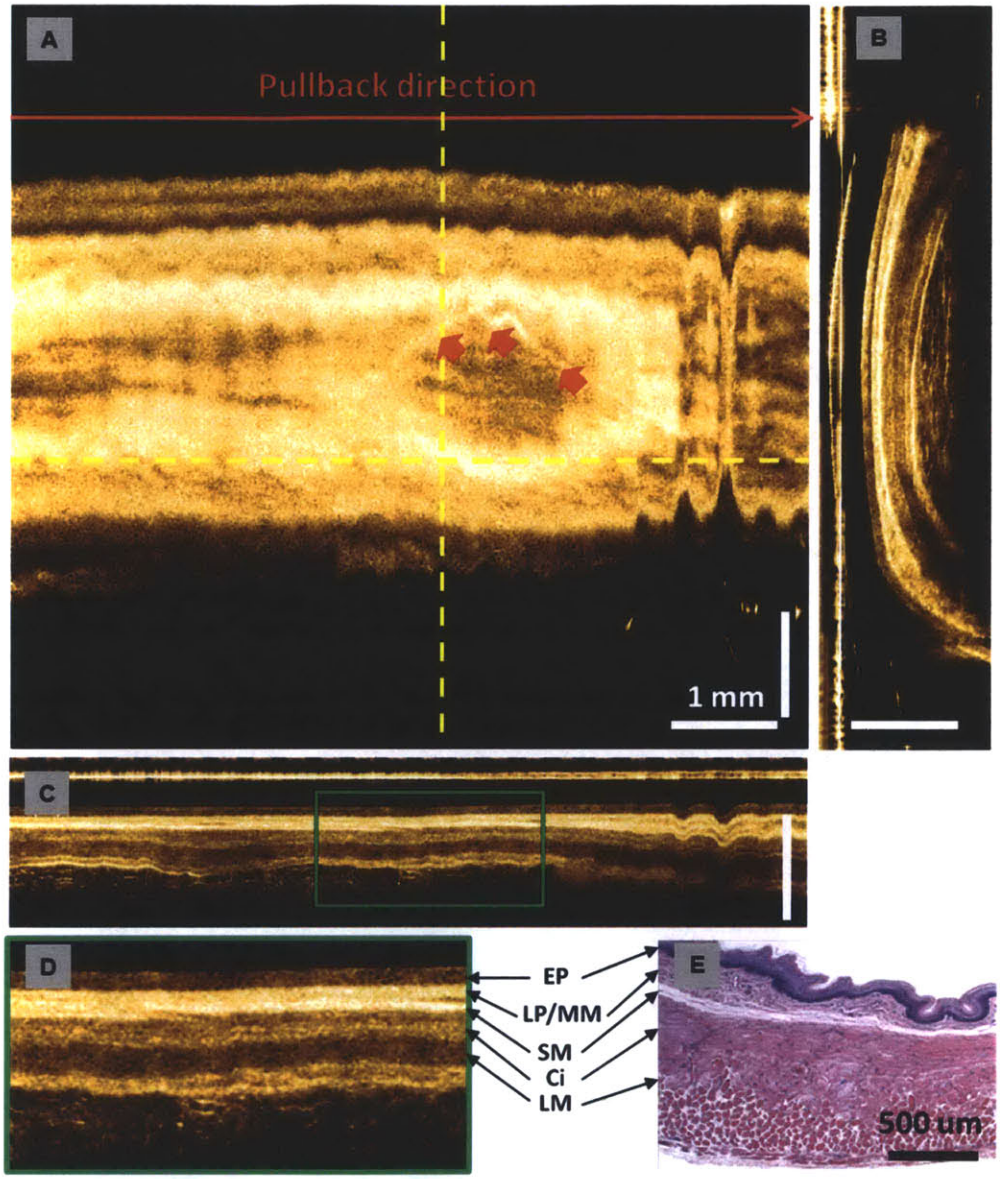

Figure 8.9. *In vivo* volumetric OCT images from rabbit esophagus. (A) *En face* image averaged over 15 um at depth of 190 um. (B) A cross-sectional image transverse to the probe direction averaged over 12 um. (C) Longitudinal cross-sectional image along the pullback direction averaged over 7.5 um. (D) Enlarged view of (C). (E) Representative histology of the rabbit esophagus. Red arrows: blood vessels. Originally published in [15].

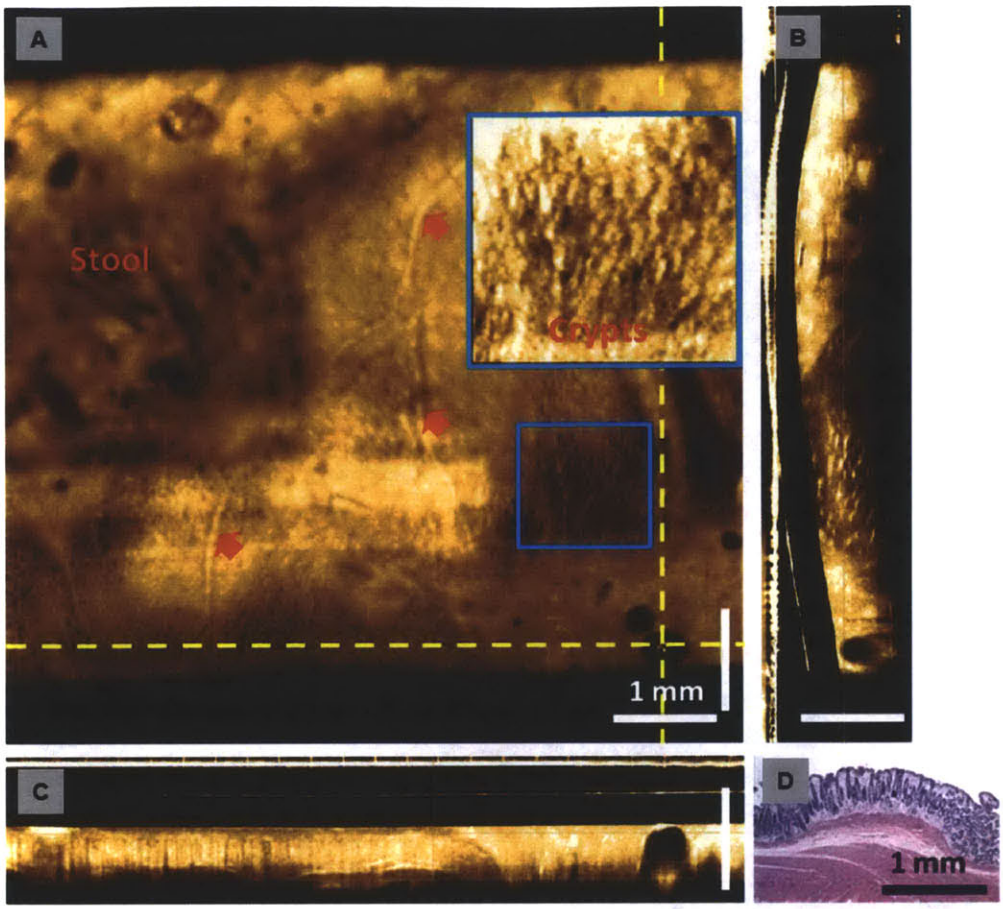

Figure 8.10. *In vivo* volumetric OCT images from rabbit colon. (A) *En face* image at imaging depth of 300 um. (B) Cross-sectional images along the rotary direction. (C) Cross-sectional image along the pullback direction. (D) Representative cross-sectional histology of the rabbit colon with hematoxylin and eosin stain. Red arrows: blood vessels. Originally published in [15].

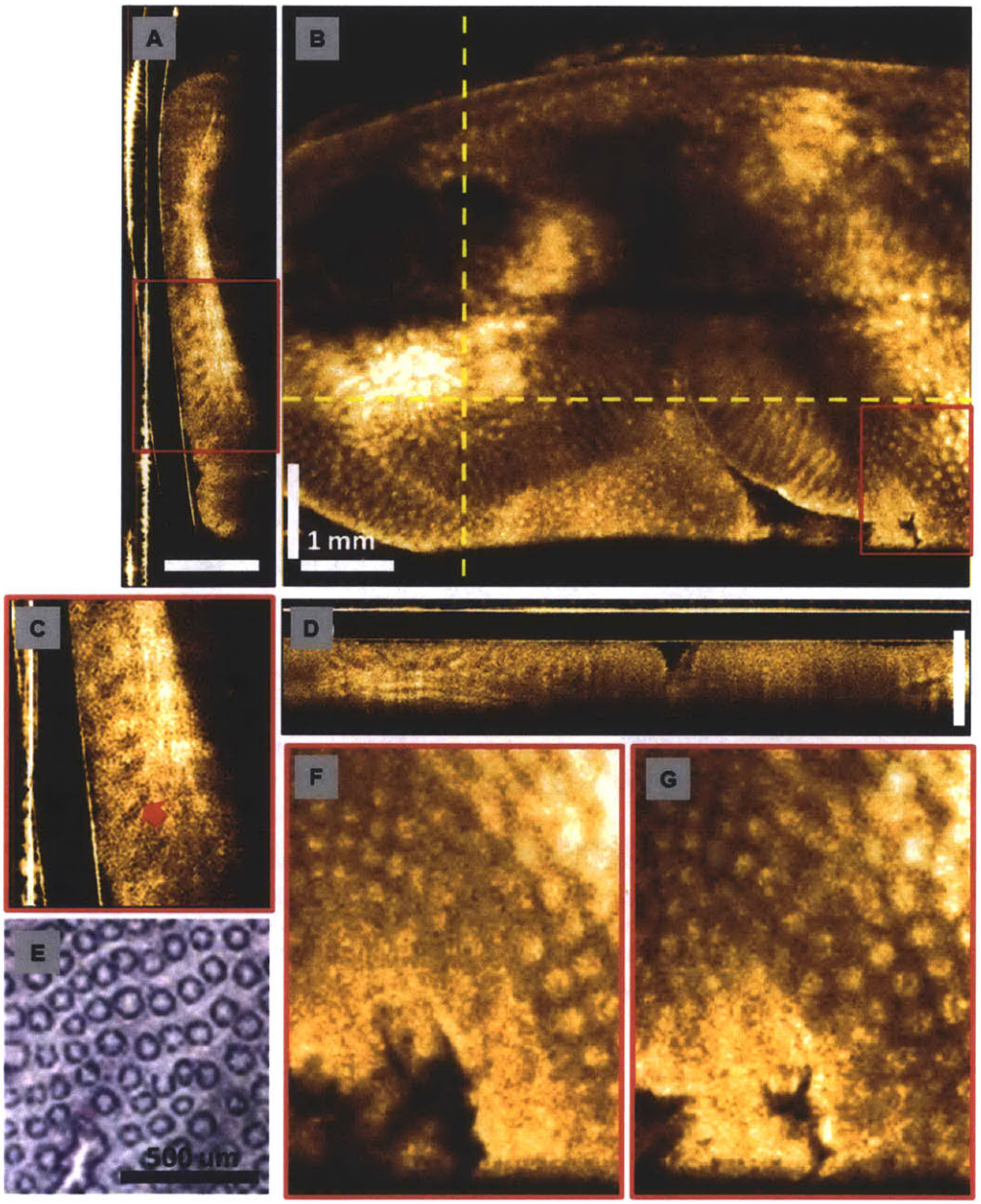

Figure 8.11. *Ex vivo* volumetric OCT images from human colon. (A) Cross-sectional image along the rotary direction. (B) *En face* image at imaging depth of 350 um. (C) Enlarged view of the red box in (A). (D) Cross-sectional image along the pullback direction. (E) Representative *en face* histology of the human colon with hematoxylin and eosin stain. (F, G) Enlarged view of the *en face* image at the same location as the red box in (B) at imaging depths of 250 um and 350 um. Red arrows: crypts. Originally published in [15].

8.9 References

[1] P. R. Herz, Y. Chen, A. D. Aguirre, K. Schneider, P. Hsiung, J. G. Fujimoto, K. Madden, J. Schmitt, J. Goodnow, and C. Petersen, "Micromotor endoscope catheter for in vivo, ultrahigh-resolution optical coherence tomography," *Optics Letters,* vol. 29, pp. 2261-2263, Oct 2004.

[2] P. H. Tran, D. S. Mukai, M. Brenner, and Z. P. Chen, "In vivo endoscopic optical coherence tomography by use of a rotational microelectromechanical system probe," *Optics Letters,* vol. 29, pp. 1236-1238, Jun 2004.

[3] S.-W. Lee, A. E. Heidary, D. Yoon, D. Mukai, T. Ramalingam, S. Mahon, J. Yin, J. Jing, G. Liu, Z. Chen, and M. Brenner, "Quantification of airway thickness changes in smoke-inhalation injury using in-vivo 3-D endoscopic frequency-domain optical coherence tomography," *Biomed. Opt. Express,* vol. 2, pp. 243-254, Feb 2011.

[4] S. Liang, A. Saidi, J. Jing, G. Liu, J. Li, J. Zhang, C. Sun, J. Narula, and Z. Chen, "Intravascular atherosclerotic imaging with combined fluorescence and optical coherence tomography probe based on a double-clad fiber combiner," *Journal of Biomedical Optics,* vol. 17, Jul 2012.

[5] J. Li, M. de Groot, F. Helderman, J. Mo, J. M. A. Daniels, K. Grünberg, T. G. Sutedja, and J. F. de Boer, "High speed miniature motorized endoscopic probe for optical frequency domain imaging," *Opt. Express,* vol. 20, pp. 24132-24138, Oct 2012.

[6] R. Huber, M. Wojtkowski, and J. G. Fujimoto, "Fourier Domain Mode Locking (FDML): A new laser operating regime and applications for optical coherence tomography," *Optics Express,* vol. 14, pp. 3225-3237, Apr 2006.

[7] B. Potsaid, B. Baumann, D. Huang, S. Barry, A. E. Cable, J. S. Schuman, J. S. Duker, and J. G. Fujimoto, "Ultrahigh speed 1050nm swept source / Fourier domain OCT retinal and anterior segment imaging at 100,000 to 400,000 axial scans per second," *Opt. Express,* vol. 18, pp. 20029-20048, Sep 2010.

[8] V. Jayaraman, G. D. Cole, M. Robertson, A. Uddin, and A. Cable, "High-sweep-rate 1310 nm MEMS-VCSEL with 150 nm continuous tuning range," *Electronics Letters,* vol. 48, pp. 867-868, Jul 2012.

[9] I. Grulkowski, J. J. Liu, B. Potsaid, V. Jayaraman, C. D. Lu, J. Jiang, A. E. Cable, J. S. Duker, and J. G. Fujimoto, "Retinal, anterior segment and full eye imaging using ultrahigh speed swept source OCT with vertical-cavity surface emitting lasers," *Biomed. Opt. Express,* vol. 3, pp. 2733-2751, Nov 2012.

[10] T.-H. Tsai, B. Potsaid, M. F. Kraus, C. Zhou, Y. K. Tao, J. Hornegger, and J. G. Fujimoto, "Piezoelectric-transducer-based miniature catheter for ultrahigh-speed endoscopic optical coherence tomography," *Biomed. Opt. Express,* vol. 2, pp. 2438-2448, Aug 2011.

[11] R. Huber, K. Taira, M. Wojtkowski, and J. G. Fujimoto, "Fourier domain mode-locked lasers for swept source OCT imaging at up to 290 kHz scan rates," in *Coherence Domain Optical Methods and Optical Coherence Tomography in Biomedicine X*, San Jose, 2006, pp. 142-147.

[12] D. C. Adler, Y. Chen, R. Huber, J. Schmitt, J. Connolly, and J. G. Fujimoto, "Three-dimensional endomicroscopy using optical coherence tomography," *Nature Photonics,* vol. 1, pp. 709-716, Dec 2007.

[13] B. R. Biedermann, W. Wieser, C. M. Eigenwillig, T. Klein, and R. Huber, "Dispersion, coherence and noise of Fourier domain mode locked lasers," *Optics Express,* vol. 17, pp. 9947-9961, Jun 2009.

[14] W. Choi, B. Potsaid, V. Jayaraman, B. Baumann, I. Grulkowski, J. J. Liu, C. D. Lu, A. E. Cable, D. Huang, J. S. Duker, and J. G. Fujimoto, "Phase-sensitive swept-source optical coherence tomography imaging of the human retina with a vertical cavity surface-emitting laser light source," *Opt. Lett.,* vol. 38, pp. 338-340, Feb 2013.

[15] T.-H. Tsai, B. Potsaid, Y. K. Tao, V. Jayaraman, J. Jiang, P. J. S. Heim, M. F. Kraus, C. Zhou, J. Hornegger, H. Mashimo, A. E. Cable, and J. G. Fujimoto, "Ultrahigh speed endoscopic optical coherence tomography using micromotor imaging catheter and VCSEL technology," *Biomed. Opt. Express,* vol. 4, pp. 1119-1132, Jun 2013.

CHAPTER 9

9.0 Ultrahigh Speed OCT System for Clinical Gastroenterology

9.1 Motivation

Chapter 7 and Chapter 8 have shown the superb scanning stability of the distally actuated imaging catheters compared to the traditional proximally rotary catheters. The imaging stability is important for any clinical application using high speed OCT technology because this ensures the frame-by frame consistency and avoids distortion of the 3D features from the scanning or motion artifacts. Therefore, the yield of high quality volumetric OCT data sets is dramatically improved and more usable information can be revealed in a single data set, which enhances the efficiency of imaging acquisition, processing, and analysis. To translate this technology from the laboratory bench to the patients' bedside, there exist several challenges because the clinical environments require a degree of reliability and robustness in the imaging system. Real-time data acquisition and display are needed to provide continuous feedback to the operator. Reliability, ease of use, and rapid data storage are also required to maintain short procedure times and efficient patient flow. For these reasons, typical bench-top 3D-OCT systems are not suitable for clinical use and must be heavily modified prior to conducting human studies in a clinical environment.

As introduced in Chapter 2, several customized or commercial OCT systems have previously been applied to numerous biomedical applications including gastroenterology [1-6]. Previously, clinical 2D-OCT and 3D-OCT imaging of the gastrointestinal (GI) tract have been demonstrated with high resolution and imaging speeds up to 60 kHz [7-11]. 3D-OCT provides a significant advantage since it allows a larger region of tissue to be analyzed and reduces the risk of failing to detect an abnormal lesion. By modifying a prototype cardiovascular OCT imaging engine developed by Lightlab Imaging Inc. / St. Jude Medical Inc., Prof. Fujimoto's group at MIT recently performed several clinical studies in the GI tract using standard rotary imaging catheters and 3D-OCT imaging with axial line rate of 45 kHz to 60 kHz and axial resolution of 5 μm to 8 μm in tissue, showing a wide range of image analysis and visualization techniques can be applied and resulting in a more complete characterization of tissue microstructure [9, 12, 13]. Researchers at the Massachusetts General Hospital (MGH) also demonstrated the use of balloon based catheters and novel tethered capsules using 3D-OCT imaging with ~50 kHz axial line rate for several clinical applications in the GI tract, allowing the visualization of the full circumference of esophagus in single data set and mapping of different structural features [8, 11, 14]. However, the proximally rotary design used in these studies showed intrinsic instability in the volumetric data sets, especially while the catheters were bent during the acquisition, so the amount of data completely with no motion artifact and can be used for analysis was limited. Furthermore, the rotary catheters cannot be used in the locations that require bending of the catheter such as the stomach wall, duodenum, and most sections of the colon, which also limits the workable regions in the human body using current 3D-OCT systems.

In this section of the thesis work, an ultrahigh speed OCT imaging system was built in collaboration with Praevium Research, Inc. and Thorlabs, Inc., and assistance from members in Prof. Fujimoto's group

mentioned in earlier chapters. Dr. Yuankai Tao and Osman Ahsen helped building the patient interface unit for the clinical imaging. This system enabled clinical studies using endoscopic OCT in the GI tract unprecedented imaging speeds supported by state-of-the-art micromotor, VCSEL, detection, data acquisition, and computation technologies. The light source and data processing system were modified to provide an optimal combination of imaging speed, ranging depth, axial resolution, and sensitivity. This technology development effort produced a ultrahigh speed endoscopic OCT platform that can be used to support clinical pilot studies of a range of human pathologies and improving current treatment modalities. The system will continue to serve this purpose for the foreseeable future.

9.2 System Overview

The system constructed here was a swept-source OCT configuration using a VCSEL original equipment manufacturer (OEM) module produced by Praevium Research, Inc. and Thorlabs, Inc. as the light source. Data acquisition, real-time processing, and display was carried out by a C++ based software originally developed by Prof. Fujimoto's group and modified for the endoscopic applications. Post-processing and image visualization was performed using a combination of purpose-built Matlab software, a public domain image processing software, and a commercial 3D rendering package (Amira, Visage Imaging, Inc.). The imaging catheters used to conduct clinical research are mainly the distally actuated imaging catheters and have been described fully in Chapter 7 and Chapter 8. Preliminary ultrahigh speed endoscopic OCT data used to guide development of the system, signal processing, and visualization methods was acquired using the micromotor-based imaging catheter, also described in Chapter 8.

To be practical in a clinical setting, an endoscopic OCT imaging system must provide continuous real-time data capture and display with dense spatial sampling. Extremely large data sets must be digitized, transferred to computer memory, processed, and displayed in milliseconds. The OCT imaging engine developed here operated at a sustained speed compatible with the VCSEL by using an optical frequency clock (OFC) integrated with a 1.8 GSPS 12 bit analog-to-digital (A/D) converter. The prototype OFC circuitry was designed and constructed by Thorlabs, Inc. OFC optimization for use with the VCSEL was carried out as part of this thesis work as described in Section 9.4.

The formation of OCT images from frequency domain interference fringes requires the interference signal to be evenly spaced in optical frequency ν prior to Fourier transformation [15, 16]. Since the frequency sweeps of the VCSEL are not linear in time, it needs to be calibrated to correct for this effect. One typical approach, referred as the software calibration method, is to acquire a reference interference fringes simultaneously with the OCT signal. The ν evolution of the reference signal can be analyzed and used to later correct the ν spacing of the OCT signal [15, 17]. The software calibration has the disadvantages of doubling the required DAQ bandwidth since two signals must be captured, requiring

signal post-processing to correct the OCT data and limiting real-time operation. The OCT imaging system developed here used an optical triggering technique to automatically correct for nonlinear ν spacing during the data acquisition without storing a separate reference signal. **Figure 9.1** shows a schematic diagram of the system. A small portion (5%) of the laser output was coupled to an asymmetric Mach-Zehnder interferometer (MZI) that produces interference fringes with zero crossings evenly spaced in ν domain. This concept is shown in the left inset of **Figure 9.1**. The MZI fringes are detected by a dual-balanced photodetector and the zero crossings are identified by an analog voltage comparator in the clock generator, creating a digital pulse train that functions as an OFC. The OFC is synchronized to the start of each laser sweep by a trigger signal from the function generator that generates the driving waveform to operate the VCSEL.

A dual-balanced Michelson interferometer consisting of a pair of optical circulators and a 50/50 fiberoptic splitter was used to generate the OCT interference fringes. Dual-balanced detection cancels excess noise, reducing the dynamic range requirement of the DAQ system and increasing the sensitivity. The same frequency sweep from the laser generated both the MZI and OCT fringes, so the spacing of the OFC pulses corresponded to evenly spaced ν intervals in the OCT signal. The OFC triggers the A/D card with 12 bit and 1 GSPS that samples the OCT fringes. Since the resulting signal is evenly spaced in ν, only the acquired OCT signal needed to be digitized and stored, and no calibration process was required for ν correction. The sample arm of the Michelson interferometer included a Patient Interface Unit (PIU), designed and prototyped by the MIT group, that produced linear pullback motion at 0.2 – 2.0 mm/s. The PIU was attached to the proximal end of the imaging catheter and can pullback the distal tip of the catheter, which generates the scan in the second dimension and producing 3D-OCT imaging.

After digitization, the OCT signal was continuously streamed to the computer DDR3 SDRAM at a peak transfer rate of 12.8 GB/s. A fast Fourier transform (FFT) was then performed directly on the OCT fringe data in software to synthesize the image. Each frame was display in Cartesian coordinates as a rectangular image in real-time at > 32 frames per second (fps). During 3D acquisition, sustained acquisition rates of 1 GHz were achieved while maintaining real-time display. **Figure 9.2** shows the photograph of the full ultrahigh speed OCT imaging system for clinical use. The bottom level of the cart is the personal computer of the imaging system. On the second level of the cart is the swept laser, including the VCSEL module, drivers and the function generator that are used to control the VCSEL. On the top level are the MZI, the OCT interferometer, and the OFC generation circuitry. On top of the cart are the monitor, a keyboard and a mouse for the operators to control the system.

9.3 Light Source Selection and Optimization

The swept laser source was a key component of the endoscopic OCT imaging system. Laser performance directly affects imaging performance and therefore careful selection of each swept laser design was necessary to ensure optimal clinical utility. Fourier domain mode-locked (FDML) lasers have been used in several clinical systems and showed 3D imaging capability in the coronary vessel and the GI tract. Due to the dispersion in the long fiber cavity, the instantaneous linewidth of FDML lasers is limited and a 5~10 dB sensitivity drop over a 3 mm depth range was reported [9, 18-20]. For OCT imaging applications, it is desirable to have more uniform imaging sensitivity over a large depth range.

In Chapter 7 and Chapter 8, both the FDML laser technology and the recently developed VCSEL technology were used to perform high speed imaging and it was found that VCSEL can provide much longer coherent length and more flexible operation in terms of sweep rate and tuning range. Therefore, the endoscopic OCT imaging system developed here was using a VCSEL OEM module manufactured by Praevium Research, Inc. and Thorlabs, Inc. **Figure 9.3** shows a schematic diagram of the VCSEL used in the ultrahigh speed endoscopic OCT system and its basic specifications. A VCSEL chip with central wavelength of 1,310 nm, a wavelength-division multiplexing (WDM) coupler, and a pump laser with wavelength of 976 nm were packaged in the module and all the components were controlled by the drivers via one 15-pin D-Sub cable (DB15). As shown in **Fig. 9.3B**, the MEMS-tunable filter of the VCSEL had a resonant frequency around 325 kHz and can be driven with a broad range of operation frequency from 100 kHz to 500 kHz, corresponding to an bi-directional sweep rate from 200 kHz to 1 MHz. It is possible to operate the laser at sweep rates higher than 1 MHz but, as described in Section 9.3.1, a lower sweep rate resulted in optimal imaging performance for the human GI tract. The nominal maximum tuning range of the laser was 115 nm, as shown in **Fig. 9.3C**.

The semiconductor optical amplifier (SOA) chip was a high-gain, broadband, polarization-sensitive device that can provide a gain bandwidth > 90 nm (full width at half maximum, FWHM) and amplified spontaneous emission (ASE) power of > 10 mW, which was used as a booster amplification stage for VCSEL. The output from the VCSEL cavity went through an optical isolator to avoid feedback from the system reflection and the polarization of the output was controlled to provide maximum tuning range while maintaining a post-booster output power that was sufficiently high to reach the tissue exposure limit of 20 mW after transmission through the OCT interferometer and the imaging catheter. With proper polarization adjustment, the total tuning range was >100 nm and the average output power after booster amplification was 60 mW. Power output directly from the VCSEL cavity was ~150 μW.

Figure 9.4 shows a series of point spread function (PSF) measured by connecting the VCSEL operating at 500 kHz to an unbalanced MZI and varying the path imbalance. Data was collected using a digital oscilloscope with bandwidth of 1 GHz and the backward sweep was used for analysis. Sweep recalibration and Fourier transformation was performed offline using Matlab software with the same

method described in Chapter 7 and 8. A reference fringe at an MZI delay of 1 mm was used to recalibrate all of the other fringes in the data set. It is generally not advisable to use a MZI delay that generates interference fringe with frequency close to the bandwidth limit of the instruments used in the measurement, due to the decreased coherence length, and degradation of the signal intensity and fringe contrast. Use of extremely short delays (< 100 μm) is also not advisable due to an insufficient number of fringe cycles to calculate an accurate phase evolution curve. This measurement gives the axial resolution and sensitivity roll off supported by the laser without taking into account the effects of the OFC and real-time data processing algorithms used in the complete endoscopic OCT imaging system. Sensitivity rolls off by 2 dB at an imaging depth of 3.1 mm in air and the FWHM of the PSF is 11 μm on a linear scale, corresponding to an axial resolution of 8 μm in tissue. It should be noted that the sensitivity roll off and axial resolution specifications for the entire system are slightly different compared to the values supported by the laser itself, as described in Section 9.6, due to the effects of the OFC, DAQ card, and real-time data processing methods.

9.3.1 Tuning Range

The tuning range of the VCSEL determines the axial resolution of the endoscopic OCT imaging system. A broader tuning range results in better resolution, which requires the length of the Fabry-Perot cavity varying a broader range. In order to perform high sweep rate operation, the Fabry-Perot cavity also needs to be short enough to allow lasing quickly. The MEMS tunable filter in the VCSEL is driven by electrostatic force [21-24], which can be written as

$$F = \frac{1}{4\pi\varepsilon_0}\frac{q_1 q_2}{r^2} \tag{9.1}$$

where q_1 and q_2 are the charges of the two objects, r is the distance between the two objects, and ε_0 is the permittivity constant. The electrostatic force becomes extremely large when the two objects, that is, the two mirror surfaces in the MEMS tunable filter are too close to each other. "Snap-down" of the filter can occur when the force is large enough to move the surfaces in contact and the filter would not be able to move until the electrostatic charges are gradually neutralized. Although the VCSELs are engineered to prevent permanent damage to the mirrors when "snap-down" happens, the VCSELs still require days to recover from the fully charged condition, which is not ideal for clinical applications. Increasing the tuning range of the VCSEL increases the chance of "snap-down" of the filter, so the trade-off between the VCSEL stability and the wavelength tuning range needs to be carefully managed to achieve the optimal performance.

Another issue need to be considered is that, the output from the VCSEL can have high amplitude on both sides of the sweep when the tuning range is much narrower than the emission bandwidth of the

VCSEL. If there are sharp edges in the laser sweeps, those edges will be transformed into high sidelobes in the PSFs. **Figure 9.5** shows examples of the sidelobe effect in the PSFs caused by different amplitude on the edges of the sweep. The interference fringes were generated by connecting the VCSEL to an unbalanced MZI with a fixed path imbalance. When operating the VCSEL with tuning range of 100 nm, the resulting interference fringes in **Fig. 9.5A** have high amplitude on both sides of the sweep, and the corresponding PSF shows ~20% sidelobes compared to the main lobe (**Fig. 9.5B**). Higher sidelobes can degrade the image quality since OCT images typically are displayed in LOG scale and the sidelobes can be easily observed next to the main reflection peak, causing blurring effect and difficult to identify detailed structural features. The sidelobes can be suppressed by post-processing techniques such as spectral shaping or windowing, but these techniques also make the PSF wider because the bandwidth is effectively narrowed during the numerical suppression of the edges of the sweeps. The other method is increasing the tuning range to cover the full emission bandwidth of the laser. As shown in **Fig. 9.5C**, when the tuning range is increased to 120 nm, which is comparable with the VCSEL emission bandwidth, the edges of interference fringes have reduced. In this case, the PSF shown in **Fig. 9.5D** has much lower sidelobes and slightly better axial resolution. The computational efficiency can also be further improved without the need of spectral shaping.

The tuning range of the VCSEL used in the clinical system was chosen to be ~120 nm to maintain lower edges in the sweep. **Figure 9.6** shows the optical spectrum of the post-amplified laser output measured by the optical spectral analyzer. The peaks shown on both side of the spectrum indicate the accumulating power on the spectrometer at the turnaround points of the sine-wave-driven MEMS tunable filter, corresponding to the lowest frequency portion of the interference fringe observed in **Fig. 9.5C**.

9.3.2 Sweep Rate

The sweep rate of the VCSEL directly determines the imaging speed of the endoscopic OCT imaging system. Although higher imaging speeds are desirable to maximize the sampling density and minimize motion artifacts, imaging speed also trades off against ranging depth and sensitivity. As the sweep rate increases, the frequency associate with the interference fringe generated at a fixed imaging depth increases in direct proportion. From Equation (1.11) in Chapter 1, the maximum ranging depth $z_{\max}$ can be calculated from the sampling rate of the digitizer (F_s), duty cycle of the sweep (D), group refractive index of the sample medium (n_s), optical frequency tuning range of the laser (Δf), and the sweep rate of the swept source (f_{SS}), assuming the laser sweep in linear in frequency domain.

$$z_{\max} = \frac{F_s \cdot c \cdot D}{4 n_s \cdot \Delta f \cdot f_{SS}} \tag{9.2}$$

The VCSEL used in the clinical system was operated at 1,310 nm with a tuning range of 120 nm, corresponding to an optical frequency tuning range of 1.926×10^{13} Hz. If the sweep is assumed to occupy 50% of the VCSEL driving period and the signal is digitized with sampling frequency of 1 GHz, a driving frequency of 300 kHz and 500 kHz give a maximum ranging depth of 5.9 mm and 3.6 mm in air, respectively. Since the VCSEL was driven by sinusoidal wave, the actual maximum fringe frequency is usually higher than the fringe frequency of the linear sweep by a factor of $\pi/2$, making the effective ranging depth shorter than the calculation. Since most applications require a ranging depth of at least 1.5 mm in tissue in addition to the 1.6 mm radius of the imaging catheter (total range of ~3.9 mm in air), an effective sweep rate lower than 300 kHz is a suitable operation point. Some other applications such as balloon imaging and anatomic imaging may require even longer ranging depth, so lower sweep rates are needed for those long range applications. Note that this is a rough approximation and assumes no wavelength dependence in coherence length.

Figure 9.7 shows a comparison of interference fringes from MZI taken with different VCSEL operation sweep rates. The resonant frequency of the MEMS tunable filter is at 325 kHz so the filter tunes symmetrically around the resonant frequency (**Figs. 9.7A and B**). However, if the operation frequency is lower than the resonant frequency too much, the filter would start tuning asymmetrically, as shown in **Fig. 9.7C**. Asymmetry causes different performance in the forward and backward sweeps, and the effect becomes more severe when the fringe frequency is closer to the Nyquist limit, which prevents the use of bi-directional operation and loses one half of the imaging speed. On the other hand, when the operation frequency is higher than resonant frequency, the filter can also provide more symmetric tuning compared to that of lower sweep rat, indicating operation at higher sweep rate is possible in the future using VCSEL technology. **Table 9.1** shows a summary of laser performance at different operation frequency. Note that the tuning range is independent from the operation frequency, also demonstrating the flexibility of the VCSEL operation. In this clinical system, the operation frequency was chosen to be 300 kHz, corresponding to an effective sweep rate of 600 kHz to achieve both sufficient imaging depth as well as symmetric sweep performance.

Table 9.1 Comparison between different VCSEL operation frequencies.

Operation Frequency	**500 kHz**	**350 kHz**	**300 kHz**	**250 kHz**
Sweep symmetry	Symmetric	Symmetric	Symmetric	Asymmetric
Tuning range [nm]	120	120	120	120
Axial resolution [μm]	11	11	11	11
Imaging range [mm]@1 GSPS	1.8	2.8	3.3	3.6

9.4 Optical Frequency Clock Optimization

The OFC used in the endoscopic OCT imaging system is a unique way to enable real-time imaging at speeds up to 1,000,000 axial lines per second by removing the requirement to sample a second interference individually to recalibrate the OCT data. Since most of the sweep lasers are operated with sinusoidal driving waveform, the OFC must be used to remove residual ν nonlinearity in the sweep to provide optimal axial resolution and minimal sidelobe levels. Although the OFC is extremely useful, it is important and requires additional care to set up correctly especially under high speed operation. Since all the OCT raw data sets are stored after optical frequency clocked, all data sets are not recoverable if they are clocked incorrectly. There are two scenarios that incorrect OFC can happen. First, the path lengths between the MZI and OCT interferometer are not matched, which causes unevenly ν space in acquired OCT data. Second, instability of OFC from bandwidth limitation of the acquisition hardware can cause the loss of samples in the OCT data. The configuration details are described below.

9.4.1 Path Length Match between MZI and OCT Interferometers

As described in Section 9.2, the OFC uses an unbalanced MZI and analog electronics to generate one digital clock pulse every time the MZI interference signal crosses 0V. These zero crossings are evenly spaced in optical frequency ν so the OFC ensures that the OCT signal is sampled at evenly-spaced ν intervals, as shown in **Figure 9.8**. Hence it is important to make sure that the MZI and OCT signals start at exactly the same time. Any timing difference between the MZI and OCT signals produces uneven ν space and the resulting PSF is no longer narrow and become asymmetric. **Figure 9.9** shows examples of ν spacing and PSFs when the MZI signal/OFC starts earlier than, later than, and exactly the same time as the OCT signal from a fixed reflective surface. The ν spacing is presented as the unwrapped phase of the OCT trace after OFC, which is obtained by applying Hilbert transform on the trace and extracting its phase information. Only when the MZI and OCT signals start at the same time, the phase is linear and the PSF is not distorted.

Based on the characteristic shown in **Figure 9.9**, the timing mismatch of the MZI and OCT signals can be recognized and can be corrected by adding optical fiber (for larger scale time difference, $\geq$ 5 ns) or electrical cable length (for smaller scale time difference, $<$ 5 ns) to the interferometer where its sweep signal start earlier. Large-scale timing mismatch usually happens due to longer optical fiber length in the OCT interferometer, which involves the imaging devices such as endoscopic imaging catheters. After correcting the large-scale timing mismatch, short electrical cables shorter than 50 cm can be used for fine adjustment of the path length mismatch. The linearity of the optical clocked OCT data can also be examined by overlapping the PSF of the acquired data with the FFT of its envelope. Since the envelope is

a real function, the FFT result would show perfectly symmetric PSF, so any nonlinearity in the optical clocked data can be easily distinguished by direct comparing the two PSFs. **Figure 9.10** shows the PSF generated from the optical clocked OCT signal acquired using the clinical system, which overlapped perfectly with the FFT of its envelope, indicating the path length was matched well in the system.

9.4.2 Stable Configuration of High Speed OFC

The path imbalance in the MZI determines the maximum imaging depth of the system. The OFC generates exactly one sample clock for every MZI interference fringe period. Therefore Nyquist-limited sampling is achieved for OCT signal frequencies equal to one half of the MZI fringe frequency, so maximum imaging range is one half of the MZI path imbalance. For sample ranges higher than the half of the MZI path imbalance, the OCT signal would be under-sampled and aliasing would occur. The aliasing can be prevented by placing an anti-aliasing lowpass filter in the A/D circuitry once the maximum OFC frequency is determined.

As mentioned earlier, the VCSEL was driven with sinusoidal waveform so the sweep is highly nonlinear and the frequency variation within single MZI interference fringe can easily span from 30 MHz to more than 1 GHz. This high nonlinearity limits the maximum MZI frequency that can be used for OFC to trigger the commercially available high speed A/D card. The A/D card used in the endoscopic OCT system was manufactured by AlazarTech, Inc. and can support up to 1.8 GSPS sampling rate with its internal clocking. The A/D card also supports the external clock function that allows the use of MZI/OFC signal as a reference to sample the OCT data. With the nonlinear nature of the MZI/OFC signal, this A/D card was found randomly missing samples if the maximum frequency of the MZI interference fringe was higher than 1.1 GHz. **Figure 9.11** shows the sample-missing effect when using a MZI/OFC signal with 1.1 GHz maximum fringe frequency as the source of the external clock to sample the OCT signals generated from reflection at different imaging depth. The sample-missing effect was not apparent when the OCT signals came from shorter imaging depth, but became severe when the imaging depth closer to the maximum ranging depth, where the frequency of the OCT signal was very close to the Nyquist limit. The optical clocked OCT trace showed discontinuity and the resulting PSF had higher sidelobes than others. This instability of OFC can potentially generate incorrect samples in the OCT data sets, which are not reliable for further analysis, especially for applications that require high phase stability such as Doppler OCT and phase-sensitive OCT.

To ensure the OFC can be reliably used in the clinical system, a series of characterizations can be performed. First, the stable external clock operation is achieved when the OCT signal generated from the reflection outside of the maximum imaging range can be correctly clocked. The under-sampled/aliasing signal is extremely sensitive to any missing sample so its PSF would become distorted or have much

higher sidelobes due to unstable external clock. **Figure 9.12** shows a series of PSFs generated from reflection at different imaging range across the maximum ranging depth. Symmetric PSFs with consistent level of sidelobes indicate the MZI/OFC frequency for stable external clock. The performance of the OFC can be further evaluated by recording a large amount of consecutive PSFs from the same imaging depth to ensure the stability of the optical clock. **Figure 9.13** shows overlapping PSFs obtained from consecutive 20,000 OCT interference fringe from a fixed reflective surface with maximum OFC frequency of 1.04 GHz. All PSFs appear to be almost identical, indicating the OFC works correctly. In this endoscopic OCT imaging system, the maximum MZI/OFC frequency was found to be 1.04 GHz for a long term and stable external clock using the AlazarTech A/D card.

9.5 System Characterization

The light source, OFC, and A/D configurations determine the basic performance of the endoscopic OCT imaging system. In reality, the overall performance of the system including axial resolution, sensitivity, and sensitivity roll off can be different from the values supported by the light source itself. The transmission, coupling efficiency, and the possible dispersion mismatch introduced by the imaging catheter can significantly affect the actual performance of the imaging system. The true resolvable feature size or "true resolution" of the system is also a function of the spatial sampling density in addition to the optical resolution determined by the laser tuning range and the imaging catheter spot size. The characterization of the full system performance is described as below.

9.5.1 Axial Resolution

Axial resolution was measured by placing a metallic mirror around the focal plane of the imaging catheter and a fiberoptic neutral density filter in the sample arm. The mirror provides a point reflection at an adjustable position away from the imaging catheter, while the fiber provides 35 dB of double-pass attenuation to prevent detector saturation. The MZI was set to a path mismatch of 6.6 mm to generate a maximum OFC frequency of 1.04 GHz, corresponding to a 3.3 mm maximum imaging range typically used for the clinical studies. The resulting OCT interference signal was captured by the A/D card and converted to a linear PSF in real time using the system's signal processing software. The linear PSF at an imaging depth of 1.43 mm is shown in **Figure 9.14**. The PSF is symmetric and the FWHM of the linear PSF is 11 μm in air, which is the same as the value measured with the VCSEL alone, indicating there is no degradation caused by the dispersion mismatch in the imaging catheter and no instability of the OFC. The corresponding axial resolution in tissue is 8 μm for the full system. The sidelobes of the PSF is less than 10% without the need of spectral shaping.

9.5.2 Sensitivity and Roll Off

The sensitivity measurement was similar to the method used in Chapter 7 and 8. System sensitivity was measured using the similar sample arm setup as described in Section 9.5.1. Optical power coming out of the imaging catheter was ~20 mW and the same -35 dB attenuation was used to prevent the detector saturation. Sensitivity was obtained as the ratio of the peak signal values of the PSF at a short imaging depth (~0.5 mm) to the standard deviation of the system noise floor recorded with the sample arm blocked. The measured sensitivity was -101 dB. The theoretical shot-noise limited sensitivity for sweep duration of 1.67 ms, 20 mW of power on the sample, and 100% detector sensitivity is -107 dB from Equation 1.9. The estimated system losses were ~5dB arising from the losses in the optics, PIU, mirror reflectivity, and backcoupling, which accounted for the variation in sensitivity away from the shot-noise limited value.

Sensitivity roll off for the full system was measured by translating the mirror in the reference arm away and recording a PSF at each new position. The measurement results are shown in **Figure 9.15**. There is no significant roll off can be observed in the full system across the whole imaging depth, indicating the detection and A/D bandwidth of the acquisition hardware was broad enough to support the 500 MHz Nyquist frequency of the current MZI/OFC configuration. The extremely low sensitivity roll off can potentially introduce unwanted signal if there is any highly reflective surface within the sample arm, such as the GRIN lens surfaces. This reflection can generate high frequency interference signal that is aliased into the acquired OCT data and creates line artifacts in the images. As mentioned in Section 9.4.2, these effects can be eliminated by applying an anti-aliasing lowpass filter.

9.5.3 Spatial Sampling Density

Theoretically the optical resolution, determined by the focal spot size of the imaging catheter and the FWHM of the axial PSF, defines smallest distance between two spots that the system can distinguished. Any features that smaller than the optical resolution cannot be resolved using the imaging system. On the other hand, spatial sampling refers to the physical distance between the pixels in the digitized images, that is, the distance between consecutive axial scans in the fast scan direction and consecutive frames in the slow scan direction. Spatial sampling density in the axial direction can be arbitrarily set by selecting the length of Fourier transform in the signal processing step.

In order to make the most of the optical resolution of the system, the sampling density should be sufficient. According to the Nyquist criterion, at least two spatial samples in each dimension are required to truly resolve the features close to the level of optical resolution. For the endoscopic OCT imaging system reported here, the optical resolution is tissue in 8 x 8 x 8 μm (fast scan x pullback scan x axial direction), so the spatial samples should be acquired every 4 x 4 x 4 μm (fast scan x pullback scan x axial direction). The spatial sampling density in the transverse directions is fundamentally limited by the

imaging speed, tissue surface area, and maximum imaging duration. The surface area is determined by the imaging probe dimensions and tissue anatomy of interest, while the imaging duration is determined by the memory size of the imaging system. Hence the only parameter available for adjusting the spatial sampling density is imaging speed. Therefore, the high imaging speeds, which determined by the axial line rate of the light source and acquisition speed of the data acquisition system are required to obtain true optical resolution using the OCT system.

The transverse spatial sampling density of the imaging system developed here could be adjusted by varying the micromotor rotation speed and pullback speed. To obtain a reasonable tradeoff between spatial sampling density and field of view, the rotational speed is typically set to 400 Hz (24,000 rpm) and the pullback speed to 2.0 mm/s. With effective axial line rate at 600 kHz, this provided 1,500 lines per frame with 5 μm between consecutive frames. The pixel spacing in the frame was approximately 6.7 μm, given an average imaging depth of 1.5 mm in tissue (70% of the maximum imaging depth) and a corresponding circumferential scan length of 10 mm. As mentioned in Chapter 8, the actual transverse pixel spacing varies with depth due to the rotational nature of the imaging catheter. Axial pixel spacing was 2.4 μm with a 1,024-point Fourier transform performed on 800 k-space samples per line. These parameters gave a truly resolvable size of 13 x 10 x 5 μm (650 μm^3) compared to the optical resolution of 8 x 8 x 8 (512 μm^3).

It is also practical to reduce the rotary and pullback speeds to increase the transverse spatial sampling density for certain applications that require distinguishing smaller features or calculating speckle variance. In the future, faster imaging and acquisition speed will be necessary to make full use of the optical resolution supported by the VCSEL and the imaging catheter. However, the current performance of the system represents 10x faster and a significant improvement over the fastest 3D-OCTsystem that has been used in the GI clinics, which used FDML lasers and achieved optical resolution of 12 x 12 x 6 μm with transverse spatial sampling densities of only 16 x 33 μm due to restricted imaging speed of 60 kHz [9].

9.6 Data Storage and Post-Processing

During the imaging acquisition, the acquired raw data was firstly streaming into the memory allocated by the software. Since each data set is more than 8 gigabytes, it is important to store the data into the large volume database of the system as fast as possible in order to maintain the smooth work flow of the clinical environment. To visualize the acquired images after the data sets were stored, several data post-processing algorithm were developed to achieve optimal visualization of tissue microstructures. Since the mucosal structure of GI tract is difficult to evaluate in the cylindrical form, the individual OCT frames must be converted from radial images to rectangular image. To facilitate the formation of enface images at different depths, the frames must then be flattened to prevent curvature artifacts. Finally, the volumetric

data sets can be displayed in different perspectives to reveal information that cannot be obtained by individual cross-sectional images. Quantitative 3D measurement can also be performed on tissue structures in order to assess pathologic state. In general, 3D-OCT imaging provides more comprehensive information of the tissue architectural morphology. The following sections describe the data storage and post-processing after the image acquisition.

9.6.1 High Speed Storage for Gigabytes Data Sets

The data sets acquired using the endoscopic OCT system developed here can be more than 8 gigabytes with an acquisition time less than 10 seconds. To move the acquired data from the memory to the database hard disk drive (HDD) in the computer, it can take up to two minutes to store the whole data set and the data acquisition software cannot work during the period due to the resource limitation. Hence a solid state drive (SSD) with a total volume of 512 gigabytes was used in the system as a "buffering storage". Although the current SSD technology does not provide large volume storage as HHD does, it can support much faster data transferring rate. In the endoscopic OCT system using the SSD, an 8-gigabyte data set can be stored within 30 seconds, so the OCT imaging procedure time thus can be dramatically reduced and smooth work flow during the entire endoscopy session can be maintained.

After the imaging session, the data sets in SSD were then transferred into the large volume database HDD for permanent storage, as well as into an external drive, which can be brought back to MIT for post-processing and visualization.

9.6.2 Post-Processing – Frame Flattening

The flattening algorithm works by detecting the imaging catheter sheath's irregular surface and then shifting each axial line of each frame such that the sheath becomes flat. Since the sheath is normally in direct contact with the tissue surface, this simultaneously flattens the tissue as well. The micromotor imaging catheter can provide stable scan so the sheath location is basically consistent along the whole pullback. Hence the sheath detection can be done in single frame and the flattening can be applied on all other frames in the same data set.

The algorithm consists of two main sections. As shown in **Fig. 9.16**, single frame (typically the first frame) in the data set is chosen for the sheath surface detection. The surface detection can be done by either automatic detection or manual detection. Since the surface can be determined once per data set, one option is to directly define the surface contour by the user. The frame is firstly loaded into ImageJ, and then the user draws a line along the sheath surface using the segmentation line function. The vertical location of the segmentation line across the frame can be saved as an individual vector and used as the reference information in the flattening step.

The second section is the main flattening function and the post-processing software sequentially reads in each frame and shifts each axial line in each frame according to the vector obtained from the segmentation line. Finally the each flattened frame is saved into a stacked TIFF file, which contains all frames in the data set and can be opened by the ImageJ for rapid review or Amira for 3D visualization.

9.7 Figures

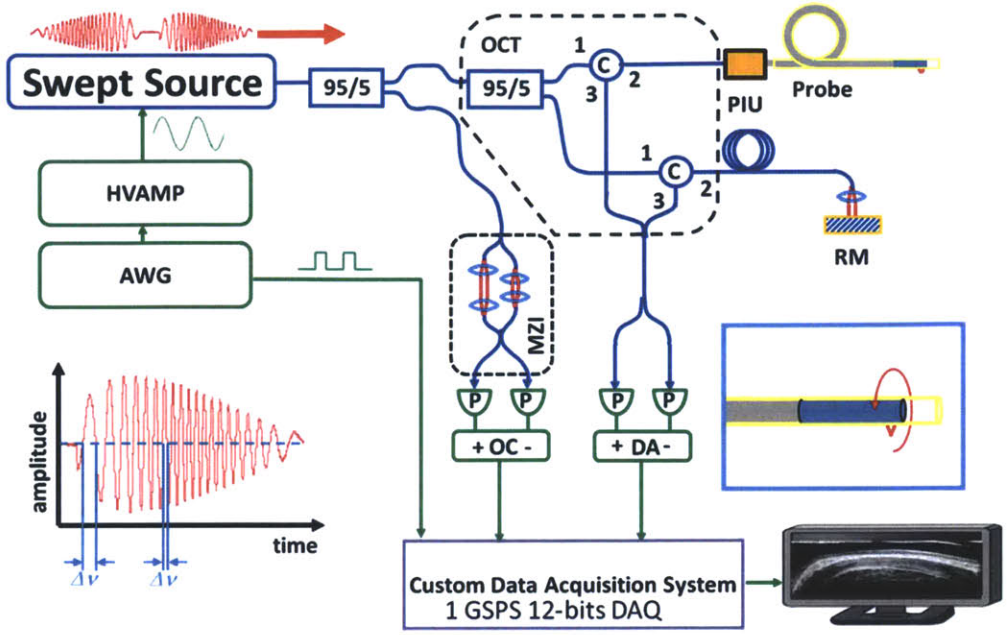

Figure 9.1. Schematic of swept source OCT system (optics: blue; electronics: green). Right inset showing the catheter indicates the rotary scanning direction of the focused spot. Left inset shows the principle of OFC generation using the MZI output. Zero crossings are unevenly spaced in time, but evenly spaced in optical frequency ν. C: circulator; MZI: Mach-Zehnder interferometer; RM: reference mirror; DA: differential amplifier; P: photodetector; PIU: patient interface unit; AWG: arbitrary waveform generator; HVAMP: high voltage amplifier.

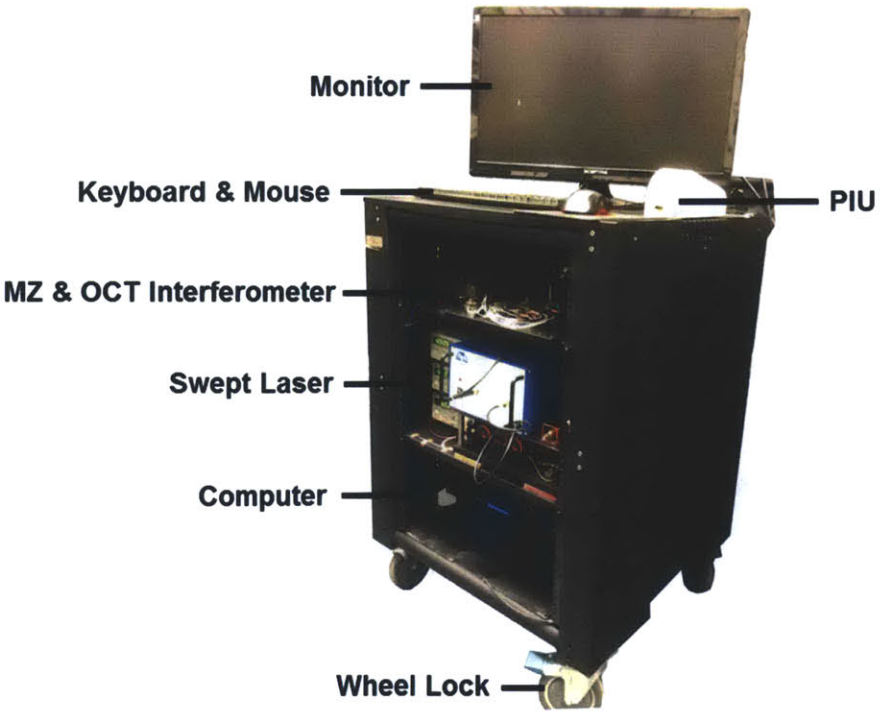

Figure 9.2. Photograph of the ultrahigh speed OCT imaging system for clinical gastroenterology.

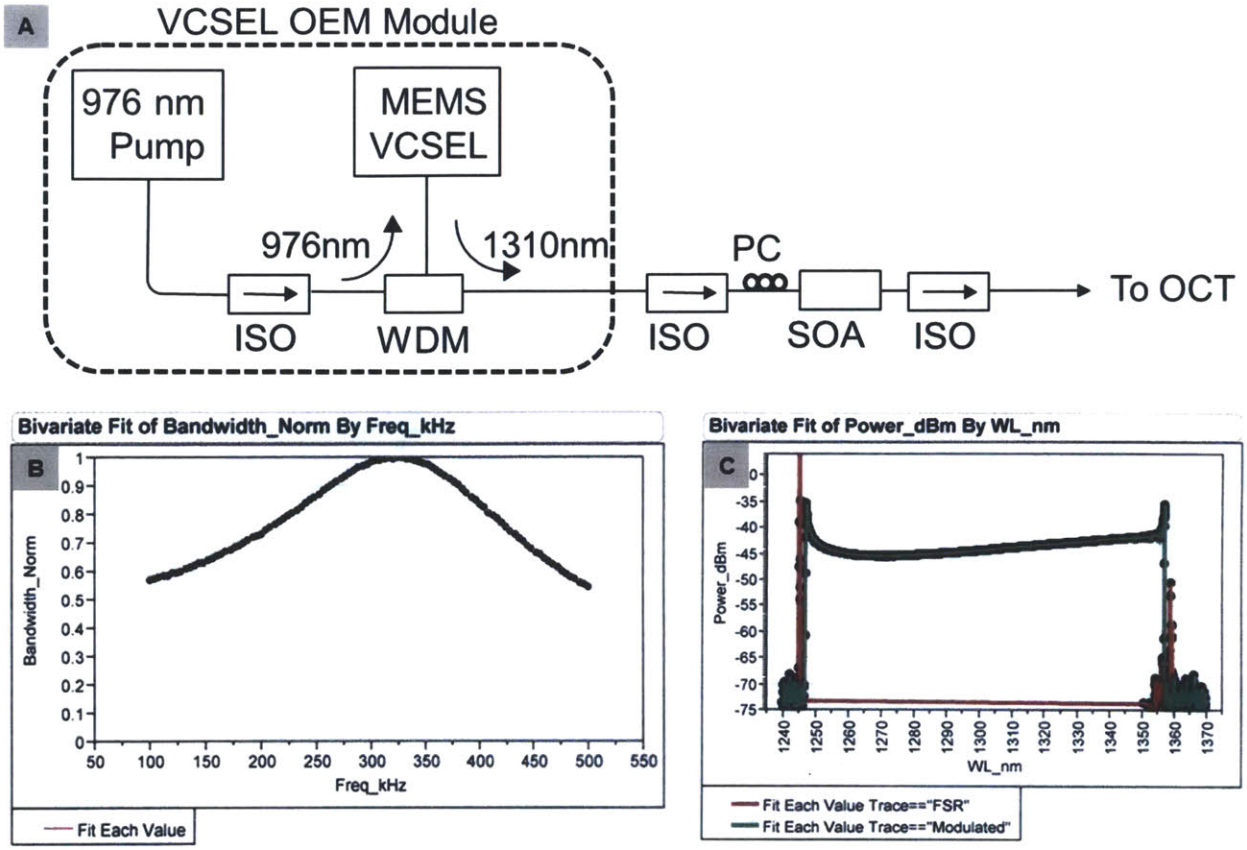

Figure 9.3. (A) Schematic diagram of the VCSEL module and the complete swept source configuration. (B) The frequency response of the MEMS-tunable filter in the VCSEL. (C) Optical spectrum of the laser output. ISO: optical isolator; WDM: wavelength-division multiplexer; SOA: semiconductor optical amplifier; PC: polarization controller.

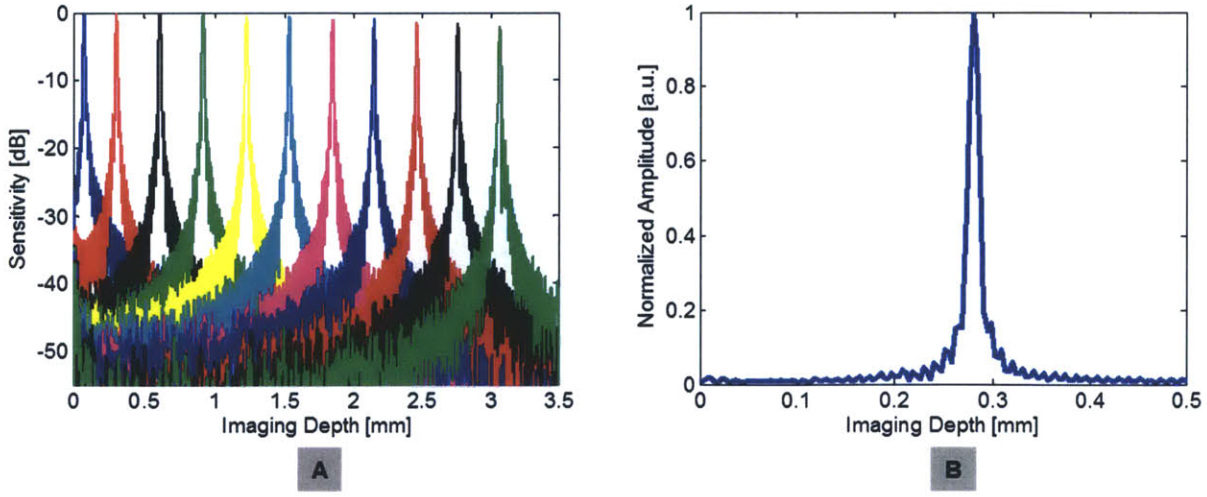

Figure 9.4. (A) PSF roll off measurement using a 1 MHz VCSEL and an unbalanced MZI. 2 dB roll off is observed at an imaging depth of 3.1 mm. (B) Linear PSF measured with 1 MHz VCSEL at a short imaging depth. Axial resolution is 11 um in air or 8 um in tissue.

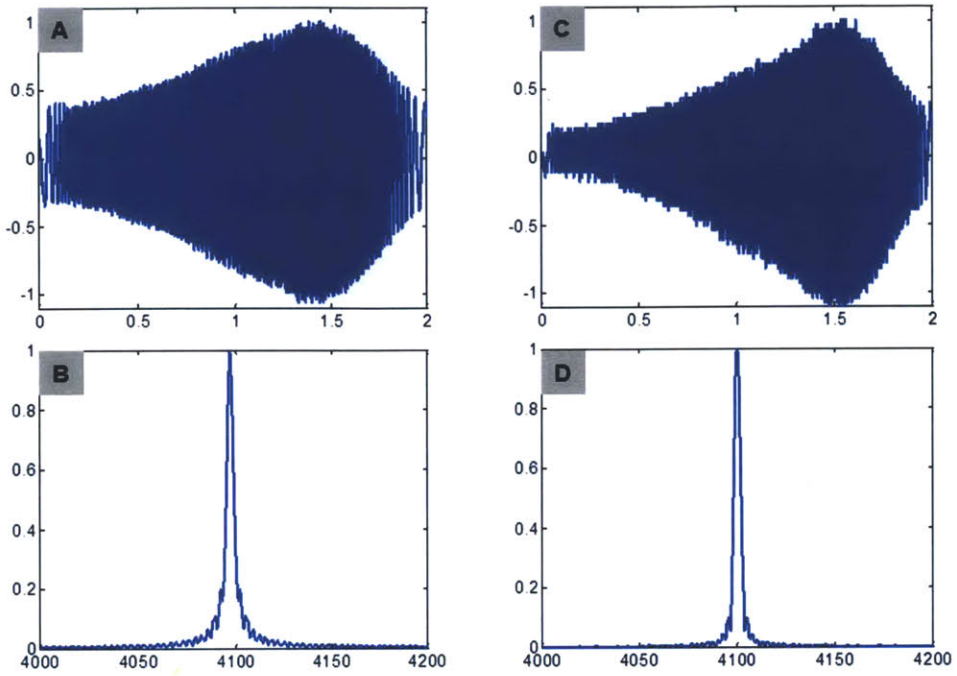

Figure 9.5. (A) Example interference fringe with high amplitude on both edges. (B) Corresponding PSF obtained from (A), showing ~20% sidelobes caused by the sharp edges in the fringe. (C) Example interference fringe with low amplitude on both edges. (D) Corresponding PSF obtained from (C), showing relatively lower sidelobes.

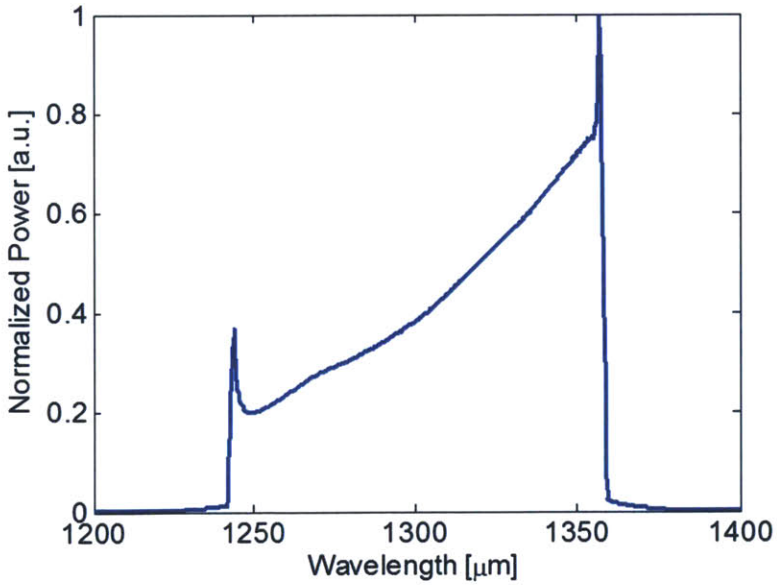

Figure 9.6. Optical spectrum of the post-amplified VCSEL output with a wavelength tuning range of 120 nm. This final VCSEL configuration was used in the ultrahigh speed OCT imaging system for clinical use.

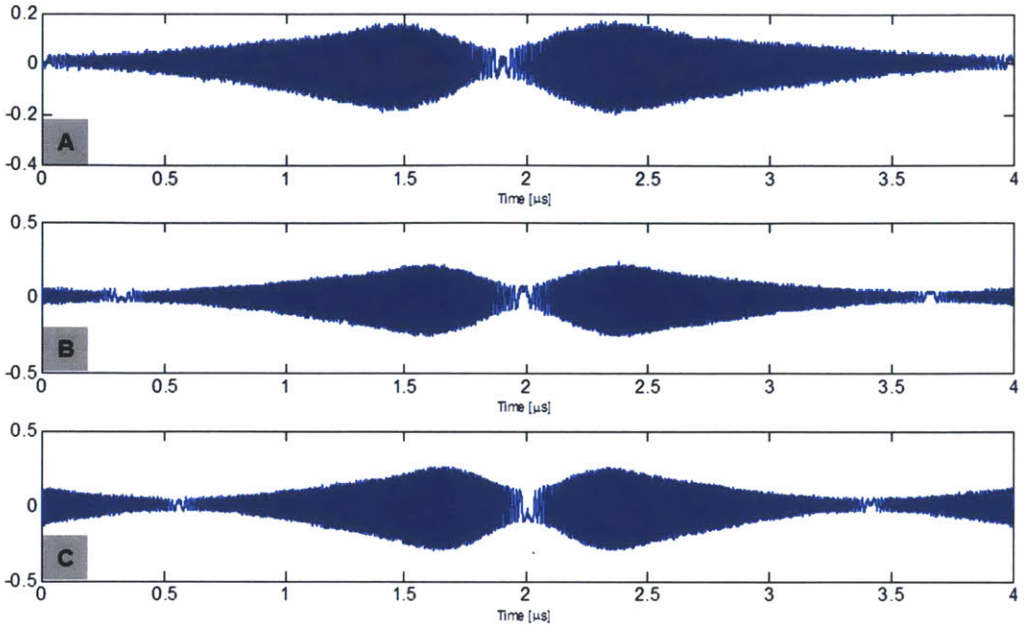

Figure 9.7. MZI interference fringes taken with different VCSEL fundamental sweep frequency. (A) Sweeps with 250 kHz sweep frequency, showing asymmetry in forward and backward sweep direction. (B) Sweeps with 300 kHz sweep frequency. (C) Sweeps with 350 kHz sweep frequency.

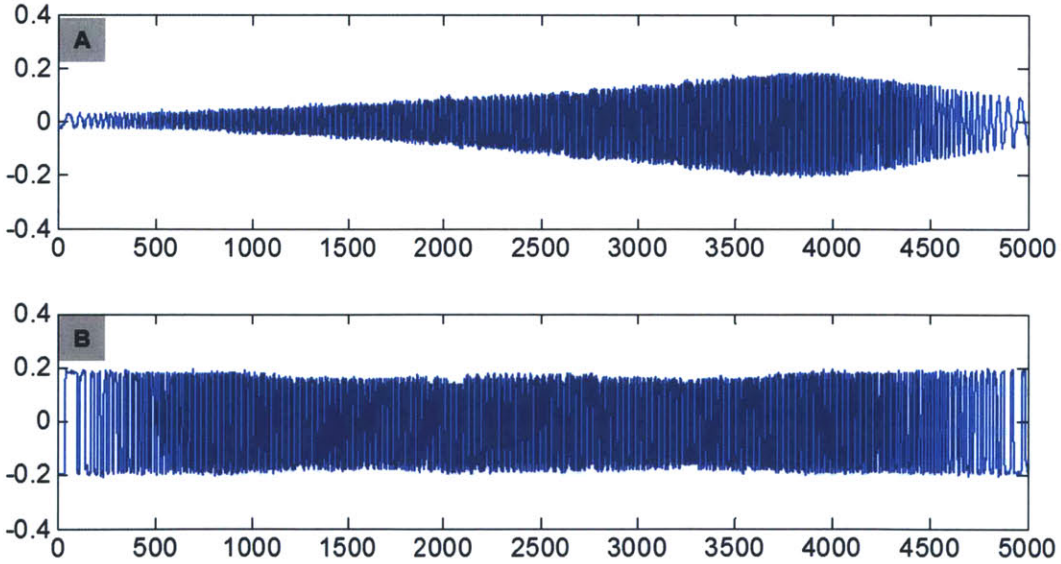

Figure 9.8. (A) MZI interference fringes used to generate OFC at every zero crossing which is evenly spaced in optical frequency ν. (B) Corresponding clock signal generated by the OFC circuitry using the MZI interference fringe in (A). The OFC signal is digital version of the MZI fringe which has constant signal amplitude.

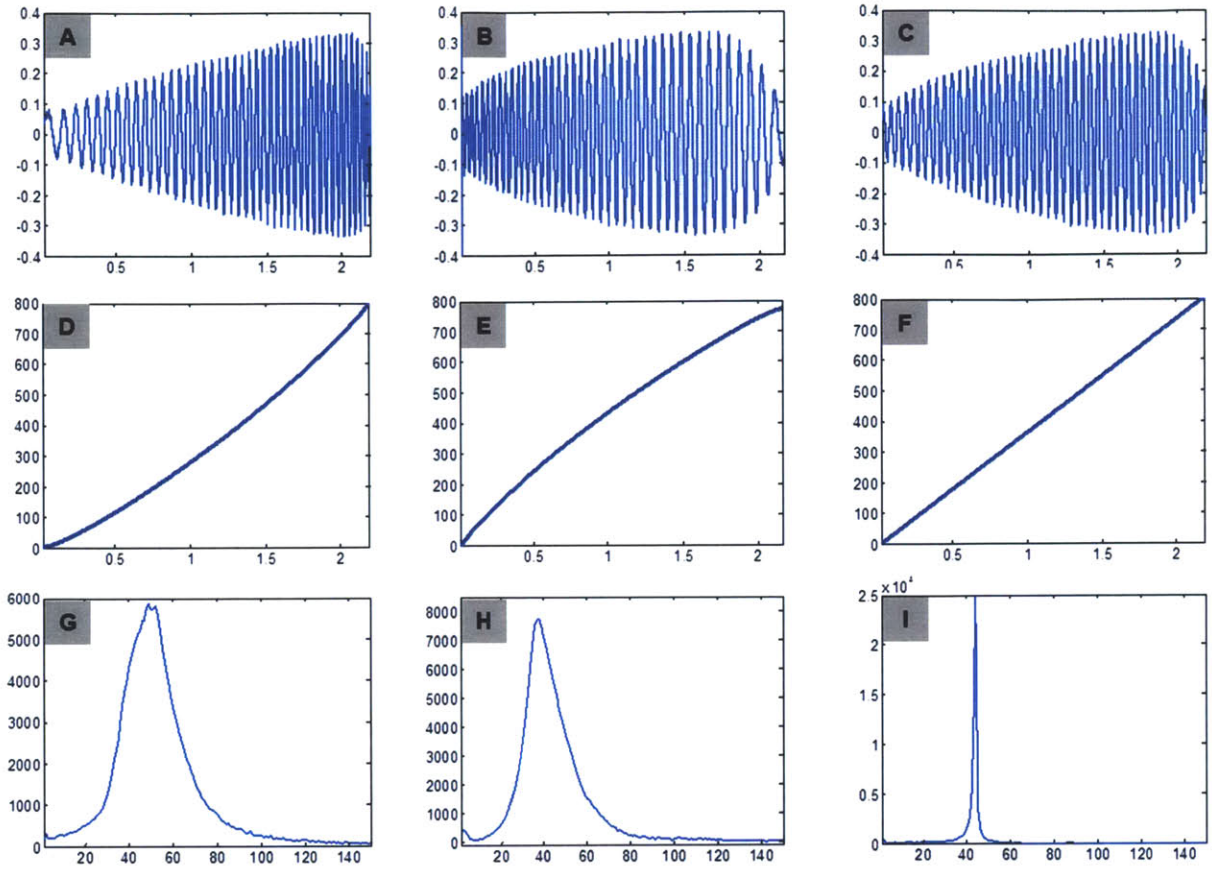

Figure 9.9. (A) OCT interference fringe from a fixed reflective surface when the OFC start earlier than the OCT signal. (B) OCT interference fringe from a fixed reflective surface when the OFC start later than the OCT signal. (C) OCT interference fringe from a fixed reflective surface when the OFC start at the same time with the OCT signal. (D-F) The optical frequency ν spacing represented by the phase of (A-C) when the OFC start earlier than, later than, and at the same time with the OCT signal. (G-I) Corresponding PSF from the same reflective surface obtained from (A-C) , showing different skewness in the PSFs when the OFC start earlier than, later than, and at the same time with the OCT signal.

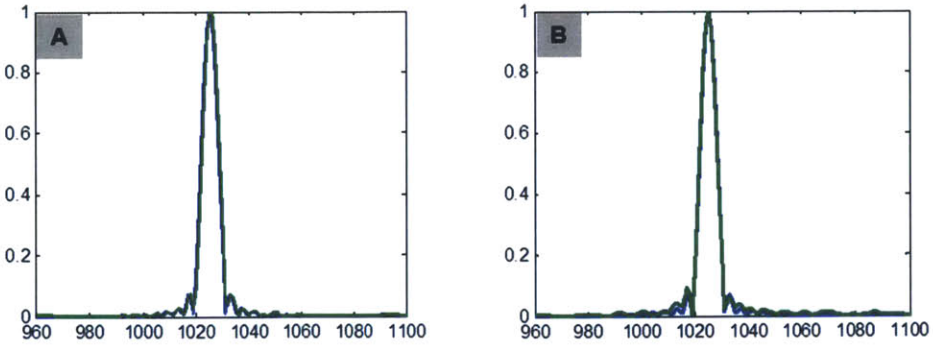

Figure 9.10. PSF comparison between the optical clocked OCT signal and its envelope to examine if there is any path length difference between the OCT interferometer and MZI/OFC. Blue line is the PSF from the optical clocked OCT signal, and green line is the PSF from the envelope of the OCT signal. (A) PSFs taken from a reflective surface at an imaging depth of 0.5 mm. (B) PSFs taken from a reflective surface at an imaging depth of 3 mm.

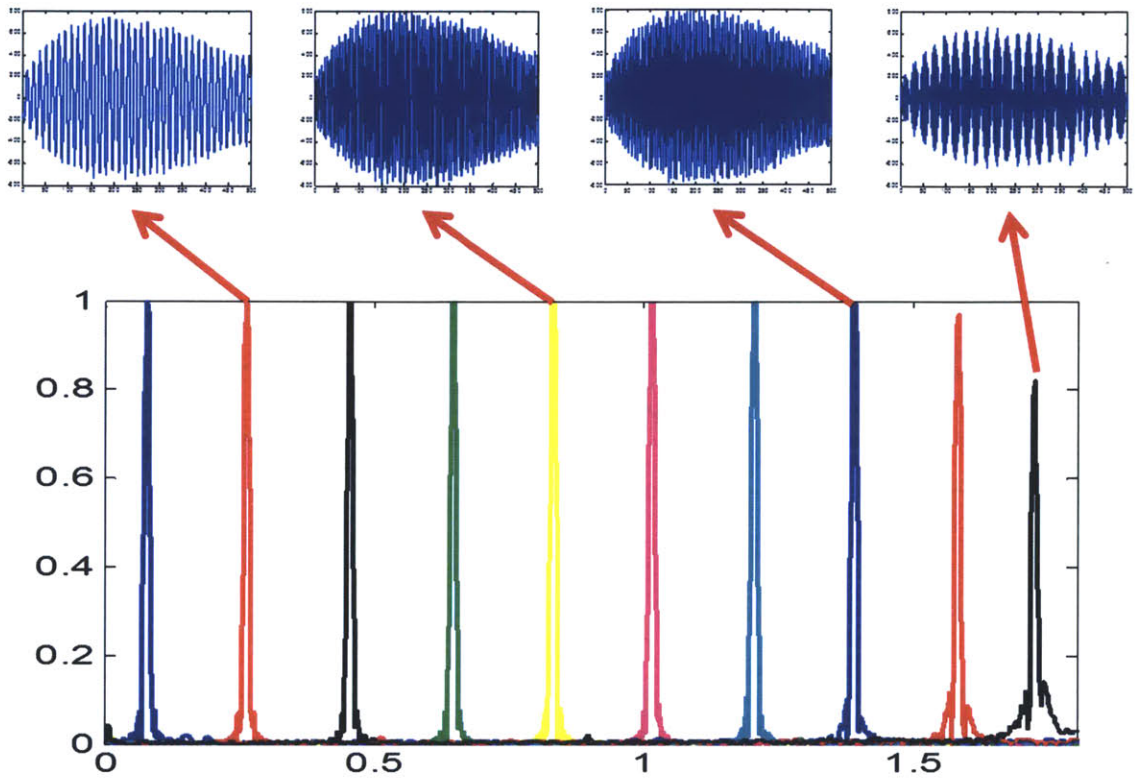

Figure 9.11. Sample-missing effect in the acquired OCT signal. The effect is not apparent when the OCT signals come from short imaging depths, but becomes severe when the imaging depth closer to the maximum imaging depth. Missing samples can also be distinguished from the discontinuity shown in the acquired OCT interference fringes.

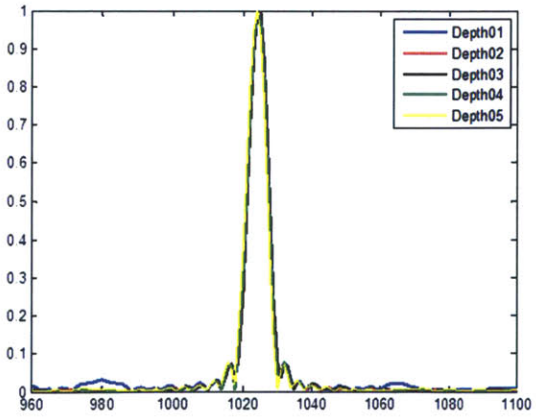

Figure 9.12. PSFs generated from reflective surfaces at different imaging range across the maximum ranging depth. Symmetric shapes with consistent level of sidelobes indicate the stable OFC.

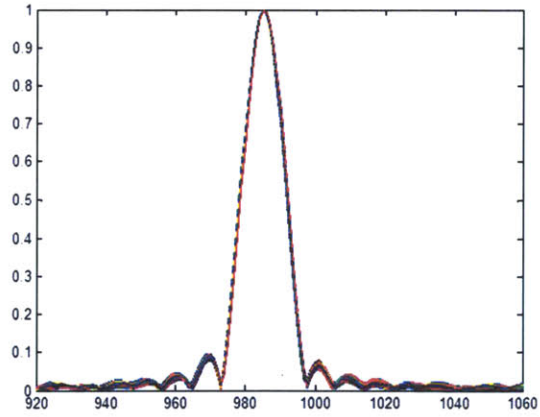

Figure 9.13. PSFs from 20,000 consecutive OCT interference fringes acquired at a fixed reflective surface with OFC frequency of 1.04 GHz. All PSFs are identical , indicating OFC works correctly.

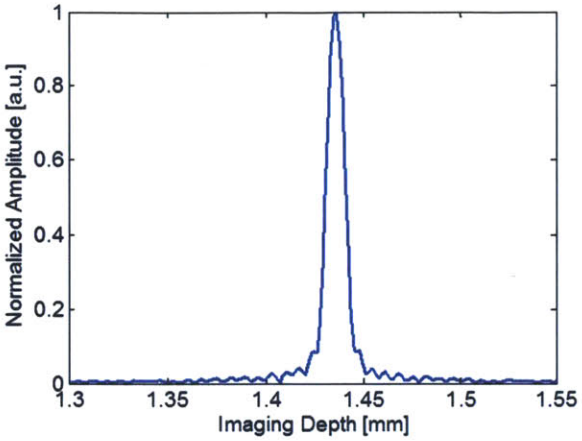

Figure 9.14. Linear PSF measured with complete ultrahigh speed OCT imaging system at imaging depth of 1.43 mm. Axial resolution is 11 um in air or 8 um in tissue.

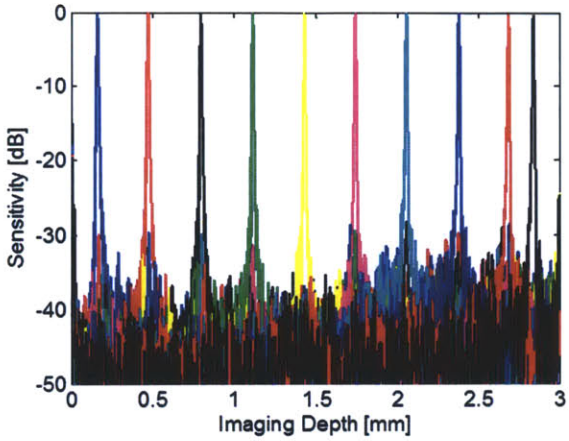

Figure 9.15. PSF roll off measured with complete ultrahigh speed OCT imaging system. No significant roll off can be observed across the whole imaging depth.

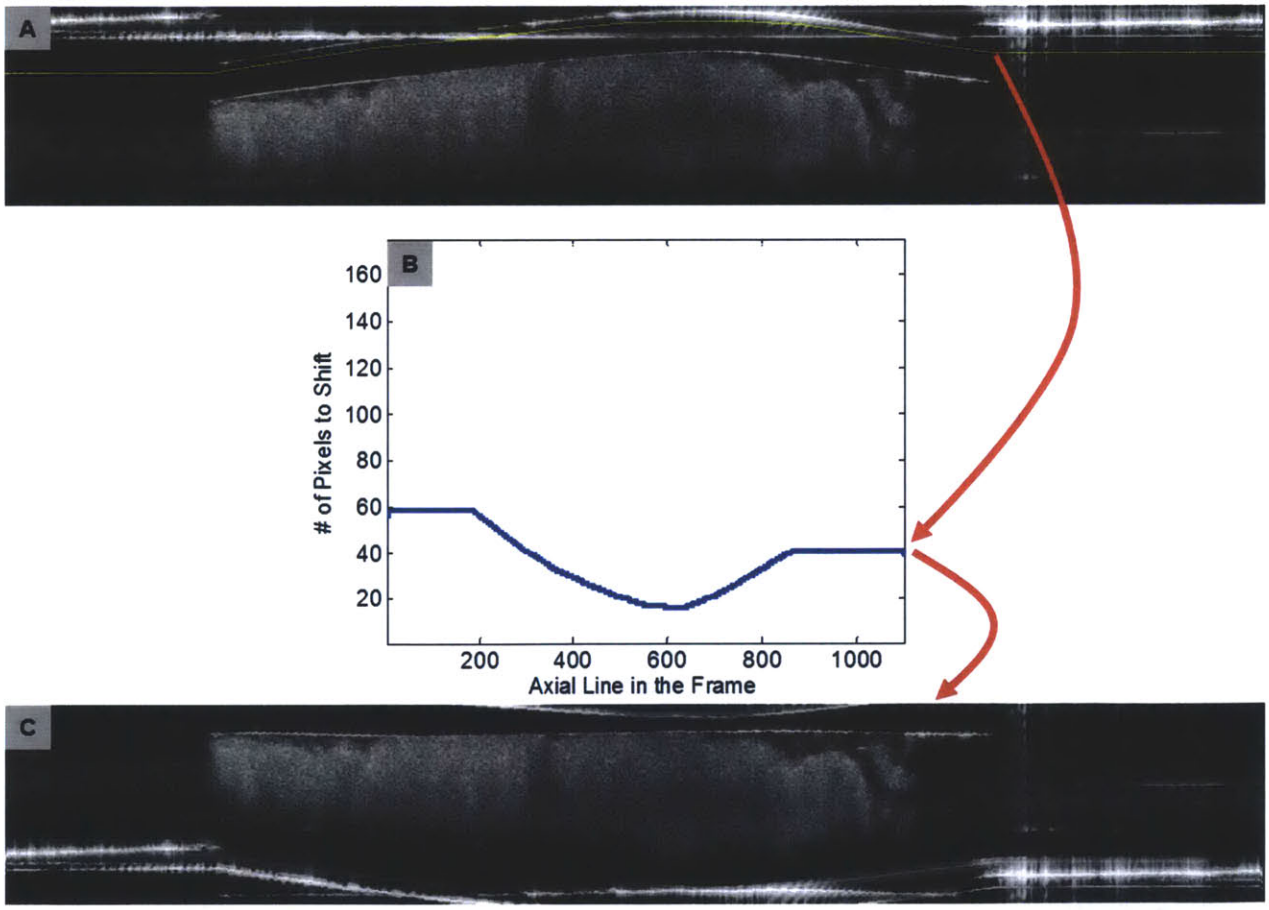

Figure 9.16. Frame flattening procedures for the data sets acquired using the ultrahigh speed OCT imaging system. (A) the user draw a segmentation line along the sheath surface. (B) The segmentation line is used to generate a vector that records the required number of pixels to shift for each axial line in the frame. (C) Each frame is flattened according to the shift vector and then stored in to a stacked TIFF file for future review.

9.8 References

[1] W. Drexler, U. Morgner, R. K. Ghanta, F. X. Kärtner, J. S. Schuman, and J. G. Fujimoto, "Ultrahigh-resolution ophthalmic optical coherence tomography," *Nature Medicine,* vol. 7, pp. 502-507, Apr 2001.

[2] G. J. Tearney, M. E. Brezinski, S. A. Boppart, B. E. Bouma, N. Weissman, J. F. Southern, E. A. Swanson, and J. G. Fujimoto, "Catheter-based optical imaging of a human coronary artery," *Circulation,* vol. 94, pp. 3013, Dec 1996.

[3] B. E. Bouma, G. J. Tearney, C. C. Compton, and N. S. Nishioka, "High-resolution imaging of the human esophagus and stomach in vivo using optical coherence tomography," *Gastrointestinal endoscopy,* vol. 51(4) Pt 1, pp. 467-74, Apr 2000.

[4] G. J. Tearney, M. E. Brezinski, J. F. Southern, B. E. Bouma, S. A. Boppart, and J. G. Fujimoto, "Optical biopsy in human urologic tissue using optical coherence tomography," *The Journal of urology,* vol. 157, pp. 1915-9, May 1997.

[5] P. F. Escobar, J. L. Belinson, A. White, N. M. Shakhova, F. I. Feldchtein, M. V. Kareta, and N. D. Gladkova, "Diagnostic efficacy of optical coherence tomography in the management of preinvasive and invasive cancer of uterine cervix and vulva," *International Journal of Gynecological Cancer,* vol. 14, pp. 470-474, May-Jun 2004.

[6] G. J. Tearney, M. E. Brezinski, B. E. Bouma, S. A. Boppart, C. Pitvis, J. F. Southern, and J. G. Fujimoto, "In vivo endoscopic optical biopsy with optical coherence tomography," *Science,* vol. 276, pp. 2037-2039, Jun 1997.

[7] S. H. Yun, G. J. Tearney, B. J. Vakoc, M. Shishkov, W. Y. Oh, A. E. Desjardins, M. J. Suter, R. C. Chan, J. A. Evans, I. K. Jang, N. S. Nishioka, J. F. de Boer, and B. E. Bouma, "Comprehensive volumetric optical microscopy in vivo," *Nature Medicine,* vol. 12, pp. 1429-1433, Dec 2006.

[8] B. J. Vakoc, M. Shishko, S. H. Yun, W. Y. Oh, M. J. Suter, A. E. Desjardins, J. A. Evans, N. S. Nishioka, G. J. Tearney, and B. E. Bouma, "Comprehensive esophageal microscopy by using optical frequency-domain imaging (with video)," *Gastrointestinal Endoscopy,* vol. 65, pp. 898-905, May 2007.

[9] D. C. Adler, Y. Chen, R. Huber, J. Schmitt, J. Connolly, and J. G. Fujimoto, "Three-dimensional endomicroscopy using optical coherence tomography," *Nature Photonics,* vol. 1, pp. 709-716, Dec 2007.

[10] T.-H. Tsai, B. Potsaid, M. F. Kraus, C. Zhou, Y. K. Tao, J. Hornegger, and J. G. Fujimoto, "Piezoelectric-transducer-based miniature catheter for ultrahigh-speed endoscopic optical coherence tomography," *Biomed. Opt. Express,* vol. 2, pp. 2438-2448, Aug 2011.

[11] M. J. Suter, P. A. Jillella, B. J. Vakoc, E. F. Halpern, M. Mino-Kenudson, G. Y. Lauwers, B. E. Bouma, N. S. Nishioka, and G. J. Tearney, "Image-guided biopsy in the esophagus through comprehensive optical frequency domain imaging and laser marking: a study in living swine," *Gastrointestinal Endoscopy,* vol. 71, pp. 346-353, Feb 2010.

[12] C. Zhou, D. C. Adler, L. Becker, Y. Chen, T.-H. Tsai, M. Figueiredo, J. M. Schmitt, J. G. Fujimoto, and H. Mashimo, "Effective treatment of chronic radiation proctitis using radiofrequency ablation " *Therapeutic Advances in Gastroenterology,* vol. 2, pp. 149-156, May 2009.

[13] T.-H. Tsai, C. Zhou, Y. K. Tao, H.-C. Lee, O. O. Ahsen, M. Figueiredo, T. Kirtane, D. C. Adler, J. M. Schmitt, Q. Huang, J. G. Fujimoto, and H. Mashimo, "Structural markers observed with endoscopic 3-dimensional optical coherence tomography correlating with Barrett's esophagus radiofrequency ablation treatment response," *Gastrointestinal Endoscopy,* vol. 76, pp. 1104-1112, Dec 2012.

[14] M. J. Suter, B. J. Vakoc, P. S. Yachimski, M. Shishkov, G. Y. Lauwers, M. Mino-Kenudson, B. E. Bouma, N. S. Nishioka, and G. J. Tearney, "Comprehensive microscopy of the esophagus in human patients with optical frequency domain imaging," *Gastrointestinal Endoscopy,* vol. 68, pp. 745-753, Oct 2008.

[15] E. Brinkmeyer and R. Ulrich, "High-resolution OCDR in dispersive wave-guides," *Electronics Letters,* vol. 26, pp. 413-414, Mar 1990.

[16] M. Wojtkowski, R. Leitgeb, A. Kowalczyk, T. Bajraszewski, and A. F. Fercher, "In vivo human retinal imaging by Fourier domain optical coherence tomography," *Journal of Biomedical Optics,* vol. 7, pp. 457-463, Jul 2002.

[17] S. H. Yun, G. J. Tearney, J. F. de Boer, N. Iftimia, and B. E. Bouma, "High-speed optical frequency-domain imaging," *Optics Express,* vol. 11, pp. 2953-2963, Nov 2003.

[18] D. C. Adler, S. W. Huang, R. Huber, and J. G. Fujimoto, "Photothermal detection of gold nanoparticles using phase-sensitive optical coherence tomography," *Optics Express,* vol. 16, pp. 4376-4393, Mar 2008.

[19] C. M. Eigenwillig, B. R. Biedermann, G. Palte, and R. Huber, "K-space linear Fourier domain mode locked laser and applications for optical coherence tomography," *Optics Express,* vol. 16, pp. 8916-8937, Jun 2008.

[20] M. Y. Jeon, J. Zhang, and Z. P. Chen, "Characterization of Fourier domain mode-locked wavelength swept laser for optical coherence tomography imaging," *Optics Express,* vol. 16, pp. 3727-3737, Mar 2008.

[21] S. P. Beeby, M. J. Tudor, and N. M. White, "Energy harvesting vibration sources for microsystems applications," *Measurement Science & Technology,* vol. 17, pp. R175-R195, Dec 2006.

[22] C. J. Chang-Hasnain, "Tunable VCSEL," *IEEE Journal of Selected Topics in Quantum Electronics,* vol. 6, pp. 978-987, Nov-Dec 2000.

[23] G. D. Cole, E. Behymer, T. C. Bond, and L. L. Goddard, "Short-wavelength MEMS-tunable VCSELs," *Optics Express,* vol. 16, pp. 16093-16103, Sep 2008.

[24] M. S. Wu, E. C. Vail, G. S. Li, W. Yuen, and C. J. Changhasnain, "Tunable micromachined vertical-cavity surface-emitting laser," *Electronics Letters,* vol. 31, pp. 1671-1672, Sep 1995.

CHAPTER 10

10.0 *In Vivo* Ultrahigh Speed OCT Imaging in the Human Gastrointestinal Tract

10.1 Motivation

As discussed in Chapter 2, gastrointestinal (GI) cancer is one of the most common cancers in the United States and is highly lethal [1, 2]. By early detecting the pre-malignant lesion such as dysplasia in the GI tract, early treatment can be applied to achieve a high percentage of regression in patients with dysplasia [3], indicating the importance of early detection and treatment of dysplasia to prevent cancer progression in the GI tract [3]. However, dysplastic tissue is not easy to identify using conventional endoscopic surveillance, as studies indicated that up to 85% of these lesions appear to have very subtle changes in the mucosal and vascular patterns compared to non-dysplastic tissue under endoscopic visualization, and only 13% of the dysplastic lesions are presented in the form of a readily discernible nodular lesion [4, 5]. For upper GI tract, the current standard of care, also known as Seattle protocol, is to perform biopsies in 4 quadrants every 2 cm in regions of endoscopically visible Barrett's esophagus. The increment is decreased to 1 cm for patients with a known history of dysplasia [6]. Because of the low fraction of tissue covered by the biopsy forceps and the lack of guidance, this method suffers from issue such as sampling error and complication risk associated with multiple biopsies [7]. For lower GI tract, the standard of care is to remove all endoscopically visible polyps in the colon. In addition to the polypoid lesions, standard white light colonoscopy is limited in differentiate normal colonic mucosa from nonpolypoid lesions based on the morphological difference, so some of the dysplastic lesions in the colon may be underdiagnosed during the screening [8, 9]. Moreover, both Seattle protocol and polytecomy procedures generate a significant workload for the pathology lab, so endoscopic imaging methods that can effectively detect dysplasia in the GI tract are highly desired.

Several advanced imaging technologies have been developed to increase the yield of the endoscopy surveillance. Chromoendoscopy with topically applied dyes such as methylene blue or indigo carmine over the regions of interest facilitates the detection of nonpolypoid lesions based on the enhancement of surface morphology [10-13], but the main limitation of chromoendoscopy are the requirement of large volume of dye and high quality bowel preparations for standard colon screening [14, 15]. Virtual chromoendoscopy such as narrow-band imaging (NBI), where light of specific blue or green wavelengths is used, can enhance the detail of certain aspects of the tissue surface such as blood vessels without any application of dye [16, 17]. Although chromoendoscopy and NBI are able to enhance the tissue contrast and distinguish lesions from normal tissue, the optical resolution of these methods with standard endoscope is not sufficient to distinguish dysplasia from non-dysplastic tissues. In conjunction with high-magnification endoscope, which has not yet been widely available in the United States, it is possible to use chromoendoscopy or NBI to visualize different pit patterns of the lesion and detect dysplasia in the colon based on Kudo classification [18] and in the esophagus based on Paris classification [19, 20]. Confocal laser endomicroscopy (CLE) is another emerging technology that allows microscopic

examination of the GI tract and has been demonstrated having high sensitivity and specificity in differentiating neoplasia in both esophagus and colon [21-26]. CLE requires the use of exogenous contrast agents such as intravenous fluorescein and topical acriflavine (not approved for human use in the United States), so the time for imaging is limited due to excretion of fluorescein [27, 28]. The high magnification of CLE also limits its field of view (FOV) and imaging depth, making it impractical to survey large area for possible malignancy or detecting important features in the deeper regions. Recently, several "red flag" techniques, such as the application of fluorescence-labeled peptides that can specifically bind the dysplastic regions [29-32] and angle resolved low coherence interferometry (a/LCI) that uses depth-resolved nuclear morphology measurements to detect dysplasia [33-36], also showed promising results in identifying dysplastic tissue over a large field in the GI tract. These techniques can potentially be very powerful once they are validated with large clinical studies in the future.

Endoscopic optical coherence tomography (OCT), on the other hand, has been demonstrated its volumetric imaging capability in the GI tract since 2006 [37-39], but to date whether it can be used to identify dysplastic regions remains controversial. One study conducted by the group at Massachusetts General Hospital suggested it is possible to classify different types of Barrett's esophagus using the cross-sectional images based on the surface maturation and subsurface glandular structure [40]. *Ex vivo* studies using OCT and optical coherence microscopy (OCM) conducted by Prof. Fujimoto's group also showed both OCT and OCM were able provide of *en face* images similar to those from CLE without the use of any contrast agent [41], and thus can be used to identify dysplastic lesions based on the pit patterns. However, current clinical endoscopic OCT systems using proximally rotary imaging catheter are not able to provide good quality volumetric data sets due to the limitation of imaging speed and the scanning uniformity, so the true capability of OCT has not yet been fully realized in the endoscopic applications. In this section of the thesis work, the new generation of the clinical OCT imaging system developed in Chapter 9 with ultrahigh speed and more stable imaging capability was deployed to the endoscopy suite at the Veterans Affairs Boston Healthcare System (VABHS) and *in vivo* endoscopic OCT imaging was performed in the human GI tract. The yield of good quality volumetric data sets was high, which not only allows visualization of the tissue structure in any orientation, but also provided more structural information that helps distinguishing dysplasia but cannot be clearly identified in the data sets acquired with the previous systems. The distally actuated imaging catheter was able to sustain greater bending and even retroflexion of the endoscope, and ability to image locations that are hard to reach such as terminal ileum was also demonstrated. The endoscopic OCT data that is presented in this chapter was taken in collaboration with Dr. Hiroshi Mashimo, MD, PhD who performed all of the endoscopy sessions. Dr. Yuankai Tao, PhD, participated in the discussion of balloon catheter design and helped the documentation of disinfection procedures. Multiple group members including Hsiang-Chieh Lee, Osman Ahsen,

Kaicheng Liang, Dr. Yuankai Tao, and Dr. Michael Giacomelli shared the experimental responsibilities in the endoscopy clinics on alternating weekly basis. All the data processing and analysis were done by the author of the thesis work.

10.2 Imaging Procedure

This study was conducted in collaboration with Dr. Hiroshi Mashimo and Dr. Qin Huang at the Veterans Affairs Boston Healthcare System (VABHS), Jamaica Plain Campus, and the study protocol was approved by institutional review boards (IRB) of the VABHS, Harvard Medical School, and the Massachusetts Institute of Technology. Healthy volunteers and volunteers with known Barrett's esophagus or inflammation bowel disease (IBD) were enrolled in this study. After informed consent, the subjects underwent standard esophagogastroduodenoscopy (EGD) procedures or colonoscopy. For EGD, a high-definition dual-channel endoscope (Olympus GIF-2TH180) was used. Immediately following diagnostic endoscopic investigation, regions of interest (ROIs) identified by the clinician were imaged with OCT imaging. A disinfected micromotor imaging catheter was introduced in the field of view of the endoscope through the 3.7 mm accessory channel. During the image acquisition, the imaging catheter was gently placed in contact with each ROI, and two volumetric OCT data sets were recorded for each ROI. After the acquisition of OCT data sets, each ROI was biopsied or resected for histology comparison. For colonoscopy, a high-definition colonoscope (Olympus PCF-H190) was used. During the screening colonoscopy, regions of interest (ROIs) identified by the clinician were imaged with OCT imaging. A disinfected micromotor imaging catheter was introduced in the field of view of the colonoscope through the accessory channel and gently placed in contact with each ROI. After the acquisition of OCT data sets, each ROI was biopsied or resected for histology comparison. After each imaging session, the micromotor imaging catheter was disinfected for reuse in accordance with the standard procedure for the disinfection of endoscopic instruments.

Table 10.1 Summary of clinical OCT data collected in the study.

Group	Number of Patients	Number of Data Sets
Normal Esophagus	2	12
Esophagus with BE	2	15
Normal Colon	3	20
Colon with IBD	3	24
Other Pathology	3	23

BE: Barrett's esophagus; IBD: inflammatory bowel disease.

In total, 94 volumetric OCT data sets from 13 unique patients were taken during this study from April to June 2013. **Table 10.1** shows a summary of the collected volumetric OCT image data. The "Other Pathology" group includes pathologic tissues that were outside the main scope of the study and difficult to be imaged using conventional endoscopic OCT system. The following sections show representative OCT data, characteristic features, and comparison to histology for each main tissue type.

10.3 Esophagus

Figure 10.1 shows a diagram of the human GI tract. As the beginning section of the GI tract, esophagus is one of the most accessible organs that can be evaluated by a variety of imaging modalities. In fact, a majority of clinical studies in the GI tract were performed in the esophagus using endoscopic OCT, and the structural features of normal and abnormal esophagus observed in OCT images are well known in comparison with other organs in the GI tract. Therefore, it is important to firstly validate the new generation imaging system in esophagus to understand the performance of the system. In this section, volumetric OCT data sets from normal esophagus, non-dysplastic BE, and dysplastic BE with corresponding histology will be presented and structural features that potentially correspond to dysplastic lesions will be investigated.

10.3.1 Normal Esophagus

Obtaining normal esophagus data was a necessary step in this study in order to establish a baseline for comparison to pathologic tissue. Volumetric OCT images of normal esophageal mucosa were obtained from one patient. The patient tolerated the procedure well and there was no known immediate or long-term complication reported.

Figure 10.2 shows a representative volumetric OCT data set obtained from the normal esophagus. **Fig. 10.2A** shows a volumetric rendering of the entire 1,500 x 3,200 x 512 (fast scan x pullback scan x axial direction) data set, which was acquired in 8 seconds. The pullback length was 16 mm, the rotational circumference was 10 mm, and the imaging range was 2.4 mm in tissue. The images in **Fig. 10.2** have been axially cropped to remove the sheath of the catheter and non-usable points beyond the penetration depth of light in tissue. The useable imaging depth in tissue was approximately 1.2 mm. Unless otherwise specified, all cross-sectional and *en face* images shown below are formed by averaging the volumetric data over 20 μm thick section to reduce speckle noise. Since 20 μm is approximately the size of a single epithelial cell, minimal image blurring is observed from this process [38]. In this and all subsequent volumetric OCT image data, the frame rate provided by the micromotor imaging catheter was 400 fps (24,000 rpm) and the pullback speed provided by the patient interface unit (PIU) was 2 mm/s.

Fig. 10.2B shows an *en face* image centered at a tissue depth of 240 μm, corresponding to the center of the lamina propria layer. This image is similar in concept to a conventional microscopy image obtained by setting the focus to a depth of 240 μm. Consistent with previous 2D-OCT and 3D-OCT studies [39, 42, 43], the *en face* image of the normal esophagus is featureless and unremarkable. The small, hyposcattering regions in this image (indicated by red arrows) are the subsquamous intestinal metaplasia (SSIM or buried glands), which can be distinguished from vessel due to its isolated feature. Motion artifacts due to the heartbeat of the patient can be observed in the *en face* image, which are inevitable for imaging of the esophagus.

One of the main benefits of the use of distal scanner and high imaging speed compared to conventional endoscopic OCT is the ability to precisely align cross-sectional image to *en face* tissue features. **Fig. 10.2C** shows a cross-sectional image along the pullback direction at the position indicated by the green dashed line in **Fig. 10.2B**. The typical well-defined layered architecture of the normal esophagus can be appreciated throughout the length of pullback. **Fig. 10.2D** shows a cross-sectional image along the rotary direction at the position indicated by the blue dashed line in **Fig. 10.2B**. The regular layered structure is visible as well. Since the stable scan allows much better frame-by-frame alignment, it is easier to distinguish regular blood vessel in the lamina propria and submucosa layers (first and second hyperscattering layers in **Figs. 10.2C and D**) from SSIM between the squamous epithelium and lamina propria, based on their axial shadows and interconnectivity across numerous cross-sectional images. **Fig. 10.2E** shows an *en face* image from the same data set at an imaging depth of 500 μm, corresponding to the submucosa layer. The shadow of vessels from the lamina propria layer and the vessels in the submucosa layer can be clearly appreciated. The ability to definitively distinguish vascular from glandular features without the use of Doppler processing is unique to the volumetric OCT imaging. This ability can be valuable in the assessment of pathologic tissues, as discussed in the following sections.

The dense spatial sampling density, high optical resolution, and large field of view of ultrahigh speed endoscopic OCT enables high-magnification analysis of each tissue layer over arbitrary ROIs. This principle is demonstrated in **Fig. 10.3**. **Figs. 10.3A-D** show *en face* images at the ROI shown as a red dashed box in **Fig. 10. 2B**. Images are shown at tissue depths of squamous epithelium, lamina propria, muscularis mucosa, and submucosa. Regular vascular networks are visible in the submucosa layer while the SSIM can be identified in the lamina propria layer. The SSIM and individual vessels can be identified in the *en face* images (red and blue arrows in **Figs. 10.3B and D**) as well as the cross-sectional images shown in **Figs. 10.3E and F**.

Comparison of endoscopic OCT images to histology slides obtained from excisional biopsy or mucosal resection and to white light video endoscopy examination is a good method for linking image features to known tissue structures. **Fig. 10.4A** shows an endoscopic video capture obtained prior to

endoscopic OCT imaging of the same patient. The esophageal mucosa appears pale-pink, smooth, and regular, consistent with normal squamous tissue. **Fig. 10.4B** shows corresponding histology of normal esophageal squamous mucosa. After identifying SSIM in the imaged region, multiple biopsies were taken within this region. The histology was later diagnosed by the pathologist as a normal squamous epithelium with SSIM in the lamina propria layer. Excellent correlation is shown between the histology image and the cross-sectional OCT image. The epithelium, lamina propria, muscularis mucosa, submucosa, and muscularis propria are visible as well-separated and distinct layers with alternating hypo- and hyperintensity under the OCT image (**Fig. 10.4C**). The pinch biopsy sample did not extend deeper than the muscularis mucosa, highlighting another advantage of volumetric OCT compared to conventional histology.

10.3.2 Non-dysplastic BE

Endoscopic OCT images of non-dysplastic BE were obtained in 6 data sets from one patient with known BE, who was initially diagnosed with low grade dysplasia and was treated with RFA 3 months prior to endoscopic OCT imaging to remove the dysplastic lesion, but presented on the imaging day with residual BE. The patient had been medically treated with proton pump inhibitors or other pharmaceuticals to control BE progression. The patient tolerated the procedure well and there were no known immediate or long-term complications.

Figure 10.5 shows a representative volumetric OCT data set obtained from the BE region. This patient presented with short segment BE in the distal esophagus near the gastroesophageal junction (GEJ). BE may also present as ultra-short segment or invisible lesions at the GEJ. These cases may represent situations where endoscopic OCT can provide enhanced visualization over endoscopic examination alone. **Fig. 10.5A** shows a volumetric rendering of the entire 1,500 x 3,200 x 512 (fast scan x pullback scan x axial direction) data set, which was acquired in 8 seconds. The pullback length was 16 mm, the rotational circumference was 10 mm, and the imaging range was 2.4 mm in tissue.

Fig. 10.5B shows an *en face* image centered at a tissue depth of 80 μm, corresponding to the center of the squamous epithelial layer. The imaging catheter was pulled back over the squamous-columnar junction (SCJ) during the acquisition of the data set and a clear delineation can be appreciated between the BE mucosa on the left-hand side of the image (distal) and normal esophageal mucosa on the right (proximal). **Fig. 10.5C** shows a second *en face* image at a tissue depth of 220 μm. The esophageal tissue on the left reveals atypical glandular structures consistent with BE. **Figs. 10.5D-F** shows cross-sectional images at multiple positions within the data set. In **Fig. 10.5D**, a 3.5 mm length of BE tissue is adjacent to the normal squamous mucosa with regular layered architecture. In cross-sectional images, the non-dysplastic BE mucosa exhibits presence of vertical pit patterns without serious distortion of the layered

architecture. "Distortion" refers to localized, atypical variation in mucosal layer thickness as well as changes in layer-to-layer contrast compared with normal esophageal tissue. An orthogonal cross-section through a region containing transitionary BE tissue and normal esophageal mucosa is shown in **Fig. 10.5E**. These images illustrate that BE glands are located beneath 200-300 μm of overlying tissue.

Figure 10.6 shows an enlarged view of the ROI illustrated in **Figs. 10.5B and C**. This ROI spans a portion of BE as well as an adjacent normal area. There is clear demarcation between the normal (right) and BE (left) regions. The presence of glands and layer distortion are hallmarks of BE. Although it was reported that identification of high grade dysplasia/intramucosal carcinoma using cross-sectional images is possible based on the surface maturation and glandular architecture, previous studies using 3D-OCT have not conclusively established criteria for differentiating dysplastic BE from non-dysplastic BE. In this case, both *en face* and cross-sectional information can be used to classify the tissue type due to the high quality of the volumetric data set. The irregular pattern observed from the *en face* view and minor distortion of layered architecture observed from the cross-sectional images suggest non-dysplastic feature of the tissue.

Figure 10.7 shows a comparison of endoscopic OCT data to high definition NBI and histology analysis of the BE region. **Fig. 10.7A** shows an endoscopic video capture obtained prior to OCT imaging of the same patient. The esophageal mucosa contains discrete regions that appear dark red, inflamed, and irregular under NBI, consistent with BE. **Fig. 10.7B** shows histology of BE taken at the imaged location. Excellent correlation is shown between the histology image and the endoscopic OCT image. Numerous BE glands are visible in both the histology and OCT images with minor distortion of the regular layered architecture. This patient was diagnosed with BE without dysplasia after histology analysis, which agrees with the observation from the volumetric OCT data. This highlights an advantage of 3D information that OCT can provide for characterizing BE. With good quality *en face* information, the accuracy of the tissue classification based on the structural features can be further improved.

10.3.3 Dysplastic BE

Endoscopic OCT images of non-dysplastic BE were obtained in 9 data sets from one patient with known BE, who was initially diagnosed with high grade dysplasia and never received any endoscopic treatment prior to endoscopic OCT imaging, but had been medically treated with proton pump inhibitors or other pharmaceuticals to control BE progression. After OCT imaging, the patient was treated with endoscopic mucosal resection (EMR) to remove the dysplastic lesion. The patient tolerated the procedure well and there were no known immediate or long-term complications.

Figure 10.8 shows a representative volumetric OCT data set obtained from the BE region. This patient presented with 6 cm BE in the distal esophagus near the GEJ. **Fig. 10.8A** shows a volumetric

rendering of the entire 1,500 x 3,200 x 512 (fast scan x pullback scan x axial direction) data set, which was acquired in 8 seconds. The pullback length was 16 mm, the rotational circumference was 10 mm, and the imaging range was 2.4 mm in tissue.

Fig. 10.8B shows an *en face* image centered at a tissue depth of 70 μm, similar to the imaging depth that conventional white light endoscopy, NBI, or CLE typically can achieve. The *en face* image here shows completely different pit patterns from the pit pattern observed in the non-dysplastic BE (**Fig. 10.6B**). **Fig. 10.8C** shows another *en face* image centered at a tissue depth of 170 μm, so the subsurface feature of the BE region such as the glandular can be evaluated. Some distorted portions noticeable in the *en face* images are caused by the imaging catheter movement during the image acquisition. It is also noticeable that the pit pattern in the distal region (more branching) is different from that in the proximal region (more round), which may indicate these two regions contain different types of BE. **Figs. 10.8D-F** show cross-sectional OCT images of the BE region along the pullback and rotary directions. In this case, the layered architecture that can be seen in the normal esophagus or non-dysplastic BE no longer exists, and the surface OCT signal is stronger than the subsurface OCT signal, indicating incomplete surface maturation in the region and thus suggesting the imaged area can be dysplastic BE.

Figure 10.9 shows a comparison of endoscopic OCT data to high definition NBI and histology analysis of the BE region. **Fig. 10.9A** shows an endoscopic video capture obtained prior to OCT imaging of the patient. The BE mucosa in this patient is also dark red, inflamed, and irregular, which is difficult to tell whether the type of BE is different from that in **Fig. 10.7A** just by looking at the endoscopic image. **Fig. 10.9B** shows histology of EMR specimen taken at the imaged location. This histology is diagnosed as BE with extensive low grade dysplasia and focal high grade dysplasia, which agrees with the observation from the volumetric OCT data. These results demonstrate for the first time that the ultrahigh speed endoscopic OCT allows comprehensive visualization of the 3D tissue architectures and enables the identification of dysplastic BE based on both *en face* and cross-sectional OCT images. The ability to show *en face* images that comparable to magnified chromoendoscopy or CLE images, without the need of any exogenous contrast, potentially makes OCT a powerful imaging modality to *in vivo* detect the dysplasia in the GI tract more accurately, as the tissue type can be classified according to criteria including both Paris classification (*en face* images) and surface maturation (cross-sectional images) immediately after the volumetric OCT data set is acquired.

10.4 Colon

Colon, also known as large bowel, is the end section of the GI tract so endoscopic examination for lower GI tract can be performed through the anus and the whole colon can be examined with the standard colonoscope. To date, most OCT imaging studies were performed at the very distal part of the colon, that

is, the rectum and the recto-anal junction because typical OCT catheters using proximally rotary scan usually cannot provide smooth scanning once passing through the first sharp bend into the sigmoid colon. In this section, volumetric OCT data sets from normal rectum, recto-anal junction, and radiation proctitis (RP), the chronic inflammation in the rectum, will be presented with corresponding histology first to evaluate the performance of the new imaging system. To demonstrate the imaging capability of the distally actuated imaging catheter, a volumetric OCT data set from a polyp in the right colon with corresponding histology will also be presented.

10.4.1 Normal Colon

Endoscopic OCT images of normal colonic mucosa were obtained in 20 data sets from 3 patients scheduled for standard colon screening. All patients tolerated the procedure well and there were not known immediate or long-term complications. OCT imaging was performed around rectum and recto-anal junction. **Fig. 10.10A** shows the diagram of human GI tract with imaged locations highlighted and **Fig. 10.10B** shows an example endoscopic view of the imaging catheter placed on the recto-anal junction (RAJ). Since the anal canal consists of squamous mucosa, it also shows pale-pink and uniform surface feature similar to the normal esophagus.

Figure 10.11 shows a typical volumetric OCT data set obtained from the normal proximal rectum (close to recto-sigmoid junction). **Fig. 10.11A** shows an *en face* image centered at a tissue depth of 250 μm, corresponding to the bottom of the columnar epithelial layer of the rectum. Consistent with previous OCT studies on excised pathology lab samples [44], the normal columnar epithelium of the colon shows low light penetration. Colonic crypts are visible as round or slightly oval hyperscattering regions, which is caused by increased light transmission through the crypt lumen [44]. Transverse motion artifact is reduced in the colon compared to the esophagus due to a complete lack of heartbeat motion. The tissue folding on the proximal side of the image indicates the imaged area was on the recto-sigmoid junction and covered a small portion of sigmoid tissue. A dark stripe along the pullback direction is caused by a scratch on the plastic sheath, which blocked the light while scanning through the scratch. This can be solved by replacing the plastic sheath immediately. **Fig. 10.11B** shows a cross-sectional image along the pullback direction indicated by the green dashed line in **Fig. 10.11A**. Vertical streaks are presented due to increase light transmission through crypt lumens. The layered structure in the colonic mucosa cannot be observed all the time due to the poor transmission through the columnar epithelium. **Figs. 10.11C and D** shows a cross-sectional image along the rotary direction at the position indicated by the blue and dark blue dashed lines in **Fig. 10.11A**, respectively. Similar features to the pullback image can be appreciated. **Fig. 10.11E** shows representative histology of normal rectum. Since there was no clinical indication to biopsy at normal looking rectum, the histology image was taken from another subject where biopsy was

required in the rectum but a normal diagnosis was made by the pathologist. Good correlation is shown between the histology image and the cross-sectional OCT image. The columnar epithelium, muscularis mucosa, and submucosa are visible under histology image and under OCT image as shown in **Fig. 10.11C**. The lamina propria is not generally distinguishable from the epithelium under OCT images because it surrounds the crypts. The muscularis mucosa and submucosa boundary is visible at this particular location but is generally not appreciable.

Figure 10.12 shows a typical volumetric OCT data set obtained from a normal RAJ. **Fig. 10.12A** shows an *en face* image centered at a tissue depth of 200 μm, corresponding to the epithelial layer of this region. The dentate line, indicating the transition location from columnar to squamous epithelium, can be clearly identified in the *en face* image, with the typical crypt structure on the rectum side and uniform structure on the anus side. **Fig. 10.12B** shows a cross-sectional image along the pullback direction indicated by the green dashed line in **Fig. 10.12A**. The different features in the rectum and anus region can also be distinguished in the cross-sectional image. **Fig. 10.12C** shows a cross-sectional image along the rotary direction indicated by the blue dashed line in **Fig. 10.12A**, which is right on the dentate line and the transition between squamous and columnar epithelium can be observed. The anal glands, which are mainly present near the dentate line, can also be identified in the image. The depth of submucosa layer in the rectum part is apparently deeper, again showing the difficulty to visualize the layered architecture in the colonic mucosa. **Fig. 10.12D** shows representative histology around the RAJ. Since there was no clinical indication to biopsy at normal looking RAJ, the histology image was taken from another subject where biopsy was required around the region but a normal diagnosis was made by the pathologist. Good correlation is shown between the histology image and the cross-sectional OCT image.

10.4.2 Radiation Proctitis

Radiation Proctitis (RP) is a form of chronic inflammation and injury of the lower GI tract. This condition is common side effect of radiation therapy used to treat prostate cancer and occurs in some form in approximately 10-15% of patients. RP causes lower GI bleeding and is generally treated with radiofrequency ablation (RFA) to help regenerating thicker neosquamous tissue on top of the RP region. Therefore, imaging modalities that can provide cross-sectional visualization *in vivo* such as OCT can be helpful in terms of treatment assessment. Endoscopic OCT images of RP around RAJ were obtained in 8 data sets from 1 patients scheduled for RFA treatment. The patient tolerated the procedure well and there was not known immediate or long-term complications. **Figure 10.13** shows the endoscopic view of the RP region that OCT data sets were acquired. The vessels are very close to the surface so the area becomes red and can easily cause rectal bleeding.

Figure 10.14 shows a volumetric OCT data set obtained from the RP region. **Fig. 10.14A** shows an *en face* image centered at a tissue depth of 240 μm, corresponding to the bottom of the epithelial layer of the RAJ. Unlike the normal squamous epithelial layer observed in the normal anus, the *en face* image shows a large amount of subsurface structures, similar to the vessel structures observed in the endoscopic view shown in **Fig. 10.13**. **Figs. 10.14B and C** shows the cross-sectional images along the pullback and rotary directions indicated by the green and blue dashed line in **Fig. 10.14A**. The shadow of vessels from the lamina propria layer can be clearly appreciated, consistent with previous 3D-OCT imaging of RP using the Lightlab system [45, 46], but with much better image quality due to precise registration between each consecutive frame, so the detailed subsurface structure can be easily appreciated. The patient was scheduled to receive RFA treatment after the OCT imaging, so there is no indication to take biopsy in the region and the comparison between histology and OCT images cannot be performed in this case.

10.4.3 Polyps in Ascending (Right) Colon

One of the main purposes of the colonoscopy is to remove visible polyps inside the colon. After the polyps are removed, the histology of these polyps will later be reviewed by pathologist to determine if they are malignant. If there are a large amount of polyps in the colon, the colonoscopy plus a full polypectomy procedure can be time-consuming, and the workload of the pathology lab increases to process and review all removed polyps, which is not efficient especially when most of the polyps are hyperplastic. The ultrahigh speed endoscopic OCT system allows the image acquisition in the whole colon and can potentially work as an optical biopsy to pre-screen the polyps found endoscopically before remove them. Therefore, the image guided biopsy/polypectomy can help the whole process more time- and cost-effective. The endoscopic OCT data sets of a polyp in the ascending (right) colon were obtained from one patient underwent the standard colon screening, as shown in **Figure 10.15**, to demonstrate the concept of imaging guided biopsy.

Fig. 10.15A shows the endoscopic view of the right colon polyp that OCT data sets were acquired. The polyp was around 3 mm in diameter and was right on top of a fold, so its contact with the OCT imaging catheter was limited. **Fig. 10.15B** shows an enlarged *en face* OCT image centered at a tissue depth of 300 μm, corresponding to the bottom of the epithelial layer of the polyp. The well organized, round crypt structure can be observed in the *en face* image, while a portion of the image shows stripe-like structure due to the tilted crypt structure pressed by the imaging catheter. **Figs. 10.15C and D** show cross-sectional images along the pullback and rotary directions, respectively. Both vertical and tilted crypt structure can also be clearly seen in these cross-sectional images. There is no branching feature observed in the polyp based on the volumetric OCT images, suggesting it can be a benign polyp. The right colon polyp was resected immediately after the OCT imaging for histology comparison. **Fig. 10.15E** shows the

corresponding histology of the polyp and it was diagnosed as a hyperplastic polyp, consistent with the observation of the OCT images. The ability to investigate the 3D structure of the polyps *in vivo* can provide instant feedback to the clinician and might improve the efficiency of the overall colonoscopy in the future.

10.5 Other Organs in the GI Tract

The use of micro-motor based imaging catheter in the system also extend endoscopic OCT imaging into other organs in the GI tract that are difficult to access with the typical proximal rotary catheters. Although the length of proximal rotary catheters were designed to work with standard endoscopes or colonoscopes, they are not able to produce uniform and stable scanning if there are multiple bends or tight bending curvature, so volumetric OCT imaging has not been demonstrated in the GI tract other than esophagus or colon. In this section, volumetric OCT data sets from normal duodenum and terminal ileum with corresponding histology will be presented, demonstrating the new clinical applications of endoscopic OCT.

10.5.1 Duodenum

Fig. 10.16A shows the diagram of the GI tract with the duodenum highlighted. Duodenum is the first section of the small intestine with a length of 25-38 cm in adult and connects the stomach and the jejunum. The duodenum is mainly responsible for the breakdown of food using enzyme. The main feature of the duodenum is its villi, which has a leafy-looking appearance. The duodenum has a unique Brunner's glands that can produce a mucus-rich alkaline secretion to protect the acidic content from the stomach, keep the intestine enzyme to be active, and lubricate the intestine wall. The diseases that can happen in the duodenum include Crohn's disease, celiac disease, peptic ulcer (duodenal ulcer), and duodenal cancer. The use of endoscopic OCT can potentially benefit the diagnosis of pathology in the duodenum with its optical sectioning capability, and can help the clinician determine the treatment option in the same endoscopy session.

Endoscopic OCT images of the duodenum were obtained in 3 data sets from 1 patients scheduled for standard upper endoscopy surveillance. The patient tolerated the procedure well and there was not known immediate or long-term complications. **Fig. 10.16B** shows the endoscopic view with the OCT imaging catheter placed on top of the normal duodenum. The healthy villi can be distinguished from the endoscopic view without any irregularity on the surface. **Fig. 10.16C** shows an *en face* OCT image centered at a tissue depth of 50 μm, corresponding to the top surface of the villi. The *en face* image on the duodenum surface shows similar structure observed in the endoscopic view but with higher magnification, allowing better evaluation of the morphology of the duodenum. **Fig. 10.16D** shows another *en face* OCT

image centered at a tissue depth of 300 μm, corresponding to the base of the duodenal villi. The round, crypt-like structure can be distinguished in the *en face* image at the depth, showing the transverse cross-section of the villi. There is a slight motion artifact can be observed in the middle of the image, which was caused by the imaging catheter movement during the image acquisition, but in general the data set is still usable for diagnosis purpose. The high imaging speed can lower the distortion effect from the motion and thus improve the quality yield of the volumetric data sets. **Figs. 10.16E and F** show cross-sectional images along the pullback and rotary direction. Vertical streaks observed in the cross-sectional images are the typical feature of the villi. Brunner's glands can be distinguished as from the submucosa layer in **Fig. 10.16F**, as indicated by the red arrow. The imaged duodenum area was biopsied immediately after the OCT imaging for histology comparison. **Fig. 10.16G** shows the corresponding histology and it was diagnosed as a normal duodenum, consistent with the observation of the OCT images. In this case, the depth of the standard biopsy barely reaches the muscularis mucosa, while OCT images consistently show as deep as the submucosa layers with much larger coverage, suggesting endoscopic OCT can be used as an imaging-guided biopsy tool to minimize the sampling error of random biopsy, the current gold standard of diagnosis.

10.5.2 Terminal Ileum

Fig. 10.17A shows the diagram of the GI tract with the terminal ileum highlighted. In contrast with the duodenum, the terminal ileum is the most distal section of the small intestine and connects to cecum, the pouch between the small intestine and the ascending colon. The main function of the ileum is to absorb nutrition that is not absorbed by the jejunum, the middle section of the small intestine. The epithelial feature of the ileum is also villi, which confers the ileum with an extremely large surface area for absorbing nutrition. The ileum also secretes the protease and carbohydrase enzymes, responsible for the final stage of protein and carbohydrate digestion, into the intestine. The main feature of the terminal ileum is high concentration of lymphatic follicles, also known as Preyer's patches, scattering between the lamina propria and muscularis mucosa. The diseases that can happen in the ileum include Crohn's disease, ileitis, and ileum cancer (very rare). The use of endoscopic OCT can potentially benefit the diagnosis of pathology in the duodenum with its optical sectioning capability, and can help the clinician determine the treatment option in the same endoscopy session.

Endoscopic OCT images of the terminal ileum were obtained in 5 data sets from 2 patients scheduled for standard colon screening. The patient tolerated the procedure well and there was not known immediate or long-term complications. **Fig. 10.17B** shows the endoscopic view with the OCT imaging catheter placed on top of the normal terminal ileum. The healthy villi can be distinguished from the endoscopic view without any irregularity on the surface. **Fig. 10.17C** shows an *en face* OCT image centered at a

tissue depth of 50 μm, corresponding to the top surface of the villi. The *en face* image on the terminal ileum surface shows similar structure observed in the endoscopic view but with high magnification, allowing better evaluation of the morphology of the duodenum. **Fig. 10.17D** shows another *en face* OCT image centered at a tissue depth of 300 μm, corresponding to the base of the ileum villi. The round, crypt-like structure can be distinguished in the *en face* image at the depth, showing the transverse cross-section of the villi. Most of the villi in the data set are tilted due to the pressure from the imaging catheter, which is common for imaging modalities that require direct tissue contact. **Fig. 10.17E** and **Fig. 10.17F** show cross-sectional images along the pullback and rotary direction. The tilted villous structure can be observed in the cross-sectional images. The Preyer's patches can be observed in **Fig 10.17E** as the thick, hyposcattering layer between the hyperscattering lamina propria and submucosa layers. The imaged terminal ileum area was biopsied immediately after the OCT imaging for histology comparison. **Fig. 10.17G** shows the corresponding histology and it was diagnosed as a normal terminal ileum, consistent with the observation of the OCT images. In this case, similar to the biopsy in the duodenum, the depth of the standard biopsy barely reaches the muscularis mucosa, while OCT images consistently show as deep as the submucosa layers with much larger coverage, suggesting endoscopic OCT can be used as an imaging-guided biopsy tool to minimize the sampling error of random biopsy, the current gold standard of diagnosis.

10.6 Other Pathology

The ultrahigh speed endoscopic OCT system can also be used to investigate the pathology in the GI tract that is difficult to access with the typical proximal rotary catheters. Locations where require sharp bending or retroflexion of the endoscope to visualize are usually extremely difficult to perform OCT imaging due to the limitation of the catheter robustness and the scanning uniformity. In this section, volumetric OCT data sets from gastric antral vascular ectasia (GAVE), hiatal hernia, and squamous papilloma with corresponding histology will be presented, suggesting more pathology can be studies *in vivo* using endoscopic OCT.

10.6.1 Gastric Antral Vascular Ectasia (GAVE)

GAVE, also known as watermelon stomach, is a condition in the stomach associated with dilated small blood vessels [47-49]. GAVE results in chronic GI bleeding and can cause anemia as well as occult blood in the stool. The symptom of GAVE is similar to duodenal ulcer, but each of these diseases has different etiology so the treatment/management can be different. With the watermelon stripes observed in the stomach, GAVE is usually diagnosed definitively by endoscopic biopsy. GAVE is characterized by dilated capillary in the lamina propria layer with fibrin thrombi. Similar to radiation proctitis (RP) in the

distal colon, GAVE can be treated with ablation therapies such as argon plasma coagulation (APC), radiofrequency ablation (RFA), and cryospray ablation (CSA), while surgery is usually not required. GAVE occurs in the antrum, the most distal part of the stomach, so the distal end of the endoscope is required to bend more than 90° to evaluate the ROI, as **Fig. 10.18A** shows [50]. Doppler 2D-OCT has been used to study the vasculature of GAVE in single cross-section [51], but to date no 3D-OCT is used to study its volumetric morphology structure due to the scanning stability of the traditional endoscopic system. The use of volumetric endoscopic OCT can potentially benefit the diagnosis of pathology in the antrum with its optical sectioning capability, and can help the clinician determine the treatment option in the same endoscopy session.

Endoscopic OCT images of the GAVE were obtained in 3 data sets from 1 patients scheduled for upper endoscopy with potential GAVE treatment. The patient tolerated the procedure well and there was not known immediate or long-term complications. **Fig. 10.18B** shows the endoscopic view with the OCT imaging catheter placed on top of the GAVE region. The typical watermelon stripes can be clearly distinguished in the endoscopic view. **Fig. 10.18C** shows an *en face* OCT image centered at a tissue depth of 150 μm, corresponding to the top surface of the gastric pits in the antrum. The OCT data set was acquired right on the edge of on watermelon stripe, so lower side of the *en face* image shows randomly distributed dark spots on the lower side, which can be the fibrin thrombi in the lamina propria, while the upper half of the *en face* image shows relatively normal gastric pit pattern. **Figs. 10.18D and E** show cross-sectional images along the pullback and rotary direction. Multiple dilated, hyposcattering, but transparent glandular structure can be observed within the submucosa layer of the GAVE region. The imaged GAVE site was biopsied immediately after the OCT imaging for histology comparison. **Fig. 10.18E** shows the corresponding histology and it was diagnosed as GAVE, consistent with the observation of the OCT images. In this case, the depth of the standard biopsy does not reach the submucosa so does not cover the dilated glands observed in the cross-sectional OCT images, which consistently show as deep as the submucosa layers with much larger coverage, suggesting endoscopic OCT can be used as an imaging-guided biopsy tool to minimize the sampling error of random biopsy, the current gold standard of diagnosis.

10.6.2 Hiatal Hernia

The hiatal hernia is the protrusion of the upper part of the stomach into the thorax through a weakness in diaphragm [52]. Most of the hiatal hernia cases (95%) are sliding hiatal hernia, where the GEJ moves above the diaphragm together with a small portion of the stomach. The other type, rolling hiatal hernia, is caused by the protrusion of the stomach only without involving the GEJ. Hiatal hernia is usually asymptomatic but can cause symptoms similar to other diseases such as non-cardiac chest pain (NCCP) or

discomfort in lower esophagus. Its condition also promotes reflux of gastric content and thus is associated with gastroesophageal reflux disease (GERD) such as esophagitis, Barrett's esophagus, and esophageal cancer. Retroflexion endoscopy allows inspection of the GEJ or hiatal hernia from the stomach side, and the evaluation of the acid reflux can be performed by observing how tightly or loosely the tissues are applied to the endoscope [53]. Due to the small radius of curvature of the hiatal hernia structure, OCT imaging usually cannot be performed in the hiatal hernia with the distal end of the endoscope in the neutral position due to maintain imaging catheter contact with the tissue. The new generation system allows OCT imaging even when the endoscope is in the retroflex position, as **Fig. 10.19A** shows, so more comprehensive 3D information of the hiatal hernia can be obtained and can be used to study the risk attribution of hiatal hernia to GERD.

Endoscopic OCT images of the hiatal hernia were obtained in 6 data sets from 1 patient scheduled for upper endoscopy for GAVE screening. During the procedure, the patient was found having a rolling hiatal hernia. Then the clinician introduced the imaging catheter until a small portion of the distal tip showed up in the endoscopic field of view, retroflexed the endoscope, and then push the imaging catheter all the way out to its normal operating position. The patient tolerated the procedure well and there was not known immediate or long-term complications. **Fig. 10.19B** shows the endoscopic view with the OCT imaging catheter placed on top of the GEJ (top of the hiatal hernia). The typical GEJ can be clearly distinguished in the endoscopic view from the gastric side. **Fig. 10.19C** shows an *en face* OCT image centered at a tissue depth of 200 μm, corresponding to the base of the glandular structure around GEJ. The image window of the catheter was right on the fold of GEJ so the *en face* image shows a big gap in the middle with tissue on both upper and lower sides. The *en face* features on both sides are different but either of them is uniform as the normal esophagus, indicating that the esophagus side of GEJ might be BE. **Fig. 10.19D** shows a cross-sectional image cut through the lower side of GEJ along the pullback direction, and multiple dilated, hypointense, but transparent glandular structure can be observed within the submucosa layer similar to the glandular structure observed in the GAVE case, suggesting this portion is the stomach side of GEJ. **Fig. 10.19E** shows a cross-sectional image cut through the upper side of GEJ along the pullback direction, where irregular glandular structure on top of the hyperintensive submocosa layer. The feature is similar to non-dysplastic BE observed in **Figure 10.5**, suggesting this portion is esophagus side of GEJ with non-dysplastic BE. **Fig. 10.19F** shows a cross-sectional image along the rotary direction, and different cross-sectional features are observed on different side of the tissue. The orientation of the data set is not typically pulled back from the proximal side to the distal side of GEJ (note it was retroflexed). Instead, the imaging catheter was placed along one fold of GEJ with stomach on one side and BE on the other side, which caused this particular orientation. The imaged GEJ site was biopsied immediately after the OCT imaging for histology comparison. **Fig. 10.19G** shows the

corresponding histology and it was diagnosed as non-dysplastic BE, consistent with the observation of the OCT images. These results demonstrate that the new generation endoscopic OCT imaging is no longer limited by the orientations of the endoscope and provides new prospective to evaluate the GI tract.

10.6.3 Squamous Papilloma

Squamous papilloma is a benign papilloma that arises from the squamous epithelium, and is a result of infection with human papillomavirus [54]. Squamous papilloma is usually painless, and is not treated unless it causes pain. It does not generally mutate to cancerous growth, nor do they grow or spread. When the treatment is required, squamous papilloma is typically removed using ablation therapies or endoscopic mucosal resection (EMR).

Endoscopic OCT data sets of the squamous papilloma were obtained in 4 data sets from 1 patient scheduled for sigmoidoscopy. The squamous papilloma was found on the anal canal side of RAJ with the retroflexion of the sigmoidoscope. **Figure 10.20** shows a series of cross-sectional OCT images along the rotary direction and the corresponding histology of the squamous papilloma. The epithelium layer shown on right sides of the OCT images is significantly thicker than that shown on the left. There are hyperintensive stripes observed in the thick epithelium layer in **Fig. 10.20D**, which are the typical papilloma structures thin lamina propria inside the thick squamous epithelium. The squamous papilloma was removed using EMR immediately after acquiring OCT data sets. **Fig. 10.20E** shows the corresponding histology, and excellent correlation is shown between the OCT images and histology, again demonstrating the optical biopsy utility of the endoscopic OCT imaging as well as the retroflexion imaging capability of the new generation system.

10.7 Endoscopic Angiography

In addition to the surface maturation and the pit pattern, vascular pattern on the surface of the lesion is also another important indicator in detecting dysplasia. Imaging technologies that can enhance the surface vascular contrast, such as chromoendoscopy or NBI combined with magnified endoscopy, have been demonstrated extremely sensitive to detect high grade dysplasia (HGD) [16, 17]. Several OCT techniques have been developed to image microvasculature networks without the need of exogenous contrast agents. Both phase-based methods (Doppler OCT [51, 55-67], optical microangiagraphy [68-70], and phase sensitive OCT [71-75]) and amplitude-based methods (speckle variance OCT [76-80]) have been demonstrated in human retina and skin, and are useful for monitoring the microvasculature changes after therapeutic intervention and assessment of disease progression [58, 81, 82]. To date, most of the OCT angiography applications are based on table-top microscope systems because dense sampling and high frame-by-frame scanning stability are very critical to resolve the microvasculature with high sensitivity.

Although Doppler OCT has been used to measure the blood flow of vessels in the GI tract, it is limited in the relatively larger vessels that can be visualized in the standard intensity-based images due to the limitation of imaging speed and scanning stability [63], so the potential of endoscopic OCT angiography has not been fully explored yet.

The ultrahigh speed endoscopic OCT system using micromotor imaging catheter can provide 10 times faster imaging speed than commercially available system and extremely high frame-by-frame scanning stability and is very ideal to perform OCT angiography. In this section, endoscopic OCT angiography will be demonstrated using this new generation system and an amplitude-based OCT angiography algorithm known as split-spectrum amplitude-decorrelation angiography (SSADA) [80]. The world's first endoscopic OCT 3D angiography in the normal esophagus, Barrett's esophagus, and colon presented here could provide important information on the detection of dysplasia and assessment of vascular diseases in the GI tract.

10.7.1 Split-spectrum Amplitude-decorrelation Angiography

Figure 10.21 shows the basic concept of SSADA. The main point of SSADA is to split the acquired full spectrum (one sweep from the swept source OCT) into multiple sub-spectra, each with a narrower bandwidth. Narrower bandwidths are intentionally created to lower the OCT axial resolution, which minimize the pulsatory bulk motion noise along the axial direction and optimized the flow detection along the transverse direction. Low resolution OCT images generated from the narrow-bandwidth spectra can be used to calculate decorrelation. Frame-by-frame decorrelation map can be generated at each sub-spectrum separately and averaged. Recombining the decorrelation images from the multiple sub-spectra yields high quality cross-sectional angiograms that used the full information in the entire OCT spectral range.

The decorrelation (D) can be simply considered as the fluctuation value of OCT intensity at one pixel. The fluctuation in the amplitude of OCT fringes can be caused by blood flow as red blood cells enter and exit a particular voxel. Hence the three consecutive frames contain fluctuation values of OCT output intensities at any given voxel within vessels, and the fluctuation intensities yield higher D values. In contrast, pixels in consecutive frames that contain static tissue have relatively constant intensities, yielding lower D values. In SSADA, D is a function of the flow velocity regardless the direction, but can be saturated at the maximum detectable flow velocity due to a limit of time resolution for each scan parameters [80]. In this preliminary experiment, the main purpose is to simply generate angiograms showing the vasculature in different tissue, so the quantification of flow velocity is not in the scope of this study.

10.7.2 Endoscopic OCT Angiography in the GI tract

Figure 10.22 shows the endoscopic OCT angiogram generated from the normal esophagus OCT data set shown in **Fig. 10.2**. **Fig. 10.22A** shows the *en face* intensity image at the imaging depth corresponding to the lamina propria layer, which contains a large amount of blood vessels including arteries, veins, and capillaries. Based on the intensity contrast, there are some larger vessels that can be distinguished as vague contours with slightly lower intensity in the *en face* image. **Fig. 10.22B** shows an *en face* image using the same data set processed by SSADA, at the exactly same depth. SSADA dramatically enhances the contrast of the vasculature in the tissue and thus the vessel network in the lamina propria layer can be clearly visualized. Some line artifacts can be observed along the rotary and pullback directions, which are caused by the heartbeat of the patient and the longitudinal textures on the sheath of the imaging catheter. **Figs. 10.22C and D** show cross-sectional SSADA images along the pullback and rotary directions. Most of the vessel signal comes from the lamina propria layer, while the high signal level in the submucosa layer is caused by the projection of decorrelation of flow in the upper layers onto the lower layer with strong reflection signal. These results indicate that, for the first time, endoscopic OCT angiography is successfully realized.

Figure 10.23 shows the endoscopic OCT angiogram generated from the non-dysplastic BE OCT data set shown in **Fig. 10.5**. **Fig. 10.23A** shows the *en face* intensity image where the SCJ can be delineated based on the difference of surface structures. **Fig. 10.23B** shows an *en face* SSADA image at the tissue depth of 80 μm, corresponding to the epithelium layer and exactly same depth as **Fig. 10.23A**. At this tissue depth, the vascular network can be visualized in the BE region while there is not much decorrelation observed in the normal region, which is consistent with the imaging results using chromoendoscopy and NBI. It is also notable that the vascular structure along the SCJ is denser than other regions, which may be related to the progression of BE. **Fig. 10.23C** shows an *en face* SSADA image at the tissue depth of 250 μm, corresponding to the lamina propria layer. The vasculature in the normal regions shows similar structure as that in **Fig. 10.22B**, while the BE region shows no apparent structure due to the projection artifact mentioned earlier. Based on the results shown here, endoscopic OCT angiography can reveal the surface vascular pattern in BE without the need of any additional contrast agent and thus can provide valuable information for identification of dysplastic BE.

SSADA can also be used in the lower GI tract. **Figure 10.24** shows the angiogram generated from the recto-anal junction (RAJ) OCT data set shown in **Figure 10.12**. **Fig. 10.24A** shows the *en face* intensity image where the dentate line can be delineated based on the difference of surface structures. **Fig. 10.24B** shows an *en face* image centered at a tissue depth of 200 μm, corresponding to the epithelial layer of this region layer and exactly same depth as **Fig. 10.24A**. At this tissue depth, the vascular network can be visualized in the rectum side while there is not much decorrelation observed in the anal canal side,

consistent with the structural difference between the columnar and squamous. Unlike the SCJ, the density of vascular structure around the dentate line is not apparently different from other rectum region. **Fig. 10.24C** shows an *en face* SSADA image at the tissue depth of 250 μm, corresponding to the lamina propria layer. The vasculature in the anal canal side can be observed, while the BE region shows no apparent structure due to the projection artifact mentioned earlier. Endoscopic OCT angiography can reveal the surface vascular pattern in the colon without the need of any additional contrast agent and thus can be used to *in vivo* evaluate the polyps and guide biopsy.

In summary, the world's first endoscopic OCT angiography in the human GI tract is demonstrated here. The use of SSADA enhances the contrast of vasculature in tissue using the intensity decorrelation between consecutive frames. Although it was not covered in this section, the speed of blood flow is proportional to decorrelation and potentially the blood flow can be quantified. The heartbeat and the parasitic reflection of the imaging catheter can generate artifacts in the angiograms and degrade the image quality, which are possible to minimize with more advanced signal processing methods. The projection effect of SSADA causes the loss of the flow information in the deeper region, but this should not be a critical issue because most of the applications focus on the surface vascular structure. The ability to visualize the vasculature in the GI tract opens a whole new window of investigating tumor-associated neovascularization and 3D reconstruction of its aberrant architecture, as well as the research of vessel-related diseases such as radiation proctitis and GAVE.

10.8 Figures

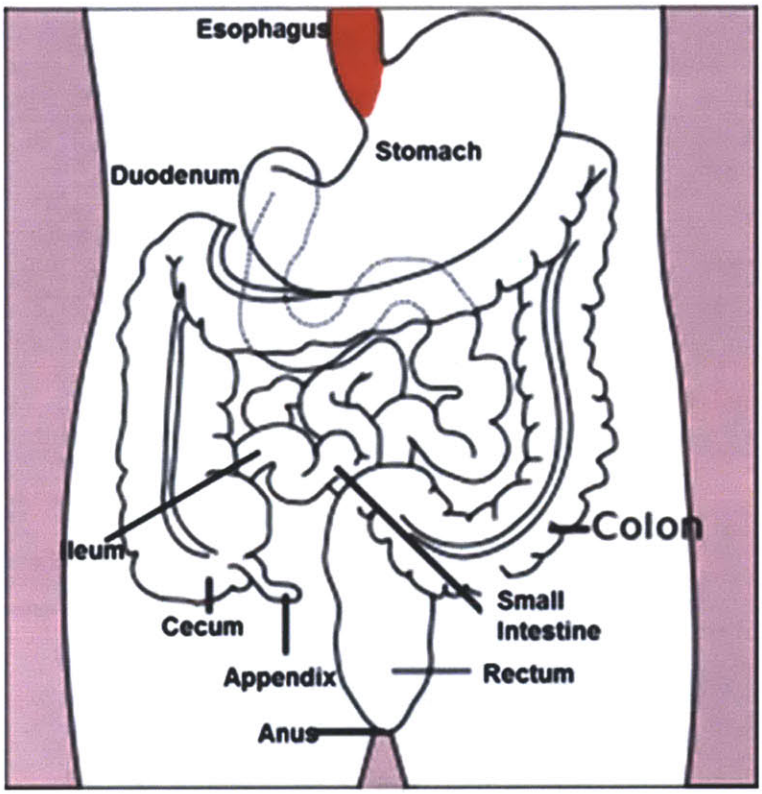

Figure 10.1. Diagram of the human gastrointestinal (GI) tract, with the esophagus highlighted with red. This diagram is from public domain source at http://www.cancer.gov/cancerinfo/wyntk/colon-and-rectum.

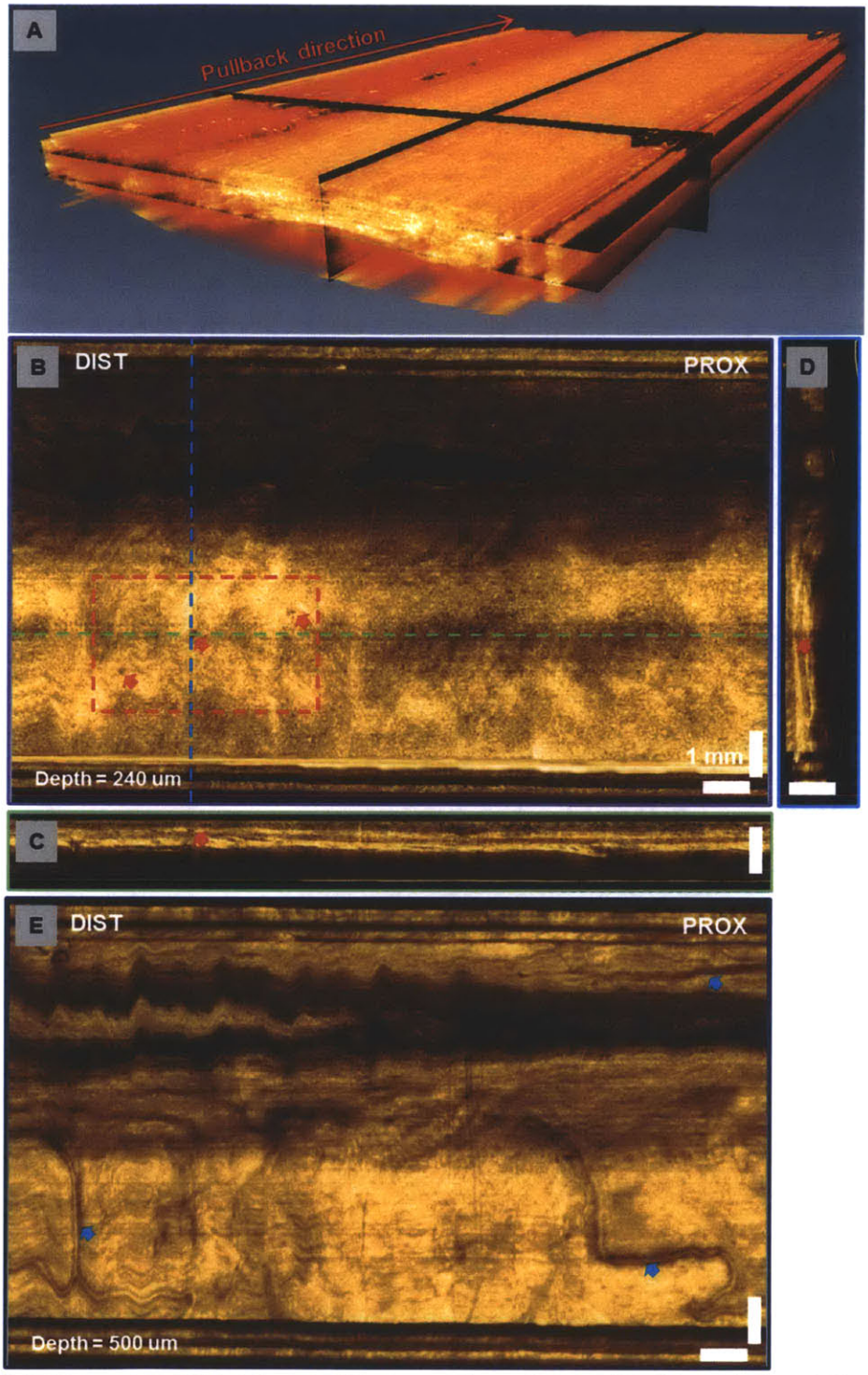

Figure 10.2. Volumetric OCT data set of the normal esophagus. (A) 3D rendering of the data set. (B) *En face* image at the imaging depth of 240 um. (C) Cross-sectional image along the pullback direction. (D) Cross-sectional image along the rotary direction. (E) *En face* image at the imaging depth of 500 um. Red arrows: SSIM. Blue arrows: Vessels.

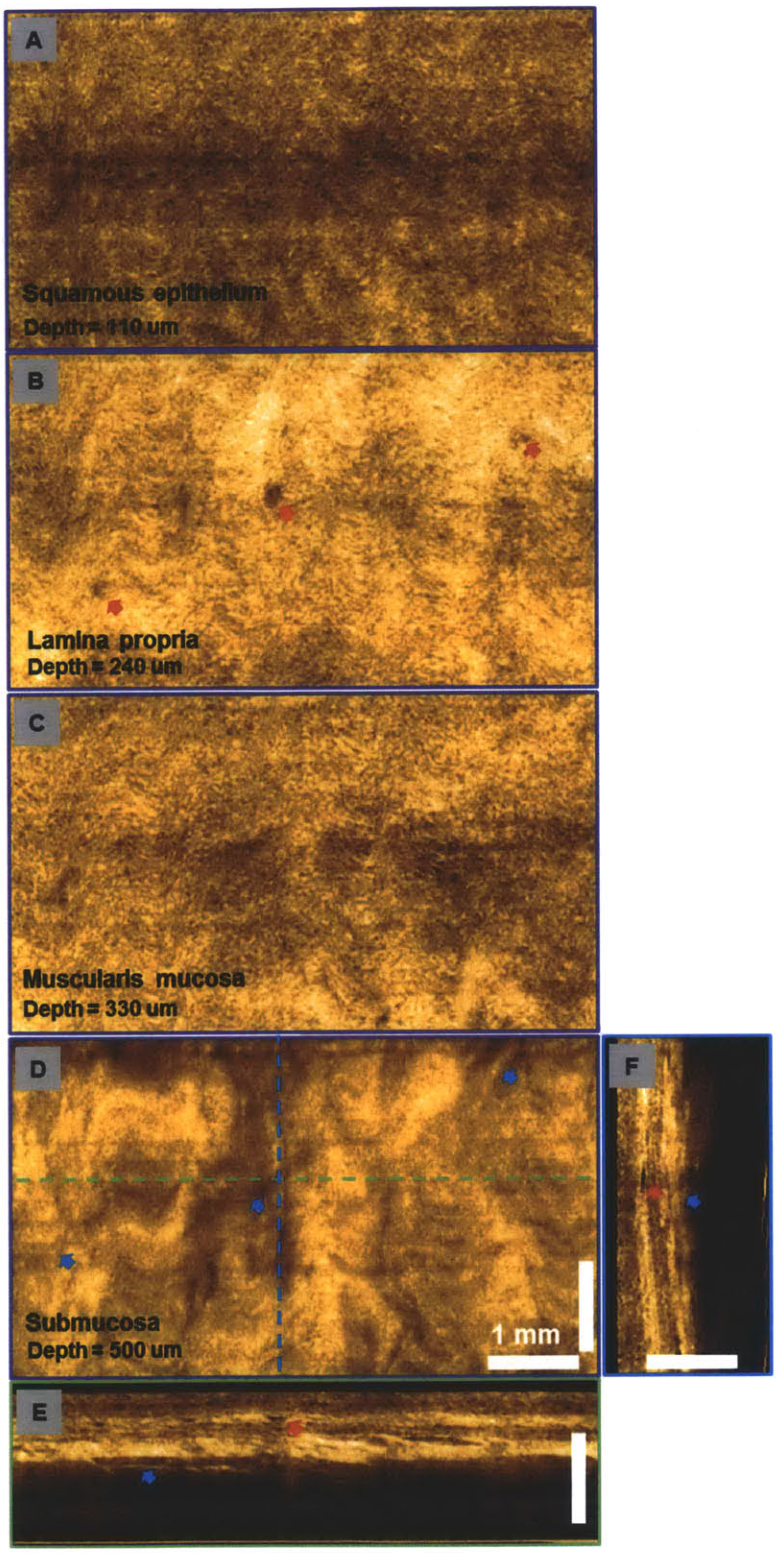

Figure 10.3. Enlarged view of the volumetric OCT data set of the normal esophagus at different imaging depth. (A) Squamous epithelium. (B) Lamina propria. (C) Muscularis mucosa. (D) Submucosa. (E) Cross-sectional image along the pullback direction. (F) Cross-sectional image along the rotary direction. Red arrows: SSIM. Blue arrows: Vessels.

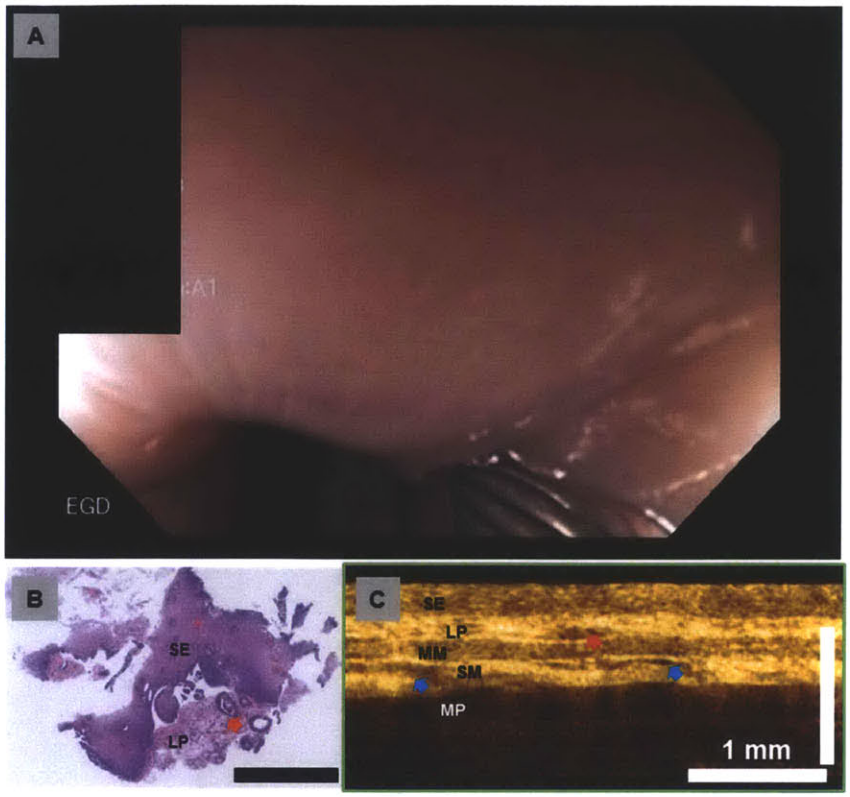

Figure 10.4. (A) Endoscopic view of the normal esophagus, which shows pale-pink, smooth, and uniform surface feature. (B) Corresponding histology taken from the imaged region, where SSIM can be identified underneath the squamous epithelium. (C) Enlarged view of the cross-sectional image along the pullback direction. SE: squamous epithelium; LP: lamina propria; MM: muscularis mucosa; SM: submucosa; MP: muscularis propria. Red arrows: SSIM. Blue arrows: Vessels.

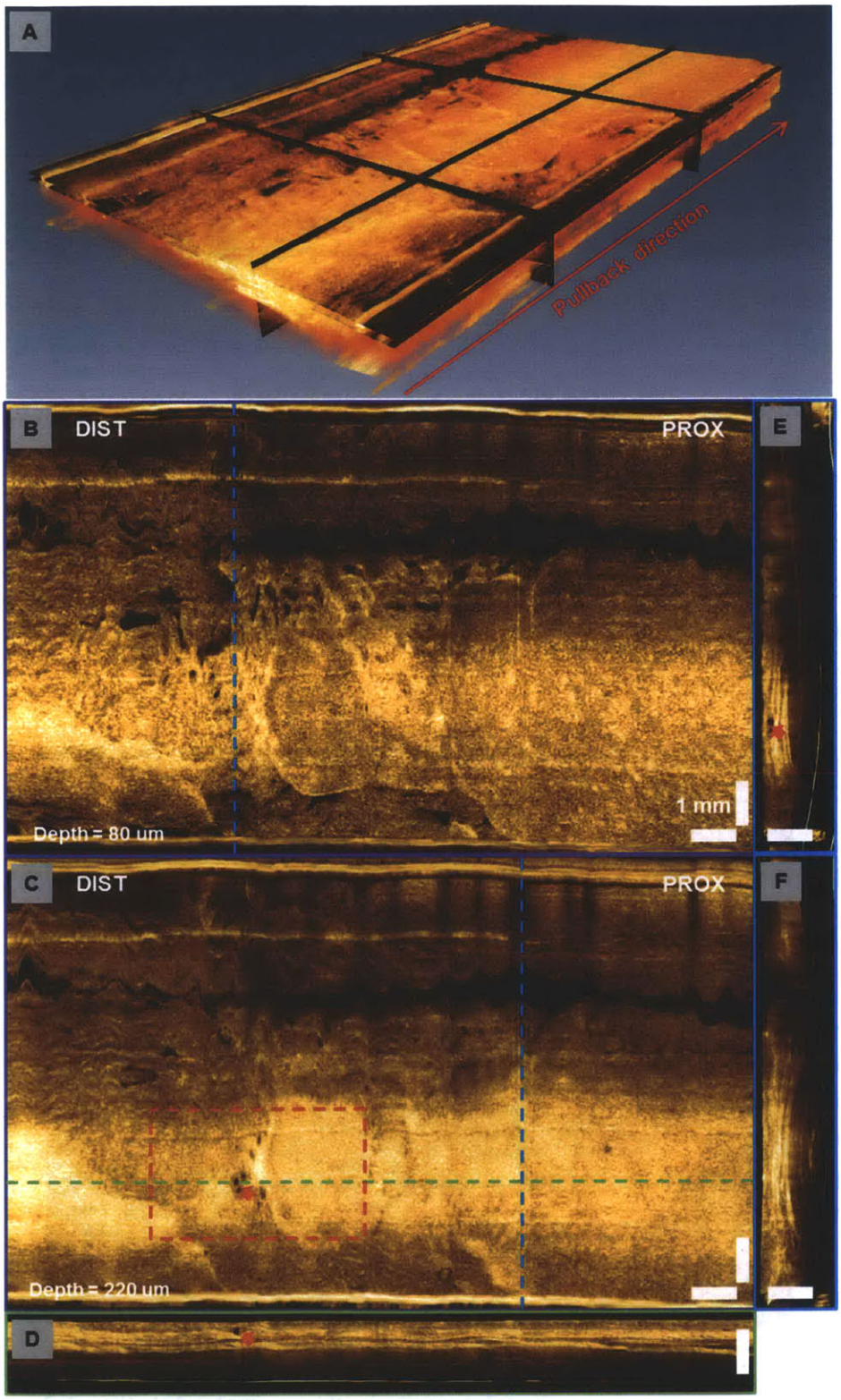

Figure 10.5. Volumetric OCT data set of the non-dysplastic Barrett's esophagus. (A) 3D rendering of the data set. (B) *En face* image at the imaging depth of 80 um. (C) *En face* image at the imaging depth of 220 um. (D) Cross-sectional image along the pullback direction. (E) Cross-sectional image along the rotary direction in BE region. (F) Cross-sectional image along the rotary direction in normal esophagus region. Red arrows: BE glands.

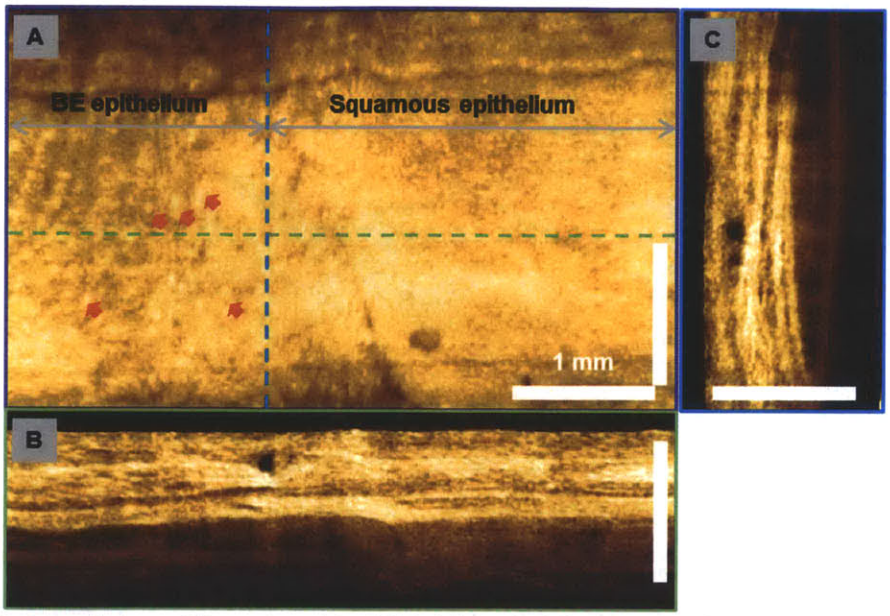

Figure 10.6. Enlarged view of the volumetric OCT data set of the non-dysplastic BE. (A) *En face* image at the imaging depth within epithelium layer. (B) Cross-sectional image along the pullback direction. (C) Cross-sectional image along the rotary direction. Red arrows: pit pattern in the BE region.

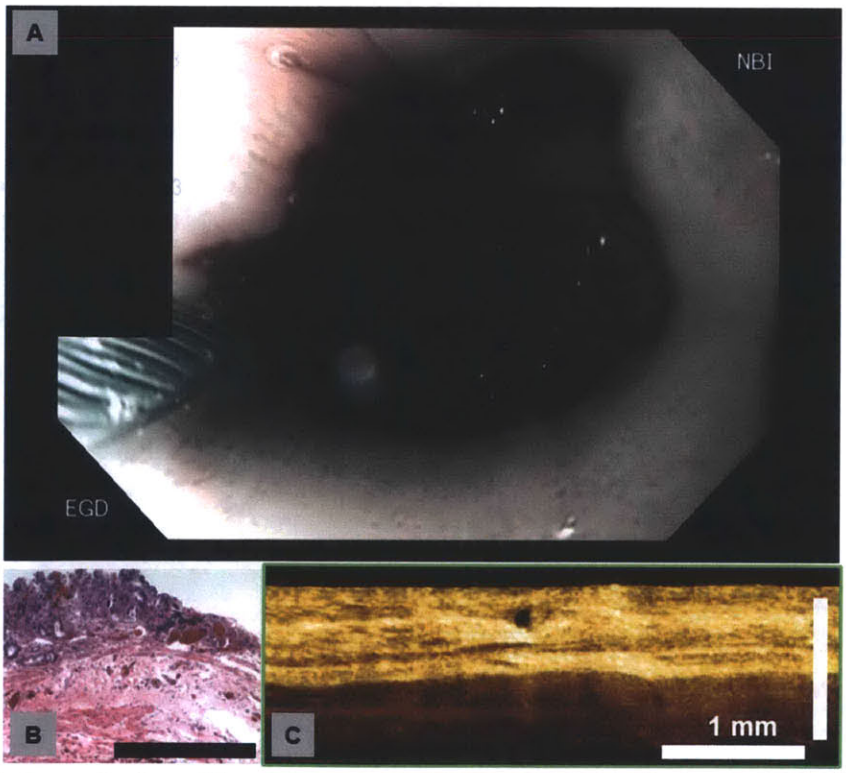

Figure 10.7. (A) Endoscopic view of the non-dysplastic BE using NBI, which shows dark-red, inflamed, and irregular surface feature. (B) Corresponding histology taken from the imaged region, numerous BE glands can be observed with minor distortion of the layered architecture. (C) Enlarged view of the cross-sectional image along the pullback direction.

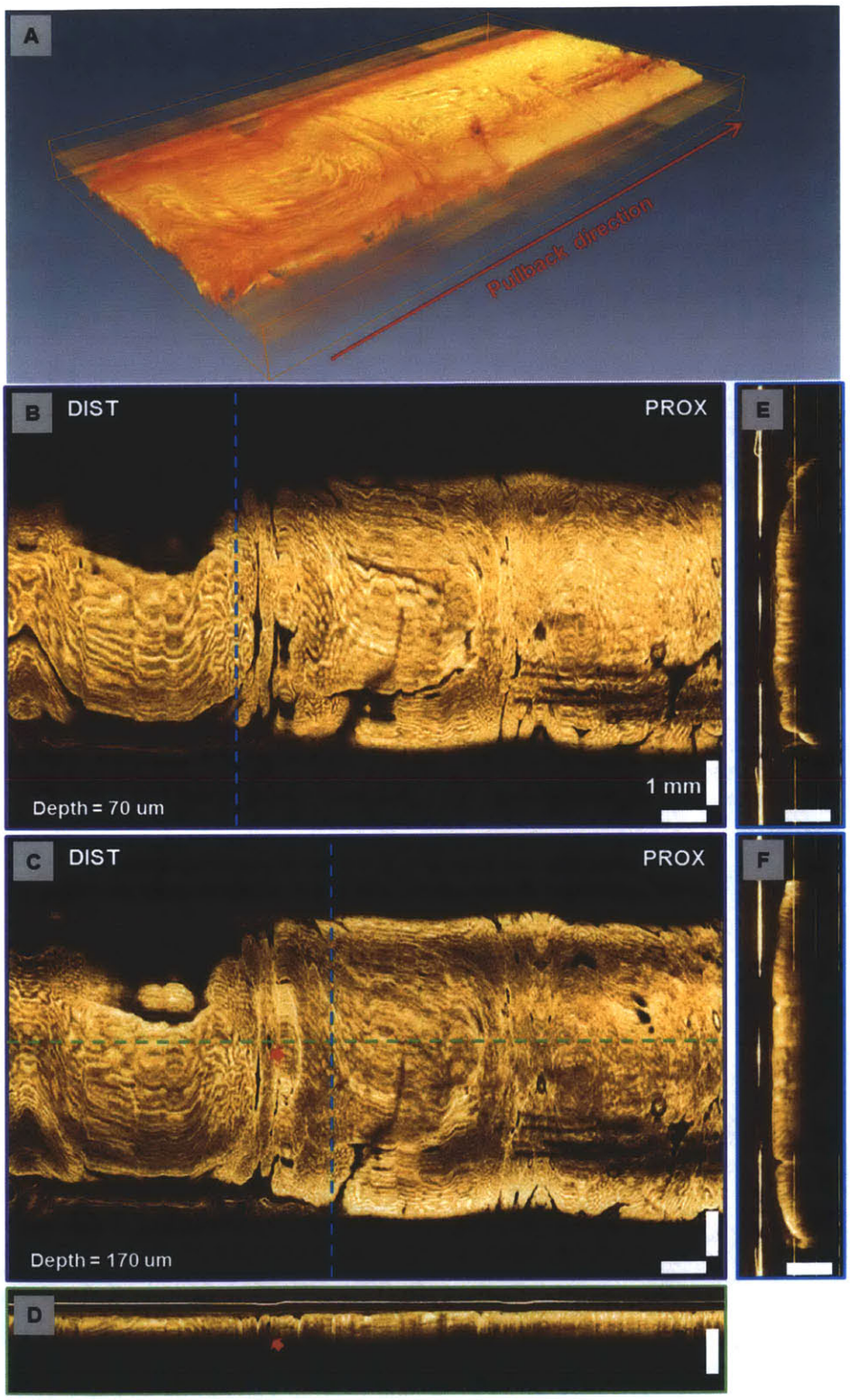

Figure 10.8. Volumetric OCT data set of dysplastic Barrett's esophagus. (A) 3D rendering of the data set. (B) *En face* image at the imaging depth of 70 um. (C) *En face* image at the imaging depth of 170 um. (D) Cross-sectional image along the pullback direction. (E) Cross-sectional image along the rotary direction in the BE region with branching pit pattern. (F) Cross-sectional image in the BE region with round pit pattern. Red arrows: BE glands.

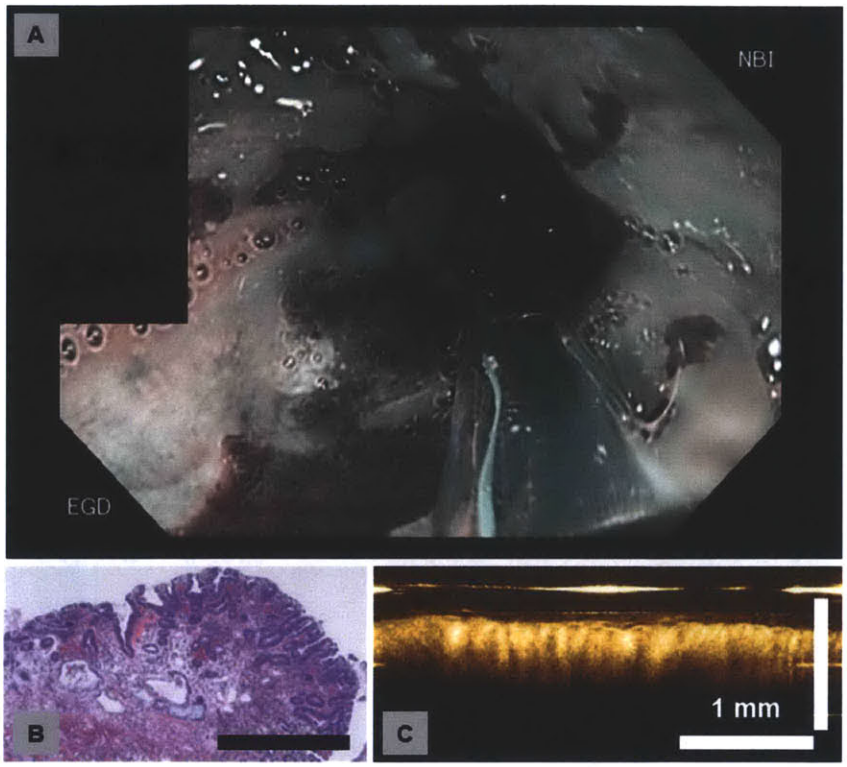

Figure 10.9. (A) Endoscopic view of the dysplastic BE using NBI, which shows dark-red, inflamed, and irregular surface feature similar to non-dysplastic BE. (B) Corresponding histology taken from the imaged region, which is diagnosed as focal high grade dysplasia. (C) Enlarged view of the cross-sectional image along the rotary direction.

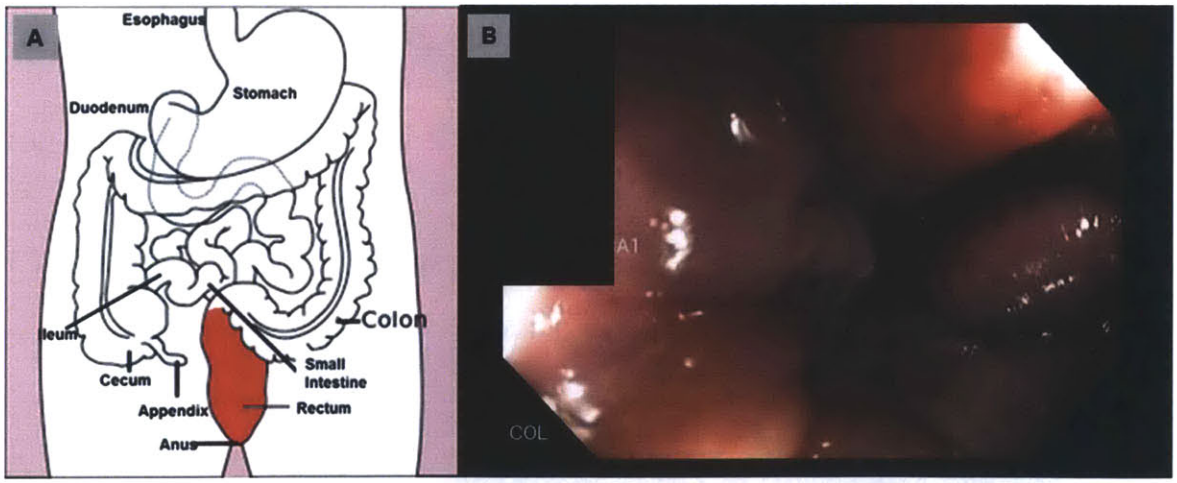

Figure 10.10. (A) Diagram of the human gastrointestinal (GI) tract, with the rectum and anal canal highlighted with red. (B) Endoscopic view of the recto-anal junction, with rectum on the distal side and anal canal on the proximal side in the field of view.

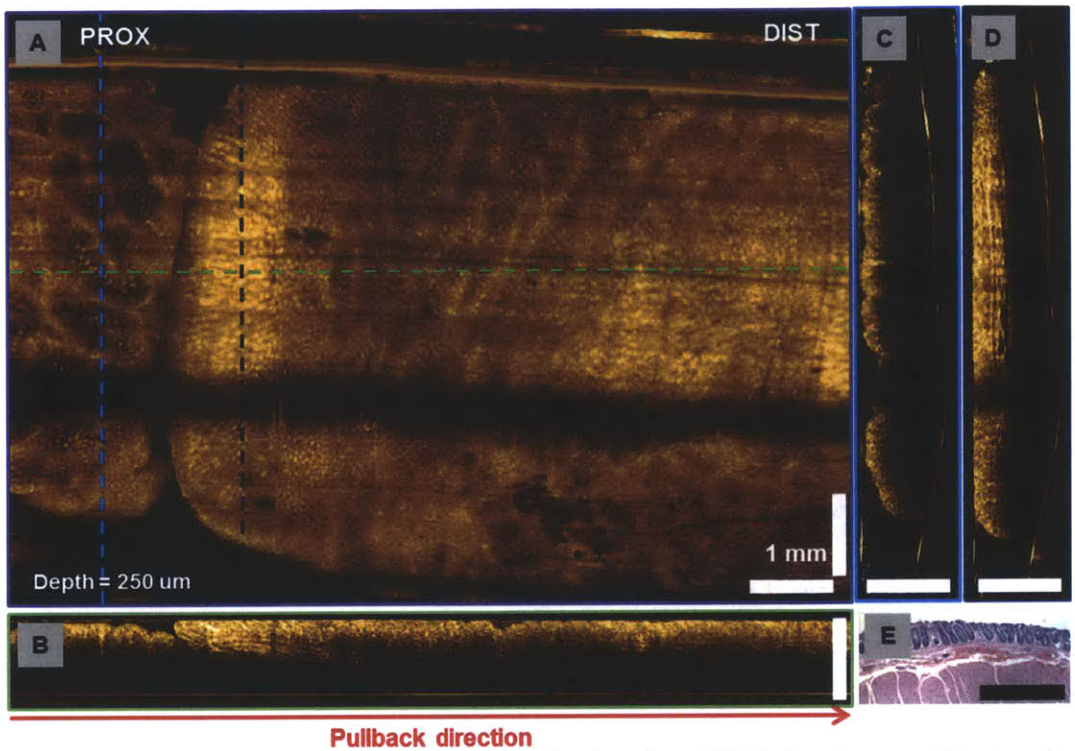

Figure 10.11. Volumetric OCT data set of human proximal rectum. (A) *En face* image at the imaging depth of 250 um. (B) Cross-sectional image along the pullback direction. (C) Cross-sectional image along the rotary direction in the BE region with branching pit pattern. (D) Cross-sectional image in the BE region with round pit pattern. (E) Representative histology of human rectum.

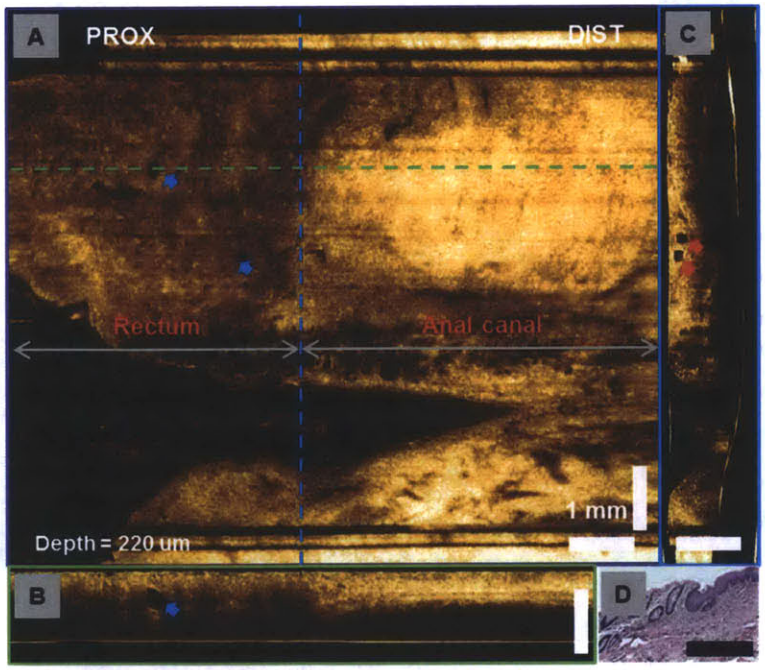

Figure 10.12. Volumetric OCT data set of the recto-anal junction. (A) *En face* image at the imaging depth of 220 um. (B) Cross-sectional image along the pullback direction. (C) Cross-sectional image along the rotary direction on top of the dentate line. (D) Representative histology of human RAJ. Red arrows: anal gland. Blue arrows: rectal glands.

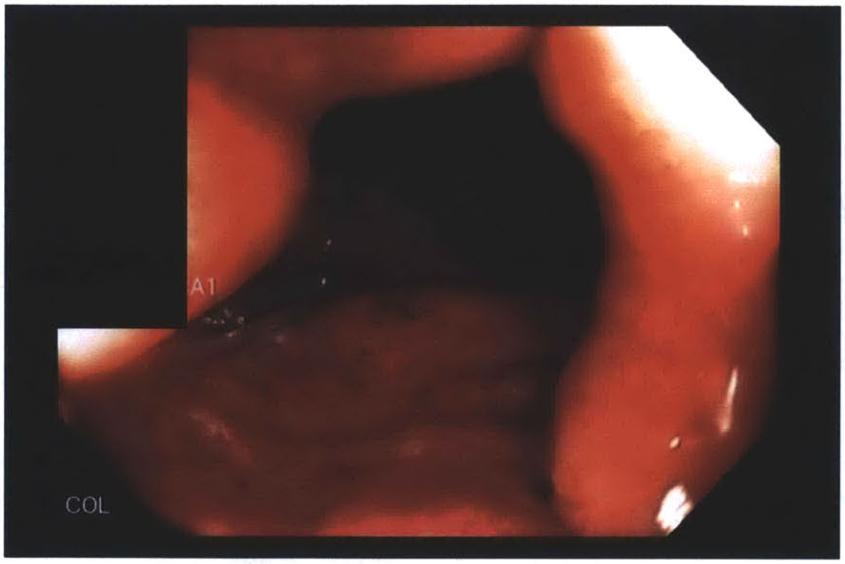

Figure 10.13. Endoscopic view of radiation proctitis near the recto-anal junction, with rectum on the distal side and anal canal on the proximal side in the field of view.

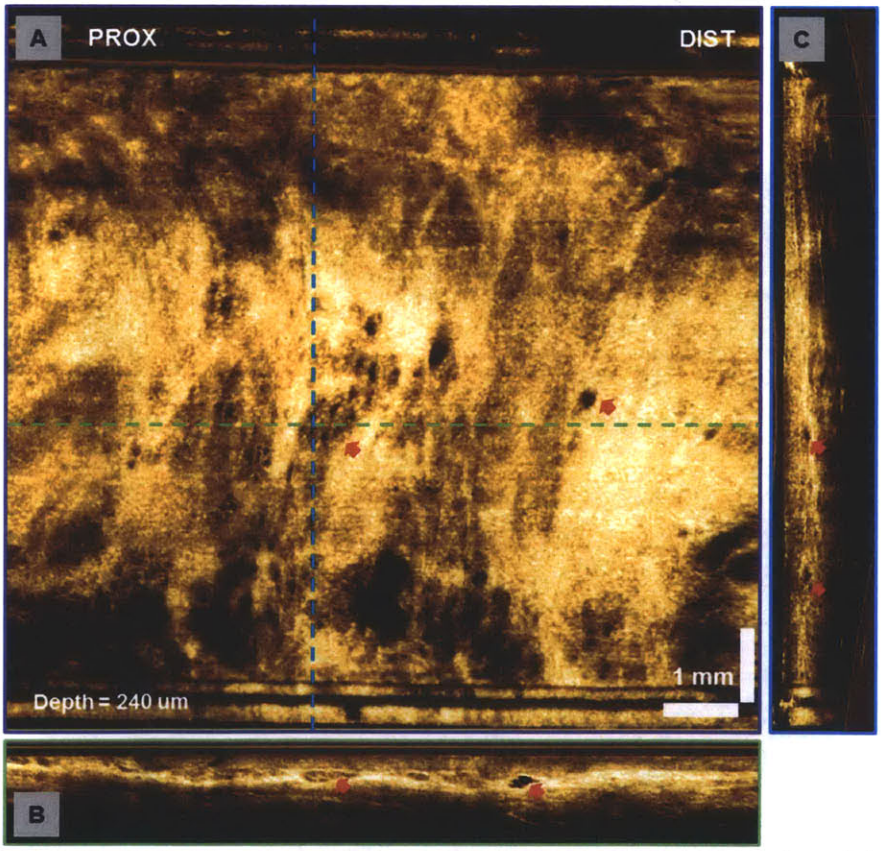

Figure 10.14. Volumetric OCT data set of radiation proctitis near the recto-anal junction. (A) *En face* image at the imaging depth of 240 um shows numerous subsurface vessel structure. (B) Cross-sectional image along the pullback direction. (C) Cross-sectional image along the rotary direction. Red arrows: vessels.

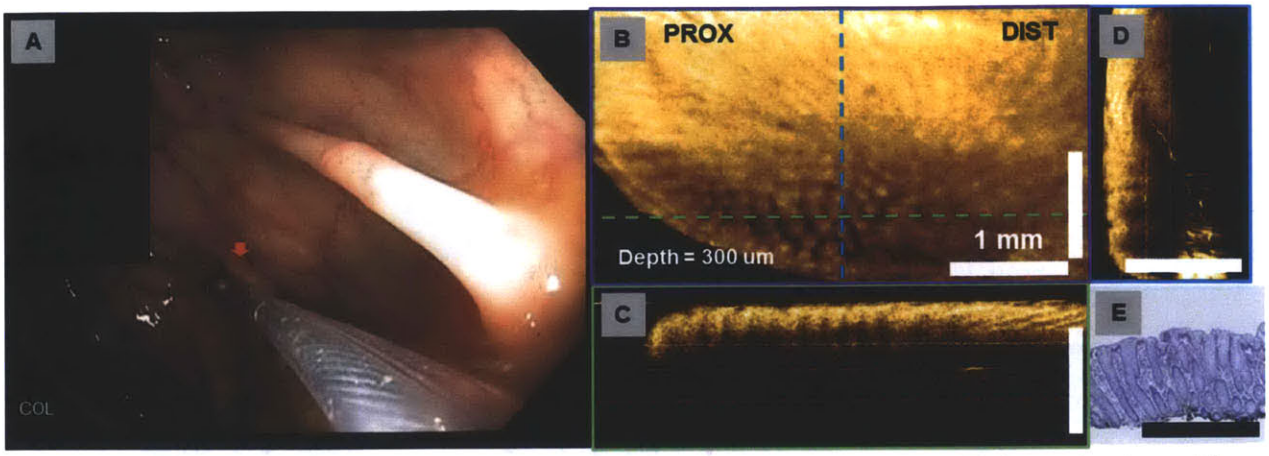

Figure 10.15. *In vivo* imaging of a polyp in the ascending (right) colon. (A) Endoscopic view of the ascending colon with the OCT imaging catheter gently in contact with the polyp on top of a fold. (B) *En face* image at the imaging depth of 300 um shows regular crypt structure. (B) Cross-sectional image along the pullback direction. (D) Cross-sectional image along the rotary direction. (E) Corresponding histology of the polyps, which is diagnosed as a benign hyperplastic polyp. Red arrow: the location of the polyp.

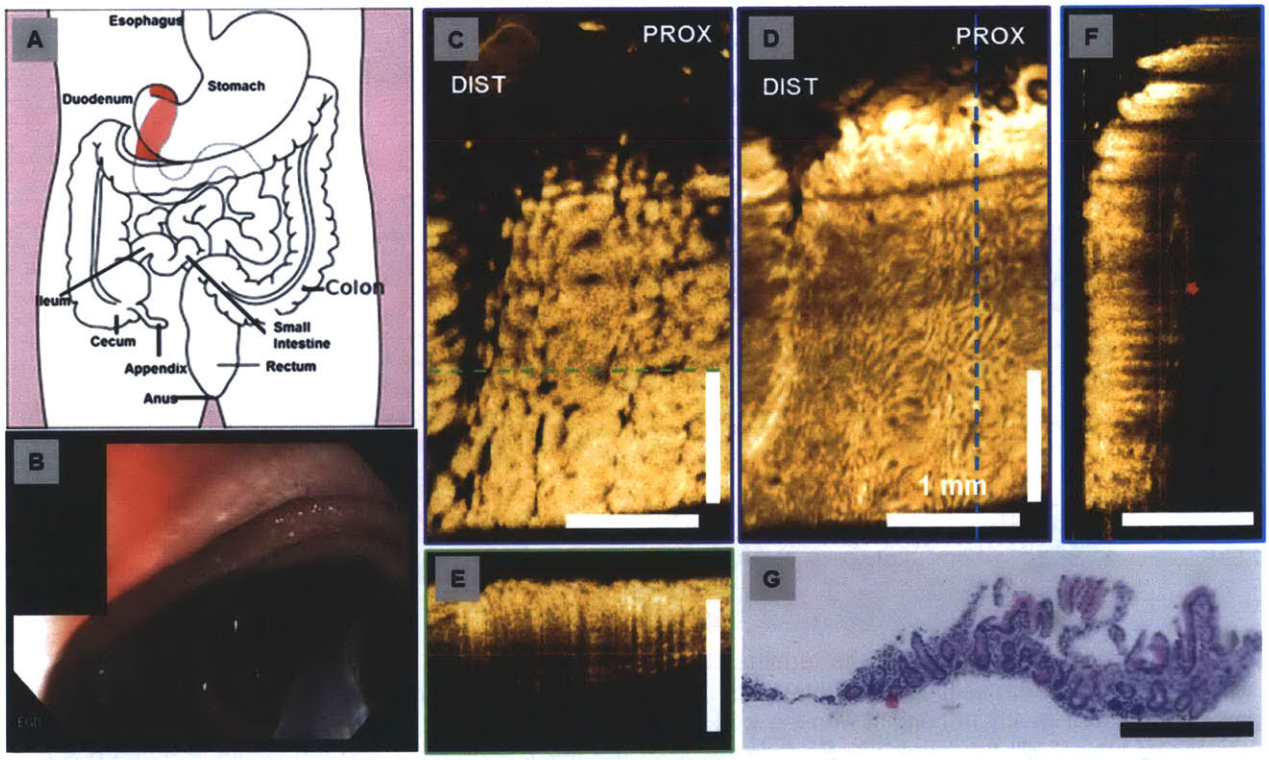

Figure 10.16. *In vivo* imaging of the normal duodenum. (A) Diagram of the human gastrointestinal (GI) tract, with the duodenum section highlighted with red. (B) Endoscopic view of the duodenum with the OCT imaging catheter gently in contact with the wall of the duodenum. (C) *En face* image at the imaging depth of 50 um shows typical villi structure. (D) *En face* image at the imaging depth of 300 um shows transverse cross-section of duodenal villi, similar to the crypt structure.(E) Cross-sectional image along the pullback direction. (F) Cross-sectional image along the rotary direction. (G) Corresponding histology of the duodenum, which is diagnosed as a normal duodenum. Red arrow: the location of the polyp.

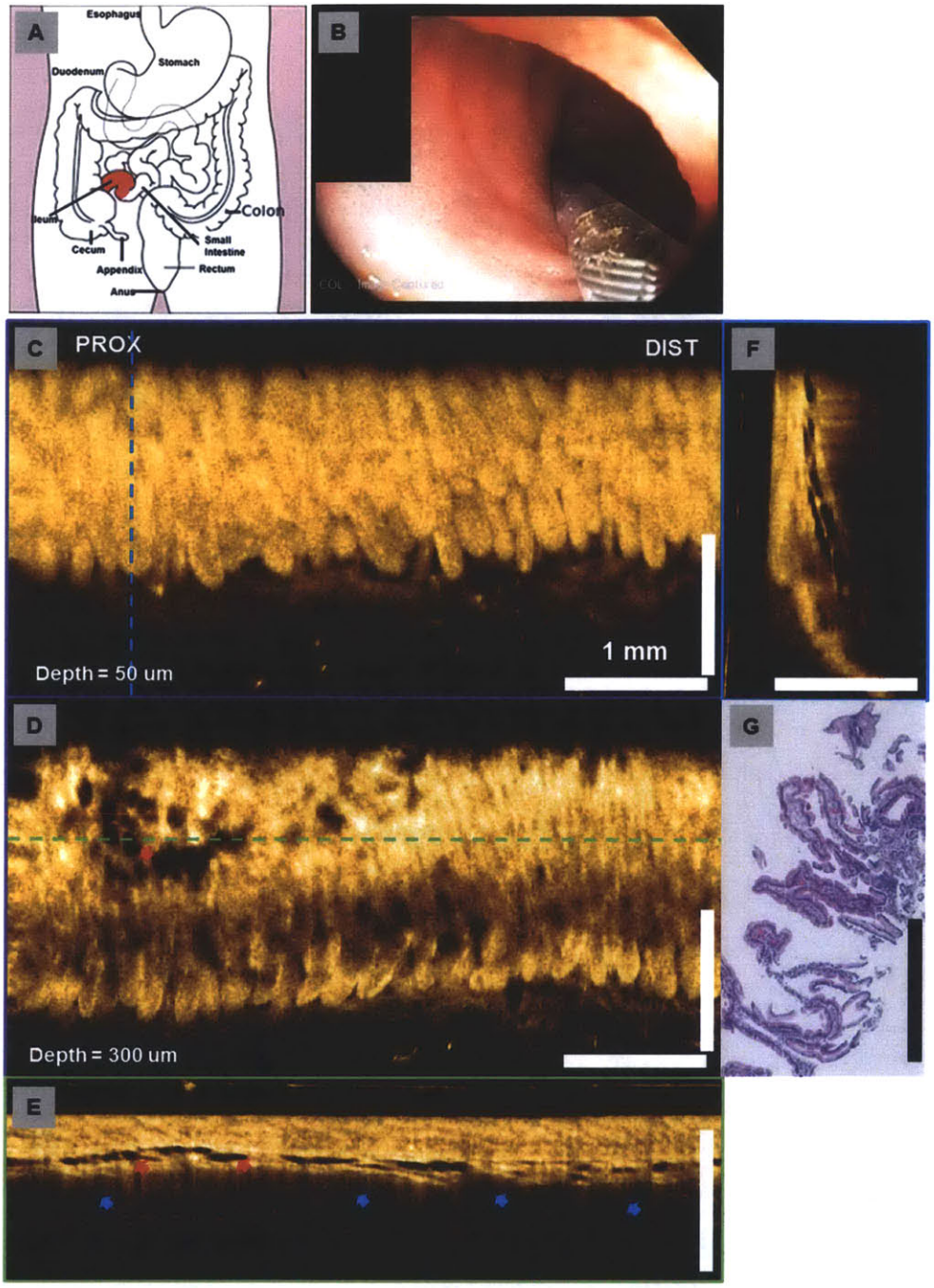

Figure 10.17. *In vivo* imaging of the terminal ileum. (A) Diagram of the human gastrointestinal (GI) tract, with the terminal ileum section highlighted with red. (B) Endoscopic view of the terminal ileum with the OCT imaging catheter gently in contact with the wall of the ileum. (C) *En face* image at the imaging depth of 50 um shows typical villi structure. (D) *En face* image at the imaging depth of 300 um shows a numerous of glandular structure underneath the tissue surface.(E) Cross-sectional image along the pullback direction. (F) Cross-sectional image along the rotary direction. (G) Corresponding histology of the terminal ileum, which is diagnosed as a normal ileum. Red arrow: ileum glands. Blue arrows: Preyer's patches.

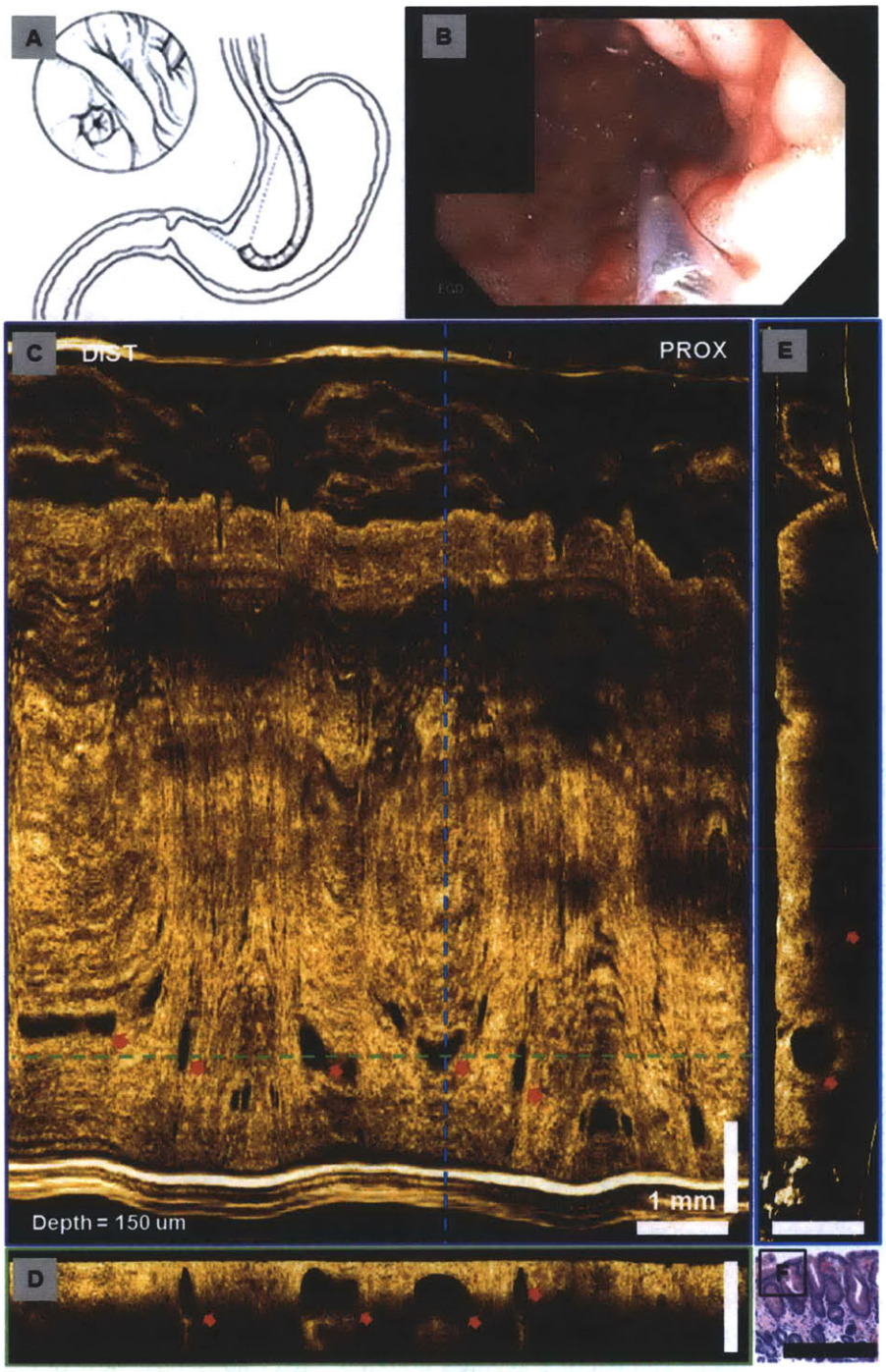

Figure 10.18. *In vivo* imaging of the antrum with GAVE. (A) Diagram of endoscopic examination of distal stomach. The distal tip of the endoscope is required to bend more than 90° to visualize the antrum. The figure originates from [50]. (B) Endoscopic view of the antrum with the OCT imaging catheter on the GAVE region. (C) *En face* image at the imaging depth of 150 um shows large glandular structure underneath the GAVE region. (D) Cross-sectional image along the pullback direction. (E) Cross-sectional image along the rotary direction.(F) Corresponding histology of the terminal ileum, which is diagnosed as a normal ileum. Red arrow: Large glands in the GAVE region.

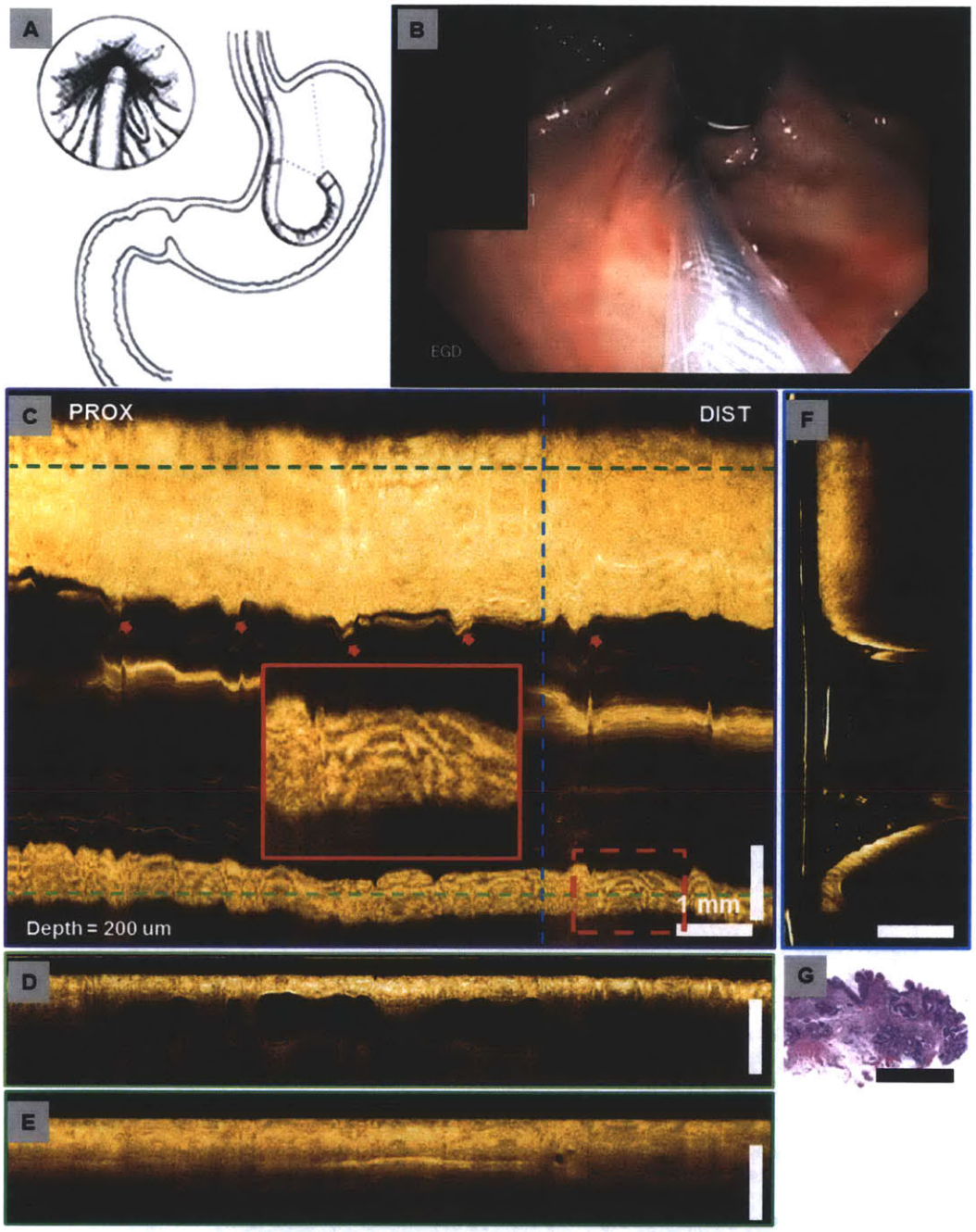

Figure 10.19. *In vivo* imaging of the hiatal hernia in retroflex position. (A) Diagram of endoscopic examination in retroflex position. The figure originates from [50]. (B) Endoscopic view of the hiatal hernia with the OCT imaging catheter on the GEJ. (C) *En face* image at the imaging depth of 150 um shows two different surface features at the GEJ. Inlet shows the enlarged view of the region in the dashed red box. (D) Cross-sectional image along the pullback direction shows gastric features. (E) Cross-sectional image along the pullback direction shows BE features. (F) Cross-sectional image along the rotary direction. (G) Corresponding histology near the GEJ, which is diagnosed as non-dysplastic BE. Red arrow: Heartbeat induced motion artifact.

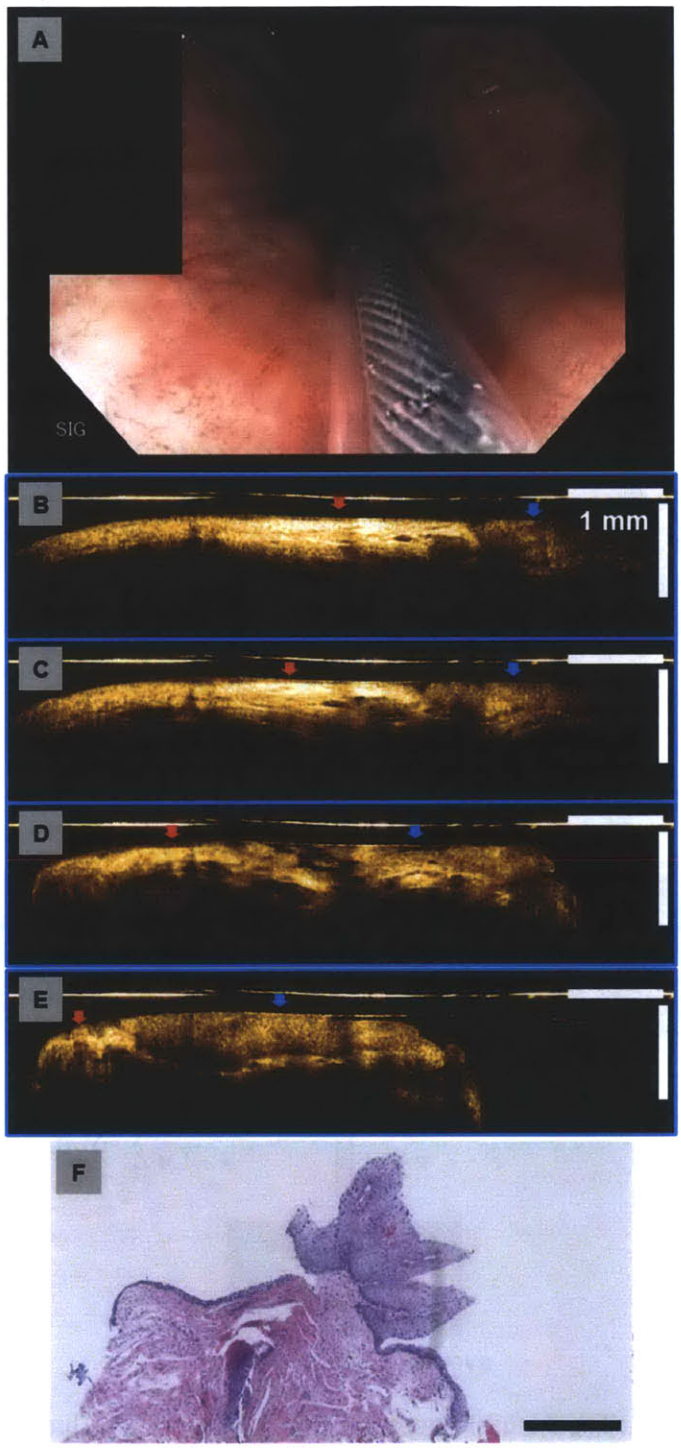

Figure 10.20. *In vivo* imaging of squamous papilloma at the RAJ. (A) Endoscopic view of the squamous papilloma with the OCT imaging catheter on the RAJ. (C-E) Cross-sectional image along the rotary direction acquired at different imaged locations. (G) Corresponding histology of the squamous papilloma. Red arrow: normal anal mucosa. Blue arrows: squamous papilloma.

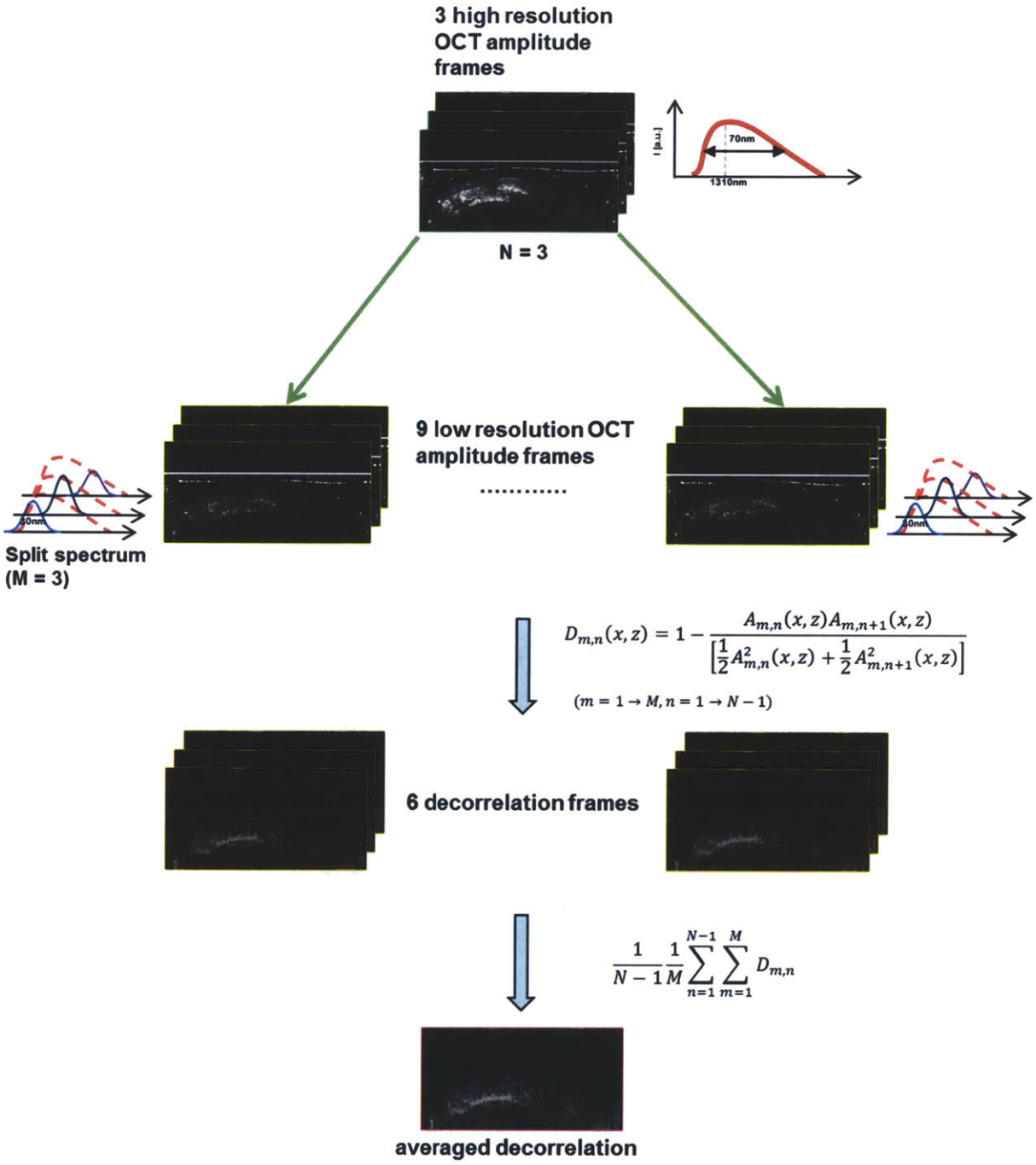

Figure 10.21. Flow chart detailing the basic steps of the SSADA algorithm. Three consecutive OCT frames were used to calculate the speckle decorrelation. In SSADA, each full spectral interferogram was split into 3 spectral bands. There were 3 OCT image frames at each spectral band, from which 2 decorrelation frames were calculated. The 6 decorrelation frames were averaged to produce on final decorrelation-based flow cross-sectional of much higher quality.

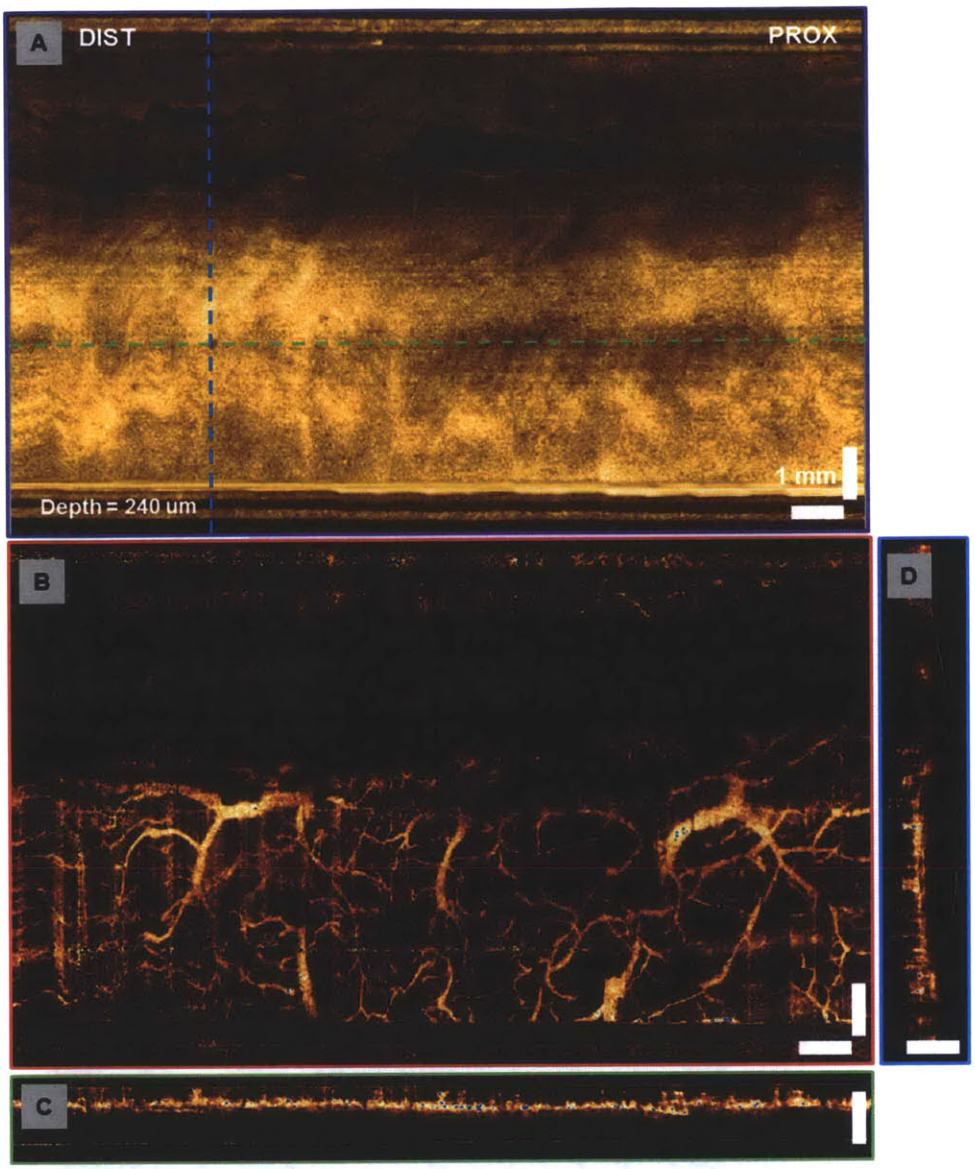

Figure 10.22. Endoscopic OCT angiography in the normal esophagus. (A) *En face* intensity image at the imaging depth of 240 um, corresponding to the lamina propria layer. (B) OCT angiogram in the lamina propria layer generated using SSADA algorithm. (C) Cross-sectional decorrelation map generated using SSADA algorithm along the pullback direction. (D) Cross-sectional decorrelation map generated using SSADA algorithm along the rotary direction.

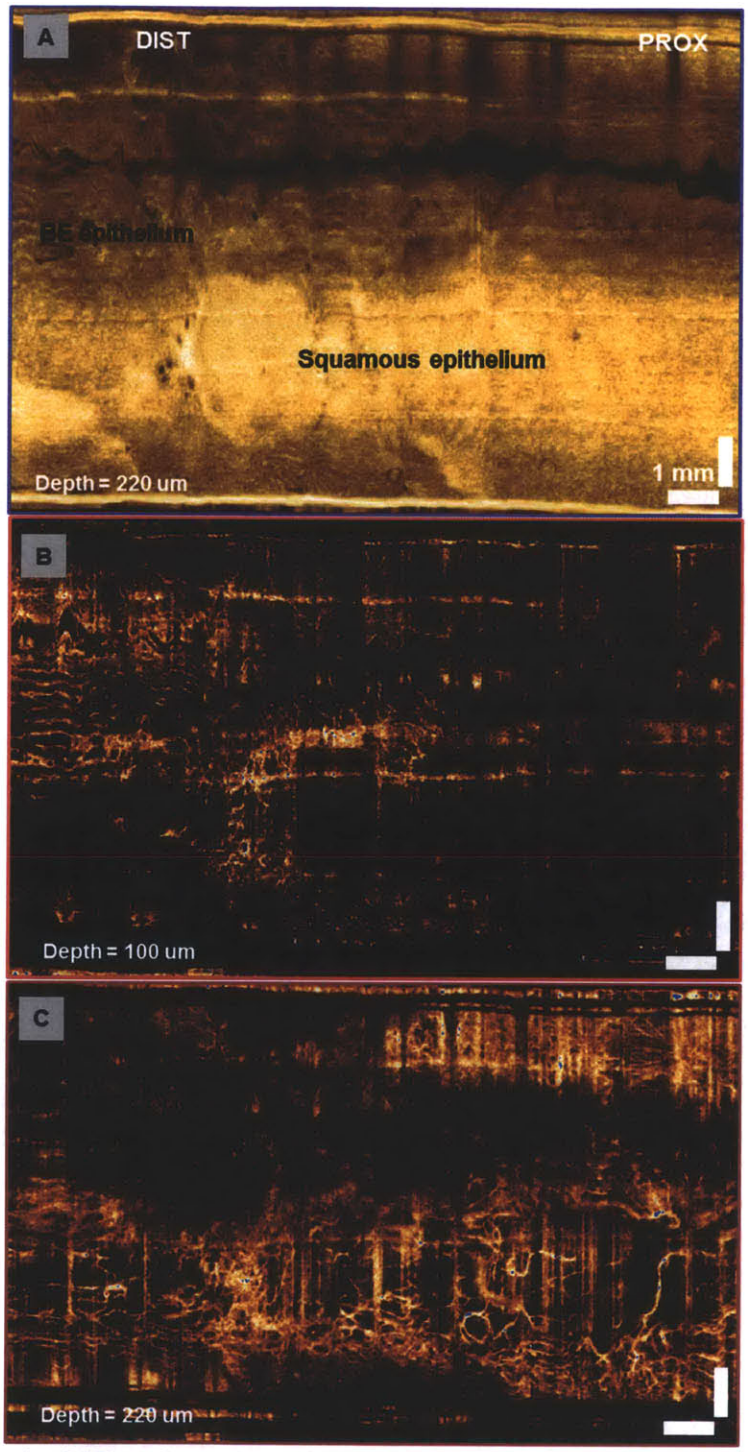

Figure 10.23. Endoscopic OCT angiography of the Barrett's esophagus near the squamous columnar junction. (A) *En face* intensity image at the imaging depth of 220 um, corresponding to the lamina propria layer. (B) OCT angiogram generated using SSADA algorithm at the imaging depth of 100 um shows the surface vasculature in the BE region. (C) OCT angiogram generated using SSADA algorithm at the imaging depth of 220 um shows high density of microvesculature on the edge of squamous columnar junction.

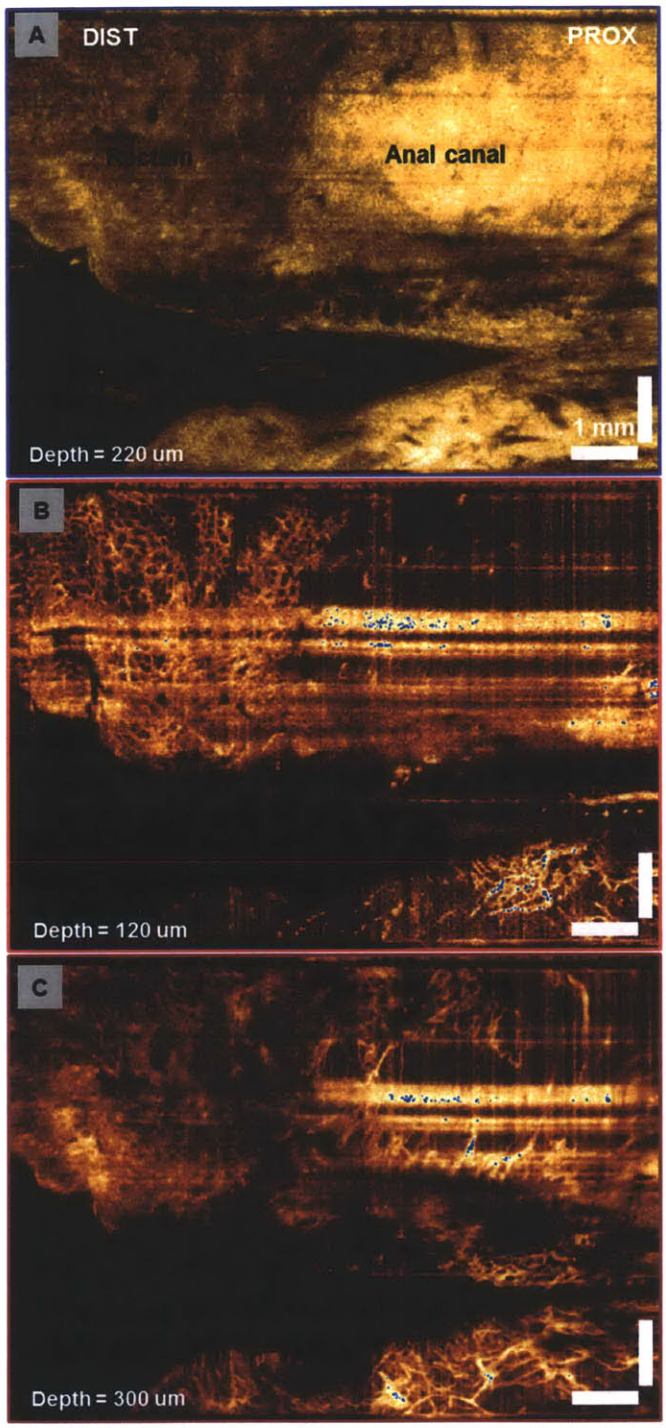

Figure 10.24. Endoscopic OCT angiography of the normal recto-anal junction. (A) *En face* intensity image at the imaging depth of 220 um, corresponding to the lamina propria layer. (B) OCT angiogram generated using SSADA algorithm at the imaging depth of 120 um shows the surface vasculature of the crypts in the rectum. (C) OCT angiogram generated using SSADA algorithm at the imaging depth of 300 um shows typical vasculature in the normal squamous epithelium.

10.9 References

[1] "Cancer Facts and Figures," American Cancer Society 2013.

[2] A. Jemal, R. Siegel, E. Ward, T. Murray, J. Q. Xu, and M. J. Thun, "Cancer statistics, 2007," *Ca-a Cancer Journal for Clinicians,* vol. 57, pp. 43-66, Jan-Feb 2007.

[3] B. F. Overholt, M. Panjehpour, and J. M. Haydek, "Photodynamic therapy for Barrett's esophagus: follow-up in 100 patients," *Gastrointestinal Endoscopy,* vol. 49, pp. 1-7, Jan 1999.

[4] O. Pech, L. Gossner, H. Manner, A. May, T. Rabenstein, A. Behrens, M. Berres, J. Huijsmans, M. Vieth, M. Stolte, and C. Ell, "Prospective evaluation of the macroscopic types and location of early Barrett's neoplasia in 380 lesions," *Endoscopy,* vol. 39, pp. 588-593, Jul 2007.

[5] O. Pech, "Declaration of Bankruptcy for Four-Quadrant Biopsies in Barrett's Esophagus?," *Clinical Gastroenterology and Hepatology,* vol. 7, pp. 610-612, Jun 2009.

[6] S. J. Spechler, P. Sharma, R. F. Souza, J. M. Inadomi, and N. J. Shaheen, "American Gastroenterological Association Technical Review on the Management of Barrett's Esophagus," *Gastroenterology,* vol. 140, pp. e18-e52, Mar 2011.

[7] M. Bajbouj, M. Vieth, T. Rösch, S. Miehlke, V. Becker, M. Anders, H. Pohl, A. Madisch, T. Schuster, R. M. Schmid, and A. Meining, "Probe-based confocal laser endomicroscopy compared with standard four-quadrant biopsy for evaluation of neoplasia in Barrett's esophagus," *Endoscopy,* vol. 42, pp. 435-440, May 2010.

[8] D. K. Rex, "Maximizing detection of adenomas and cancers during colonoscopy," *American Journal of Gastroenterology,* vol. 101, pp. 2866-2877, Dec 2006.

[9] R. Kiesslich, M. von Bergh, M. Hahn, G. Hermann, and M. Jung, "Chromoendoscopy with indigocarmine improves the detection of adenomatous and nonadenomatous lesions in the colon," *Endoscopy,* vol. 33, pp. 1001-1006, Dec 2001.

[10] M. I. F. Canto, S. Setrakian, J. E. Willis, A. Chak, R. E. Petras, and M. V. Sivak, "Methylene blue staining of dysplastic and nondysplastic Barrett's esophagus: An in vivo and ex vivo study," *Endoscopy,* vol. 33, pp. 391-400, May 2001.

[11] P. Sharma, M. Topalovski, M. S. Mayo, and A. P. Weston, "Methylene blue chromoendoscopy for detection of short-segment Barrett's esophagus," *Gastrointestinal Endoscopy,* vol. 54, pp. 289-293, Sep 2001.

[12] T. Endo, T. Awakawa, H. Takahashi, Y. Arimura, F. Itoh, K. Yamashita, S. Sasaki, H. Yamamoto, X. F. Tang, and K. Imai, "Classification of Barrett's epithelium by magnifying endoscopy," *Gastrointestinal Endoscopy,* vol. 55, pp. 641-647, May 2002.

[13] J. Pohl, A. May, T. Robenstein, O. Pech, M. Nguyen-Tat, A. Fissler-Eckhoff, and C. Ell, "Comparison of computed virtual chromoendoscopy and conventional chromoendoscopy with acetic acid for detection of neoplasia in Barrett's esophagus," *Endoscopy,* vol. 39, pp. 594-598, Jul 2007.

[14] J. R. Olliver, C. P. Wild, P. Sahay, S. Dexter, and L. J. Hardie, "Chromoendoscopy with methylene blue and associated DNA damage in Barrett's oesophagus," *Lancet,* vol. 362, pp. 373-374, Aug 2003.

[15] A. M. Panossian, M. Raimondo, and H. C. Wolfsen, "State of the art in the endoscopic imaging and ablation of Barrett's esophagus," *Digestive and Liver Disease,* vol. 43, pp. 365-373, May 2011.

[16] P. Sharma, A. Bansal, S. Mathur, S. Wani, R. Cherian, D. McGregor, A. Higbee, S. Hall, and A. Weston, "The utility of a novel narrow band imaging endoscopy system in patients with Barrett's esophagus," *Gastrointestinal Endoscopy,* vol. 64, pp. 167-175, Aug 2006.

[17] R. Singh, G. K. Anagnostopoulos, K. Yao, H. Karageorgiou, P. J. Fortun, A. Shonde, K. Garsed, P. V. Kaye, C. J. Hawkey, and K. Ragunath, "Narrow-band imaging with magnification in Barrett's esophagus: validation of a simplified grading system of mucosal morphology patterns against histology," *Endoscopy,* vol. 40, pp. 457-463, Sep 2008.

[18] S. E. Kudo, S. Tamura, T. Nakajima, H. O. Yamano, H. Kusaka, and H. Watanabe, "Diagnosis of colorectal tumorous lesions by magnifying endoscopy," *Gastrointestinal Endoscopy,* vol. 44, pp. 8-14, Jul 1996.

[19] "The Paris endoscopic classification of superficial neoplastic lesions: esophagus, stomach, and colon - November 30 to December 1, 2002," *Gastrointestinal Endoscopy,* vol. 58, pp. S3-S43, Dec 2003.

[20] A. Axon, M. D. Diebold, M. Fujino, R. Fujita, R. M. Genta, J. J. Gonvers, M. Guelrud, H. Inoue, M. Jung, H. Kashida, S. Kudo, R. Lambert, C. Lightdale, T. Nakamura, H. Neuhaus, H. Niwa, K. Ogoshi, J. F. Rey, R. Riddell, M. Sasako, T. Shimoda, H. Suzuki, G. N. J. Tytgat, K. Wang, H. Watanabe, T. Yamakawa, and S. Yoshida, "Update on the Paris classification of superficial neoplastic lesions in the digestive tract," *Endoscopy,* vol. 37, pp. 570-578, Jun 2005.

[21] T. Wilson, "Confocal microscopy," *Academic Press: London, etc,* vol. 426, pp. 1-64, Nov 1990.

[22] D. R. Sandison and W. W. Webb, "Background rejection and signal-to-noise optimization in confocal and alternative fluorescence microscopes," *Applied Optics,* vol. 33, pp. 603-615, Feb 1994.

[23] G. S. Kino and T. R. Corle, *Confocal scanning optical microscopy and related imaging systems*: Academic Press, 1996.

[24] J. Pawley, *Handbook of biological confocal microscopy*: Springer, 2006.

[25] A. L. Polglase, W. J. McLaren, and P. M. Delaney, "Pentax confocal endomicroscope: a novel imaging device for in vivo histology of the upper and lower gastrointestinal tract," *Expert Rev Med Devices,* vol. 3, pp. 549-556, Sep 2006.

[26] K. B. Dunbar and M. I. Canto, "Confocal endomicroscopy," *Techniques in Gastrointestinal Endoscopy,* vol. 12, pp. 90-99, Sep 2010.

[27] A. Hoffman, M. Goetz, M. Vieth, P. R. Galle, M. F. Neurath, and R. Kiesslich, "Confocal laser endomicroscopy: technical status and current indications," *Endoscopy,* vol. 38, pp. 1275-1283, Dec 2006.

[28] M. I. Canto, "Endomicroscopy of Barrett's Esophagus," *Gastroenterology Clinics of North America,* vol. 39, pp. 759-769, Dec 2010.

[29] M. Goetz and T. D. Wang, "Molecular Imaging in Gastrointestinal Endoscopy," *Gastroenterology,* vol. 138, pp. 828-U54, Mar 2010.

[30] S. J. Miller, B. P. Joshi, Y. Feng, A. Gaustad, E. R. Fearon, and T. D. Wang, "In Vivo Fluorescence-Based Endoscopic Detection of Colon Dysplasia in the Mouse Using a Novel Peptide Probe," *Plos One,* vol. 6, Mar 2011.

[31] M. B. Sturm, B. P. Joshi, S. Lu, C. Piraka, S. Khondee, B. J. Elmunzer, R. S. Kwon, D. G. Beer, H. D. Appelman, D. K. Turgeon, and T. D. Wang, "Targeted imaging of esophageal neoplasia with a fluorescently labeled peptide: first-in-human results," *Science translational medicine,* vol. 5, pp. 184ra61-184ra61, May 2013.

[32] Z. Liu, S. J. Miller, B. P. Joshi, and T. D. Wang, "In vivo targeting of colonic dysplasia on fluorescence endoscopy with near-infrared octapeptide," *Gut,* vol. 62, pp. 395-403, Mar 2013.

[33] A. Wax, C. H. Yang, M. G. Muller, R. Nines, C. W. Boone, V. E. Steele, G. D. Stoner, R. R. Dasari, and M. S. Feld, "In situ detection of neoplastic transformation and chemopreventive effects in rat esophagus epithelium using angle-resolved low-coherence interferometry," *Cancer Research,* vol. 63, pp. 3556-3559, Jul 2003.

[34] A. Wax, J. W. Pyhtila, R. N. Graf, R. Nines, C. W. Boone, R. R. Dasari, M. S. Feld, V. E. Steele, and G. D. Stoner, "Prospective grading of neoplastic change in rat esophagus epithelium using angle-resolved low-coherence interferometry," *Journal of Biomedical Optics,* vol. 10, Sep-Oct 2005.

[35] N. G. Terry, Y. Zhu, M. T. Rinehart, W. J. Brown, S. C. Gebhart, S. Bright, E. Carretta, C. G. Ziefle, M. Panjehpour, J. Galanko, R. D. Madanick, E. S. Dellon, D. Trembath, A. Bennett, J. R. Goldblum, B. F. Overholt, J. T. Woosley, N. J. Shaheen, and A. Wax, "Detection of Dysplasia in

Barrett's Esophagus With In Vivo Depth-Resolved Nuclear Morphology Measurements," *Gastroenterology,* vol. 140, pp. 42-50, Jan 2011.

[36] L. Qiu, D. K. Pleskow, R. Chuttani, E. Vitkin, J. Leyden, N. Ozden, S. Itani, L. Guo, A. Sacks, J. D. Goldsmith, M. D. Modell, E. B. Hanlon, I. Itzkan, and L. T. Perelman, "Multispectral scanning during endoscopy guides biopsy of dysplasia in Barrett's esophagus," *Nature Medicine,* vol. 16, pp. 603-U140, May 2010.

[37] S. H. Yun, G. J. Tearney, B. J. Vakoc, M. Shishkov, W. Y. Oh, A. E. Desjardins, M. J. Suter, R. C. Chan, J. A. Evans, I. K. Jang, N. S. Nishioka, J. F. de Boer, and B. E. Bouma, "Comprehensive volumetric optical microscopy in vivo," *Nature Medicine,* vol. 12, pp. 1429-1433, Dec 2006.

[38] D. C. Adler, Y. Chen, R. Huber, J. Schmitt, J. Connolly, and J. G. Fujimoto, "Three-dimensional endomicroscopy using optical coherence tomography," *Nature Photonics,* vol. 1, pp. 709-716, Dec 2007.

[39] M. J. Suter, B. J. Vakoc, P. S. Yachimski, M. Shishkov, G. Y. Lauwers, M. Mino-Kenudson, B. E. Bouma, N. S. Nishioka, and G. J. Tearney, "Comprehensive microscopy of the esophagus in human patients with optical frequency domain imaging," *Gastrointestinal Endoscopy,* vol. 68, pp. 745-753, Oct 2008.

[40] J. A. Evans, J. M. Poneros, B. E. Bouma, J. Bressner, E. F. Halpern, M. Shishkov, G. Y. Lauwers, M. Mino–Kenudson, N. S. Nishioka, and G. J. Tearney, "Optical Coherence Tomography to Identify Intramucosal Carcinoma and High-Grade Dysplasia in Barrett's Esophagus," *Clinical Gastroenterology and Hepatology,* vol. 4, pp. 38-43, Jan 2006.

[41] A. D. Aguirre, Y. Chen, B. Bryan, H. Mashimo, Q. Huang, J. L. Connolly, and J. G. Fujimoto, "Cellular resolution ex vivo imaging of gastrointestinal tissues with optical coherence microscopy," *Journal of Biomedical Optics,* vol. 15, Jan-Feb 2010.

[42] Y. Chen, A. D. Aguirre, P. L. Hsiung, S. Desai, P. R. Herz, M. Pedrosa, Q. Huang, M. Figueiredo, S. W. Huang, A. Koski, J. M. Schmitt, J. G. Fujimoto, and H. Mashimo, "Ultrahigh resolution optical coherence tomography of Barrett's esophagus: preliminary descriptive clinical study correlating images with histology," *Endoscopy,* vol. 39, pp. 599-605, Jul 2007.

[43] D. C. Adler, C. Zhou, T. H. Tsai, H. C. Lee, L. Becker, J. M. Schmitt, Q. Huang, J. G. Fujimoto, and H. Mashimo, "Three-dimensional optical coherence tomography of Barrett's esophagus and buried glands beneath neosquamous epithelium following radiofrequency ablation," *Endoscopy,* vol. 41, pp. 773-776, Sep 2009.

[44] P. L. Hsiung, L. Pantanowitz, A. D. Aguirre, Y. Chen, D. Phatak, T. H. Ko, S. Bourquin, S. J. Schnitt, S. Raza, J. L. Connolly, H. Mashimo, and J. G. Fujimoto, "Ultrahigh-resolution and 3-dimensional optical coherence tomography ex vivo imaging of the large and small intestines," *Gastrointest Endosc,* vol. 62, pp. 561-574, Oct 2005.

[45] D. C. Adler, C. Zhou, T. H. Tsai, J. Schmitt, Q. Huang, H. Mashimo, and J. G. Fujimoto, "Three-dimensional endomicroscopy of the human colon using optical coherence tomography," *Optics Express,* vol. 17, pp. 784-796, Jan 2009.

[46] C. Zhou, D. C. Adler, L. Becker, Y. Chen, T.-H. Tsai, M. Figueiredo, J. M. Schmitt, J. G. Fujimoto, and H. Mashimo, "Effective treatment of chronic radiation proctitis using radiofrequency ablation " *Therapeutic Advances in Gastroenterology,* vol. 2, pp. 149-156, May 2009.

[47] M. Jabbari, R. Cherry, J. O. Lough, D. S. Daly, D. G. Kinnear, and C. A. Goresky, "Gastric antral vascular ectasia - the watermelon stomach," *Gastroenterology,* vol. 87, pp. 1165-1170, Nov 1984.

[48] E. Quintero, J. M. Pique, J. A. Bombi, J. M. Bordas, J. Sentis, M. Elena, J. Bosch, and J. Rodes, "Gastric-mucosal vascular ectasias causing bleeding in cirrhosis - a distinct entity associated with hypergastrinemia and low serum levels of pepsinogen-I," *Gastroenterology,* vol. 93, pp. 1054-1061, Nov 1987.

[49] P. F. Suit, R. E. Petras, T. W. Bauer, and J. L. Petrini, "Gastric antral vascular ectasia - a histologic and morphometric study of the watermelon stomach," *American Journal of Surgical Pathology,* vol. 11, pp. 750-757, Oct 1987.

[50] *The SAGES Manual: Fundamentals of Laparoscopy, Thoracoscopy, and GI Endoscopy*, 2 ed.: Springer, 2006.

[51] V. X. Yang, S. J. Tang, M. L. Gordon, B. Qi, G. Gardiner, M. Cirocco, P. Kortan, G. B. Haber, G. Kandel, I. A. Vitkin, B. C. Wilson, and N. E. Marcon, "Endoscopic Doppler optical coherence tomography in the human GI tract: initial experience," *Gastrointest Endosc,* vol. 61, pp. 879-890, Jun 2005.

[52] P. R. Allison, "Reflux esophagitis, sliding hiatal hernia, and the anatomy of repair," *Surgery Gynecology & Obstetrics,* vol. 92, pp. 419-431, Apr 1951.

[53] N. P. Trujillo, Slaughte.Rl, and H. W. Boyce, "Endoscopic diagnosis of sliding-type diaphragmatic hiatal hernias," *American Journal of Digestive Diseases,* vol. 13, pp. 855-867, Oct 1968.

[54] H. zurHausen, "Papillomavirus infections - A major cause of human cancers," *Biochimica Et Biophysica Acta-Reviews on Cancer,* vol. 1288, pp. F55-F78, Oct 1996.

[55] X. J. Wang, T. E. Milner, and J. S. Nelson, "Characterization of fluid-flow velocity by optical doppler tomography," *Optics Letters,* vol. 20, pp. 1337-1339, Jun 1995.

[56] Z. Chen, T. E. Milner, D. Dave, and J. S. Nelson, "Optical Doppler tomographic imaging of fluid flow velocity in highly scattering media," *Optics Letters,* vol. 22, pp. 64-66, Jan 1997.

[57] J. A. Izatt, M. D. Kulkami, S. Yazdanfar, J. K. Barton, and A. J. Welch, "In vivo bidirectional color Doppler flow imaging of picoliter blood volumes using optical coherence tomography," *Optics Letters,* vol. 22, pp. 1439-1441, Sep 1997.

[58] Y. Zhao, Z. Chen, C. Saxer, S. Xiang, J. F. de Boer, and J. S. Nelson, "Phase-resolved optical coherence tomography and optical Doppler tomography for imaging blood flow in human skin with fast scanning speed and high velocity sensitivity," *Optics Letters,* vol. 25, pp. 114-116, Jan 2000.

[59] V. X. D. Yang, M. L. Gordon, B. Qi, J. Pekar, S. Lo, E. Seng-Yue, A. Mok, B. C. Wilson, and I. A. Vitkin, "High speed, wide velocity dynamic range Doppler optical coherence tomography (Part I): System design, signal processing, and performance," *Optics Express,* vol. 11, pp. 794-809, Apr 2003.

[60] B. R. White, M. C. Pierce, N. Nassif, B. Cense, B. H. Park, G. J. Tearney, B. E. Bouma, T. C. Chen, and J. F. de Boer, "In vivo dynamic human retinal blood flow imaging using ultra-high-speed spectral domain optical Doppler tomography," *Optics Express,* vol. 11, pp. 3490-3497, Dec 2003.

[61] R. A. Leitgeb, L. Schmetterer, W. Drexler, A. F. Fercher, R. J. Zawadzki, and T. Bajraszewski, "Real-time assessment of retinal blood flow with ultrafast acquisition by color Doppler Fourier domain optical coherence tomography," *Optics Express,* vol. 11, pp. 3116-3121, Nov 2003.

[62] S. Makita, Y. Hong, M. Yamanari, T. Yatagai, and Y. Yasuno, "Optical coherence angiography," *Optics Express,* vol. 14, pp. 7821-7840, Aug 2006.

[63] B. J. Vakoc, M. Shishko, S. H. Yun, W. Y. Oh, M. J. Suter, A. E. Desjardins, J. A. Evans, N. S. Nishioka, G. J. Tearney, and B. E. Bouma, "Comprehensive esophageal microscopy by using optical frequency-domain imaging (with video)," *Gastrointestinal Endoscopy,* vol. 65, pp. 898-905, May 2007.

[64] J. Fingler, R. J. Zawadzki, J. S. Werner, D. Schwartz, and S. E. Fraser, "Volumetric microvascular imaging of human retina using optical coherence tomography with a novel motion contrast technique," *Optics Express,* vol. 17, pp. 22190-22200, Nov 2009.

[65] V. Srinivasan, S. Sakadzic, I. Gorczynska, A. Yaseen, J. Fujimoto, and D. Boas, "Depth-resolved microscopy of cerebral blood flow and volume during somatosensory stimulation with doppler optical coherence tomography," *Journal of Cerebral Blood Flow and Metabolism,* vol. 29, pp. S111-S112, Oct 2009.

[66] J. J. Liu, B. Potsaid, Y. L. Chen, I. Gorczynska, V. J. Srinivasan, J. S. Duker, and J. G. Fujimoto, "Ultrahigh Speed Imaging of the Rat Retina Using Ultrahigh Resolution Spectral/Fourier Domain OCT," *Ophthalmic Technologies Xx,* vol. 7550, Mar 2010.

[67] B. Baumann, B. Potsaid, J. J. Liu, M. F. Kraus, D. Huang, J. Hornegger, J. S. Duker, and J. G. Fujimoto, "Retinal blood flow measurement with ultrahigh-speed swept-source/Fourier domain optical coherence tomography," in *Ophthalmic Technologies Xxi.* vol. 7885, Feb 2011.

[68] R. K. Wang, S. L. Jacques, Z. Ma, S. Hurst, S. R. Hanson, and A. Gruber, "Three dimensional optical angiography," *Optics Express,* vol. 15, pp. 4083-4097, Apr 2007.

[69] Y. K. Tao, K. M. Kennedy, and J. A. Izatt, "Velocity-resolved 3D retinal microvessel imaging using single-pass flow imaging spectral domain optical coherence tomography," *Optics Express,* vol. 17, pp. 4177-4188, Mar 2009.

[70] L. An, J. Qin, and R. K. Wang, "Ultrahigh sensitive optical microangiography for in vivo imaging of microcirculations within human skin tissue beds," *Optics Express,* vol. 18, pp. 8220-8228, Apr 2010.

[71] M. C. Pierce, B. Hyle Park, B. Cense, and J. F. de Boer, "Simultaneous intensity, birefringence, and flow measurements with high-speed fiber-based optical coherence tomography," *Optics Letters,* vol. 27, pp. 1534-1536, 1 Sep 2002.

[72] H. W. Ren, T. Sun, D. J. MacDonald, M. J. Cobb, and X. D. Li, "Real-time in vivo blood-flow imaging by movingscatterer-sensitive spectral-domain optical Doppler tomography," *Optics Letters,* vol. 31, pp. 927-929, Apr 2006.

[73] S. Makita, M. Yamanari, M. Miura, and Y. Yasuno, "High-sensitive blood flow imaging of the retina and choroid by using double-beam optical coherence angiography," *Ophthalmic Technologies Xx,* vol. 7550, Mar 2010.

[74] W. Choi, B. Baumann, J. J. Liu, A. C. Clermont, E. P. Feener, J. S. Duker, and J. G. Fujimoto, "Measurement of pulsatile total blood flow in the human and rat retina with ultrahigh speed spectral/Fourier domain OCT," *Biomedical Optics Express,* vol. 3, pp. 1047-1061, May 2012.

[75] W. Choi, B. Potsaid, V. Jayaraman, B. Baumann, I. Grulkowski, J. J. Liu, C. D. Lu, A. E. Cable, D. Huang, J. S. Duker, and J. G. Fujimoto, "Phase-sensitive swept-source optical coherence tomography imaging of the human retina with a vertical cavity surface-emitting laser light source," *Optics Letters,* vol. 38, pp. 338-340, Feb 2013.

[76] A. Mariampillai, B. A. Standish, E. H. Moriyama, M. Khurana, N. R. Munce, M. K. K. Leung, J. Jiang, A. Cable, B. C. Wilson, I. A. Vitkin, and V. X. D. Yang, "Speckle variance detection of microvasculature using swept-source optical coherence tomography," *Optics Letters,* vol. 33, pp. 1530-1532, Jun 2008.

[77] A. Mariampillai, M. K. K. Leung, M. Jarvi, B. A. Standish, K. Lee, B. C. Wilson, A. Vitkin, and V. X. D. Yang, "Optimized speckle variance OCT imaging of microvasculature," *Optics Letters,* vol. 35, pp. 1257-1259, Apr 2010.

[78] E. Jonathan, J. Enfield, and M. J. Leahy, "Correlation mapping method for generating microcirculation morphology from optical coherence tomography (OCT) intensity images," *Journal of Biophotonics,* vol. 4, pp. 583-587, Sep 2011.

[79] J. Enfield, E. Jonathan, and M. Leahy, "In vivo imaging of the microcirculation of the volar forearm using correlation mapping optical coherence tomography (cmOCT)," *Biomedical Optics Express,* vol. 2, pp. 1184-1193, May 2011.

[80] Y. Jia, O. Tan, J. Tokayer, B. Potsaid, Y. Wang, J. J. Liu, M. F. Kraus, H. Subhash, J. G. Fujimoto, J. Hornegger, and D. Huang, "Split-spectrum amplitude-decorrelation angiography with optical coherence tomography," *Optics Express,* vol. 20, pp. 4710-4725, Feb 2012.

[81] J. S. Nelson, K. M. Kelly, Y. Zhao, and Z. Chen, "Imaging blood flow in human port-wine stain in situ and in real time using optical Doppler tomography," *Archives of dermatology,* vol. 137, pp. 741-744, Jun 2001.

[82] R. C. Wong, S. Yazdanfar, J. A. Izatt, M. D. Kulkarni, J. K. Barton, A. J. Welch, J. Willis, and M. V. Sivak, Jr., "Visualization of subsurface blood vessels by color Doppler optical coherence tomography in rats: before and after hemostatic therapy," *Gastrointestinal endoscopy,* vol. 55, pp. 88-95, Jan 2002.

CHAPTER 11

11.0 Conclusion, Future Work, and Publications

11.1 Summary of Thesis Work

This thesis project involved a combination of technology development, pre-clinical imaging experiment, and human clinical studies in gastroenterology with the use of three-dimensional optical coherence tomography (3D-OCT). First, a frequency comb swept laser was developed, which can provide narrower instantaneous linewidth and higher phase stability compared to conventional swept lasers while maintaining the compactness and robustness. The demonstration of the light source has enormously enhanced and broadened the applications of the OCT technology, from the volumetric imaging in biomedical specimens, to the profilometry of micro-circuits and micro-fluid, as well as several other areas of research.

A state-of-the-art, Fourier domain mode locked (FDML) laser based cardiovascular 3D-OCT imaging system was modified into an endoscopic system for OCT imaging in the human gastrointestinal (GI) tract, in collaboration with Lightlab Imaging / St. Jude Medical, Inc. Using this system, a 13-patient study was conducted to compare the changes of 3D tissue architectures immediately after the radiofrequency ablation (RFA) and cryospray ablation (CSA), which can be used to assess the treatment efficacy of different ablation therapies. In another 33-patient study, 3D-OCT was used to identify structural features that correlate with RFA treatment response, which can be used to investigate the cause of poor treatment response. These clinical studies demonstrated the clinical utility of endoscopic 3D-OCT imaging that it can reveal the tissue structural information with intrinsic tissue contrast and much larger volumetric coverage than standard biopsy forceps, and potentially can be used to real-time guide biopsy to reduce sampling errors and provide feedback to clinician to make real-time treatment decisions, improving the treatment efficacy of existing ablative therapies.

The development of the balloon based imaging catheters expands the coverage of the endoscopic OCT imaging to the full circumference of the esophagus, allowing the comprehensive mapping the Barrett's esophagus and structural features. The balloon provides uniform pressure over the tissue in contact, so the acquired volumetric OCT data sets are consistent without structural variation due to different pressure applied by the thin imaging catheter. The feature mapping in the esophagus and uniform tissue contact enable better registration of the biopsies taken based on the OCT images, and helps monitoring the tissue architectural changes in the regions of interest (ROIs) due to the treatment in the longitudinal studies.

To overcome the scanning stability issue and the speed limitation of traditional proximally rotary imaging catheters, several miniaturized distally scanning imaging catheter designs were investigated, including piezoelectric transducer (PZT) based actuator and micromotor. The PZT based imaging catheter was demonstrated to achieve record in vivo imaging speed of 960 frames per second (fps) in the rabbit GI tract by sweeping the fiber at the distal end of the imaging catheter. The micromotor based imaging

catheter provides tunable scanning speed from 100 fps to more than 600 fps and can covers much broader scanning area than the PZT based catheters, which was also validated in the rabbit GI tract with an imaging speed of 400 fps. These imaging catheter designs outperformed the traditional scanning method for endoscopic imaging and were the first demonstrated that the ultrahigh speed imaging in live bodies is possible. The ultrahigh speed scanning provides numerous advantages such as less sensitive to the motion in the live bodies, reduced imaging acquisition time, and enhanced imaging quality due to the dense sampling.

With the recent development of vertical-cavity surface-emitting lasers (VCSEL) in collaboration with Praevium Research / Thorlabs, Inc., an ultrahigh speed endoscopic system was developed for clinical studies in gastroenterology. Using the micromotor based imaging catheter, ultrahigh speed OCT imaging was performed in the GI clinics at the Veterans Affairs Boston Healthcare System (VABHS). This system was used in a series of clinical pilot studies including the first demonstration of dysplasia detection in the esophagus based on *en face* pit pattern, the first volumetric imaging in the terminal ileum, and first retroflex volumetric imaging in the hiatal hernia. With the high scanning stability and high speed of imaging system, the world's first endoscopic OCT angiography was also performed in the human GI tract, showing the capability of differentiating the 3D microvasculature between normal and diseased tissues without the need of applying exogenous contrast agents.

These studies have not only demonstrated the clinical utility of the endoscopic OCT imaging in gastroenterology but opened the windows for new applications that could not be done in vivo due to technical limitations. The core technology developed in this thesis work can also be applied to the more traditional OCT niches of screening and initial detection or diagnosis of pathology. With recent focus on the effectiveness and the durability of the endoscopic therapies within the gastroenterology community, ultrahigh speed endoscopic OCT can fill an unmet need for providing on-demand, real-time 3D visualization, and contrast enhancement of subsurface tissue microstructure both pre- and post-treatment, and provide valuable feedback information to further improve the treatment efficacy in the future.

11.2 Future Work

Future efforts for the projects described in this thesis work should focus on three main areas: 1) Advanced imaging catheter designs; 2) Image processing techniques for volumetric data analysis; and 3) Long-term clinical studies.

First, the endoscopic imaging results using the micromotor imaging catheter described in this thesis work emphasize the importance of stable scanning and suggests the use of distal scanning methods for the clinical GI studies. The same idea can be translated into other imaging catheter designs such as balloon or capsule based imaging catheters, so the volumetric data sets with high imaging quality in all dimensions

and full circumference coverage of the GI tract can be obtained and provide comprehensive structural information as well as the precise mapping. The size of the imaging catheter can be further reduced to improve its feasibility in the clinical environment and extend ultrahigh speed OCT imaging applications at more locations in the human body, by using smaller micromotors or distally actuated scanners. Current imaging catheter designs used proximal pullback to achieve slow scan, which can potentially limit the scanning uniformity due to the frictions inside the imaging catheter especially while the imaging catheter is seriously bent. Miniaturized linear actuators, such as squiggle motors, can be used at the distal end of the imaging catheter to achieve true micrometer-level-precision scan in both fast and slow scanning directions so endoscopic optical coherence microscopy (OCM) can be realized to study the in vivo pathology in the GI tract.

Second, volumetric OCT data sets with high frame-by-frame registration can reveal the detailed tissue structure with minimized distortion due to motion or scanning artifacts, so advanced image processing techniques can be used to extract the volumetric information more efficiently. Segmentation techniques can be applied to separate different tissue layers in the squamous mucosa or BE mucosa so the structural features such as thickness of BE epithelium can be automatically quantified immediately after the acquisition of volumetric data set. Pattern recognition techniques can be applied on both cross-sectional and en face images to detect other structural features including subsquamous intestinal metaplasia (SSIM, also known as buried glands), residual/untreated glandular structure immediately after the treatment, and pit patterns of crypts in colon or BE. The development of these techniques will benefit the treatment management as the structural information is immediately fed back to the clinician so appropriate treatment options and dosage can be determined to further improve the treatment outcomes. The algorithms for the endoscopic OCT angiography should also be investigated and the scanning parameters should be adjusted to optimize the performance of the angiography. It is important to reliably show the microvasculature of the lesions in the GI tract so the dysplasia can be accurately detected. The endoscopic angiography can also be useful in other vasculature related studies such as the investigation of tumor-associated neovascularization with the 3D reconstruction of its aberrant architecture.

Finally, long-term clinical studies must build on the initial results demonstrated in this thesis work to decisively convince the clinical community of the utility of endoscopic OCT imaging. Studies of endoscopic OCT for pre- and post-therapy analysis can be conducted with long term follow-up of patients treated with RFA, CSA, endoscopic mucosal resection, photodynamic therapy, argon plasma coagulation, or other emerging endoscopic treatments. Endoscopic OCT could also be studied as an intra-therapy tool for guiding the dosage or resection depth of these therapeutic techniques. Studies in endoscopic OCT screening for dysplasia in the setting of BE or inflammatory bowel disease could also be revisited as fields of view become larger, resolutions become higher, and 3D information becomes more reliable.

Successful clinical studies are the only way for endoscopic OCT to become an accepted clinical tool outside of the specialty research field, and are critical for long-term success of the technology.

11.3 Publications Produced During Thesis Work

Publications [1-16] were produced between 2009 – 2013 during work on PhD thesis.

[1] O. O. Ahsen, Y. K. Tao, Y. Sheykin, B. M. Potsaid, J. Jiang, I. Grulkowski, T.-H. Tsai, V. Jayaraman, M. F. Kraus, J. L. Connolly, J. Hornegger, A. E. Cable, and J. G. Fujimoto, "Swept Source Optical Coherence Microscopy using a 1,310 nm VCSEL Light Source," *Optics Express,* vol. 21, pp. 18021-18033, Jul 2013.

[2] T.-H. Tsai, B. Potsaid, Y. K. Tao, V. Jayaraman, J. Jiang, P. J. S. Heim, M. F. Kraus, C. Zhou, J. Hornegger, H. Mashimo, A. E. Cable, and J. G. Fujimoto, "Ultrahigh speed endoscopic optical coherence tomography using micromotor imaging catheter and VCSEL technology," *Biomed. Opt. Express,* vol. 4, pp. 1119-1132, Jun 2013.

[3] T.-H. Tsai, C. Zhou, H.-C. Lee, Y. K. Tao, O. O. Ahsen, M. Figueiredo, D. C. Adler, J. M. Schmitt, Q. Huang, J. G. Fujimoto, and H. Mashimo, "Comparison of Tissue Architectural Changes between Radiofrequency Ablation and Cryospray Ablation in Barrett's Esophagus Using Endoscopic Three-Dimensional Optical Coherence Tomography," *Gastroenterology Research and Practice,* Article 684832, pp. 1-8, May 2012.

[4] T.-H. Tsai, C. Zhou, Y. K. Tao, H.-C. Lee, O. O. Ahsen, M. Figueiredo, T. Kirtane, D. C. Adler, J. M. Schmitt, Q. Huang, J. G. Fujimoto, and H. Mashimo, "Structural markers observed with endoscopic 3-dimensional optical coherence tomography correlating with Barrett's esophagus radiofrequency ablation treatment response," *Gastrointestinal Endoscopy,* vol. 76, pp. 1104-1112, Dec 2012.

[5] C. Zhou, T. Kirtane, T.-H. Tsai, H.-C. Lee, D. C. Adler, J. Schmitt, Q. Huang, J. G. Fujimoto, and H. Mashimo, "Three-dimensional endoscopic optical coherence tomography imaging of cervical inlet patch," *Gastrointestinal Endoscopy,* vol. 75, pp. 675-677, Mar 2012.

[6] C. Zhou, T. Kirtane, T.-H. Tsai, H.-C. Lee, D. C. Adler, J. M. Schmitt, Q. Huang, J. G. Fujimoto, and H. Mashimo, "Cervical inlet patch-optical coherence tomography imaging and clinical significance," *World Journal of Gastroenterology,* vol. 18, pp. 2502-2510, May 28 2012.

[7] C. Zhou, T.-H. Tsai, H.-C. Lee, T. Kirtane, M. Figueiredo, Y. K. K. Tao, O. O. Ahsen, D. C. Adler, J. M. Schmitt, Q. Huang, J. G. Fujimoto, and H. Mashimo, "Characterization of buried glands before and after radiofrequency ablation by using 3-dimensional optical coherence tomography (with videos)," *Gastrointestinal Endoscopy,* vol. 76, pp. 32-40, Jul 2012.

[8] T.-H. Tsai, B. Potsaid, M. F. Kraus, C. Zhou, Y. K. Tao, J. Hornegger, and J. G. Fujimoto, "Piezoelectric-transducer-based miniature catheter for ultrahigh-speed endoscopic optical coherence tomography," *Biomedical Optics Express,* vol. 2, pp. 2438-2448, Aug 2011.

[9] A. Li, C. Zhou, J. Moore, P. Zhang, T.-H. Tsai, H.-C. Lee, D. M. Romano, M. L. Mckee, D. A. Schoenfeld, M. J. Serra, K. Raygor, H. F. Cantiello, J. G. Fujimoto, and R. E. Tanzi, "Changes in the Expression of the Alzheimer's Disease-Associated Presenilin Gene in Drosophila Heart Leads to Cardiac Dysfunction," *Current Alzheimer Research,* vol. 8, pp. 313-322, May 2011.

[10] C. Zhou, D. W. Cohen, Y. H. Wang, H.-C. Lee, A. E. Mondelblatt, T.-H. Tsai, A. D. Aguirre, J. G. Fujimoto, and J. L. Connolly, "Integrated Optical Coherence Tomography and Microscopy for Ex Vivo Multiscale Evaluation of Human Breast Tissues," *Cancer Research,* vol. 70, pp. 10071-10079, Dec 2010.

[11] C. Zhou, T.-H. Tsai, D. C. Adler, H.-C. Lee, D. W. Cohen, A. Mondelblatt, Y. H. Wang, J. L. Connolly, and J. G. Fujimoto, "Photothermal optical coherence tomography in ex vivo human breast tissues using gold nanoshells," *Optics Letters,* vol. 35, pp. 700-702, Mar 2010.

[12] C. Zhou, Y. H. Wang, A. D. Aguirre, T.-H. Tsai, D. W. Cohen, J. L. Connolly, and J. G. Fujimoto, "Ex vivo imaging of human thyroid pathology using integrated optical coherence tomography and optical coherence microscopy," *Journal of Biomedical Optics,* vol. 15, Jan-Feb 2010.

[13] T.-H. Tsai, C. Zhou, D. C. Adler, and J. G. Fujimoto, "Frequency comb swept lasers," *Optics Express,* vol. 17, pp. 21257-21270, Nov 2009.

[14] D. C. Adler, C. Zhou, T.-H. Tsai, H.-C. Lee, L. Becker, J. M. Schmitt, Q. Huang, J. G. Fujimoto, and H. Mashimo, "Three-dimensional optical coherence tomography of Barrett's esophagus and buried glands beneath neosquamous epithelium following radiofrequency ablation," *Endoscopy,* vol. 41, pp. 773-776, Sep 2009.

[15] D. C. Adler, C. Zhou, T.-H. Tsai, J. Schmitt, Q. Huang, H. Mashimo, and J. G. Fujimoto, "Three-dimensional endomicroscopy of the human colon using optical coherence tomography," *Optics Express,* vol. 17, pp. 784-796, Jan 2009.

[16] C. Zhou, D. C. Adler, L. Becker, Y. Chen, T.-H. Tsai, M. Figueiredo, J. M. Schmitt, J. G. Fujimoto, and H. Mashimo, "Effective treatment of chronic radiation proctitis using radiofrequency ablation," *Therapeutic Advances in Gastroenterology,* vol. 2, pp. 149-156, May 2009.